

1 February 2013 | \$10

# Science

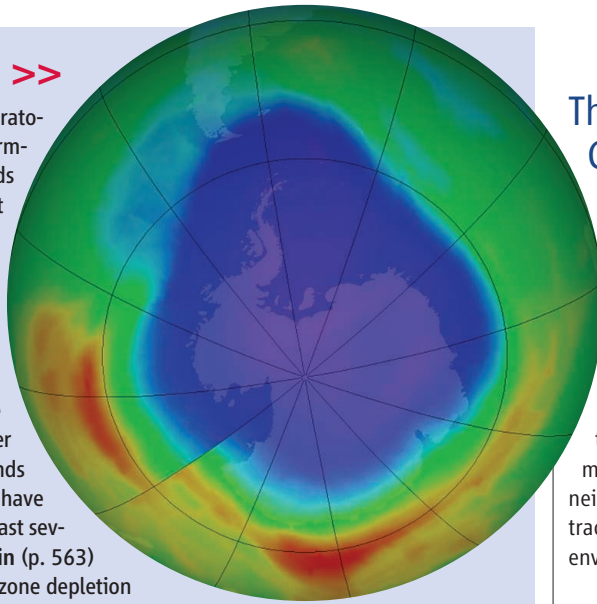
2012 Visualization Challenge

 AAAS



## The Change of Winds >>

As the combined effects of Antarctic stratospheric ozone depletion and climate warming have forced the westerly surface winds in the Southern Hemisphere to shift toward the pole, mixing between the upper ocean and deeper waters has also changed. **Waugh *et al.*** (p. 568) now show that water originating at the surface at subtropical latitudes is mixing into the deeper ocean at a higher rate than 20 years ago, while the reverse is true for those originating at higher latitudes. The summer westerly winds that blow in the Southern Hemisphere have shifted toward the South Pole over the past several decades, but why? **Lee and Feldstein** (p. 563) show that greenhouse gas forcing and ozone depletion impart different signatures to wind patterns and conclude that ozone depletion has been responsible for more than half of the observed shift.



## Exploiting Carbon Nanotubes

Individual defect-free carbon nanotubes can have exceptional mechanical, thermal, and electrical properties, which has led to speculation on a wide range of potential applications. However, challenges in growing large quantities of pure nanotubes, and for some applications tubes of only one type, have limited their widespread use. **De Volder *et al.*** (p. 535) review the efforts that have been made to scale up carbon nanotube production and discuss a number of applications where enhanced materials have made use of carbon nanotubes.

## The Third Way

Because organic carbon contains a larger fraction of the light isotope  $^{12}\text{C}$  than inorganic carbonate, variations in the carbon isotopic record of sedimentary rocks are thought to represent changes in the amount of organic carbon buried as sediments (and thus removed from the rest of the carbon cycle). **Schrag *et al.*** (p. 540; see the Perspective by **Canfield and Kump**) suggest that historically a third component was important: authigenic carbonate. Authigenic carbonate is not produced in any appreciable quantity today, but was much more abundant when the level of atmospheric oxygen was low.

## Not Just Wasting

Malnutrition is well known in Malawi, including a severe form—kwashiorkor—in which children do not simply waste away, they also suffer edema,

liver damage, skin ulceration, and anorexia. **Smith *et al.*** (p. 548; see the Perspective by **Relman**) investigated the microbiota of pairs of twins in Malawian villages and found notable differences in the composition of the gut microbiota in children with kwashiorkor. In these children, a bacterial species related to *Desulfovibrio*, which has been associated with bowel disease and inflammation, was noticeable. When the fecal flora from either the healthy or the sick twin was transplanted into groups of germ-free mice, the mice that received the kwashiorkor sample started to lose weight, like their human counterpart.

## Nanoscale NMR with Diamond Defects

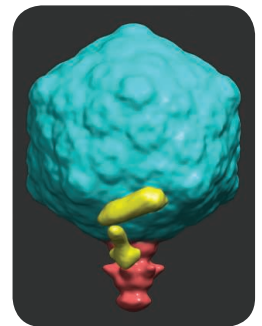
Although nuclear magnetic resonance (NMR) methods can be used for spatial imaging, the low sensitivity of detectors limits the minimum sample size. Two reports now describe the use of near-surface nitrogen-vacancy (NV) defects in diamond for detecting nanotesla magnetic fields from very small volumes of material (see the Perspective by **Hemmer**). The spin of the defect can be detected by changes in its fluorescence, which allows proton NMR of organic samples only a few nanometers thick on the diamond surface. **Mamin *et al.*** (p. 557) used a combination of electron spin echoes and pulsed NMR manipulation of the proton spins to detect the very weak fields. **Staudacher *et al.*** (p. 561) measured statistical polarization of a population of about  $10^4$  spins near the NV center with a dynamical decoupling method.

## The Power of the Collective

Sensing the environment is generally considered to require significant cognitive sampling and comparison, not to mention time. However, species that do not necessarily have the cognitive ability, or the time, have also proven to be quite adept at sensing and evaluating their environment. **Berdahl *et al.*** (p. 574) show that in shiners, a species of schooling fish, mere attraction to, and movement toward, neighboring individuals allows the group to track preferred darkness in a variable-light environment.

## Phage Invasion

Bacteriophages are responsible for much of bacterial evolution, both by imposing selection for resistance to infection and by horizontal gene transfer of host genes to new bacteria. However, we know surprisingly little about the initiation of phage infection. **Hu *et al.*** (p. 576, published online 10 January) used high-throughput cryo-electron tomography and sub-volume analysis to examine *Escherichia coli* mini-cells infected with both wild-type and mutant T7 bacteriophages. High-resolution views of phage structures at different stages of infection reveal the de novo formation of an extended tail by the ejection of internal head proteins, in order to form the channel for DNA transport into the cytoplasm.



## Dissecting Microtubule Stability

Microtubule-stabilizing agents (MSAs), like taxol, inhibit cell division and are widely used in cancer chemotherapy. **Prota *et al.*** (p. 587, published online 3 January) present structural data on the molecular mechanism of action of antimetabolic drugs. Tubulin structures in complex with the MSAs zampanolide and epothilone A, revealed a general mechanism for how MSAs promote microtubule assembly and stability by affecting lateral tubulin interactions.





Janet Coffey is a program officer with a focus on science learning at the Gordon and Betty Moore Foundation, Palo Alto, CA, and a former faculty member in science education at the University of Maryland, College Park, MD. E-mail: janet.coffey@moore.org.



Bruce Alberts is Editor-in-Chief of *Science*.

## Improving Education Standards

THIS MONTH, ACHIEVE, AN ORGANIZATION ESTABLISHED BY THE 50 U.S. STATE GOVERNORS to improve academic standards and testing, will begin finalizing its draft document (released in January 2013) of the Next Generation Science Standards (NGSS).<sup>\*</sup> This document aims to establish new common standards for science education for students aged 5 to 18 in the United States, and it explicitly builds on the U.S. National Academies' 2011 Framework for K-12 Science Education.<sup>†</sup> The Framework put forth a vision of science education that is notable for emphasizing student participation in key science and engineering practices, such as asking questions and defining problems; developing and using models; engaging in argument from evidence; and learning cross-cutting concepts such as energy and matter, cause and effect, and structure and function. To allow room for these in the school day, the Framework stressed the importance of minimizing the number of disciplinary core ideas that standards require to be taught. Now that the NGSS document has entered its final revision stage, it is important to ask how well these standards match the powerful vision for them that was laid down by the Framework.

There is much to be commended in the draft. In particular, its emphasis on science and engineering practices could lay the groundwork for productive shifts toward helping students understand how science helps us make sense of the natural world, instead of just what science has learned. But the sheer volume of content referenced in the Framework moves to the foreground in the NGSS draft and threatens to undermine this promise. Any emphasis on practices requires a science-rich conceptual context, and certainly the core ideas and cross-cutting concepts presented are useful here. However, the draft contains a vast number of core disciplinary ideas and sub-ideas, leaving little or no room for anything else. In the three grades of middle school (ages 11 to 13) alone, the NGSS draft specifies more than twice the disciplinary content than did the 1996 National Science Education Standards. Thus, before finalizing the new standards, we urge Achieve to quickly convene small groups of the nation's best teachers at the primary, middle-school, and high-school levels. Although teachers have been involved in the writing effort, their new charge should be to bring ground truth to the NGSS by determining the maximum number of disciplinary core ideas that can be covered in a single school year, while still leaving time for a productive focus on practices and cross-cutting ideas. And scientists should immediately be charged with prioritizing the disciplinary core ideas in the current draft (and their performance expectations) to reduce them to a more feasible number.

The welcome shift in priorities to teaching science and engineering practices along with the content brings an assessment challenge. The NGSS draft document addresses this challenge by delineating many performance expectations. However, current measurements and approaches do not allow these types of performances to be assessed easily; it is much more difficult to evaluate the quality of such engagement than to determine the accuracy of an explanation or a word definition. Urgently needed is a vigorous R&D agenda that pursues new methods of and approaches to assessment. This will be difficult but critically important long-term work. A systematic commitment to the wrong quantitative measures, such as the inexpensive multiple-choice testing of factoids, may well result in the appearance of gains at the tremendous cost of suppressing important aspects of learning, attending to the wrong things in instruction, and conveying to students a distorted view of science. Outstanding scientists must be willing to work side by side with measurement specialists and science educators to develop methods for evaluating what is important to measure, after completing the short-term task of prioritizing and reducing the number of disciplinary core concepts in the new standards.

— Janet Coffey and Bruce Alberts

10.1126/science.1225590

<sup>\*</sup>[www.nextgenscience.org/next-generation-science-standards](http://www.nextgenscience.org/next-generation-science-standards).

<sup>†</sup>[http://www7.nationalacademies.org/bose/Standards\\_Framework\\_Homepage.html](http://www7.nationalacademies.org/bose/Standards_Framework_Homepage.html).







## ECOLOGY

### Changes at the Core

Airborne pollen grains deposited in sediments—particularly in undisturbed lake beds—are a crucial element in understanding how vegetation and its constituent species respond to changing climates. Research on the high-altitude lake sediments from the Bogotá basin in the Colombian Andes has produced a rich record of climate and vegetation over the Quaternary period. In particular, two deep sediment cores obtained in the late 1980s have provided detailed information on climatic fluctuations and vegetation change. However, interpretation of the record has been hampered by uncertainties. Torres *et al.* now present a new analysis of these cores, in which many of the technical challenges concerning the chronology have been addressed. The development of the Andean forest and high-altitude páramo vegetation—the uniquely Andean biome that occurs above the treeline and has evolved *de novo* with the uplift of the Andes—was shown to be a dynamic process, with ephemeral associations of plant species continually fluctuating over the past 2 million years as temperatures rose and fell with glacial cycles. This unbroken record provides further evidence that plant communities at any given point in time often have no analog, in terms of species composition, with past or future associations of species. — AMS

*Quat. Sci. Rev.* **63**, 59 (2013).

## BIOCHEMISTRY

### Signaling by Unfolding

In response to DNA damage, nuclear p53, a tumor suppressor, induces expression of the p53 up-regulated modulator of apoptosis (PUMA). PUMA in turn regulates the activity of cytosolic p53. In the cytosol, p53 is sequestered by the anti-apoptotic protein BCL-xL, a member of the BCL-2 family of anti-apoptotic proteins. PUMA disrupts this interaction and frees p53 to initiate apoptosis. BCL-2 proteins are composed of BCL-2 homology (BH) domains, and PUMA is a single-BH domain protein. Follis *et al.* used NMR spectroscopy and biophysical methods to

show that PUMA is intrinsically unstructured, but that its BH3 domain folds upon binding to a hydrophobic groove in BCL-xL. NMR spectroscopy and x-ray crystallography showed that PUMA binding caused partial unfolding of two helices in BCL-xL. Although PUMA forms complexes with other anti-apoptotic complexes, it did not induce similar structural perturbations in these proteins. Structural data suggested that a  $\pi$ -stacking interaction between Trp-71 of PUMA and His-113 of BCL-xL was key to the destabilization of regions of the BCL-xL structure. Thus, the p53 apoptotic pathway is activated by regulated unfolding of an anti-apoptotic protein. — VV

*Nat. Chem. Biol.* **10**, 1038/NCEMBIO.1166 (2013).

## ECOLOGY

### Downstream Discharge

Wastewater has the potential to serve as a renewable source of energy, nutrients, and clean water. However, most wastewater is treated minimally to remove pathogens and organic matter and released into the environment. In highly urbanized, developed areas, a single river may receive discharged effluent from several wastewater treatment plants, so that a sizable fraction of the downstream water is recycled wastewater. By studying two rivers in and around Chicago, Drury *et al.* showed that although wastewater effluent released into rivers may meet water quality standards, it can have an impact on downstream ecosystems. Discharged effluent resulted in increased nutrients such as nitrate and phosphate in the water column and, perhaps surprisingly, decreased sediment organic

matter. The downstream sediments showed decreased bacterial abundance and diversity, shifting from communities that included sulfate-reducing bacteria to communities dominated by nitrate-oxidizing bacteria. Although the two rivers have very different biological and chemical properties upstream of the wastewater treatment plants, they were homogenized to the point where they were nearly indistinguishable downstream. — NW

*Appl. Environ. Microbiol.*

**10.1128/AEM.03527-12** (2013).

## MOLECULAR BIOLOGY

### RNA Methylation and Metabolism

The methylation—and demethylation—of DNA play an important role in the dynamic regulation of gene expression and in genome stability. RNA in eukaryotes is also methylated on the A base ( $m^6A$ ), the most abundant posttranscriptional modification of mammalian mRNA. The modification is known to have biological function in meiosis and sporulation in yeast and potentially in RNA processing in mammalian cells.

Zheng *et al.* identify a mammalian RNA demethylase, ALKBH5, that is capable of removing the  $m^6A$  mark from RNA both *in vitro* and *in vivo*. The ALKBH5 protein localized to nuclear speckles and associated with specific mRNA processing factors there, and also affected mRNA export, with both functions requiring the ALKBH5 demethylation activity. A knockout of the ALKBH5 gene in mice resulted in reduced male fertility and revealed



that the demethylase influences the expression of many genes, including key genes involved in spermatogenesis, resulting in defects in spermatogenesis and aberrant apoptosis in the testes of the mutant male mice. Thus, the dynamic methylation and demethylation of RNA, like DNA, may play an important role in gene regulation. — GR

*Mol. Cell* **49**, 18 (2013).

## MICROBIOLOGY

### Probing the Microbial Mix

In the past decade, it has become apparent that we are colonized by microbes that probably shape many of our most important physiological processes. Much of the work has taken a metagenomics approach—characterizing what microbes are there and what genes they express. Maurice *et al.* now go one step further and begin to investigate how our microbial inhabitants respond to pharmacological perturbations. A combination of single-cell analysis by flow cytometry, DNA sequencing, and metatranscriptomics revealed that the bacteria within the human gut vary with respect to membrane integrity, polarization, and metabolic activity. Metabolic activity was enriched in Firmicutes, whereas Bacteroidetes were less metabolically active. Exposure to both antibiotics and host-targeted

drugs resulted in alterations in the physiology, structure, and gene expression profile of the bacteria. An increase in genes associated with resistance, stress responses, and metabolism was observed after antibiotic treatment. These results represent an important step toward understanding on a broad scale how specific perturbations affect our microbial communities. — KLM

*Cell* **152**, 39 (2013).

## CHEMISTRY

### Keeping Pigments in Sync

It has been clear for decades that photosynthesis involves an intricate chain of energy transfer steps, channeling the energy in light absorbed by dedicated pigments to a central complex that chemically splits water. Over the past 7 or 8 years, the advent of two-dimensional electronic spectroscopy has offered an increasingly detailed understanding of how the transfer process works. In particular, the data suggest a persistence of quantum-mechanical coherence—essentially a

steady phase relationship in electronic excitation across the donors and acceptors that facilitates efficient transfer—for a much longer time than the complex molecular structure of the system would seem to allow. The underlying mechanism for sustaining coherence has remained somewhat mysterious and subject to debate. Tiwari *et al.* have modeled the transfer process in a framework that allows mixing of vibrational and electronic excitation, and they find that anticorrelated vibrations across the associated proteins (i.e., contraction on one side concurrent with extension on the other) could mediate electronic dynamics that give rise to the spectral signatures observed in the experiments. They further note that certain pigment vibrational frequencies match the associated electronic energy gaps, lending further plausibility to this mechanism. — JSY

*Proc. Natl. Acad. Sci. U.S.A.* **110**, 1203 (2013).

## OCEAN SCIENCE

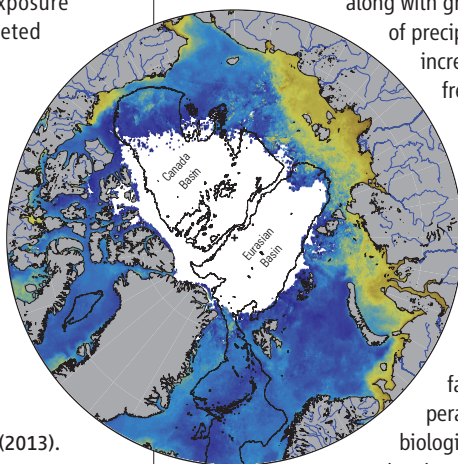
### Runoff in the Arctic

The Arctic is a bellwether region for climate change, with temperatures there increasing at approximately twice the global average rate. That rapid temperature rise has caused widespread melting of sea ice, land ice, and permafrost which,

along with greater amounts of precipitation, have increased the flux of fresh water into northern high-latitude seas. This enhanced freshwater input has many important effects on the Arctic Ocean—namely, on surface salinity, temperature structure, biological productivity, and carbon sequestration.

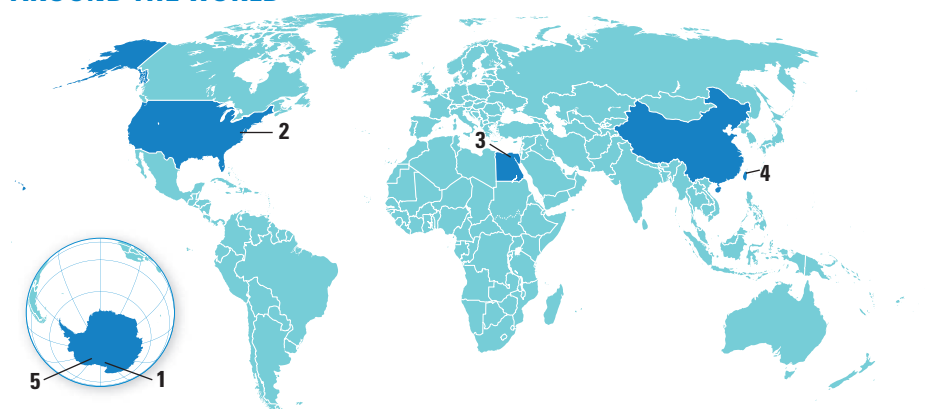
To determine the distribution of continental runoff in the Arctic Ocean over the past decade, Fichot *et al.* developed an optical proxy for terrigenous dissolved organic matter, which they implemented using remote sensing of ocean color from space. By measuring the amounts of dissolved organic matter in the ocean's surface, they illustrate how runoff has changed over the past decade across the entire pan-Arctic region. This approach should be an important tool for monitoring the effects of climate change on this high-latitude region. — HJS

*Sci. Rep.* **3**, 1053 (2013).





## AROUND THE WORLD



Mount Elizabeth, Antarctica 1

**No Survivors in Antarctic Plane Crash**

The wreckage of a Twin Otter aircraft that went missing in the Antarctic was found near the summit of a mountain in the Queen Alexandra mountain range, about 700 kilometers from both the South Pole and the United States' McMurdo Station. The plane, which was to be used as part of Italy's polar



research program, crashed on 23 January, but bad weather prevented rescuers from reaching it for several days. The three Canadian crew members that were aboard the plane are all presumed to have died in the crash. Why the plane crashed was still unclear when *Science* went to press. Citing poor weather conditions, on 28 January officials with the United States Antarctic Program and Antarctica New Zealand jointly chose to recall search-and-rescue teams from the site and delay efforts to recover any remains until the next Antarctic research season.

Washington, D.C. 2

**Sandy Relief for Hurricane Hunters**

Hurricane researchers are about to get some new wings. The U.S. Senate on 28 January approved a \$50.5 billion bill designed to help people recover from last year's superstorm

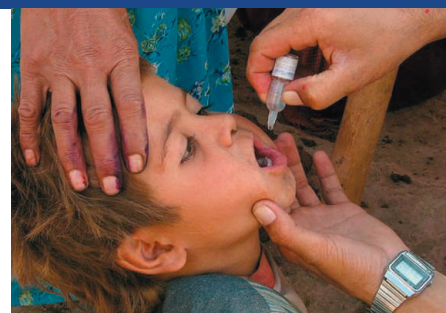
Sandy. It includes more than \$250 million to help the National Oceanic and Atmospheric Administration (NOAA) replace and repair buoys, radars, and other research assets damaged by the storm, as well as to strengthen weather and coastal science programs designed to track future storms. The total includes \$111 million to cover an expected data gap when several weather satellites die over the next few years, \$50 million for the agency's cooperative research programs in northeastern states, and \$44.5 million to put new wings on two of NOAA's aging Orion "hurricane hunter" aircraft.

Cairo 3

**Polio Virus Spreads From Pakistan to Egypt**

Egyptian and international health officials are on high alert after poliovirus from Pakistan was discovered in sewage water collected during routine sampling in Cairo in December. Genetic sleuths linked the Cairo poliovirus to one last seen in Sindh Province in Pakistan in September 2012, the World Health Organization (WHO) reported last week. How the virus got to Cairo is unclear—people can carry the virus asymptotically when they travel—but the analysis, conducted by the U.S. Centers for Disease Control and Prevention, suggests that it made the leap in the past few months. Egypt has not had a case of polio since 2004.

So far, no polio cases have been detected in Cairo, and there is no evidence that the virus is circulating widely. But the risk that this imported virus could spark an outbreak there is real, says Bruce Aylward, who runs the global polio eradication effort from WHO in Geneva, Switzerland. Emergency vaccination campaigns are slated for Cairo and the rest of the country in the



next few weeks. Meanwhile, Pakistan, one of just three countries where polio is still entrenched, is under even more pressure to stamp out the virus within its borders. <http://scim.ag/polioEgypt>

Taipei 4

**'Richer-Than-Nobel' Science Prize Comes With a Twist**

A Taiwanese tycoon has established a new science prize that will not only pay out more than the Nobel Prize but will support research as well. Individuals or institutions that have demonstrated the most creative and influential research in four fields will receive about \$1.36 million, while an additional \$341,000 will support a plan proposed by recipients to support research and develop talent in a related area over 5 years. (The Nobel Prize amount for 2012 was about \$1.2 million.)

The Tang Prizes, named after China's Tang Dynasty, will be awarded biennially for work in sustainable development, biopharmaceutical science, sinology (excluding literary works), and rule of law. Samuel Yin, who made a fortune in diversified real estate, financial, and retail investments, is endowing the prize. Academia Sinica, which oversees Taiwan's premier research labs, will be responsible for the nomination and selection process. The first prize announcement is set for July 2014.

Whillans Ice Stream, Antarctica 5

**U.S. Mission to Whillans Ice Stream a Success**

A U.S.-based team announced on 28 January that it had successfully retrieved its first samples of sediment and water from the Whillans Ice Stream, a body of water sealed nearly a kilometer below the Antarctic ice. The interdisciplinary project is looking for subglacial microbial life, and also studying the continent's climate history and ice sheet dynamics. The samples of sediment and basal ice from beneath the water are expected to help scientists understand whether subglacial lakes act to stabilize or



destabilize the West Antarctic Ice Sheet.

The team is the second of three research groups this season to achieve its goal of retrieving samples from some of the continent's mysterious buried waters. In December, a British Antarctic Survey team seeking to penetrate subglacial Lake Ellsworth was forced to pull the plug on its mission due to technical problems. Last month, a Russian team nabbed its first sample from subglacial Lake Vostok.

## NEWSMAKERS

### Three Q's

Biotechnologist **Hayat Sindi** received her Ph.D. from the University of Cambridge and was a visiting scholar at Harvard University before returning to Saudi Arabia in 2011 to create an institute to promote science and entrepreneurship. She's one of the first 30 women to be appointed to the country's 150-member Shura Council, which advises the government on science and technology.



Sindi

**Q: What issues are you hoping to address as a council member?**

**H.S.:** I'm [geared] toward entrepreneurship and how we can encourage our youth to be innovative. Also, I'm interested in women's issues. So I'm going to concentrate on innovation, scientific research, youth, and women.

**Q: How do you see the role of science in the Middle East and around the world?**

**H.S.:** Science was born to solve problems, to look at how to improve quality of life. What I'm trying to figure out is how can I make science affordable and accessible to everybody?

**Q: What does having women on the Shura Council mean for women in Saudi Arabia?**

**H.S.:** This is the best thing to happen [for Saudi women] since women were permitted to study. Women look at different problems with different angles, in terms of economics or science or health or social studies. We cannot ignore [their] contribution.

## Deep-Sea, Semiconductor Research Net Japan Prizes

Research at the bottom of the sea and wizardry in semiconductor clean rooms have netted this year's Japan Prizes, among the world's top science and technology awards.



## Astrophysics Over Antarctica: Balloon Breaks Flight Record

Now on its third orbit around the South Pole, a NASA scientific balloon has broken the record for the longest-flying balloon of its size. As it soars at an altitude of 39,000 meters—about the same stratospheric height from which daredevil Felix Baumgartner completed his record-breaking space dive last October—the balloon wields an instrument called the Super Trans-Iron Galactic Element Recorder (more pithily known as Super-TIGER), which measures heavy elements in the flux of high-energy galactic rays that bombard Earth. Super-TIGER, which launched on 8 December 2012 from a site near McMurdo Station, had stayed aloft for 46 days when *Science* went to press, shattering the previous record of 41 days for a long-duration scientific balloon, set in 2005. The team plans to continue flying it for another week or so to bring it closer to McMurdo before ending its flight.



Fréchet



Grassle



Willson

Each category carries a 50 million yen (\$550,000) award, which laureates will receive along with medals at a ceremony in Tokyo in April.

Marine ecologist **J. Frederick Grassle** of Rutgers University in New Brunswick, New Jersey, won for his studies of deep-sea hydrothermal vent ecosystems and organisms. He also helped launch the Census of Marine Life, intended to catalog the diversity of marine life, and the Ocean Biogeographic Information System, which is used in marine conservation efforts.

Chemists **Grant Willson**, now of the University of Texas, Austin, and **Jean Fréchet**, of King Abdullah University of Science and Technology in Thuwal, Saudi Arabia, won for developing chemically amplified resists: photosensitive materials that allow semiconductor makers to shrink integrated circuits for microprocessors and memory chips, such as those in personal computers and mobile phones.

## NIH Loses a Senate Champion

The National Institutes of Health (NIH) will lose one of its longtime champions with the upcoming retirement of Senator **Tom Harkin** (D-IA). Last week, Harkin announced he would not seek a sixth term, ending a 40-year congressional career.

Harkin is currently chair of the Senate panel that sets funding levels for NIH, and he also chairs the committee that oversees federal policies in health, education,



Harkin

and labor. He teamed up with his then-Republican counterpart, Arlen Specter of Pennsylvania, to win a doubling of the NIH budget from 1998 to 2003. He and Specter also led an effort to include \$10.4 billion for

NIH in the 2009 stimulus package.

With Specter, Harkin also sponsored legislation in the 2000s that would have expanded federal funding for research on human embryonic stem cells. But Harkin didn't always please scientists: In the 1990s, he pushed to create NIH's National Center for Complementary and Alternative Medicine, which critics claim wastes money testing fringe treatments. <http://scim.ag/Harkinret>

## Random Sample

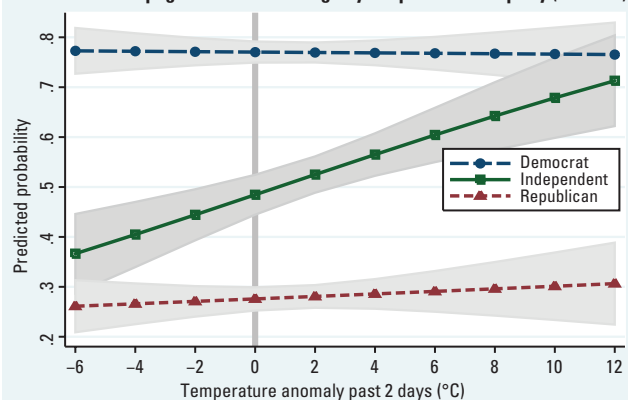
## Independents Follow Where the Wind Blows

U.S. voters who straddle the political fence—self-identifying as independents who lean neither left nor right—are most susceptible to short-term temperature fluctuations when it comes to whether they believe humans are causing climate change, according to a new study.

Sociologist Lawrence Hamilton of the University of New Hampshire (UNH), Durham, used data from some 5000 random telephone interviews of New Hampshire voters conducted over a 2.5-year span. The interviewers asked voters about their political affiliations and views on climate change—whether it's happening and, if so, whether it is "caused mainly by human activities." The poll also asked the voters to rate their political affiliation (on a scale of one to seven, with four representing independents).

Then, Hamilton and UNH geographer Mary Stampone compared the answers to temperature and precipitation data collected across the state. They found no pattern associated with precipitation. Temperature was another story. Whereas Democrats and Republicans tended to stick to their beliefs regardless of how hot or cold it was, independents were strongly influenced by temperature (see graph). When interviewed on unseason-

Belief in anthropogenic climate change by temperature and party (n = 4897)



ably warm days, independents tended to agree that humans are causing climate change. On unseasonably cool days, they tended to think the opposite, the team reported last month in *Weather, Climate, and Society*.

It's a striking graph, Hamilton notes. "If ever a logit regression plot could go viral, that might be the one." But the pattern is not totally unexpected, he says. Past studies have shown that "minor experiential things," such as room temperature, can alter how subjects answer a question.

## FINDINGS

## With Genomes, Pecking Away At Pigeons' Plumage

For centuries, bird breeders have cultivated pigeons with a startling variety of colors, feather arrangements, and behaviors, creating about 350 breeds that compete to be the fastest, longest-flying, or most beautiful.



Now, Michael Shapiro, an evolutionary biologist at the University of Utah in Salt Lake City, and his colleagues have tracked down the mutation leading to one of the pigeon's more ostentatious traits: its head crest, which ranges from

a simple peak to a hood of plumage. Using the pigeon genome newly sequenced by BGI in Shenzhen, China, Shapiro and colleagues found that the presence of a crest of any sort is determined by a gene called *EphB2*, they report online this week in *Science*. Now, researchers can look to see if this gene leads to head crests in wild birds. "The work now puts the spot on pigeons ... [and] may attract other scientists to start using pigeons as

## Science LIVE

Join us on Thursday, 7 February, at 3 p.m. EST for a live chat with experts about a hot topic in science. <http://scim.ag/science-live>

models," says Hans Ellegren, an evolutionary biologist at Uppsala University in Sweden who was not involved with the work. <http://scim.ag/pigeonplum>

## Paradox Lost

Last April, Masud Mansuripur, an electrical engineer at the University of Arizona in Tucson, claimed classical electrodynamics and relativity can lead to a paradox. Now, four physicists say in comments in press at *Physical Review Letters* that they have resolved the contradiction.

Mansuripur's paradox posited an electric charge sitting near a magnet. In the "reference frame," where both are stationary, they don't interact. But, in the "moving frame," where they glide together, the magnet feels a twisting torque, according to both relativity and the standard formula for electric and magnetic forces. Yet the magnet can't spin in one frame and not in the other—so the force formula must be wrong, Mansuripur argues.

But, others say, relativity demands that the magnet possess "hidden angular momentum," which, in the moving frame, constantly increases. So the torque in that frame feeds the hidden angular momentum instead of spinning the magnet. Problem solved.

Mansuripur says hidden momentum is an ill-defined concept that papers over the problem. But Daniel Vanzella of the University of São Paulo in São Carlos, Brazil, says it's bedrock relativity, "not an ad hoc invention put in to reconcile things." <http://scim.ag/Lorpara>

## Genes the Secret to Surviving A Siberian Winter

Frigid Siberia has been home to humans for tens of thousands of years, including *Homo sapiens* and Neandertals. A study of today's Siberian peoples, presented last month at the Unravelling Human Origins meeting in Cambridge, U.K., finds that their genes may help them adapt to cold conditions.

Alexia Cardona, a graduate student at the University of Cambridge, and her colleagues analyzed 200 DNA samples from 10 indigenous Siberian populations and looked for genes that might correlate with cold adaptation.

Using techniques that detect natural selection in the human genome—that is, genetic variants favored by evolution because they



helped humans survive and reproduce—Cardona found evidence for such variants in three genes in the Siberian populations. One gene, called *UCP1*, helps convert fat directly into heat to keep the body warm.

A second, called *ENPP7*, is implicated in the metabolism of fats from meat and dairy products. And a third gene, *PRKG1*, is involved in smooth muscle contraction, key to shivering and the constriction of blood vessels to avoid heat loss. <http://scim.ag/coldgenes>



## RESEARCH FUNDING

# Graphene and Brain Projects Win European Jackpot

**BRUSSELS**—There was no champagne and no Academy Awards-style ceremony, not even flowers for the winners, when Neelie Kroes, the Dutch vice president of the European Commission, announced the outcome of the biggest research funding competition in Europe's history here on 28 January.

The low-key proceedings were in stark contrast to the massive hopes riding on two futuristic projects that may now get up to €1 billion each—one to study a promising new material called graphene, and the other to model the entire human brain. The projects, Kroes promised, would help to “keep Europe as the home of scientific excellence” and “fertilize the green shoots of economic growth” in the struggling union. “Today,” she added, “there aren’t just two winners, there are 500 million winners.”

The anointment marked the end of a grueling process during which six international teams had produced extensive research plans for the Future and Emerging Technologies Flagship Initiatives, as well as elaborate PR campaigns. The two winning groups will now enter into negotiations with the commission to agree on the exact research plan.

Yet doubts and questions remain. Some neuroscientists are surprised that the Human Brain Project, a controversial effort to integrate data from tens of thousands of papers published in the field every year, came out on top. The selection process, opaque even to the winners, has frustrated some participants, and it’s unclear whether the promised €1 billion in funding will materialize; it could be far less.

The Flagship Initiatives were created to fund two large-scale projects with a “visionary goal.” The four that did not make it to the finish included an ambitious effort to model society, called FuturICT, in order to predict financial crises or revolutions; a computer-generated “virtual patient” to test therapies; a new generation of user-friendly robots for the home; and a project to develop “guardian angel” chips that would monitor people and environments and warn of impending dangers (*Science*, 4 January, p. 28).

For Henry Markram of the Swiss Federal Institute of Technology in Lausanne, who heads the Human Brain Project, the announce-

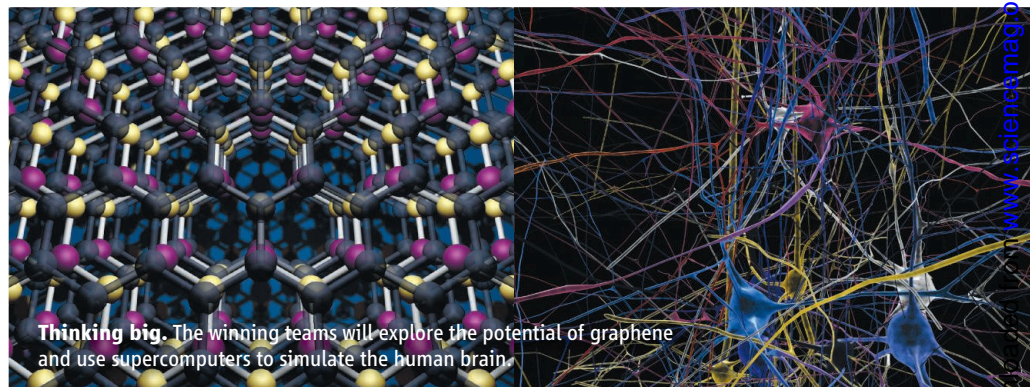
ment was a personal triumph. Critics have dismissed the effort to recreate the human brain in silico as misguided and a possible diversion of money from more immediate research questions in neuroscience (*Science*, 11 November 2011, p. 748). Rather than divide the field, Markram says he hopes to unite it by bringing everything that’s known in neuroscience together. “At the moment, everyone is digging in his little corner,” he says. “We are asking the whole world of neuroscience to come together.”

The success of Graphene, a project led by Jari Kinaret of Chalmers University of Technology in Gothenburg, Sweden, was less of

have volunteered to commit anything. Still, Kroes said that she was “nearly certain” the €1 billion promise would be fulfilled.

Scientists are still scratching their heads over the selection process. “The goalposts kept moving and that was very frustrating at times,” Kinaret says. Dirk Helbing of the Swiss Federal Institute of Technology in Zurich, who coordinated FuturICT, says planning “disruptive technologies” 10 years ahead isn’t really possible to begin with. What the Flagship Initiatives asked of scientists, he says, is, “Please write down how you would start a company like Microsoft or Facebook.”

In the end, two of the six proposals short-listed in 2011 weren’t even asked to defend their proposals before an expert panel that made the final cut last December. “After [we spent] more than a year and €1.5 million on writing a detailed research plan, they should at least have invited us and listened to us,” says Hans Lehrach, coordinator of the virtual patient proposal. Wolfgang Boch, who coor-



a surprise. The plan is to develop new applications for graphene, which is made up of single layers of carbon atoms; the research is expected to lead to innovative products such as better batteries or flexible electronics. Among the partners are groups from more than 50 universities in 17 countries, but also companies such as Airbus and Nokia.

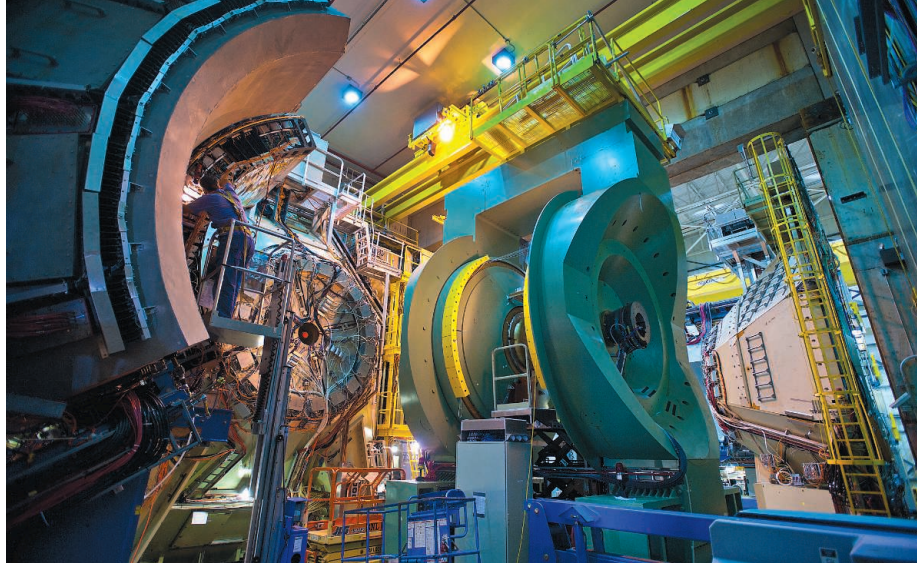
Kinaret isn’t sure, however, of what exactly his group has won. Over the first 30 months, each project will receive only €54 million—an amount that Kinaret says disappointed many of his collaborators. “We thought the budget would be higher,” he says. Funding is supposed to ramp up to €100 million a year per project, but that depends on Europe’s new science and innovation program, Horizon 2020, and its uncertain budget (*Science*, 16 November 2012, p. 872.) Moreover, the European Union is counting on member states to provide half the money; few countries so far

dinates the initiatives at the European Commission, says the two projects simply didn’t surpass a scoring threshold set by the panel.

Still, even the losers expect a payoff from their blood, sweat and tears. The Guardian Angels project has announced that it will live on with funding from its consortium. FuturICT, too, hopes to build on the momentum and visibility from crafting its proposal. “This has brought together social scientists, engineers, and other scientists in an unprecedented way,” Helbing says. “But the most important thing was that Europe dared to do this at all.”

That’s a sentiment echoed by Anne Glover, chief scientific adviser to the European Commission. Europe has a problem translating research into technological leadership, she says; the Flagship Initiatives try to address that. “Is this the right thing to do? I don’t know. Should we try it? Absolutely!”

—KAI KUPFERSCHMIDT



## NUCLEAR PHYSICS

# If Budget Woes Continue, Panel Says DOE Should Shut Last U.S. Collider

**BETHESDA, MARYLAND**—This week a committee of nuclear scientists recommended that the cash-strapped Department of Energy (DOE) shut down the last grand U.S. atom-smasher, the Relativistic Heavy Ion Collider (RHIC) at Brookhaven National Laboratory in Upton, New York. The closing would be necessary to free up money for a new nuclear physics facility, says a report to DOE's Nuclear Science Advisory Committee (NSAC).

But the physicists whose project, the Facility for Rare Isotope Beams (FRIB), came out on top in the committee's report aren't gloating. Along with the rest of the nuclear physics community, they fear that any trade-off will lead to a massive contraction of U.S. nuclear physics.

"That's what is really coming out of this report: There are no really good solutions," says Konrad Gelbke, a physicist at Michigan State University in East Lansing, which would host FRIB. That's a sentiment stressed by Robert Tribble, a nuclear physicist at Texas A&M University, College Station, who chaired the committee. "We're all losers if this comes to pass," he says. "It's pretty clear we will lose a facility that supports or will support more than a quarter of the nuclear science workforce."

The problem is that DOE's \$547-million-a-year nuclear physics program is facing the prospect of stagnating budgets at the same time that it is trying to expand its portfolio of activities. In addition to operating RHIC and readying plans for the \$615 million FRIB, the office is completing a \$310 million upgrade to the Continuous Electron Beam Accelerator Facility (CEBAF) at Thomas Jefferson National

Accelerator Facility in Newport News, Virginia. Anticipating that dire budget scenario last spring, William Brinkman, director of DOE's Office of Science, asked NSAC to prioritize the projects. NSAC enlisted Tribble and 21 other scientists.

The Tribble committee weighed the relative importance of three very different facilities. RHIC uses twin accelerators to smash heavy nuclei together to produce fleeting puffs of a weird type of matter called quark-gluon plasma that filled the newborn universe. It studies nuclear matter under the most extreme conditions, which has conceptual connections to cosmology, string theory, and condensed matter physics.

In contrast, CEBAF fires electrons into protons and neutrons to probe their inner workings, which aren't completely understood. The proposed FRIB would generate and study the structure of myriad exotic nuclei that are usually produced only in supernova explosions, addressing such questions as the origins of half the elements heavier than iron.

The committee decided that the CEBAF upgrade should be exploited, Tribble told NSAC. So the choice came down to continuing support for RHIC, which has been collecting data since 2000 and has an annual operating budget of \$160 million, or building FRIB, which could start taking data by the end of the decade. The committee included representatives from all three projects (who

**Rare bird.** The PHENIX detector is fed by the Relativistic Heavy Ion Collider.

didn't vote), and Tribble said the other members were nearly evenly split on the decision. He declined to give a vote tally.

The committee also responded to Brinkman's additional request to spell out what could be done with "modest increases" to the budget. The panel estimated that DOE could just barely keep running RHIC and CEBAF and build FRIB if its nuclear physics budget were to increase by 1.6% per year above inflation. "The field sees a very positive scenario at a very modest growth level," says Jamie Nagle, a member of NSAC and the Tribble committee from the University of Colorado, Boulder. "That's the take-home message."

That message might clash with fiscal realities, Brinkman told NSAC by video link. He noted that automatic, across-the-board cuts to all federal programs required under the Budget Control Act of 2011—the so-called sequestration—would slice \$300 million from the \$4.9 billion Office of Science budget this year if they go into effect in March. Once imposed, he added, the cuts would "set a new baseline for going forward" for all of DOE's research programs, including nuclear physics. Under such a scenario, many physicists worry

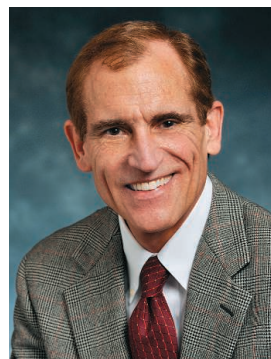
that DOE might not be able to build FRIB even if RHIC were turned off.

For the moment, however, the closure of RHIC is far from a done deal. Although DOE traditionally accepts the advice of its advisory committees on such matters, it is not required to do so. And even if it does, Congress will have the final word. In fact, physicists are banking on legislators from the three states most affected by any trade-off to push for more attractive alternatives.

In a statement released during the meeting, Doon Gibbs, interim director of Brookhaven, said, "I have been in touch with the leadership of each of the other two affected facilities, and we have agreed to work together to realize the modest growth path." He also added: "We also expect the strong support of the NY State Congressional delegation."

In other words, when impartial scientific advice proves unpalatable, look for a political solution.

—ADRIAN CHO



**Lament.** Panel chair Robert Tribble says closing RHIC would be a disaster.

CREDITS (TOP TO BOTTOM): JOSEPH RUBINO PHOTOGRAPHY/BROOKHAVEN NATIONAL LABORATORY; TEXAS A&M UNIVERSITY

Downloaded from www.sciencemag.org on January 31, 2013



## NEUROSCIENCE

# Brain Studies Stymied by Statistics

When a massive brain injury leaves a person unresponsive, physicians rely on outward signs of recovery, like reaching for a cup or saying an occasional word, to determine whether the patient is likely to regain awareness. In recent years, however, studies of patients diagnosed as “vegetative” have revealed that roughly 40% are actually aware to some extent, spurring efforts to develop clinical tools to detect hidden signs of consciousness.

In 2011, a much-publicized study in *The Lancet* suggested a way forward. Scientists at what is now the Brain and Mind Institute of Western University in London, Canada, as well as the University of Cambridge in the United Kingdom and the University of Liege in Belgium, reported that they had detected awareness in three vegetative patients using electroencephalograph (EEG) machines to measure electrical activity in the brain. But now, a team of scientists from the Weill Cornell Medical College in New York City has published a withering critique of that work.

After reanalyzing the other group’s data, the researchers report in the 26 January issue of *The Lancet* that what their colleagues interpreted as conscious behavior was actually random noise, and that hopes for a reliable new bedside EEG method of measuring awareness were premature. The Western University–led group is standing by its results, however. The disagreement hinges on different approaches to the statistical challenge of interpreting messy electrical signals from severely disordered brains.

In the 2011 study, the Canadian researchers and their collaborators, led by postdoctoral student Damian Cruse and neuroscientist Adrian Owen, used EEG machines to measure electrical activity in the brains of 16 vegetative patients and 12 healthy controls. The participants were asked to imagine clenching their right fist or moving their feet each time they heard a beep. The authors fed those recordings into a sophisticated statistical model that detects patterns in data and learns over time. Based on the output of that model, the authors claimed that three of the

16 vegetative patients and nine of the 12 controls had followed the commands—the first time a simple and affordable method had been shown to be successful in detecting awareness in unresponsive patients.

Nicholas Schiff, who heads the Weill Cornell lab, says his group had concerns about the validity of the data long before the paper was published. Schiff says the high rate of positive results among the vegetative subjects “didn’t make a lot of sense” given that only 75% healthy controls were successful.



**Tuning in.** A vegetative patient scanned for signs of consciousness with EEG.

Both research teams are part of a consortium funded by the James S. McDonnell Foundation and charged with generating different methods for detecting consciousness and validating each other’s results. The consortium’s work began 5 years ago after Owen published a series of papers showing that it was possible to use functional magnetic resonance imaging (fMRI) to communicate with people thought to be in a vegetative state.

An fMRI can detect changes with far more precision than an EEG, says Andrew Goldfine, lead author on the critique. fMRI measures blood flow, so “you know exactly what part of the brain is producing the signal,” Goldfine says. In contrast, he says, EEGs involve a vast number of variables, including the individual metal cups distributed across the skull, the wide range of frequencies produced through brain activity, and even minor movements of the scalp.

These potentially confounding factors mean that researchers need to be extremely careful in how they design their statistical analyses, Goldfine says. Cruse and his colleagues overlooked a number of important factors such as muscle twitches that can contribute to false positive results, he says. When Goldfine and colleagues reanalyzed the EEG data, taking such factors into account, all signs of consciousness in the three participants disappeared, he says.

Cruse maintains that because Goldfine did not follow the same approach it is “not at all surprising” that they came up with different results. Cruse adds that Goldfine’s approach is less sensitive than theirs. “EEG remains a viable bedside method for detecting covert awareness in the vegetative state,” he says. “What this exchange amounts to is a series of minor scientific quibbles about how that might best be demonstrated.”

One way for researchers to navigate the “morass” of EEG data is to keep things simple, says Emery Brown, an anesthesiologist and computational neuroscientist at the Massachusetts Institute of Technology in Cambridge who was not involved in either study. Rather than including a vast range of variables in their study, he says, Cruse and his colleagues could have focused on a smaller number of variables to minimize the possibility of finding patterns that

just aren’t there. Similar problems arise when sifting through massive amounts of genomic data looking for correlations, he says. “Scientifically, you should avoid hunting expeditions like that.”

The consortium is set to meet in New York next month to begin the second phase of their grant—a period when all researchers adhere to the same methodology and build a shared database. Although it’s not yet clear what methods they’ll agree upon, Cruse’s team recently published a second study in *PLOS ONE* that they say addresses many of the other team’s concerns while confirming their original results. That’s a positive sign of rigorous scientific debate, says Joseph Fins, professor of medicine at Weill Cornell Medical College and a co-author of the critique. “These tests have huge consequences,” he says. “We have to get this right.”

—EMILY UNDERWOOD

## GLOBAL CHANGE

# The Psst That Pierced the Sky Is Now Churning the Sea

Chlorofluorocarbons (CFCs) seemed like a wonder of modern chemistry: inert, nontoxic chemicals that could do it all, from cooling your fridge to spritzing your hair. But to the surprise of chemists, the gases seeped into the stratosphere and destroyed the ozone there to create the Antarctic ozone hole. And the hole, in turn, stunned meteorologists when it reached down to boost the ring of wind encircling the icy continent.

Now it's the oceanographers' turn to scratch their heads. In an ironic twist, they have used the same CFCs that created the ozone hole to track its effects on the ocean. The stronger winds induced by the hole's formation, they've shown, are stirring the Southern Ocean surrounding Antarctica harder than ever. The added churning may already be slowing the ocean's storage of greenhouse gases from fossil fuels. The lesson is that humans are not farsighted enough to be fooling with Mother Nature.

It's a winding path from hair spray to the deep sea. The first twist came in the 1970s, when atmospheric chemists realized that ultraviolet light could tear CFCs apart in the stratosphere and that the bits of chlorine would go on to destroy the stratospheric ozone that works to keep the same ultraviolet from reaching the surface. The next surprise came in the 1980s, when researchers monitoring stratospheric ozone via satellite realized that the blotch of low-ozone readings appearing over Antarctica every austral spring was no data glitch, but a hole in the stratospheric ozone layer. Much to everyone's surprise, the icy cloud particles found in the Antarctic stratosphere greatly accelerate chlorine's destruction of ozone.

In the 1980s, meteorologists did not expect things to go much further. After all, the troposphere beneath the stratosphere, where weather happens, constitutes a full 80% of the atmosphere's total mass. Changes in the stratosphere affecting the troposphere beneath would be like the tail wagging the dog. But, it turned out, around Antarctica, the tail gets its way. The near disappearance each spring of ultraviolet-absorbing ozone chilled a disk of stratosphere over Antarctica. That change in the pattern of stratosphere temperature managed to reach down into the troposphere and accelerate the ring of wind—the westerlies—that encircles Antarctica. It also shifted the westerlies slightly poleward.

That downward link in the chain worked in climate models. Now, atmospheric scientists Sukyoung Lee and Steven Feldstein of Pennsylvania State University, University Park, report on page 563 that the real atmosphere responds in the same way and even gets some help from greenhouse gases. Using a statistical technique called self-organized maps, they identified four repeating wind patterns in the wintertime troposphere around Antarctica and tracked their changing frequency from 1979 to 2008.

Two of the patterns resemble those seen in climate models simulating strengthening westerly winds. One pattern, which Lee and Feld-

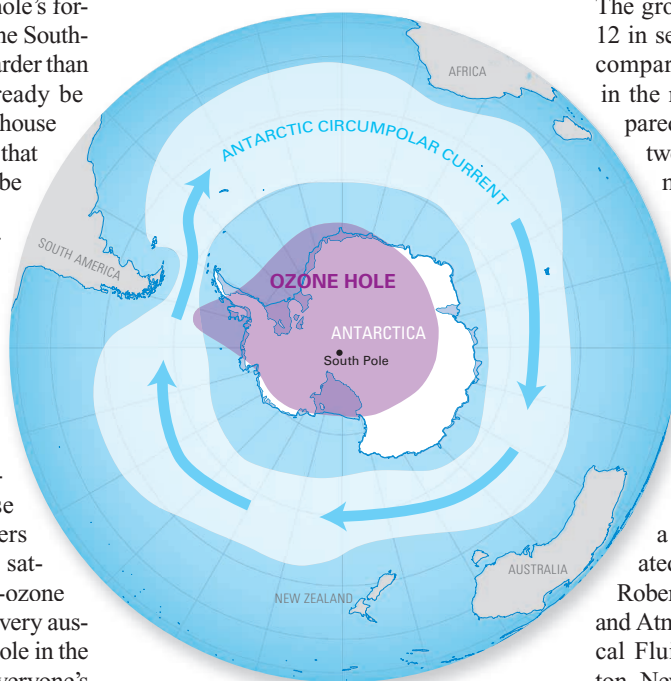
page 568, fluid dynamicist Darryn Waugh of Johns Hopkins University and colleagues answer that question by putting CFCs to work. Peaking in the lower atmosphere at more than 500 parts per trillion in the early 2000s, CFCs not only seeped into the stratosphere but also dissolved in the surface waters of the world ocean. From there, they have ridden the water wherever it was going.

Waugh and his colleagues found that—rather than merely further stirring up eddies in the Southern Ocean, as some oceanographers had thought—the intensified westerlies have accelerated ocean overturning there. The group analyzed measurements of CFC-12 in seawater made in the early 1990s and compared them with measurements made in the mid- to late 2000s. They also compared observed CFC concentrations with two ocean models that stimulated CFC movement assuming no change in currents. They found that the strengthened westerlies had accelerated an existing wind-driven circulation in which the wind draws water to the surface from deep down beneath the southern edge of the band of westerlies and draws it northward across the northern edge, where it sinks down a kilometer or more in the subtropics.

The CFC tracer work “makes a pretty strong case” for an accelerated overturning, says oceanographer J. Robert Toggweiler of the National Oceanic and Atmospheric Administration's Geophysical Fluid Dynamics Laboratory in Princeton, New Jersey. “This is a very big topic in world climate change and even paleoclimate,” he says. Faster overturning is probably slowing the ocean's uptake of carbon dioxide and therefore stoking greenhouse warming. And changes in high-latitude overturning may have been a key to changing atmospheric carbon dioxide levels in the geologic past and dragging the world out of ice ages or sending it back into them.

What the future holds depends on future human actions. Under the international Montreal Protocol, atmospheric CFCs are declining so that the ozone hole should heal by around mid-century. By Lee and Feldstein's calculation, that will eliminate the hole's effect on the westerlies, leaving a strengthening greenhouse in control. That's assuming humans do nothing about rising greenhouse gases.

—RICHARD A. KERR



**Ring around the hole.** Manmade CFCs create the ozone hole each spring. It in turn accelerates the westerlies, a ring of wind driving the underlying Antarctic Circumpolar Current. The strengthened westerlies also accelerate deep water northward.

stein attribute to the springtime ozone hole, accounts for almost two-thirds of the change in the westerlies. The researchers link the second pattern to the tropics, where greenhouse warming has pumped up the churning of the atmosphere. That enhanced convection can boost a poleward circulation that could, in turn, increase the westerlies. The added tropical driver could account for almost one-third of the strengthening of the westerlies, they report.

Oceanographers knew such stronger westerlies were sure to affect the ocean beneath. The question was how. In a second paper, on



## ANIMAL MODELS

# Advisers Urge NIH to Scale Back Chimpanzee Research

Last week, a top-level panel of advisers urged the National Institutes of Health (NIH) to phase out most medical research on chimpanzees in the United States, bringing what many researchers think is the inevitable end to a long and emotional debate. Specifically, the panel's report said NIH should retire most of the 360 research chimps it owns, end half of 22 research projects, and make sure chimps still being studied are kept in suitable living conditions.

Although the panel left room for behavioral and genomics research—many studies could continue under proper conditions—it all but ruled out invasive medical research. “Clearly there is going to be a reduction in the use of chimpanzees in research,” said veterinary researcher Kent Lloyd of the University of California (UC), Davis, who co-chaired the NIH advisory panel. “I don’t believe that that will be at the cost of research advances.”

The working group's 84-page report is a response to a December 2011 Institute of Medicine (IOM) study requested by NIH that found most research on chimps was “unnecessary” (*Science*, 16 December 2011, p. 1484). NIH Director Francis Collins asked the working group, part of the NIH Council of Councils, to help NIH implement the IOM report, which laid out criteria for when chimp studies are justified. Such a study should take place only if it is needed to advance public health, could not be done ethically in humans or in another animal model, and if the chimps are housed in an ethologically appropriate environment or natural habitat.

After applying the IOM criteria to 22 NIH-funded research studies using chimps, the working group found that half should be phased out. That includes six of nine biomedical projects; only three projects using 12 chimps should continue. The working group also recommended continuing eight of 13 comparative genomics and behavioral studies; these involve 290 animals.

Most of the approved projects could continue only if they are modified to meet new standards for living conditions. For example, each chimp should have at least 1000 square feet of outdoor space, live with no fewer than six other chimps, and have room to climb.

The working group did not reveal the list of 30 projects it reviewed because of confidentiality, said neurologist and working group co-

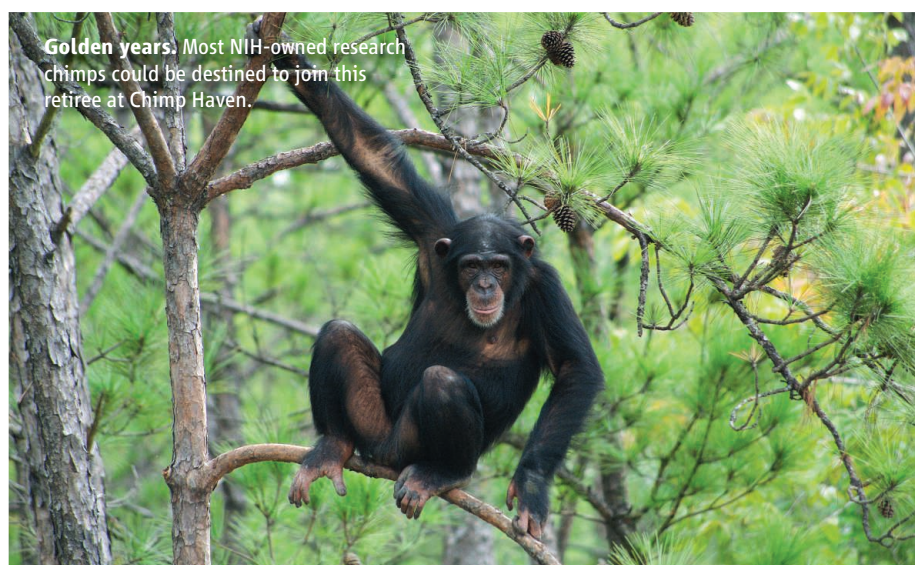
chair Daniel Geschwind of UC Los Angeles. However, the report said the three approved biomedical projects involve research on immunology and infectious agents such as hepatitis. Some researchers have been worried that studies of hepatitis C vaccines, in particular, would be ruled out, arguing that the chimp is the only good model for testing. (The IOM panel did not reach consensus on whether chimps are needed for these studies.)

Any newly proposed projects that pass scientific review will then go before a yet-to-be-created, independent NIH oversight committee that would evaluate whether the

than the 50 animals could potentially be done in nontraditional settings such as sanctuaries or zoos, the report says.

Kathleen Conlee, vice president of animal research issues for the Humane Society of the United States, which has pushed to end chimp research, praised the report. “We’re very pleased ... and we hope that NIH will move forward to implement the recommendations. I think they largely reflect what the public has been asking for,” she said.

But John VandeBerg, director of the Southwest National Primate Research Center in San Antonio, Texas, forwarded a statement to the press saying that his institution “respectfully disagrees with the Working Group’s recommendations that severely limit the future use of chimpanzees in biomedical research and that will slow urgently needed medical advances.”



project complies with the IOM principles. The bar will be high for medical studies, but much behavioral and genomics research would “sail right through,” Geschwind suggested. (For now, NIH will continue a moratorium on new chimp studies that it imposed when the IOM report came out.)

The working group also examined the number of chimps NIH owns or supports. This includes 451 chimps at research or research reserve facilities and 219 in retirement. It said that NIH should “immediately” begin planning to retire the 360 research chimps it owns to a federal sanctuary and reduce its research supply to a single colony of just 50 chimps. NIH would reassess the adequacy of this colony every 5 years but could lift its moratorium on breeding only after consulting with other agencies. Behavioral and genetics studies requiring more

After a 60-day comment period on the report, Collins will decide whether to accept it, probably by late March. But NIH has already begun to downsize its chimp collection: In December, it agreed to transfer 113 chimps from New Iberia Research Center in Louisiana to Chimp Haven in Keithville, Louisiana, which runs the federal chimp sanctuary.

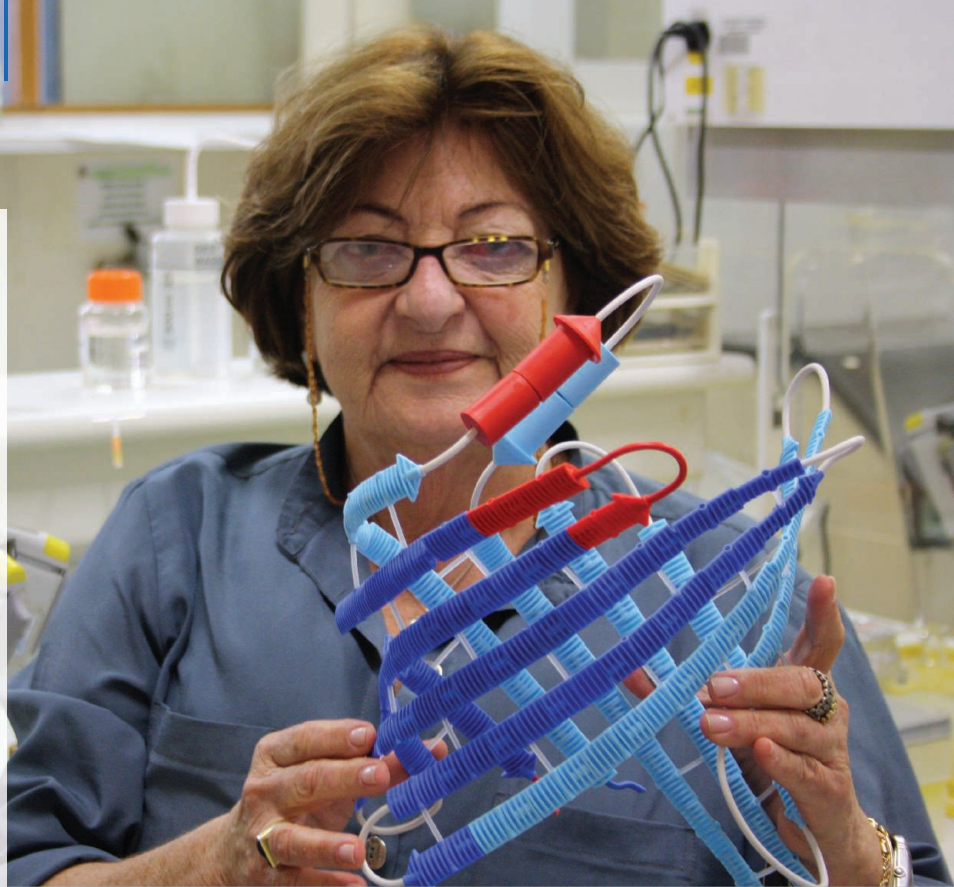
One question is who will pay the costs of chimp retirement. In 2000, Congress capped how much the agency can spend on construction and care at federal chimp sanctuaries at \$30 million, and Chimp Haven will reach that limit this summer. James Anderson, an NIH deputy director, said, “It is a concern for us and it’s something that we would have to have addressed at the congressional level.”

—JOCELYN KAISER

CREDIT: CHIMP HAVEN/AMY FULTZ

# A Worm Vaccine, Coming at A Snail's Pace

The long struggle to develop a schistosomiasis vaccine badly needs new money



**RIO DE JANEIRO, BRAZIL**—Miriam Tendler has not moved her lab in more than 20 years. Her office is cramped and filled with stacks of paper, and the hallways are lined with big filing cabinets. Yet Tendler has stayed in this old, low building on the campus of the Oswaldo Cruz Foundation, she explains, because she is afraid of doing anything that could disturb the life cycle of the microscopic worm that she has carefully nurtured in her lab all these years. Tendler has devoted her career to developing a vaccine against this worm, a pernicious parasite that is a scourge of people in eastern Brazil: *Schistosoma mansoni*.

Her target is one of at least six flatworms that cause a debilitating human disease called schistosomiasis. The worms can live for decades in blood vessels, shedding eggs that cause pain, severe blood loss, and malnutrition and that can damage the liver, kidneys, and spleen. Half of their unusual life cycle takes place in freshwater snails, which is why one room in Tendler's lab houses dozens of aquariums.

According to the World Health Organization (WHO), schistosomiasis, also known as bilharzia, is the second most devastating parasitic disease in the world, after malaria. Some 200 million people are estimated to be infected, most of them children, and another 600 million are at risk. Mortality estimates vary widely, but Lester Chitsulo, who heads

WHO's Schistosomiasis Control Programme in Geneva, Switzerland, says that there are probably almost 300,000 deaths a year in sub-Saharan Africa alone.

Vaccines could be powerful weapons against schistosomiasis, but a lack of interest and money, combined with the fact that a cheap, effective drug is available, has hampered research. "We have limped along with small amounts of money," says Alex Loukas of James Cook University, Cairns, in Australia. That could change if, as researchers hope, the Bill & Melinda Gates Foundation joins the fight. Next month, the foundation will bring experts to Seattle for a 2-day meeting to discuss schistosomiasis vaccines. If it decides to fund the research, everything could change, Loukas says.

There has been some progress; two vaccines are now in clinical trials. But there are questions about both. Bilhvax, developed at the Pasteur Institute in Lille, France, targets *S. haematobium*, a species that causes urogenital schistosomiasis and is common in Africa and the Middle East. But despite extensive trials, very little has been published so far, leading other scientists to wonder what's going on.

The other is Tendler's candidate against *S. mansoni*, backed by the Brazilian government through a public-private partnership. The vaccine, the only one from a country where *Schistosoma* is endemic, may enter

phase II trials this year. (It's based on a protein called Sm14, which a worm uses to ferry a host's fatty acids into its own cells.) But some groups have been unable to replicate the high level of protection that Tendler has shown in mouse studies.

What's more, vaccines are needed for other *Schistosoma* species as well, as there is no one-size-fits-all vaccine. "We need to develop a pipeline," says Peter Hotez, dean of Baylor College of Medicine's National School of Tropical Medicine in Houston, Texas. Hotez is working on a vaccine candidate named Sm-TSP-2 that has yet to reach the clinic; another candidate, Sm-p80, is also being developed in the United States.

## Into the groove

Different *Schistosoma* species cause different patterns of symptoms, but the parasites essentially follow the same lifecycle. They reproduce in freshwater snails that release large numbers of free-swimming larvae, called cercariae, into the water. When these find a human, for instance a child playing in the water, they burrow through that person's skin with their head. The larvae then lose their tail and migrate through the blood vessels and the lung into the liver, where they mature into adult worms and mate. The larger male worm forms a groove, which the thinner female slips into.

Together, the couple moves into veins



**Eyes on the target.** Miriam Tendler's vaccine candidate is based on Sm14, a crucial *Schistosoma* protein.

in different parts of the body, depending on the species: *S. mansoni* and *S. japonicum* reside in the bowel and rectum, for instance, whereas *S. haematobium* migrates to the bladder. The females start producing hundreds of eggs daily, sometimes for many years. Most of them are shed in urine and feces, and they can infect new snails if they end up in lakes or rivers. But some get trapped in the liver or other organs, causing an immune response that leads to the typical symptoms and sometimes death.

Public health officials tried for decades to get rid of schistosomiasis by targeting the snails. Despite sporadic successes, that strategy has proved too daunting in rivers like the Nile and the big lakes in Africa. Since the 1980s, a drug called praziquantel, which kills the worms in a person's body, has been the weapon of choice. In many endemic areas, all schoolchildren get the drug annually; Merck has provided praziquantel to WHO for free since 2007 and recently pledged to increase its annual donation to 250 million tablets.

But scientists worry that such widespread use will fuel resistance against praziquantel, the only drug available. Moreover, people in endemic areas usually get reinfected within months of treatment, so there is little long-term progress. "I think people are finally realizing that drugs alone are unlikely to control schistosomiasis," Loukas says.

Vaccines would probably not prevent human infections, but they could reduce the number of eggs that female worms produce, which in turn would reduce symptoms and slow transmission, says Maria Yazdanbakhsh of Leiden University Medical Center in the Netherlands, who heads a European project to find a vaccine against *S. mansoni*. "If the worms produce fewer eggs, the water will be less infested, and that will slowly reduce transmission." Studies suggest this is possible. Adults in endemic areas have been found to be partially immune to reinfection, and in animals, vaccines were shown to reduce the number of eggs by about half.

Hotez thinks support for a vaccine is now growing, in part because of schistosomiasis's role in the HIV epidemic: Female genital schistosomiasis increases the risk of con-

tracting HIV three- or fourfold. If the Gates Foundation steps in, it would raise the disease's profile, Yazdanbakhsh says, and that could encourage national governments to donate as well. So far, the foundation has made no commitment, and it would not comment to *Science*.

### Painful rashes

Even if more money becomes available, there are obstacles to a successful vaccine. One of them emerged in 2007 during a trial of a vaccine against a different group of parasites called hookworms. Healthy U.S. volunteers tolerated the shots well, but a study conducted in an area of Brazil where hookworm infection is common had to be suspended when three of the first seven volunteers developed painful rashes on their head,

the two in clinical trials—such data have yet to be presented.

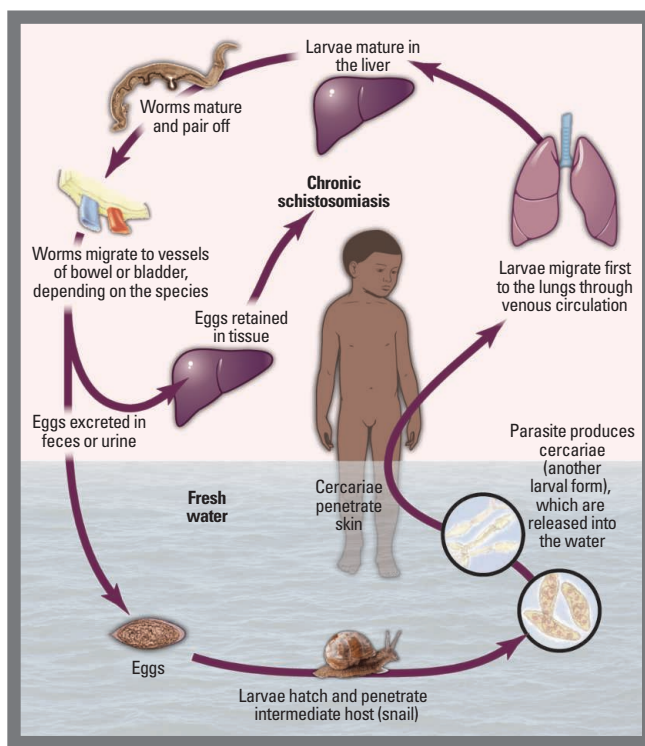
Another difficulty is that the results of several promising studies in mice—including Tendler's Sm14 vaccine—have not been replicated by researchers in other labs, for reasons that aren't clear. "This is a problem that has plagued the schistosomiasis field for many years and it has done the field an enormous amount of harm," Loukas says. How well results in mice translate to humans is also unclear. Although *S. mansoni* infects mice readily, the rodent is not a natural host; in terms of sheer size, one pair of worms in a mouse is equivalent to a very heavy infection in humans. Some researchers have switched to other animal models, such as baboons, which require special facilities and are more expensive.

The French vaccine, meanwhile, is a bit of a dark horse. A phase I trial, done in 1998 and 1999 in France, was not published until July 2012; phase II and phase III studies, both completed, have yet to appear. The team's original strategy was to go through all the phases before publishing anything, Gilles Riveau of the Pasteur Institute writes in an e-mail to *Science*. "I think today that we were wrong," he adds, saying that results on phase II may be out soon.

Others are betting on new targets, and the genomes of *S. mansoni* and *S. haematobium*, both now sequenced, have given them a wealth of choices. Yazdanbakhsh and colleagues are aiming at the earliest form of the worm that the immune system encounters: the larvae passing through the skin. Scientists in the consortium have identified genes that are turned on only in this stage; by targeting these proteins, they hope to catch the worm before it has its defenses up. Such a vaccine, they hope, might prevent infection altogether.

Loukas's group, meanwhile, has developed an array of *Schistosoma*'s surface proteins, which they have screened against the blood of resistant individuals to see which antigens are recognized by their immune system. A new vaccine candidate will be published soon, he says.

With so much new technology available, developing a vaccine is now primarily a question of political will, Tendler argues. "This is not a bet, this is not a game, this is not magic. It is just work." **—KAI KUPFERSCHMIDT**



**Circle of life.** *Schistosoma*'s life cycle takes it from freshwater snails to human blood vessels and back.

neck, and shoulders. The rash was caused by a class of antibodies called IgE, which the volunteers had developed during prior hookworm infections, says Loukas, who was involved in the trial.

To prevent such nasty surprises with *Schistosoma*, Loukas says, any new vaccine candidate needs to be screened to see whether people in endemic areas might have IgE in their blood that reacts with it. "If they do, we immediately throw the candidate out," he says. For some of the candidates already in development—including

## SPACE

# Tight Budgets Squeeze European Earth Observation

The Europe-wide financial crisis and uncertainty over the European Union's future funding are casting shadows over Earth monitoring and science missions

On the face of it, the European Space Agency's (ESA's) Earth-observation program came out of last November's budget-setting council meeting pretty well: With €1.9 billion over the next 5 years (20% of ESA's total budget), it is the agency's biggest program. But to make room in the budget for new launchers and the International Space Station, member states have put the squeeze on Earth-observing science missions (*Science*, 30 November 2012, p. 1135). And, with the funding of the European Union still in doubt, questions hang over the future of a groundbreaking environmental monitoring system, an ESA-E.U. collaboration called Global Monitoring for Environment and Security (GMES, recently renamed Copernicus by the European Union). "This is far too important for Europe not to get its act together," says

2012. The idea of GMES "emerged out of the Envisat decade. People could see what you can do with long-term data," says John Remedios, head of Earth observation science at the University of Leicester in the United Kingdom. Envisat carried nine instruments that gathered data about land, water, ice, and the atmosphere. Most will be replicated or upgraded in GMES.

ESA is close to completing the first three GMES spacecraft, known as Sentinels, which are due to launch this year. But the European Union's funding beyond the end of this year is not yet secure as the European Commission (the European Union's executive arm), the 27 member states, and the European Parliament debate the union's budget for the next 7 years (*Science*, 16 November 2012, p. 872).

decide it is too risky to launch the satellite. "We have delivered; I hope the commission can also deliver," Liebig says.

Because of the continuing uncertainty over the E.U. contribution to GMES, at the ESA council meeting in November some ESA member states were reluctant to commit the full amount for the next round of GMES satellite building. ESA secured only 80% of the required funds at the meeting.

Much of ESA's Earth observation budget goes toward meteorological satellites. But another area also came up short on funding: a series of science missions known as Earth Explorers, which seek to observe Earth and its atmosphere in new ways using innovative technology. Three have been launched so far—looking at soil moisture and ocean salinity, ice cover, and ocean circulation—and another three are under construction. A further three proposals are vying to start construction as Earth Explorer 7. A choice will be made sometime in the next few months.

The future of Earth Explorer 8, however, looks less certain after November's council meeting awarded the program only 80% of its expected €1.25 billion budget. "A variety of solutions are now being considered," says O'Neill, who is the chair of ESA's Earth Science Advisory Committee. Heinrich Bovensmann of the University of Bremen in Germany, who heads one of the teams competing to build Earth Explorer 8, says he expects ESA to adopt "the classical way space agencies deal with budget problems: delay things."

If selected, Bovensmann's CarbonSat will use absorption spectroscopy to image sources of carbon dioxide and methane—the main greenhouse gases—in high resolution. "It's the first time we'll be able to make a distinction between natural and anthropogenic sources," he says. The other contender for the mission, the Fluorescence Explorer or FLEX, aims to measure the carbon balance of plant life by detecting chlorophyll fluorescence, a sensitive marker for photosynthetic efficiency. "The signal is very small, and this is the first time it will be measured from space," says José Moreno of the University of Valencia in Spain.

There is now no guarantee that either mission will get off the ground any time soon. Moreno says: "The situation is rather difficult at the moment, and no one knows how well it will evolve in the future."

—DANIEL CLERY



**Sentinel-3.** Monitoring topography, temperature, and color of land and sea.

Alan O'Neill, director of the United Kingdom's National Centre for Earth Observation.

GMES is an unprecedented attempt to create an operational environmental monitoring system akin to the meteorological systems that have been in place for decades. GMES involves a whole fleet of spacecraft with different sensors—built and paid for by ESA—along with duplicate backup craft and operations and user facilities provided by the European Union. The aim is to provide steady, reliable data of use to European governments, industry, emergency services, and citizens. "There is no program like GMES. It's an Earth management system," O'Neill says.

European researchers got a taste for long-term, high quality data from Envisat, ESA's bus-sized satellite that operated for 10 years until ended by an unidentified failure in April

The next round of the E.U. budget negotiations will take place on 7 to 8 February. Because of the faltering economies across Europe, the commission is under enormous pressure to curb its ambitions; some states even want to cut E.U. funding below current levels. In 2011, the commission proposed €5.8 billion for GMES over 7 years. The member states countered with a suggestion of €3.8 billion, a figure that alarmed ESA, researchers, and other potential users.

At that level of funding, "there will be cuts," says ESA's head of Earth observation, Volker Liebig. "If they can't finance the recurrent [duplicate] satellites, there is a danger that we might have data gaps," he says. If the European Union has not confirmed the budget for the operations infrastructure by the time of the Sentinel-1 launch in August, Liebig says, the ESA member states could



**Hard to bear.** High out-of-pocket costs have plunged many Chinese, including the family of this badly burned boy in Hefei, deep into debt.



## CHINA

## World's Biggest Health Care System Goes Under the Knife

**Ambitious reforms of the Chinese medical system aim to expand infrastructure, cover the poor, and combat chronic diseases**

**SHENZHEN, CHINA**—In most Chinese hospitals, teeming waiting rooms and forlorn patients wheeling intravenous drips through dingy, ill-lit halls are troubling but typical sights. University of Hong Kong (HKU)-Shenzhen Hospital, however, is anything but typical. Its gleaming wards and labs, opened to outpatients last July, are at the vanguard of China's health care reforms.

The hospital here in Shenzhen, the crucible of China's economic rebirth, is the brainchild of China's health ministry, which convinced the local government to put up \$56.2 million for the 350,000-square-meter complex across the border from Hong Kong. HKU's stewardship is meant to separate the venture from the rest of the pack for more than its looks. "They don't need us to teach them how to stitch up wounds," says Sum-ping Lee, dean of HKU's medical school. The health ministry envisions the institution as "an important model in the process of reforming public hospitals," says a spokesperson. One prong of that strategy is to boost medical research: HKU professors will apply their expertise to a planned research arm of the hospital that will focus

on oncology, orthopedics, liver disease, and infectious diseases.

HKU-Shenzhen Hospital is part of a Chinese spending spree on health care, with total outlays predicted to triple from \$357 billion in 2011 to \$1 trillion in 2020, when the government hopes to have implemented universal coverage. (Only 15% of the population was insured in 2000, according to the health ministry.) The investment is largely directed at improving basic health care. In 2000, the World Health Organization (WHO) ranked China 144th out of 191 national health systems. Although some scholars dispute WHO's methodology, which is no longer used, few deny that China's health care system is ailing. Gaps in hospital capacity and quality of care have fueled rising discontent, culminating in a recent spate of murders of doctors and nurses. According to *China Daily*, Chinese hospitals reported more than 17,000 violent incidents in 2010—mostly involving disgruntled patients.

*"Families are suffering from a huge economic burden."*

—YAO HONG,  
MINISTRY OF HUMAN RESOURCES  
AND SOCIAL SECURITY

To recoup lost funds, hospitals charged a 15% markup on prescription drugs. Doctors began prescribing antibiotics indiscriminately, sparking an uptick in drug-resistant bacterial strains (*Science*, 18 May 2012, p. 795). As China's health infrastructure

frayed, diseases like syphilis, once on the ropes, reemerged with a vengeance (*Science*, 27 January 2012, p. 390). Then came the debilitating SARS outbreak in late 2002: "It was a wake-up call for the Chinese government," says Yanzhong Huang, a global health fellow at the Council on Foreign Relations in New York City.

A more enduring problem is that economic development and an aging population have driven a shift in the disease burden from infectious to chronic diseases, which today

A white paper released by China's State Council last December outlines the basic tenets of the reforms, which include expanding insurance coverage, reconfiguring drug pricing, and promoting primary care. The reform drive also includes money for research into traditional Chinese medicines and an overhaul of the drug pricing system—a move that could affect pharmaceutical research. The health ministry, meanwhile, is pushing the training of more medical professionals, updating China's mental health infrastructure (see sidebar, p. 506), and backing the development of hospitals like HKU-Shenzhen.

Health care in China today bears little resemblance to the system in place during its socialist heyday. In the 1970s, agricul-

tural communes featured rural health care centers staffed by about 1.8 million "barefoot doctors": health workers with basic training who provided primary care. Among them was Chen Zhu, China's current health minister. As the Chinese government began instituting market reforms in the 1980s, it pulled funding from hospitals and clinics. The barefoot doctor system disintegrated. By the 1990s, the government was contributing less than 20% of total health care costs—the low end of developing countries, says Gordon Liu, an economist at Peking University in Beijing who served on a health care reform taskforce under China's State Council.

## A New Dawn for Mental Health

**SHANGHAI, CHINA**—Graduates of Chinese medical schools once steered clear of mental health work. In the 1980s, recalls Michael Phillips, a psychiatrist at Shanghai Mental Health Center and Emory University School of Medicine in Atlanta, “they would do anything to get out of it.” The field then was reeling from decades of suppression. After the 1949 revolution, it had been branded a bourgeois science, with drug treatment in many psychiatric hospitals replaced by readings of Mao Zedong’s *Little Red Book*. Today, psychiatry has gained legitimacy, but psychiatrists still complain of a poor mental health infrastructure and measly salaries. Thus, many cheered when China’s health ministry announced in 2009 that it was making mental health a key focus area of its sweeping health care reforms (see p. 505).

That newfound attention culminated last October in the adoption of a mental health law that had been under discussion for 27 years. The law is “a major event for Chinese psychiatry,” Phillips says. It emphasizes the expansion of community mental health services, delineates professional duties in psychiatry and psychology, and introduces a more humane protocol for commitment to psychiatric hospitals. (An English translation of the law has been posted to the Web site of the *Shanghai Archives of Psychiatry*.)

China has an estimated 173 million people with mental disorders of whom the vast majority—some 158 million—have never received treatment. Psychiatrists have been trying for decades to change that. In 1985, Liu Xiehe, a psychiatrist at Sichuan University’s West China Hospital in Chengdu, wrote the first draft of China’s mental health law. But bureaucratic intransigence, concerns about the cost of mental health services, and resistance from some psychiatrists

stalled the process. By 2005, the draft had been revised 15 times to no avail.

In the end, studies on the heavy socioeconomic toll of mental illness prodded Chinese officials to act. In 1996, the Global Burden of Disease Study found that mental illness, neuropsychological conditions, and suicide together accounted for 20% of China’s illness burden, using a metric called disability-adjusted life years (*Science*, 1 November 1996, p. 740). The figure remained relatively stable until

***The mental health law is “a major event for Chinese psychiatry.”***

—MICHAEL PHILLIPS, SHANGHAI MENTAL HEALTH CENTER

more than \$35.3 million from the central government since 2004. Health care reforms and the new law should bump up funding even further.

The law divides China’s mental health professionals into psychiatrists, psychological counselors, and psychotherapy practitioners, or what observers understand as clinical psychologists. The distinctions are intended to strengthen professionalism. Of China’s estimated 20,000 psychiatrists, only about 20% hold a degree in the field, according to a study published in *Asia-Pacific Psychiatry* in October 2009. Clinical psychology and counseling is even more of a mixed bag. “Some people have psychology degrees, some have education degrees, and some have a background that has nothing to do with psychology,” says Xiang Yutao, a psychiatrist at Beijing Anding Hospital and the Chinese University of Hong Kong. A key provision of the new law,

2004, the last year for which data is available, Phillips says. In 2010, China committed to remodeling and expanding 550 psychiatric hospitals and wards within 2 years. Another area to benefit was community-based mental health, which has received



**Dreaming big.** Sum-ping Lee envisions the University of Hong Kong-Shenzhen Hospital as a trailblazer in research and care.

account for roughly 85% of deaths in China, up from 53% in the 1970s. “That pushed the demand for health care a lot,” Liu says. As the transition took hold, the health care system remained woefully unprepared to handle the surge of patients, with too few doctors and medical facilities. Inadequate insurance, meanwhile, meant that many Chinese could not afford care in catastrophic cases.

accounted for 69% of costs associated with China’s disease burden in 2009. Community health centers must now provide free check-ups for hypertension and diabetes patients four times a year, says Wu Yangfeng, director of The George Institute, China, and a cardiovascular specialist at Peking University Clinical Research Institute in Beijing. The health care reforms are “not just of political signifi-

“Families are suffering from a huge economic burden,” said Yao Hong, director of the Ministry of Human Resources and Social Security’s health insurance department, at a conference in Beijing in July.

To address these issues, in 2009 China unveiled a blueprint for providing basic insurance for 90% of Chinese by 2011, implementing more standardized training for doctors, constructing thousands of new county hospitals, and putting a clinic in every village. The plan also emphasized chronic diseases, which the health ministry says

cance,” he says. “The basic health services will really help to cover a broad range of the population affected by chronic disease.” A new requirement to check every patient’s blood pressure will help catch the estimated 70% of Chinese with hypertension who are not aware they have it, Wu says. The increased focus on chronic diseases may benefit research. “Our whole conceptualization of noncommunicable diseases is based on data from what is a minority of the global population today,” says Gabriel Leung, a public health researcher at HKU. “None of it came from China.” Researchers may now start to identify population-specific risk factors in China and other developing countries, he says.

One potential downside is the effect of reforms on drug development. Until recently, up to 50% of China’s total health care spending went toward drugs, Liu says—a sum that “might be the highest drug-to-total-health-care-expenditure ratio in the world.” (The Organisation for Economic Co-operation and Development states that the ratio averaged 18% in 2003.) China aims to bring expenditures down, Liu says, by restricting hospitals to lists of government-approved drugs and by outlawing profiteering on prescriptions. The selection process for the lists has set off bidding wars, with companies rushing to underbid each other. The drop in revenue will shave profit margins—a change





**No more winging it.** A new law governing psychiatric hospitals aims to strengthen professionalism and curtail involuntary admissions.

designed to limit the reach of unqualified practitioners, states that psychological counselors cannot diagnose or treat mental disorders.

Patients stand to gain leverage: Under the new law, they can no longer be hospitalized against their will, unless deemed a danger to themselves or others. Previously China had a looser policy for committing patients to

counseling remains unaffordable for many, and medical insurance in China only partially covers mental health care, says Zhang Jianxin, deputy director of the Chinese Academy of Sciences' Institute of Psychology in Beijing. But, he adds, the law sets an important precedent. "We have a saying in China: It's better to have something than not to have it."

—M. H.



**Life insurance.** Hospitals have hired guards following a wave of violence against doctors and nurses.

that could squeeze research. "Drug companies are of course nervous about the future source of income for their R&D," Liu says. But, he adds, because total health care spending in China is increasing by more than 15% each year, the country will continue to be a profitable market: Even as drug companies' share of the pie decreases, Liu says, "The total pie will increase." The health ministry contends that strong government support of pharmaceutical research will help compensate for any losses.

A larger economic challenge will be containing costs for patients. Today, 95% of Chinese have basic insurance covering some medical costs, according to the health ministry, which has gradually deepened the coverage to include some catastrophic medical expenses and outpatient treatment as well as routine checkups and tests. But broader coverage has not stemmed soaring costs. A preliminary study from the Institute for the Study of Labor in Bonn, Germany, shows that Urban Resident Basic Medical Insurance, which was launched in 2007, has increased hospital visits without reducing out-of-pocket expenses. "If health expenditure growth is not controlled, then the financial protections on the population are still going to be limited," says Winnie Yip,

institutions involuntarily—a loophole exploited in the past to lock up unruly relatives after domestic disputes and, allegedly, political dissidents. "The most important aspect of the law is that it emphasizes the protection of patients' rights," Xiang says. Not all psychiatrists are keen on the voluntary commitment clause, fearing that it will complicate their work and reduce demand for psychiatric beds. Indeed, patients deemed a danger to others now have the right to request a reevaluation by two additional psychiatrists.

The mental health community has its work cut out for it. A national epidemiological survey on mental health now under way—China's first in 20 years—should help elucidate what services are needed and where. But as needs in rural areas are clarified, convincing psychiatrists to leave cities will be difficult. "The idea is you're going to get all these psychiatrists out in the community. I don't see it," Phillips says. Another stumbling block may be convincing Chinese to seek help. Psychological

a health policy expert at the University of Oxford in the United Kingdom. Huang points out that China's roughly 200 million internal migrants—a "bridging" group that spreads HIV and other infectious diseases from high-risk groups like urban sex workers to low-risk groups like rural heterosexual women—are largely insured in their home towns, meaning far less than 95% of the population takes advantage of the new national program.

The central government has tried to better cover migrant workers by allowing them to enroll in insurance at their urban workplaces. But combating chronic diseases will ultimately require much more

***The emphasis on chronic disease "is the right direction for China."***

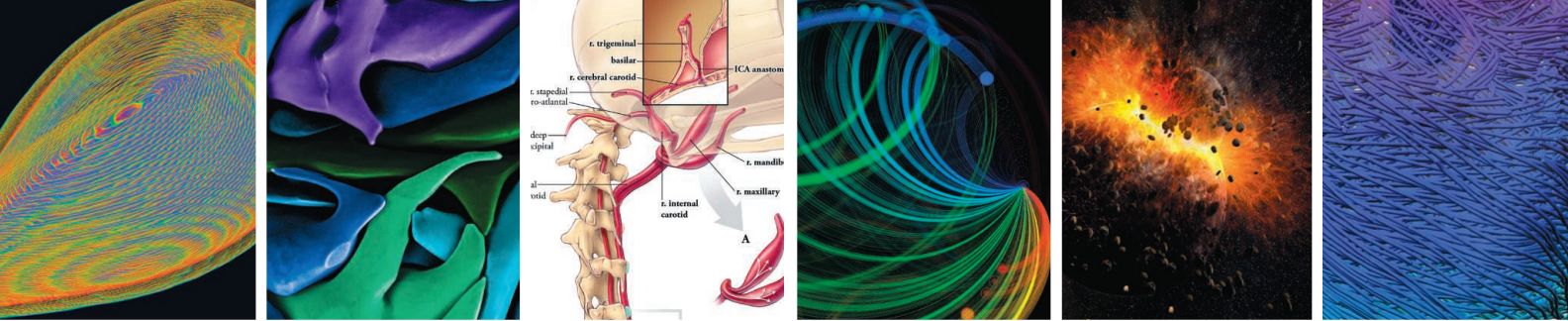
—WU YANGFENG,  
THE GEORGE INSTITUTE, CHINA

than free checkups and treatments. "The most effective control is really prevention," Yip says. At the top of the list, Huang says, should be enforcing the WHO Framework Convention on Tobacco

Control—a tough task in a country with an entrenched tobacco lobby (*Science*, 13 January 2012, p. 153). "We haven't seen any government leaders publicly speak out against smoking," he says.

"Clearly there is still a long way to go," Wu says. But the emphasis on chronic disease is an important first step, he says: "That is the right direction for China."

—MARA HVIETENDAH



# 2012 Visualization Challenge

Ten years ago, *Science* and the National Science Foundation (NSF) launched a unique experiment: an international competition to recognize the best examples of projects that bring scientific information to life. The goal was to encourage new ways to visualize data—efforts that are increasingly important for conveying scientific principles and ideas across disciplines and to the general public, and for revealing the hidden beauty of structures on scales from nanometers to the cosmos. The following pages showcase the winners of the 10th in what has become the annual International Science and Engineering Visualization Challenge.

The 10th anniversary winners merge biology and physical science in interesting ways. They include a “wiring diagram” of the macaque brain (featured on the cover of this issue), which inspired a new type of computer chip; a scanning electron micrograph that reveals the crystal structure of a sea urchin’s tooth; a poster showing how the owl manages to swivel its head without shutting off blood to its brain; and a video of a computer model of the heart that marries imaging techniques with high-powered computing.

We received 215 entries from 18 countries. A committee of staff members from *Science* and NSF screened the entries. Those selected as finalists were posted on NSF’s Web site, and visitors were invited to vote for their top choice in each category. A total of 3155 votes came in; entries that received the most votes were named the “People’s Choice.” Independently, an outside panel of experts in scientific visualization reviewed the finalists and selected the winners. The winning entries are featured on the following pages, in a slideshow and podcast at [www.sciencemag.org/special/vis2012](http://www.sciencemag.org/special/vis2012), and at [www.nsf.gov/news/scivis](http://www.nsf.gov/news/scivis). Some entries were put together by large teams, not all of whose members could be listed in print; the online presentations provide more details. Tarri Joyner of NSF organized this year’s challenge.

We encourage you to submit applications for next year’s challenge, details of which will be available on NSF’s Web site, and to join us in celebrating this year’s winners.

**JUDITH GAN, DIRECTOR, OFFICE OF LEGISLATIVE AND PUBLIC AFFAIRS, NSF**  
**COLIN NORMAN, NEWS EDITOR, SCIENCE**

## Science



## JUDGES

**Michael K. Reddy**

National Institutes of  
General Medical Sciences  
Bethesda, Maryland

**Corinne Sandone**

Johns Hopkins University School of  
Medicine  
Baltimore, Maryland

**Tierney Thys**

National Geographic Explorer  
Carmel, California

**Thomas Wagner**

NASA  
Washington, D.C.

Text by Emily Underwood

Design by Kay Engman



# Photography



## FIRST PLACE WINNER AND PEOPLE'S CHOICE

### Biominer Single Crystals

Pupa U. P. A. Gilbert and Christopher E. Killian;  
University of Wisconsin, Madison

*T*hese fantastical structures could be a creation of Antoni Gaudí, the surrealist architect. In reality, they are the microscopic crystals that make up a sea urchin's tooth. Each shade of blue, aqua, green, and purple—superimposed with Photoshop on a scanning electron micrograph (SEM)—highlights an individual crystal of calcite, the abundant carbonate mineral found in lime-

stone, marble, and shells.

The curved surfaces of the crystals look nothing like normal calcite crystal faces, however, says biophysicist Pupa U. P. A. Gilbert of the University of Wisconsin, Madison. Gilbert studies biomineralization: the process by which living organisms produce mineral structures such as bones and teeth. Sea urchin teeth in particular are “fantastic,” she says, because they defy our expectations of what a crystal should look like in nature. Instead of flat sides and sharp edges, the sea urchin produces “incredibly complex, intertwined” curved plates and fibers that interlock and fill space in the tooth as they grow. Though made of a substance normally as soft as chalk, the teeth are hard enough to grind rock, gnawing

holes where the sea urchins take shelter from rough seas and predators. Layers of continuously regenerating crystals slough off and reveal new crystals as the teeth wear down, self-sharpening with use.

On first seeing the SEM image of the tooth in black and white, Gilbert and staff scientist Christopher E. Killian were dumbstruck: “I had never seen anything that beautiful,” she says. However, the black-and-white image made it difficult to distinguish the individual crystals, so she applied the colors to highlight how the crystals intertwine and connect. The resulting image is a “virtuosic combination of chemistry, biology, and art,” says judge Michael Reddy. The fact that sea urchins have evolved to produce self-sharpening teeth is “just wild,” he says.



## HONORABLE MENTION

### X-ray micro-radiography and microscopy of seeds

Viktor Sykora, Charles University; Jan Zemlicka, Frantisek Krejci, and Jan Jakubek, Czech Technical University

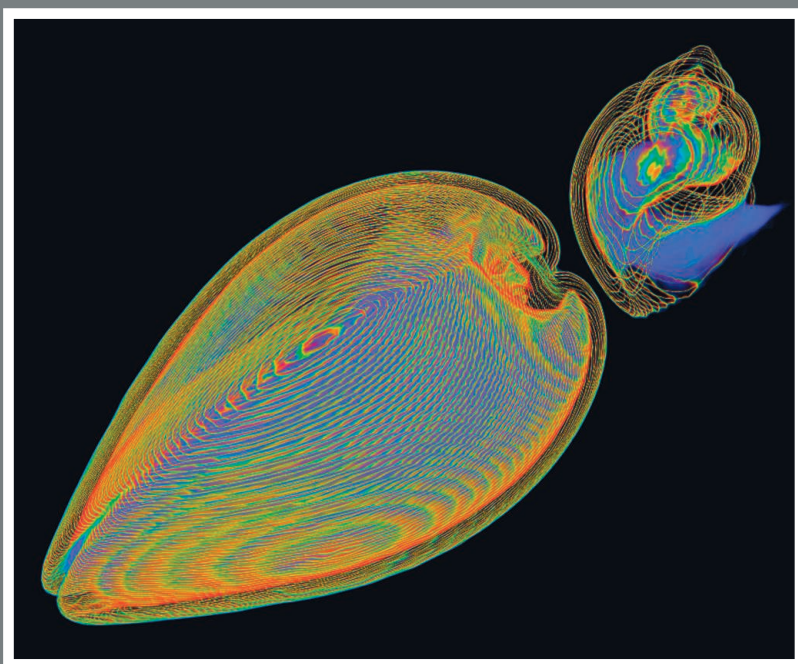
*F*urred, fringed, and barbed, these fruits with tiny seeds—each seed no bigger than 3 mm across—look almost guaranteed to get stuck in your socks. However, biologist Viktor Sykora of Charles University and his colleagues at Czech Technical University in Prague saw the seeds not as common stickers but as works of art. To image the seeds' fine details, the team used high-resolution, high-contrast x-rays (left) along with traditional microscopy (right). The most challenging part of the 20-hour process, Sykora says, was to find a way to fix the seeds in place using a material that would be invisible in the final image. Although high-resolution x-rays are commonly used to visualize the internal structures of small objects without destroying them, according to the authors it has never before been applied to the visualization of seeds. "The number of details that could be seen in the final image delighted us," Sykora says. He hopes that the images will motivate more scientists to use the technique in plant biology, as well as inspire painters, designers, and architects. "We should realize how much beauty, elegance, and wit can be found in nature and in seemingly ordinary things," he says.

## HONORABLE MENTION

### Self Defense

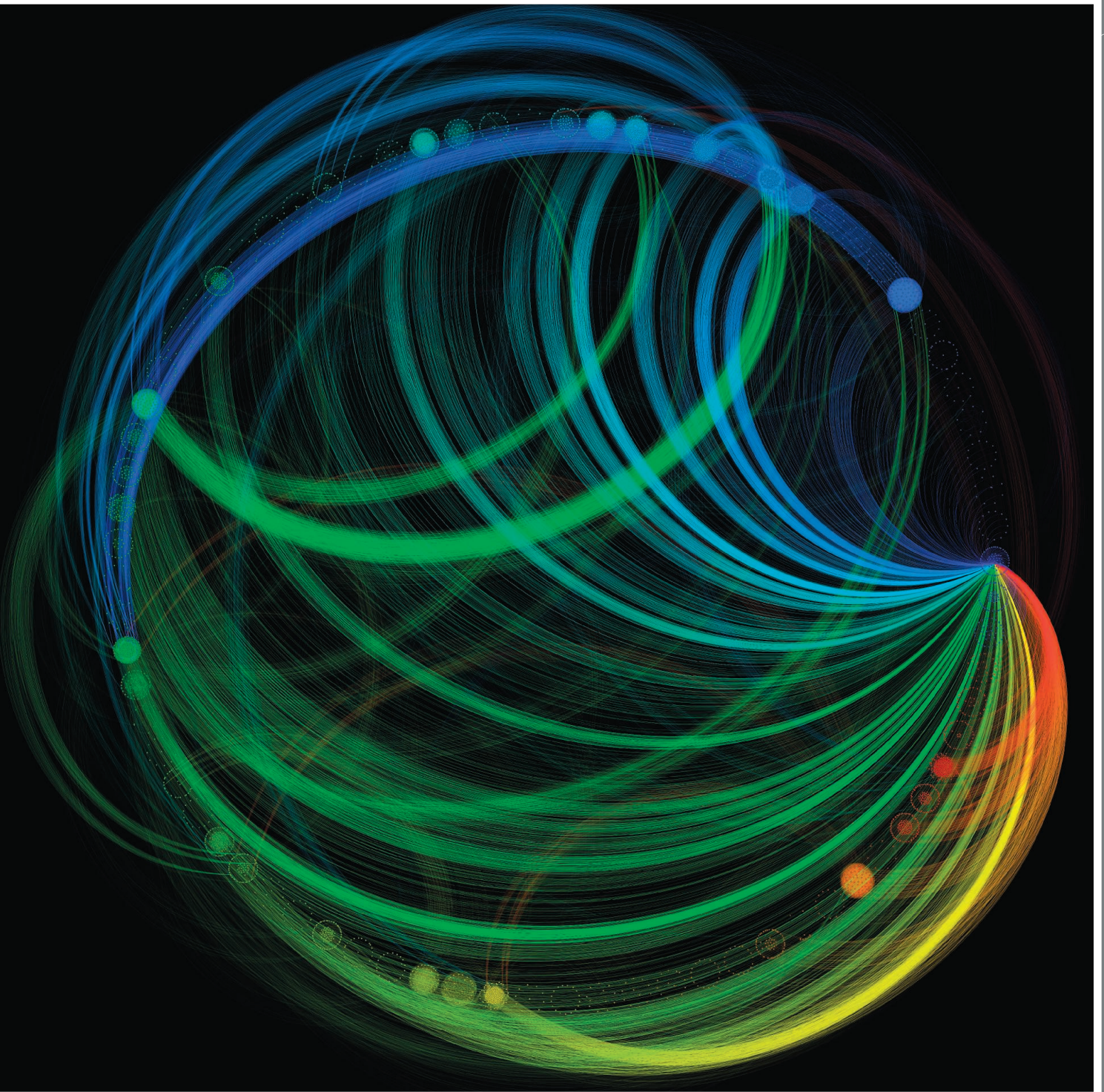
Kai-hung Fung, Pamela Youde Nethersole Eastern Hospital in Hong Kong

*T*his is no shell game, but a matter of life or death. The clam (left) can snap its bivalve shell shut at the first sign of a threat. The whelk (right) has evolved another strategy: The spiral shell provides a series of barricades to potential invaders. It also has a trick up its shell to foil the clam's defense. After softening the clam's single-layered shell with secretions, it can drill a hole right through and eat the clam for lunch. This dramatic example of two different evolutionary strategies for self-defense caught the eye of radiologist Kai-hung Fung at Pamela Youde Nethersole Eastern Hospital in Hong Kong, who has won numerous awards for his creative use of CT scanning to make art. To create this image—which he says was commissioned as a backdrop for a marine-themed musical—Fung used a CT scanner to image thin slices of the whelk and clam, then rendered their contours in rainbow colors to highlight their complex structures. Creating such images involves balancing "two sides of a coin," he says. "One side is factual information, while the other side is artistic."





# Illustration



Downloaded from [www.sciencemag.org](http://www.sciencemag.org) on January 31, 2013



## FIRST PLACE WINNER

### Connectivity of a Cognitive Computer Based on the Macaque Brain

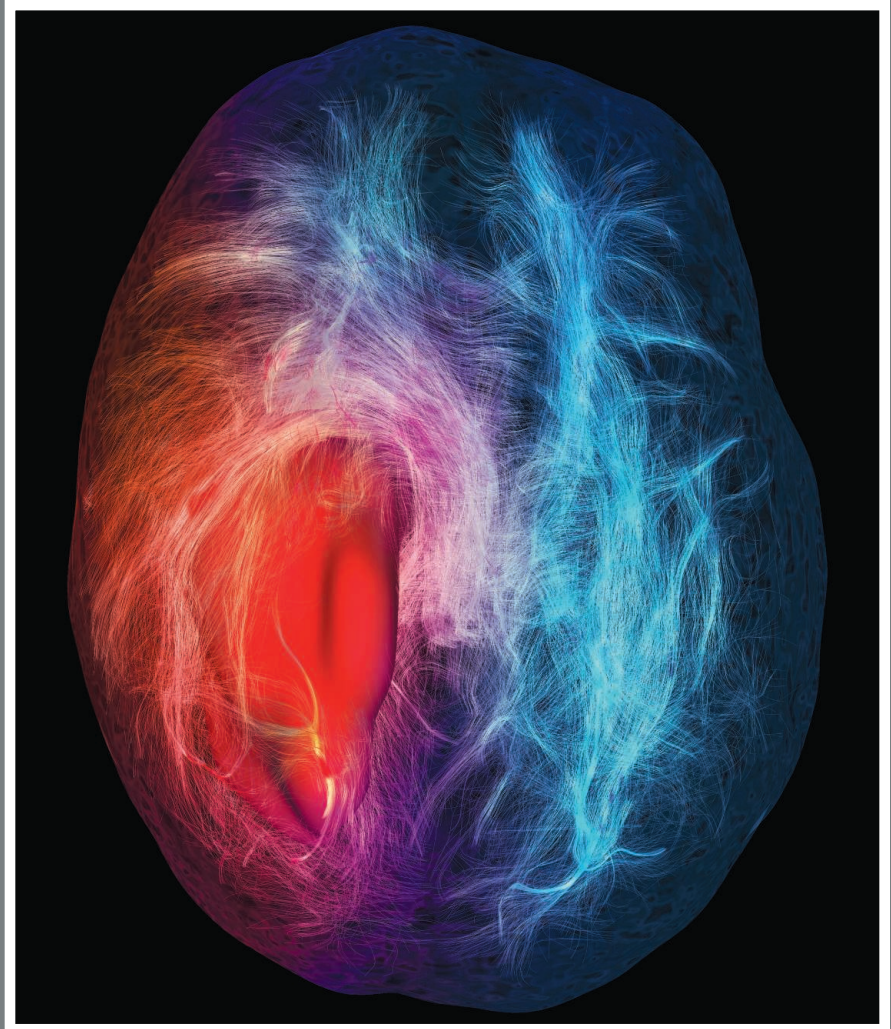
Emmett McQuinn, Pallab Datta, Myron D. Flickner, William P. Risk, and Dharmendra S. Modha, IBM Research - Almaden

The ghostly neon swirl nearly stumped the judges when they first looked at this illustration. Biologist and judge Michael Reddy says that a cognitive computer is “the last thing on Earth” he would have guessed that the image represented at first glance. Inspired by the neural architecture of a macaque, it is the wiring diagram for a new kind of computer that, by some definitions, may soon be able to think.

Over the past 2 years, IBM’s cognitive computing group in San Jose, California, has made great strides toward designing a computer that can detect patterns, plan responses, and learn from its mistakes, says Emmett McQuinn, a hardware engineer at IBM who designed the image. In 2011, the company demonstrated a new kind of computer chip, based on neural circuitry, that combines memory and computational processing for nimbler problem-solving in areas where traditional computers fall short, such as pattern recognition. Then, the company used data from studies of macaque brains to see how those “neurons” should link up, and simulated neural networks with billions of neurons and trillions of axons and synapses.

The first step in creating an illustration to communicate the new wiring system was to reduce trillions and billions of data points to less overwhelming numbers. Even roughly 4000 nodes and 300,000 connections was challenging to get on a single page, McQuinn says. “Fortunately, nature has already thought of this.” First, he clustered and colored the nodes based on the 77 different functional regions that neuroscientists have identified in the macaque brain. Then, after many draft layouts, he found a circular arrangement that pleased him.

“They took something that we know works fantastically efficiently in nature—the circuitry of the brain—and applied that geometry to computing. Then, they found an elegant and beautiful way to display it,” judge Thomas Wagner says.



## HONORABLE MENTION AND PEOPLE’S CHOICE

### Cerebral Infiltration

Maxime Chamberland, David Fortin, and Maxime Descoteaux, Sherbrooke Connectivity Imaging Lab

A malignant brain tumor (red mass, left) in this person’s brain is wreathed by fine tracts of white matter. The red fibers signal danger: If severed by the neurosurgeon’s scalpel, their loss could affect the patient’s vision, perception, and motor function. Blue fibers show functional connections far from the tumor that are unlikely to be affected during surgery. Together, the red and blue fibers provide a road map for neurosurgeons as they plan their operations.

Computer science graduate student Maxime Chamberland of the Sherbrooke Connectivity Imaging Lab in Canada produces images like these on a weekly basis, he says. Using an MRI technique that detects the direction in which water molecules move along the white matter fibers, he generates a three-dimensional image of functional connections in the brain. In addition to the image’s haunting beauty, people respond to the frightening immediacy of the tumor, he says: “They want to know if the patient is ok.” Fortunately, this story has a happy ending: The tumor was removed with no functional damage.



# Posters & Graphics

## FIRST PLACE WINNER

### Adaptations of the Owl's Cervical & Cephalic Arteries in Relation to Extreme Neck Rotation

Fabian de Kok-Mercado, Michael Habib, Tim Phelps, Lydia Gregg, and Philippe Gailloud, Johns Hopkins University School of Medicine

Most animals would suffer a stroke or worse if they tried the owl's most famous party trick. Instead of moving their large, tubular eyes in their sockets, owls swivel their heads 270°. This poster explains the likely mechanism for the eerie ability.

Owls were a "no-brainer" when Fabian de Kok-Mercado was searching for a new

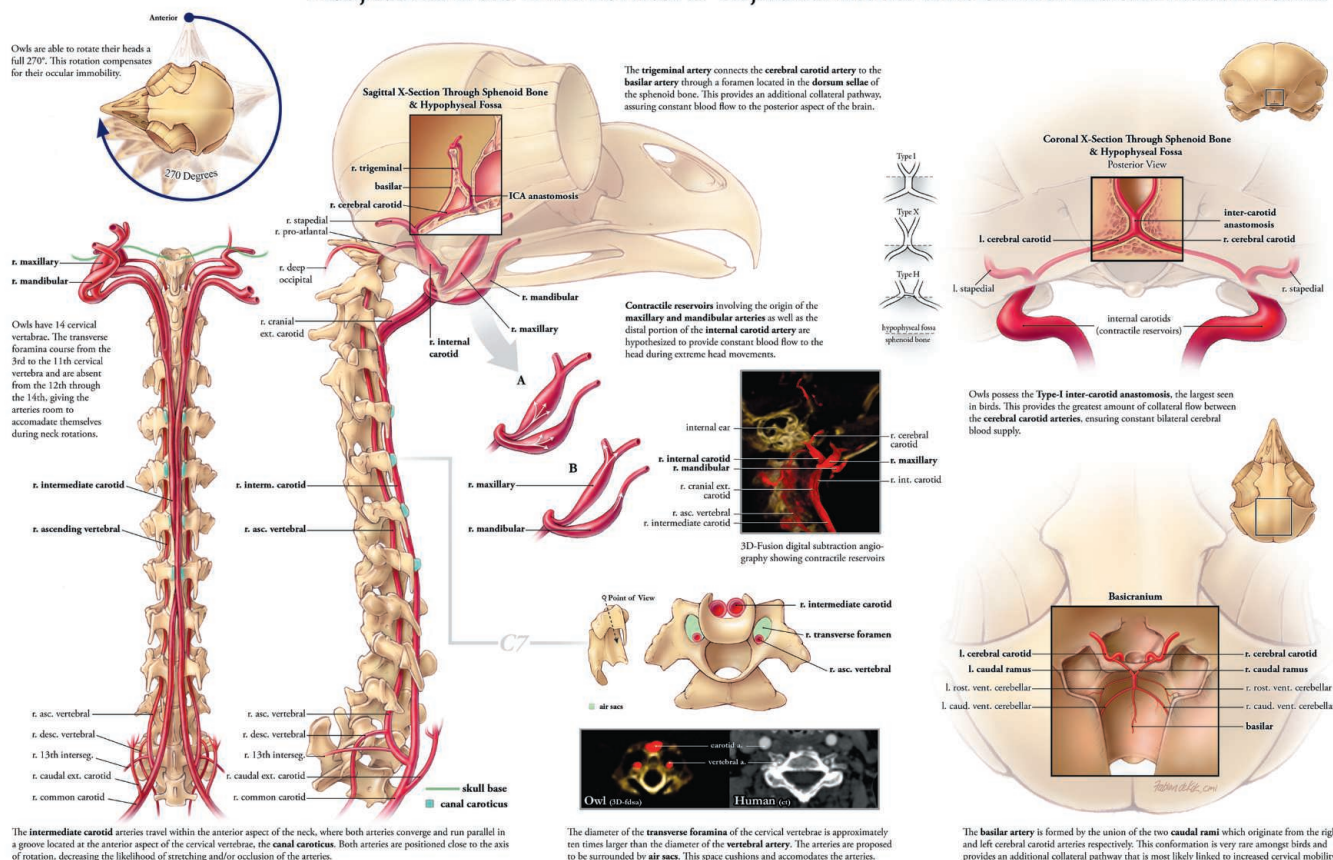
and unusual topic for his master's thesis in medical illustration at Johns Hopkins University in Baltimore, Maryland, in 2012, he says. After noticing a gap in the literature on owls' carotid and vertebral arteries, he and several colleagues obtained 12 dead birds from educational centers in Michigan and Missouri. Then they created three-dimensional images of the owls' blood vessels and bones with a CT scanner and injected the birds with radio-opaque dye and liquefied red plastic to preserve their arteries before dissecting them.

On close examination, the owls revealed surprising secrets, de Kok-Mercado says. For example, the owls' transverse foramina—holes in the vertebrae that the vertebral arteries thread through on their way up the spine to the brain—are much bigger than the arter-

ies themselves, allowing room for movement as the birds' heads twist. In contrast, human vertebral arteries sit snugly inside their foramina, he says. The researchers found swellings in the birds' arteries that likely act as reservoirs for pooling blood when the head is turned, he says, as well as "back-up" arteries that could help supply the brain when other arteries are pinched.

The poster is primarily intended to help veterinarians care for injured birds, but the judges felt it will reward anyone who looks closely. "On the first pass, someone might wonder what the big deal is. But on a second pass, you'll get pulled in," says judge Thomas Wagner. Owls can rotate their heads to a freakish degree; "this illustration answers the question 'How does that really work?'"

### Adaptations of the Owl's Cervical & Cephalic Arteries in Relation to Extreme Neck Rotation



## HONORABLE MENTION

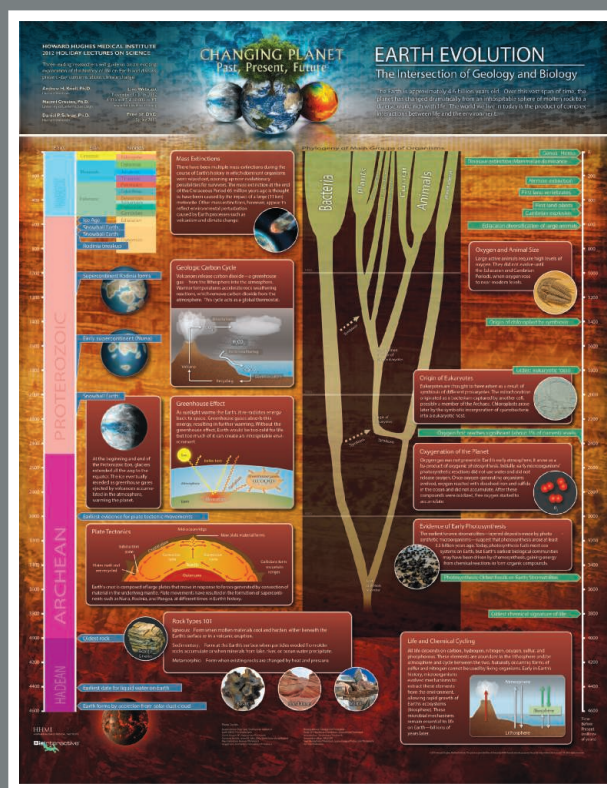
## Earth Evolution: The Intersection of Geology and Biology

Mark Nielsen, Satoshi Amagai, HHMI; Bill Pietsch, Davey Thomas, Astronaut 3 Media Group; and Andy Knoll, Harvard University

If you think Pangaea was a supercontinent a long time ago and dinosaurs are ancient history, prepare for a dose of deep time. All 4.6 billion years of Earth's history are squeezed onto this poster. The whole history of land vertebrates from dinosaurs to humans is barely visible in the top right corner. Because of its relatively young age and minor role in planetary evolution, Pangaea didn't even make the cut. Far more prominent is the evolution of photosynthetic bacteria, which enabled the evolution of many new types of metabolism, including our own by generating oxygen.

The poster draws connections between biological and geological processes in Earth's history, such as mass extinctions, plate tectonics, and the greenhouse effect, says Mark Nielsen, a scientific education fellow at the Howard Hughes Medical Institute in Chevy Chase, Maryland, who helped design the graphic.

"A lot of things happened" in the wide swath of Earth's history that isn't included on traditional posters, he says. For example, whereas many classic visualizations of life on Earth begin just 540 million years ago, when large animals became abundant, Earth Evolution tells a much longer story, stretching back 3.8 billion years to the earliest evidence of life.



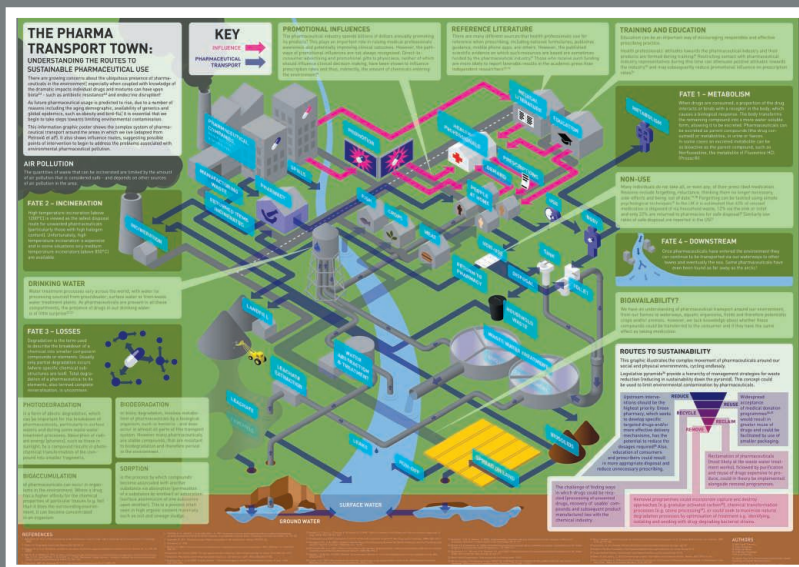
## PEOPLE'S CHOICE

## The Pharma Transport Town: Understanding the Routes to Sustainable Pharmaceutical Use

Will Stahl-Timmins, Mathew White, Michael Depledge, and Lora Fleming, University of Exeter Medical School; Clare Redshaw, Plymouth University

What started as a series of linked text boxes grew into a town. While sketching ideas for this poster, which shows the fate of drugs after people consume them or throw them away, information designer Will Stahl-Timmins of the European Centre for Environment and Human Health found his drawings "spiraling out of control."

By his second attempt, he says, "I realized that it was starting to look like a city." Stahl-Timmins decided to make the focal point of the graphic a river, and build a town around it. Working with an environmental chemist and an environmental psychologist, he added content on social factors, such as education, that affect drug usage and disposal, and showed gaps in knowledge such as how active pharmaceuticals may be when consumed unknowingly in food or water.

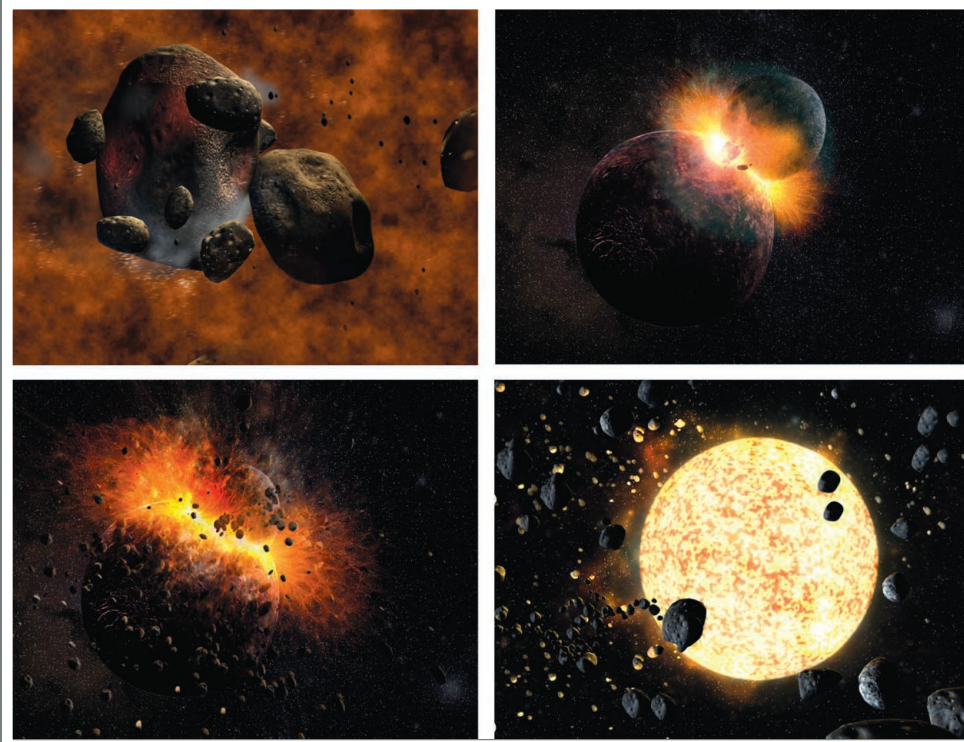


One goal of the poster is to create a tool for policy-makers, he says. So far, so good—at a recent meeting with scientists and legislators discussing the issue, he says the poster ended up covered in sticky notes.



# Games & Apps

No First Place was awarded

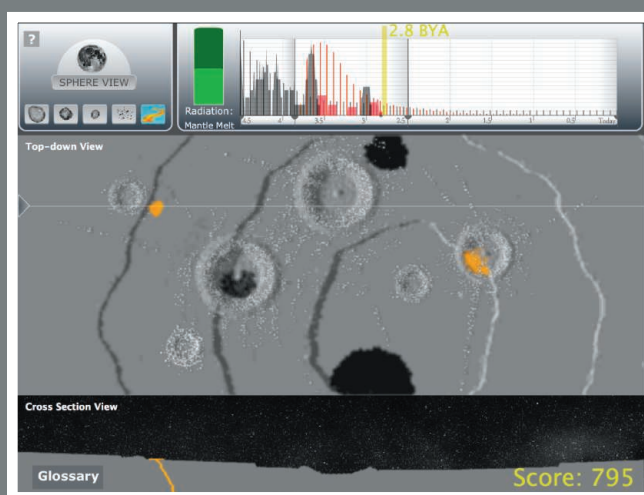


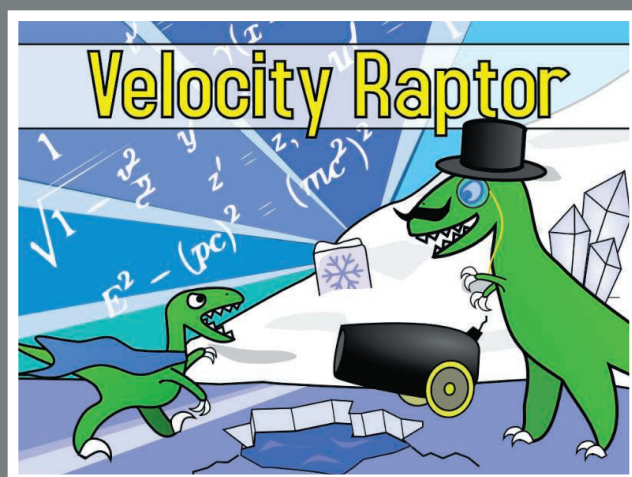
## HONORABLE MENTION

### CyGaMEs Selene II: A Lunar Construction GaME

Debbie Denise Reese, Robert E. Kosko, Charles A. Wood, and Cassie Lightfritz, Wheeling Jesuit University; Barbara G. Tabachnick, California State University, Northridge

What better way to learn how the moon was made than to build one? In this online game geared to grade 5–12 students, players create their own moon with raw space materials, then pummel it with asteroids and flood it with lava. As they adjust the rates of accretion—new materials glomming onto the moon—and differentiation—materials of varying densities settling into a core, mantle, and crust—students create different kinds of moons and gain an intuitive grasp of the physics of collisions, says game theorist and principal investigator Debbie Denise Reese at Wheeling Jesuit University in Wheeling, West Virginia. Introductory scientific concepts such as impact cratering and volcanism can be “gatekeepers” for students, she says. “Year after year, decade after decade, they block students from certain areas of study.” The goals of a CyGaMEs game like Selene are “to turn those concepts into something that the students can do with their bodies” and “measure learning while it occurs.” In CyGaMEs Selene II, she says, “getting the best score is figuring out the science.”





## HONORABLE MENTION

### Velocity Raptor

Andy Hall, TestTubeGames

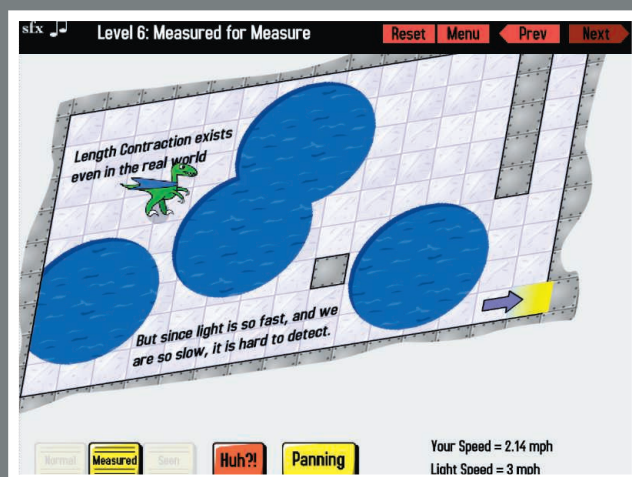
This dapper green dinosaur wearing a bright blue cape is in a hurry to save the world—in fact, she moves at nearly the speed of light. At such breakneck speeds, the world behaves

according to Albert Einstein's theory of special relativity.

This poses practical problems for players who must guide the creature through a world that morphs according to her velocity, incorporating concepts such as Doppler shift and length contraction. As she changes speeds, for example, a slow stream of easily dodged bullets becomes a rapid-fire assault, and the surfaces she must tra-

verse stretch, shrink, and bend.

While Newtonian physics are fairly easy to grasp by "walking around and throwing rocks," says game designer and physicist Andy Hall, special relativity is much more difficult to understand because we don't directly experience it. Velocity Raptor is an attempt to "give people some intuition" about the physics of special relativity by letting them play with it themselves, Hall says.

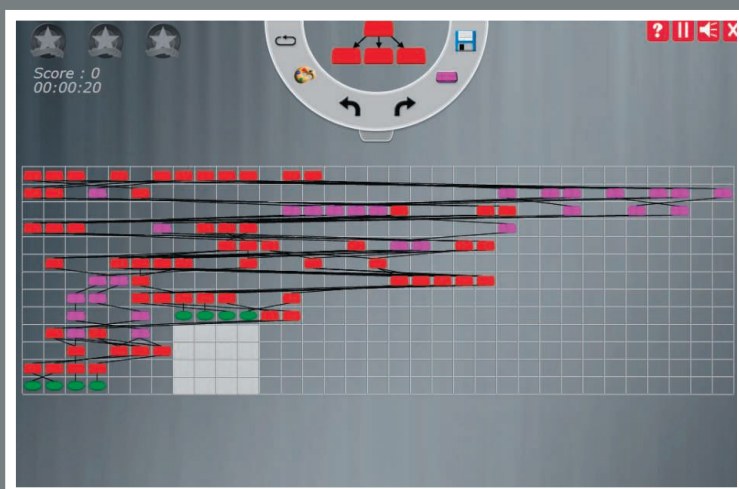


## PEOPLE'S CHOICE

### UNTANGLED

Gayatri Mehta, University of North Texas

When faced with the problem of how to wire a more efficient computer chip, engineer Gayatri Mehta of the University of North Texas in Denton turned to crowd-sourcing. Inspired by a game that recruits online players to discover novel ways to fold proteins, Mehta designed UNTANGLED, a game in which users compete to make the most compact circuit layout on a grid. The real challenge of designing the game was "how to hide all the technical details so that people don't get scared of it's being an engineering problem," she says. To entice math and sciencephobes, she used bold color blocks and left out the underlying algorithms. The game allows her to record millions of new moves and discover human strategies for circuit design that could be employed to develop smaller, more powerful, and longer-lasting electronic devices. "I've learned a lot," she says. "People have amazing skills."







# Video

## FIRST PLACE WINNER AND PEOPLE'S CHOICE

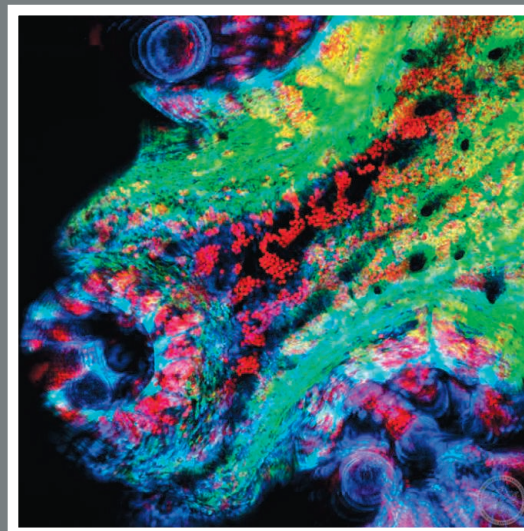
### Alya Red: A Computational Heart

Guillermo Marin, Fernando M. Cucchiatti, Mariano Vázquez, and Carlos Tripiñana, Barcelona Supercomputing Center

From this tangled swirl of fibers, scientists hope to divine the deepest secrets of the human heart. Based on MRI data, each colored strand represents linked cardiac muscle cells that transmit electrical current and trigger a model human heartbeat. The image is an artistic rendering of Alya Red, a new computer model of the heart at the Barcelona Supercomputing Center that marries modern medical imaging techniques with high-powered computing.

Despite centuries of study, scientists are still largely baffled by the heart's complex electrical choreography, says physicist Fernando Cucchiatti, who helped produce the video. When faced with the challenge of presenting Alya Red to a general audience through video, he says, "It took a lot of work to get a script that was engaging, but still scientifically deep enough for an expert eye to see interesting details." The most challenging part was to get the heart fibers in the image above to move in a realistic way, Cucchiatti says. At one point, he says, the animation showed the electrical currents moving backwards. "We had to keep going back to the scientists—did we mess something up?"

"We wanted to create a sense of wonder at the complexity" of the heart itself, he says. The awe wasn't lost on the judges. "I was literally blown away," says Michael Reddy. "After the first time I watched the video, I thought, 'I've just changed the way I thought about a heart.'"



## HONORABLE MENTION

### Observing the Coral Symbiome Using Laser Scanning Confocal Microscopy

Christine E. Farrar, Zac H. Forsman, Ruth D. Gates, Jo-Ann C. Leong, and Robert J. Toonen, University of Hawai'i, Manoa

No dyes or digital software produced the brilliant color of these corals—the glory is all their own. Fluorescent molecules, innate to the corals and to the red algae that live inside and nourish them, shine like Christmas lights under different wavelengths of light emitted by a confocal microscope.

When she saw the corals under the lens for the first time, "my jaw just dropped," says Ruth Gates, a coral biologist at the University of Hawai'i, Manoa, and the narrator of the video. "Most people think corals are inanimate rocks," she says. "We showcase how beautiful and dynamic they are as animals." In the video, which compiles the images into three-dimensional, time-lapse animations, corals extend and retract their glowing tentacles. Tiny creatures crawl over the corals, all part of a complex and threatened ecosystem. In the future, Gates says, it might be possible to use confocal microscopy to classify different coral species or diagnose coral disease by their fluorescent patterns. Prior to applying this technique, she says, "that was not even a facet in our thinking about coral biology."

## HONORABLE MENTION

## Fertilization

Thomas Brown, Nucleus Medical Media

Few narratives in biology are so iconic—or so frequently portrayed—as the epic voyage of the beleaguered sperm to the defensive egg. In most videos about human fertilization, however, “you see little parts of the journey, and then suddenly you see the sperm entering the egg,” says Thomas Brown, chief creative officer of Nucleus Medical Media in Kennesaw, Georgia. “It’s beautiful and iconic, but you don’t really know how you got there.” Given new developments in the science of conception, as well as advancements in digital media, his team decided it was time for a remake. “Fertilization” starts with 300 million sperm, following their perilous journey up the cervix and into the fallopian tube with unprecedented detail and continuity, Brown says. By the time the last few dozen surviving sperm reach the egg, he says, “you’re famished, troubled, and hopeful.” In a new twist based on recent science, he says, the first sperm to reach the egg is rewarded with an embrace, as the egg’s inner membrane encloses and absorbs it.



## HONORABLE MENTION

## Revealing Invisible Changes in the World

Michael Rubinstein, Neal Wadhwa, Frédo Durand, William T. Freeman, and Hao-Yu Wu, MIT

A sleeping infant appears still, but its chest subtly rises and falls with steady breathing. A towering crane looks stable, but rocks imperceptibly in the breeze. In this video, a team of computer scientists at the Massachusetts Institute of Technology in Cambridge demonstrates a new method of magnifying subtle changes normally invisible to the eye. “What the microscope did for visualizing minute objects, we hope to do for minute motions and changes,” says Ph.D. student Michael Rubinstein. Using video as input, the team analyzes each pixel for slight variations in color over time—for example, rhythmic reddening in a man’s face as blood pulses through his veins. Then they apply an algorithm that magnifies the variation, and extract the information they need. By amplifying the man’s slight blush, for example, they were able to obtain his heartbeat. Among other applications, they say, the technique could help doctors take their patients’ vital signs remotely.

Revealing Invisible Changes In The World





## LETTERS

edited by Jennifer Sills

Transmission Studies Resume  
For Avian Flu

IN JANUARY 2012, INFLUENZA VIRUS RESEARCHERS FROM AROUND the world announced a voluntary pause of 60 days on any research involving highly pathogenic avian influenza H5N1 viruses leading to the generation of viruses that are more transmissible in mammals (1). We declared a pause to this important research to provide time to explain the public health benefits of this work, to describe the measures in place to minimize possible risks, and to enable organizations and governments around the world to review their policies (for example, on biosafety, biosecurity, oversight, and communication) regarding these experiments.

During the past year, the benefits of this important research have been explained clearly in publications (2–7) and meetings (8–10). Measures to mitigate possible risks of the work have been detailed (11–13). The World Health Organization has released recommendations on laboratory biosafety for those conducting this research (14), and relevant authorities in several countries have reviewed the biosafety, biosecurity, and funding conditions under which further research would be conducted on the laboratory-modified H5N1 viruses (10, 15–17). Thus, acknowledging that the aims of the voluntary moratorium have been met in some countries and are close to being met in others, we declare

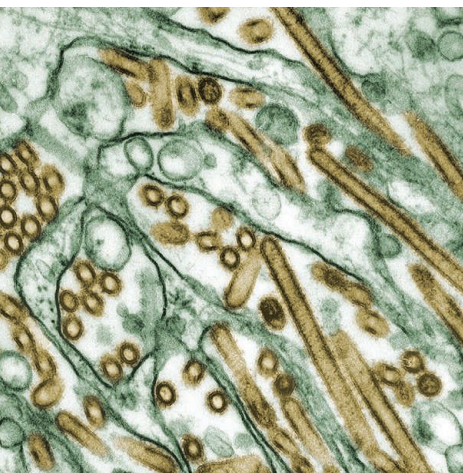
an end to the voluntary moratorium on avian flu transmission studies.

The controversy surrounding H5N1 virus transmission research has highlighted the need for a global approach to dealing with dual-use research of concern. Developing comprehensive solutions to resolve all the issues will take time. Meanwhile, H5N1 viruses continue to evolve in nature. Because H5N1 virus transmission studies are essential for pandemic preparedness and understanding the adaptation of influenza viruses to mammals, researchers who have approval from their governments and institutions to conduct this research safely, under appropriate biosafety and biosecurity conditions, have a public health responsibility to resume this important work. Scientists should not restart their work in countries where, as

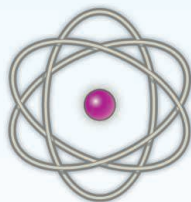
yet, no decision has been reached on the conditions for H5N1 virus transmission research. At this time, this includes the United States and U.S.-funded research conducted in other countries. Scientists should never conduct this type of research without the appropriate facilities, oversight, and all the necessary approvals. We consider biosafety level 3 conditions with the considerable enhancements (BSL-3+) outlined in the referenced publications (11–13) as appropriate for this type of work, but recognize that some countries may require BSL-4 conditions in accordance with applicable standards (such as Canada). We fully acknowledge that this research—as with any work on infectious agents—is not without risks. However, because the risk exists in nature that an H5N1 virus capable of transmission in mammals may emerge, the benefits of this work outweigh the risks.

RON A. M. FOUCHIER,<sup>1</sup> ADOLFO GARCÍA-SASTRE,<sup>2</sup> YOSHIHIRO KAWAOKA,<sup>3,4\*</sup> WENDY S. BARCLAY,<sup>5</sup> NICOLE M. BOUVIER,<sup>6,2</sup> IAN H. BROWN,<sup>7</sup> ILARIA CAPUA,<sup>8</sup> HUALAN CHEN,<sup>9</sup> RICHARD W. COMPANS,<sup>10</sup> ROBERT B. COUCH,<sup>11</sup> NANCY J. COX,<sup>12</sup> PETER C. DOHERTY,<sup>13</sup> RUBEN O. DONIS,<sup>12</sup> HEINZ FELDMANN,<sup>14</sup> YI GUAN,<sup>15</sup> JACQUELINE M. KATZ,<sup>12</sup> OLEG I. KISELEV,<sup>16</sup> H. D. KLENK,<sup>17</sup> GARY KOBINGER,<sup>18</sup> JINHUA LIU,<sup>19</sup> XIUFAN LIU,<sup>20</sup> ANICE LOWEN,<sup>21</sup> THOMAS C. METTENLEITER,<sup>22</sup> ALBERT D. M. E. OSTERHAUS,<sup>1</sup> PETER PALESE,<sup>2</sup> J. S. MALIK PEIRIS,<sup>23</sup> DANIEL R. PEREZ,<sup>24</sup> JÜRGEN A. RICHT,<sup>25</sup> STACEY SCHULTZ-CHERRY,<sup>26</sup> JOHN STEEL,<sup>21</sup> KANTA SUBBARAO,<sup>27</sup> DAVID E. SWAYNE,<sup>28</sup> TORU TAKIMOTO,<sup>29</sup> MASATO TASHIRO,<sup>30</sup> JEFFERY K. TAUBENBERGER,<sup>31</sup> PAUL G. THOMAS,<sup>13</sup> RALPH A. TRIPP,<sup>32</sup> TERRENCE M. TUMPEY,<sup>12</sup> RICHARD J. WEBBY,<sup>26</sup> ROBERT G. WEBSTER<sup>26</sup>

<sup>1</sup>Department of Virology, Erasmus Medical Center, 3015GE Rotterdam, Netherlands. <sup>2</sup>Department of Microbiology, Icahn School of Medicine at Mount Sinai, New York, NY 10029, USA. <sup>3</sup>Department of Pathobiological Sciences, School of Veterinary Medicine, University of Wisconsin–Madison, Madison, WI 53711, USA. <sup>4</sup>Division of Virology, Department of Microbiology and Immunology, The Institute of Medical Science, University Of Tokyo, Minato-ku, Tokyo 108-8639, Japan. <sup>5</sup>Department of Medicine, Imperial College, London, W2 1PG, UK. <sup>6</sup>Division of Infectious Diseases, Icahn School of Medicine at Mount Sinai, New York, NY 10029, USA. <sup>7</sup>Virology Department, Animal Health and Veterinary Laboratories Agency, Addlestone, KT15, UK. <sup>8</sup>Istituto Zooprofilattico Sperimentale delle Venezie, 35020, Padova, Italy. <sup>9</sup>Harbin Veterinary Research Institute, CAAS, Harbin 150001, China. <sup>10</sup>Influenza Pathogenesis and Immunology Research Center, Emory University, School of Medicine, Atlanta, GA 30322, USA. <sup>11</sup>Department of Molecular Virology and Microbiology, Baylor College of Medicine, Houston, TX 77030, USA. <sup>12</sup>Influenza Division, Centers for Disease Control and Prevention, Atlanta, GA 30333, USA. <sup>13</sup>Department of Immunology, St. Jude Children's Research Hospital, Memphis, TN 38105, USA. <sup>14</sup>Laboratory of Virology, National Institute of Allergy and Infectious Diseases, National Institutes of Health, Rocky Mountain Laboratories, Hamilton, MT 59840, USA. <sup>15</sup>State Key Laboratory of Emerging Infectious Diseases, School of Public Health, The University of Hong Kong, Hong Kong SAR. <sup>16</sup>D.I. Ivanovsky Institute of Virology, Ministry of Public Health, Moscow, Russia. <sup>17</sup>Institut für Virologie, 35043 Marburg, Germany. <sup>18</sup>National Microbiology Laboratory, Public Health Agency of Canada, Winnipeg, MB R3E 3R2, Canada. <sup>19</sup>Department of Preventative Veterinary Medicine, China Agricultural University, Beijing, 100193, China. <sup>20</sup>Animal Infectious Disease Laboratory, School of Veterinary Medicine, Yangzhou University, Yangzhou, Jiangsu 225009, China. <sup>21</sup>Department of Microbiology and Immunology, Emory University School of Medicine, Atlanta, GA 30322, USA. <sup>22</sup>Friedrich-Loeffler-Institut, D-17493 Greifswald–Insel Riems, Germany. <sup>23</sup>Centre of Influenza Research, School of Public Health, The University of Hong Kong, Hong Kong SAR. <sup>24</sup>Department of Veterinary Medicine, University of Maryland, College Park, College Park,



H5N1 virus.



MD 20742, USA. <sup>25</sup>College of Veterinary Medicine, Kansas State University, Manhattan, KS 66506, USA. <sup>26</sup>Department of Infectious Diseases, St. Jude Children's Research Hospital, Memphis, TN 38105, USA. <sup>27</sup>Emerging Respiratory Viruses Section, Laboratory of Infectious Diseases, National Institute of Health, Bethesda, MD 20892–3203, USA. <sup>28</sup>Southeast Poultry Research Laboratory, USDA/Agricultural Research Service, Athens, GA 30605, USA. <sup>29</sup>Department of Microbiology and Immunology, University of Rochester Medical Center, Rochester, NY 14642, USA. <sup>30</sup>Influenza Virus Research Center, National Institute of Infectious Diseases, Tokyo, 208-0011, Japan. <sup>31</sup>Viral Pathogenesis and Evolution Section, Laboratory of Infectious Diseases, National Institute of Health, Bethesda, MD 20892–3203 USA. <sup>32</sup>Department of Infectious Diseases, College of Veterinary Medicine, University of Georgia, Athens, GA 30602, USA.

\*To whom correspondence should be addressed. E-mail: kawaokay@svm.vetmed.wisc.edu

## References

1. R. A. M. Fouchier *et al.*, *Science* **335**, 400 (2012).
2. R. A. M. Fouchier, S. Herfst, A. D. M. E. Osterhaus, *Science* **335**, 662 (2012).
3. S. Herfst, A. D. Osterhaus, R. A. Fouchier, *J. Infect. Dis.* **205**, 1628 (2012).
4. Y. Kawaoka, *Nature* **482**, 155 (2012).
5. H. L. Yen, J. S. Peiris, *Nature* **486**, 332 (2012).
6. D. M. Morens, K. Subbarao, J. K. Taubenberger, *Nature* **486**, 335 (2012).
7. A. S. Fauci, F. S. Collins, *Science* **336**, 1522 (2012).
8. World Health Organization (WHO), "Report on technical consultation on H5N1 research issues" (WHO, Geneva, 2012); [www.who.int/influenza/human\\_animal\\_interface/mtg\\_report\\_h5n1.pdf](http://www.who.int/influenza/human_animal_interface/mtg_report_h5n1.pdf).
9. National Science Advisory Board for Biosecurity, "March 29–30, 2012 Meeting of the National Science Advisory Board for Biosecurity to review revised manuscripts on transmissibility of A/H5N1 influenza virus: Statement of the NSABB" (2012); [http://oba.od.nih.gov/oba/biosecurity/PDF/NSABB\\_Statement\\_March\\_2012\\_Meeting.pdf](http://oba.od.nih.gov/oba/biosecurity/PDF/NSABB_Statement_March_2012_Meeting.pdf).

10. Gain-of-Function Research on Highly Pathogenic Avian Influenza H5N1 Viruses: An International Consultative Workshop, Bethesda, MD, 17–18 December 2012; <http://oba.od.nih.gov/oba/biosecurity/meetings/Dec2012/Agenda-Dec-17-18-2012-HHS-Meeting-GOF%20Research-on-HPAI-H5N1.pdf>
11. A. Garcia-Sastre, *MBio* **3**, e00049 (2012).
12. M. Imai *et al.*, *Nature* **486**, 420 (2012).
13. S. Herfst *et al.*, *Science* **336**, 1534 (2012).
14. WHO, Influenza, Guidance for adoption of appropriate risk control measures to conduct safe research on H5N1 transmission (2012); [www.who.int/influenza/human\\_animal\\_interface/biosafety\\_summary/en/index.html](http://www.who.int/influenza/human_animal_interface/biosafety_summary/en/index.html).
15. Public Health Agency of Canada, Biosafety Advisory: Efficiently Transmissible Engineered Influenza A H5N1 Viruses (2012); [www.phac-aspc.gc.ca/lab-bio/res/adv-avis/sbn-asb-2012-01-31-eng.php](http://www.phac-aspc.gc.ca/lab-bio/res/adv-avis/sbn-asb-2012-01-31-eng.php).
16. Commissie Genetische Modificatie, Publications, 21 March 2012 Letter in response to influenza research Erasmus MC (CGM/111125-04) (2012); [www.cogem.net/index.cfm/nl/publicaties/publicatie/brief-nav-influenza-onderzoek-erasmus-mc](http://www.cogem.net/index.cfm/nl/publicaties/publicatie/brief-nav-influenza-onderzoek-erasmus-mc) [in Dutch].
17. United States Government Policy for Oversight of Life Sciences Dual Use Research of Concern (2012); [http://oba.od.nih.gov/oba/biosecurity/PDF/United\\_States\\_Government\\_Policy\\_for\\_Oversight\\_of\\_DURC\\_FINAL\\_version\\_032812.pdf](http://oba.od.nih.gov/oba/biosecurity/PDF/United_States_Government_Policy_for_Oversight_of_DURC_FINAL_version_032812.pdf).

Published online 23 January 2013;  
10.1126/science.1235140

## Eco-Compensation For Giant Panda Habitat

CHINA'S ACHIEVEMENTS IN GIANT PANDA CONSERVATION (1) are now jeopardized by recent tenure reform of its 167 million hectares of collective forest (2). The reform enables individual farming households to transfer or lease operation rights to outside enterprises. By allowing commercial logging, increased collection of firewood and nontimber forest products, unmanaged tourism, and certain types of industrial development in collective forests where these activities were previously restrained, the reform threatens to deforest, degrade, or disturb up to 3457 km<sup>2</sup> of giant panda habitat, or 15% of what remains. In one recent transaction, a timber company purchased 150 km<sup>2</sup> of collective forest in Shizhu County, Chongqing Province at a reported price of \$2.3 million USD (\$153 USD/ha) (3).

China spent more than \$100 billion USD on eco-compensation to buy back development rights from local communities to secure the continued provision of ecosystem services (4). Extending the eco-compensation program to giant panda habitats could reduce the threat that tenure reform poses to the giant panda while fulfilling the intention of the reform to increase local economic benefits. Communities would sign long-term binding preservation agreements for forest habitats outside of existing reserves in exchange for monetary compensation from county departments. A reasonable price for eco-compensation payments might be \$70 USD per hectare per year for 48 years, following the successful experience of the People's Government of Kaihua County leasing 63 km<sup>2</sup> of collective forest in Gutianshan National Nature Reserve of Zhejiang (5). \$240 million USD in effective eco-compensation payments could prevent a decline in the wild giant panda population. An additional \$2.25 billion USD for effective eco-compensation and habitat restoration could increase the population to substantially more than the threshold of 1000 individuals below which a stable population is classified as vulnerable (6).

BIAO YANG,<sup>1</sup> JONAH BUSCH,<sup>2</sup> LI ZHANG,<sup>3\*</sup>  
JIANGHONG RAN,<sup>1</sup> XIAODONG GU,<sup>4</sup> WEN ZHANG,<sup>5</sup>  
BEIBEI DU,<sup>6</sup> RUSSELL A. MITTERMEIER<sup>2</sup>

<sup>1</sup>Key Laboratory of Bio-Resources and Eco-Environment of Ministry Education, College of Life Science, Sichuan University, Chengdu 610064, China. <sup>2</sup>Conservation International, Arlington, VA 22202, USA. <sup>3</sup>College of Life Sciences, Beijing

Normal University, Beijing 100875, China. <sup>4</sup>Sichuan Wildlife Resource Survey and Conservation Management Station, Chengdu 610081, China. <sup>5</sup>Sichuan Provincial Institute of Forestry Survey and Planning, Chengdu 610081, China. <sup>6</sup>Conservation International, Beijing 100027, China.

\*To whom correspondence should be addressed. E-mail: lzhang@conservation.org

## References

1. State Forestry Administration, *The 3rd National Survey Report on Giant Panda in China* (Science Press, Beijing, 2006).
2. Q. Ping, F. Carlsson, J. Xu, *Land Econ.* **87**, 473 (2011).
3. "A road leads to richness: A case study of collective forest tenure reform in Longtan township, Shizhu County of Chongqing," Chongqing Forestry Bureau (2010); [www.forestry.gov.cn/portals/main/s/102/content-452659.html](http://www.forestry.gov.cn/portals/main/s/102/content-452659.html) [in Chinese].
4. G. Liu, J. Wan, H. Zhang, L. Cai, *Rev. Eur. Community Int. Environ. Law* **17**, 234 (2008).
5. "The Lease embodiment of collective forest in Gutianshan National Nature Reserve," Gutianshan National Nature Reserve (2012); [http://xxgk.kaihua.gov.cn/gzxx/gttx/201203/t20120329\\_257377.htm](http://xxgk.kaihua.gov.cn/gzxx/gttx/201203/t20120329_257377.htm) [in Chinese].
6. IUCN Red List Categories and Criteria, version 3.1 (2001); [www.iucnredlist.org/apps/redlist/static/categories\\_criteria\\_3\\_1#critical](http://www.iucnredlist.org/apps/redlist/static/categories_criteria_3_1#critical).

## Letters to the Editor

Letters (~300 words) discuss material published in *Science* in the past 3 months or matters of general interest. Letters are not acknowledged upon receipt. Whether published in full or in part, Letters are subject to editing for clarity and space. Letters submitted, published, or posted elsewhere, in print or online, will be disqualified. To submit a Letter, go to [www.submit2science.org](http://www.submit2science.org).





## Environmental Health Crucial to Food Safety

IN ITS FIRST DECADE, THE EUROPEAN FOOD Safety Authority (EFSA) has made huge advances in addressing the risks posed by pathogens, contaminants, and additives along the whole food chain, from primary production to final consumption ("Amid Europe's food fights, EFSA keeps its eyes on the evidence," K. Kupferschmidt, *News Focus*, 30 November 2012, p. 1146). Consistent with its role in protecting food security, EFSA also has a mandate to assess risks to plant health from introduced pests and diseases (1). Yet, measures to secure the integrity of the food chain increasingly require assessments of risks, not to humans, crops, or livestock, but to the environment.

EFSA is charged with assessing the environmental risks of biocides used in food decontamination, additives in animal feeds, pesticides, genetically modified organisms, and alien pests and weeds (2). The interrelationship between food safety and the environment can only be expected to strengthen as

the environmental impacts of new food technologies, such as artificial sweeteners (3) and antimicrobial nanoparticles in food packaging (4), become more clearly understood.

However, approaches to environmental risk assessment differ considerably among EFSA's panels, ranging from species-specific ecotoxicology to measures of impacts at the level of entire ecosystems (5–7). A major future challenge will be the harmonization of environmental risk assessments. Harmonization has the potential to herald a new era of comparative risk assessments in which, for example, the environmental impact of pest-resistant genetically modified crops could be directly compared with the alternative pesticide regime. Unfortunately, despite its best efforts, the European Commission has struggled to achieve such harmonization across risk sectors (8).

EFSA might also run into conflict regarding jurisdiction with national environmental protection agencies and the European Environment Agency (EEA). The future will call for both EFSA and EEA to operate more closely together, much as the U.S. Food and Drug Administration and Environment Pro-

tection Agency work to eliminate duplicative jurisdiction (9, 10). Given the pressing global challenge of food security (11), the next decade will require a more integrated approach to European food safety that weighs the risks to human, animal, and environmental health in a coordinated, objective, and transparent manner.

PHILIP E. HULME

Bio-Protection Research Centre, Lincoln University, Lincoln 7647, Canterbury, New Zealand. E-mail: philip.hulme@lincoln.ac.nz

### References

1. P. E. Hulme, P. Pyšek, W. Nentwig, M. Vilà, *Science* **324**, 40 (2009).
2. V. Silano, A. Knaap, D. Lovell, D. Liem, *EFSA J.* **10**, s1001 (2012).
3. M. G. Kokotou, A. G. Asimakopoulou, N. S. Thomaidis, *Anal. Methods* **4**, 3057 (2012).
4. J. H. Priester et al., *Proc. Natl. Acad. Sci. U.S.A.* **109**, E2451 (2012).
5. EFSA, *EFSA J.* **8**, 1821 (2010).
6. EFSA, *EFSA J.* **8**, 1877 (2010).
7. EFSA, *EFSA J.* **9**, 2460 (2011).
8. European Commission, "The future of risk assessment in the European Union: The second report on the harmonisation of risk assessment procedure" (European Commission, Brussels, 2003).
9. S. Reardon, *Science* **332**, 652 (2011).
10. M. A. Hamburg, *Science* **336**, 299 (2012).
11. H. C. J. Godfray et al., *Science* **327**, 812 (2010).

## AAAS Travels

### Arizona Skies



New Discoveries  
April 21-28, 2013

Join us in the "Astronomy Capital of the World" as we learn about new discoveries on Mars and the Moon and see the natural wonders of this desert paradise. Visit Kitt Peak, Arizona-Sonora Desert Museum, Biosphere 2, and see the Phoenix Botanic Garden, Sedona, Sunset Crater, and Wupati near Flagstaff, as well as visit Lowell Observatory where dark skies make the Milky Way a wonder to see! \$2,995 + air.

For a detailed brochure,  
please call (800) 252-4910

All prices are per person twin share + air



BETCHART EXPEDITIONS inc.

17050 Montebello Rd, Cupertino, CA 95014  
Email: AAASinfo@betchartexpeditions.com  
www.betchartexpeditions.com

## Support the sciences. Get rewarded.

Show your AAAS pride and reward yourself with the new AAAS Platinum Advantage Rewards Card from NASA Federal Credit Union.

Apply now and get **10,000 bonus points!**  
Go to [nasafcu.com/AAASpromo](http://nasafcu.com/AAASpromo)



Get **10,000 bonus points** if you sign up for a card and spend \$3,000 within 90 days of account opening.

Learn more at [nasafcu.com/AAASpromo](http://nasafcu.com/AAASpromo).

Subject to credit approval. Membership in AAAS and NASA FCU is required. NASA FCU is federally insured by NCUA.



## ART AND SCIENCE

# The Pleasure of Not Knowing

Camillia Matuk

When in an interview, Richard Feynman lauded “the pleasure of finding things out” (1), he echoed the driving motivations of many other scientists: not just the satisfaction of achieving answers, but the enjoyment of their pursuit—of crafting questions to be both testable and answerable and designing ways to investigate them. We often blame the popular image of science as one of objective, predetermined truth on the way education and the media reduce such narratives (2). But we might also blame the changing tools used to access scientific knowledge, as these also affect how we engage with its questions.

Designers Jenny Volvovski, Julia Rothman, and Matt Lamothe lament the loss of taking pleasure in the “sense of the unknown.” Topics that once would have engaged extended debate are now settled at the touch of a mobile device, where the Google search box stands poised to deliver its archive of human knowledge at our command. With information now so accessible, we demand immediate answers, but we lose the “most fun, the period of wonder and funny guesses.” “Fortunately, there are still mysteries that can’t be entirely explained in a few mouse clicks.”

In *The Where, the Why, and the How*, the trio behind the Chicago- and New York-based design company Also pays homage to scientific uncertainty. After commissioning more than 50 contributors—researchers, academics, teachers, and librarians from mostly North American institutes—to pen summaries of current thinking on unanswered questions in science, they invited 75 prominent and emerging international artists and illustrators to respond with origi-

nal visual interpretations. The resulting hardcover features lavish two-page spreads, in which full-color illustrations face brief essays on an array of topics, including the physics

of the universe, the social organization of primates, the intricacies of the human mind, and ecological relationships between plants and animals. The table of contents reads as a litany of our curiosities and fears and is a measure of the scope of our worries (“Are nanomaterials dangerous?”) and existential concerns (“What

existed before the Big Bang?”). Many entries overlap with the big unanswered questions identified in *Science*’s special 125th anniversary issue from 2005 (3). But whereas some touch on socially relevant issues (“Is sexual orientation innate?”) and globally important ones (“Where will the next pandemic come from?”), others entertain more idle curiosities that widen the book’s appeal to a general audi-

## The Where, the Why, and the How

75 Artists Illustrate Wondrous Mysteries of Science

Jenny Volvovski, Julia Rothman, and Matt Lamothe, Eds.

Chronicle, San Francisco, 2012.

167 pp. \$24.95, £15.99.

ISBN 9781452108223.



John Hendrix's *Do rogue waves exist?*

ence (“Why do we hiccup?”).

This highly browsable volume puts a new lens to the long-time relationship between art and science. As the editors explain, its very concept was inspired by historical medical illustrations: depictions of the structure of red blood cells from classroom diagrams of the 1950s and charmingly inaccurate renderings of human anatomy from Japan’s Edo period. Today, such snapshots of our understanding at earlier times are records of the human pursuit of knowledge. At the same time, they exude a quaint air of naiveté. Developed from traditions in editorial illustration, comics, graphic design, and the fine arts, the illustrations in *The Where, the Why, and the How* reflect on many levels a consciousness of their place in history. Whimsically modern-retro with a pop aesthetic, they appear to comment on the very practice of scientific illustration, putting images to our uncertainty that are less explanatory than they are metaphorical, allegorical, and symbolic. For example, in “Can anything escape a black hole?” Romeo and Juliet reach toward one another across a black hole to exchange the two particles created through Hawking radiation. For “Why do placebos work?” a blue elephant clutches a feather in its trunk and leaps into the air. In “Why do pigeons bob their heads when they walk?” we see a Muybridge-style cartoon of a bird’s locomotion. And for “Why do we fall

for optical illusions?” clever reproductions of canonical illusions fool us into anticipating the tricks our eyes would play (e.g., “These cows are the same size. It’s true.”). Even the book trailer (4) is an artwork in its own right.

Because the book shines in so many respects, it may leave readers wanting more in others. I would have appreciated references to theories cited, pointers to seminal studies, and short biographies if not links to the profiles of the science contributors to match the websites already printed beneath each artist’s name. And whereas variety adds to the book’s visual appeal, it may weaken the collective impact of the written contributions. Admittedly, each entry admirably articulates a complex topic in concise and engaging ways. The most effective essays convey the importance of the question, the logic behind the competing hypotheses, and the methods pursued for finding the answers. The less effective ones meanwhile point unceremoni-

The reviewer is at the Graduate School of Education, University of California, Berkeley, CA 94720, USA. E-mail: cmatuk@berkeley.edu



ously to answers and thus defeat the very feature that otherwise sets this book apart from a conventional encyclopedia.

*The Where, the Why, and the How* serves as a lovely time capsule of our contemporary concerns, curiosities, ignorance, and future ambitions. It repositions science as a field that poses and investigates questions and will surely be as engaging a read in the

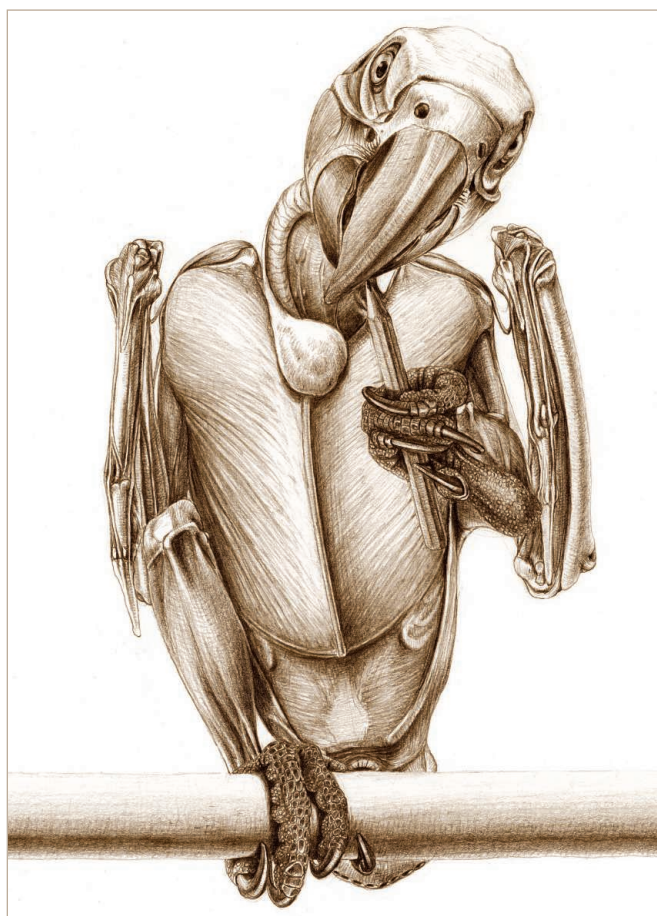
not-too-distant future (already, the entry for “What is the ‘god particle’?” is outdated). Volvovski, Rothman, and Lamothe offer a stunning collection that reimagines scientific wonder and that is an eloquent argument for slow living in an age of immediate access. Drawing on Feynman’s wisdom, the authors invite readers to savor the visceral pleasure of not knowing—taking delight in allowing

thoughts to unravel and meander through alternative possibilities.

#### References

1. “The pleasure of finding things out,” *Horizon*, BBC (23 November 1981).
2. S. D. Kolstø, *Sci. Educ.* **85**, 291 (2001).
3. What We Don’t Know, *Science* **309**, 75–102 (2005).
4. <http://vimeo.com/50786051#>.

10.1126/science.1232334



Red-and-green macaw (*Ara chloropterus*) with skin removed.

**The Unfeathered Bird.** Katrina van Grouw. Princeton University Press, Princeton, NJ. 2013. 301 pp. \$49.95, £34.95. ISBN 9780691151342. Although her detailed drawings of bones, skeletons, muscles, and other internal tissues would not be out of place in a treatise on avian anatomy, van Grouw intends them to reveal how birds’ “appearance, posture, and behavior influence, and are influenced by, their internal structure.” To this end, many of the birds are shown in lifelike poses or engaged in typical activities (e.g., a Eurasian sparrowhawk plucking its prey, a red-throated loon swimming underwater, and a Wilson’s storm petrel patting the water’s surface with its feet). All 385 illustrations are from actual specimens—wherever possible, ones that the artist prepared at home. The 200 species depicted span most of the anatomical diversity of birds. Reflecting the book’s concerns with outward appearances and the effects of convergent adaptive evolution, the chapters are ordered on the basis of Linnaeus’s *Systema Naturae*. But the author includes discussions of the actual relationships in her informative text.

**Extinct Boids.** Ralph Steadman and Ceri Levy. Bloomsbury, London. 2012. 244 pp. £35. ISBN 9781408178621. Bloomsbury, New York, \$50. ISBN 9781620401064.

In early 2011, Levy invited Steadman to paint an extinct bird for an art project, *Ghosts of Gone Birds*, that was organized to raise awareness of endangered birds. The cartoonist’s enthusiasm for the project eventually led him to produce 110 paintings. This portfolio comprises iconic vanished species (such as great auk, passenger pigeon, and dodo), less-known taxa (e.g., robust white-eye and Colombian grebe), extant birds (some critically endangered; a few rather widespread), and numerous fantastic boids Steadman discovered in his imagination (including wizened twit and splattered shag). Levy’s commentary describes the genesis of these vibrantly colored, often humorous creations.



Cuban macaw (*Ara tricolor*). Driven extinct by hunting, this island endemic was last reported in 1885.



ously to answers and thus defeat the very feature that otherwise sets this book apart from a conventional encyclopedia.

*The Where, the Why, and the How* serves as a lovely time capsule of our contemporary concerns, curiosities, ignorance, and future ambitions. It repositions science as a field that poses and investigates questions and will surely be as engaging a read in the

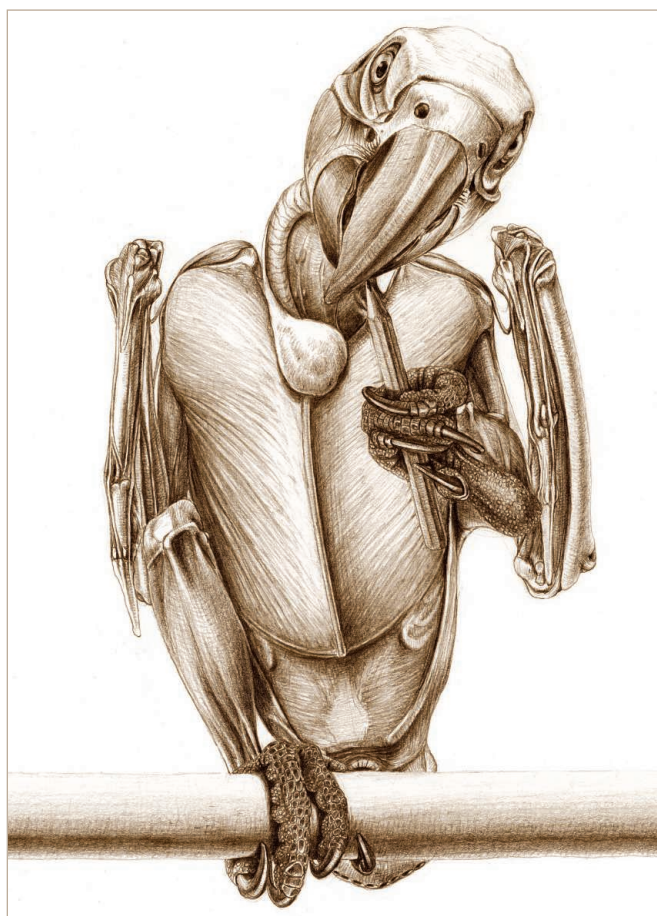
not-too-distant future (already, the entry for “What is the ‘god particle’?” is outdated). Volvovski, Rothman, and Lamothe offer a stunning collection that reimagines scientific wonder and that is an eloquent argument for slow living in an age of immediate access. Drawing on Feynman’s wisdom, the authors invite readers to savor the visceral pleasure of not knowing—taking delight in allowing

thoughts to unravel and meander through alternative possibilities.

#### References

1. “The pleasure of finding things out,” *Horizon*, BBC (23 November 1981).
2. S. D. Kolstø, *Sci. Educ.* **85**, 291 (2001).
3. What We Don’t Know, *Science* **309**, 75–102 (2005).
4. <http://vimeo.com/50786051#>.

10.1126/science.1232334



Red-and-green macaw (*Ara chloropterus*) with skin removed.

**The Unfeathered Bird.** Katrina van Grouw. Princeton University Press, Princeton, NJ. 2013. 301 pp. \$49.95, £34.95. ISBN 9780691151342. Although her detailed drawings of bones, skeletons, muscles, and other internal tissues would not be out of place in a treatise on avian anatomy, van Grouw intends them to reveal how birds’ “appearance, posture, and behavior influence, and are influenced by, their internal structure.” To this end, many of the birds are shown in lifelike poses or engaged in typical activities (e.g., a Eurasian sparrowhawk plucking its prey, a red-throated loon swimming underwater, and a Wilson’s storm petrel patting the water’s surface with its feet). All 385 illustrations are from actual specimens—wherever possible, ones that the artist prepared at home. The 200 species depicted span most of the anatomical diversity of birds. Reflecting the book’s concerns with outward appearances and the effects of convergent adaptive evolution, the chapters are ordered on the basis of Linnaeus’s *Systema Naturae*. But the author includes discussions of the actual relationships in her informative text.

**Extinct Boids.** Ralph Steadman and Ceri Levy. Bloomsbury, London. 2012. 244 pp. £35. ISBN 9781408178621. Bloomsbury, New York, \$50. ISBN 9781620401064.

In early 2011, Levy invited Steadman to paint an extinct bird for an art project, *Ghosts of Gone Birds*, that was organized to raise awareness of endangered birds. The cartoonist’s enthusiasm for the project eventually led him to produce 110 paintings. This portfolio comprises iconic vanished species (such as great auk, passenger pigeon, and dodo), less-known taxa (e.g., robust white-eye and Colombian grebe), extant birds (some critically endangered; a few rather widespread), and numerous fantastic boids Steadman discovered in his imagination (including wizened twit and splattered shag). Levy’s commentary describes the genesis of these vibrantly colored, often humorous creations.



Cuban macaw (*Ara tricolor*). Driven extinct by hunting, this island endemic was last reported in 1885.



**A World in One Cubic Foot: Portraits of Biodiversity.**

David Liittschwager. University of Chicago Press, Chicago. 2012.  
204 pp. \$45, £29. ISBN 9780226481234.

Photographer Liittschwager focuses on six cubic feet, each carefully chosen to characterize a particular rich habitat. He examines saltwater bay (beneath San Francisco's Golden Gate Bridge), cloudforest canopy (Monteverde, Costa Rica), coral reef (Moorea, Polynesia), deciduous forest floor (Central Park, New York), freshwater river (Duck River, Tennessee), and mountain fynbos shrubland (Table Mountain, South Africa). Deploying a metal cube to frame his samples, he recorded all the organisms visible to the naked eye that could be found in the cube over a typical 24 hours. The book presents selected individual portraits of these animals and plants, along with synoptic collages (and accompanying keys) that highlight the abundance of life at each site. Short essays by researchers and writers introduce the six settings.



Survey spot with sampling cube. The Duck River at Lillard's Mill, Tennessee.



**Duck River collage.** These 107 animals include 81 species of fish, turtles, and invertebrates.



**Grazing gastropod.** Pleurocerids such as panel elimia (*Elimia laqueata*) (2 cm) feed on the periphyton attached to submerged surfaces.



**Filter feeder.** Pistolgrip (*Quadrula verrucosa*) (6.2 cm), a unionid bivalve.

## ECOLOGY

# Hurdles and Opportunities for Landscape-Scale Restoration

Myles H. M. Menz,<sup>1,2\*</sup> Kingsley W. Dixon,<sup>1,2</sup> Richard J. Hobbs<sup>2</sup>

A priority outcome from the 2012 United Nations Rio+20 Conference on Sustainable Development (1) was the target to restore, by 2020, 150 million ha of disturbed and degraded land globally (2). An initiative of this scale is estimated to cost U.S. \$18 billion per year and to provide U.S. \$84 billion per year to the global economy (2). Although such initiatives have transformative potential because of their scope and backing, they require technology and knowledge capacity to deliver proven, scalable restoration (3). Restoration processes must achieve the greatest value for money, as far as socioeconomic and biodiversity conservation outcomes, while avoiding costly and simplistic plantings (4).

Although we recognize that preventing loss and damage in the first place is a far better investment than restoration after damage has occurred, we propose a four-point plan to ensure that restoration sustains and enhances ecological values: (i) identify focal regions with high restoration demands, (ii) identify knowledge gaps and prioritize research needs to focus resources on building capacity, (iii) create restoration knowledge hubs to aggregate and disseminate knowledge at the science-practice interface, and (iv) ensure political viability by establishing economic and social values of functioning restored ecosystems. These points are interrelated and may occur in parallel.

Ecological restoration, not just a matter of planting trees (5), involves assisting the recovery of a damaged or destroyed ecosystem (6). Landscape-scale restoration includes large, contiguous, or fragmented areas (equal to or greater than several km<sup>2</sup>). Restoration often takes place in an unpredictable socio-ecological context, involving multiple stakeholders and interests, where local actions aggregate into a broader context that considers landscape flows and connectivity (see the figure). A realistic assessment of prior knowledge, technological capacity, financial viability, and

social license is needed for understanding scientific and practical constraints to achieving global restoration targets. Recent examples, such as China's Great Green Wall and Grain for Green programs, although politically viable, could threaten ecosystem services through ill-placed restoration (7). In such situations, the scientific support behind less-popular options may have been ignored or simply may not be available. A key limitation is the lack of information on successes and failures in landscape-scale restoration projects (8) to guide more effective practice. Early engagement with science will be critical, such as Future Earth: Research for Sustainability, launched at Rio+20, which proposes coordination and facilitation of global science (9).

## Identification of Focal Regions

Success of landscape-scale restoration projects will be more likely in some ecosystems and regions than others (10). We should set

Gaps in knowledge must be identified, capacities developed, and research translated into policy and practice.

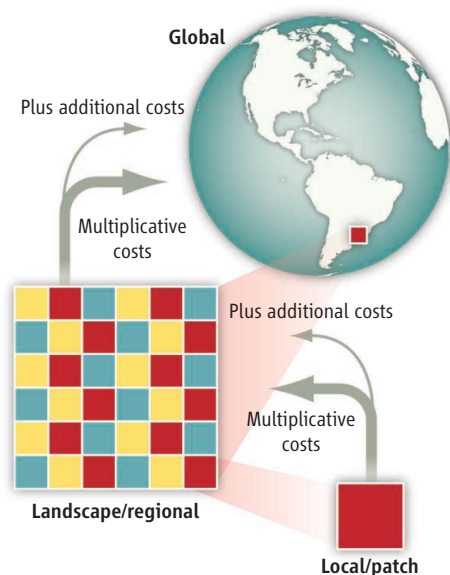
realistic goals (11–13) and identify ecosystems where resources are best positioned to achieve the most cost-effective results to maximize ecosystem services and biodiversity gains. Professional societies, governments, the private sector, and nongovernmental organizations must collaborate through umbrella organizations such as the International Union for Conservation of Nature (IUCN) to set standards and prioritize ecosystems and regions for resource allocation. Such an approach has identified 2 billion ha globally that provide forest restoration opportunities (14) where ecosystem services could be delivered through cost-effective natural and assisted regeneration.

Drylands also provide landscape-scale restoration opportunities. Drylands, extensive in many parts of the world, have been identified as ecosystems that will suffer greatly from climate change, with desertification likely to affect 30% of the world's population (15). Many drylands are major resource hubs that provide financial capacity to fund and implement research and restoration (15).

## Prioritization of Research Needs

Once areas have been prioritized and funding has been secured, key knowledge gaps for achieving landscape-scale restoration should be identified. There are few ecosystems for which we have sufficient knowledge to achieve restoration success beyond the local scale. A range of scalable, proven, and cost-effective capacities will be needed, e.g., the scaling-up of resources such as seed banks, to facilitate landscape-scale restoration (3). Approaches are being developed to prioritize actions depending on landscape conditions and likely effectiveness (16, 17).

Although long-term cost-effectiveness of most interventions remains unclear and may be potentially costly, some regional-scale projects may be relatively inexpensive. Linking restoration initiatives with evolving knowledge will allow for targeted, cost-effective interventions (12), while avoiding actions that may make things worse in the longer term [e.g., (18)]. For example, wetland systems where altered water flows have caused system decline can



**Scaling up restoration.** Costs multiply as local patches are added, each requiring site treatment, seed or plant input, management, and so on. Additional costs and knowledge are necessitated by landscape and regional structures and processes (e.g., hydrological management or transaction costs among different land uses). Economies of scale may be possible. Scaling up to the global level requires multiplicative and additional costs relating to social and political requirements.

<sup>1</sup>Kings Park and Botanic Garden, Perth 6005, Australia.

<sup>2</sup>Plant Biology, University of Western Australia, Perth 6009, Australia.

\*Author for correspondence. E-mail: myles.menz@bgpa.wa.gov.au



be restarted by reinstating prior conditions, such as in the Mesopotamian Marshes (19). Dryland restoration can be kick-started by providing simple physical barriers to water movement (20).

There is growing awareness of the interdisciplinary science packages required for restoration (16) [e.g., microbiology (21), seed science (3), and pollination ecology (22, 23)], integrated with socioeconomic expertise (24). There needs to be a balance between generally applicable approaches and solutions tailored to region- or ecosystem-specific requirements. Interdisciplinary actions—facilitated by umbrella organizations such as the Society for Ecological Restoration, IUCN, and Conservation International—would provide project carriage beyond the typical 3- to 5-year funding cycles. Although funding agencies and universities need to play a key role in supporting these programs, lobbying by umbrella organizations would be an important step in establishing the process. Successful collaborative initiatives [e.g., (25)] provide solid footing for future programs.

#### Restoration Knowledge Hubs

Effective information transfer is paramount to the success of landscape-scale restoration projects and to avoid repeating costly mistakes while closing the science-practice gap (13). Attempts to bridge this gap are often local in focus. Restoration ecologists need to take responsibility for translating their science into on-the-ground actions (13, 26). Successful science-practice communication must be two-way to achieve the greatest benefit, as practitioners are valuable for identifying knowledge gaps and guiding research. Evidence-based literature and information repositories should be developed for the restoration sciences (27).

Few restoration initiatives provide for dialogue with the restoration sciences. The Australian government is spending A\$1 billion (U.S. \$1 billion) to restore 18 million ha of degraded land, yet, is silent on links to science or provision of investment in research (28). This is despite the acknowledgment of the southwest Australian biodiversity hot spot as a region where restoration need far outstrips scientific knowledge (3).

Professional scientific associations can compile scientific knowledge and restoration practice and act as information clearing-houses (13). The Global Restoration Network (29) provides a Web-based hub for information on restoration projects. Initiatives such as Future Earth provide hope for linking technology, innovation, and science (30). Gov-

ernments and funders of ecological restoration must develop practice-based templates for global capacity-building and measures for streamlining knowledge dissemination.

#### Political Viability of Restoration

Landscape-scale restoration projects are likely to work best when initiators are motivated by both environmental and social issues or either one [e.g., (31)]. Good science is required to ensure that the programs are a success, although achieving long-term, dual ecological and social goals remains challenging [e.g., (32, 33)]. Restoration will provide economic benefits worldwide (34), particularly if ecosystem services are matched with biodiversity conservation, including nonmarket services (35, 36). Creating rigorous economic valuation and efficient markets for the wide range of ecosystem services is a critical step, with much still to be done.

Net benefits of sustainable, ecologically resilient restoration (13, 37) must be communicated in a compelling way to policymakers and practitioners if longer-term funding opportunities are to be realized, particularly support for science programs to fill knowledge gaps. Scientists need to shift from a focus on journal writing and professional conferences to reach a broader community and political audience who will make the call on restoration funding. Such a dialogue must remain science-based. For example, evaluation of cost-effectiveness based on ecosystem service return showed that many dry forest restoration approaches may be economic failures (38). Robust analyses like this are important for identifying false, politically damaging assumptions of restoration programs, e.g., China's Great Green Wall (7).

However, in some cases, given the social and ecological values of restoration, costs need not be considered a hurdle, but a challenge to improve our technology in developing more cost-effective techniques.

#### Not a Magic Bullet

Restoration is often viewed simplistically, as if science and practice were well established. Restoration ecology is not a magic bullet that provides instant ecosystems of the desired type, but an emerging science less than four decades old. In many cases, restoration projects fall short of reinstating functional ecosystems akin to their natural reference sites (10). For example, restoration projects developed in exchange for habitat destruction elsewhere are becoming more prevalent, resulting in losses of high-

quality ecosystems that we are not yet able to restore (10). Deciding on useful targets in a period of rapid environmental change is another area of discussion in restoration ecology (11, 13).

Restoration knowledge hubs are most often associated with developed, boreal economies. For landscape-scale restoration to be effective, science funding and technology development need to realize targets that go beyond such local scales. Restoration is but one tool; with effective management and prevention of further damage to natural areas, restoration would become less urgent.

#### References and Notes

1. Rio+20 Dialogues, <http://vote.riodialogues.org/>.
2. IUCN, restoring lost forest; [www.iucn.org/?uNewsID=8147](http://www.iucn.org/?uNewsID=8147).
3. D. J. Merritt, K. W. Dixon, *Science* **332**, 424 (2011).
4. R. J. Hobbs, *Aust. J. Bot.* **55**, 371 (2007).
5. J. Tollefson, *Nature* **486**, 13 (2012).
6. Society for Ecological Restoration, [www.ser.org](http://www.ser.org).
7. J. Xu, *Nature* **477**, 371 (2011).
8. L. A. Brudvig, *Am. J. Bot.* **98**, 549 (2011).
9. International Council for Science, [www.icsu.org/future-earth/](http://www.icsu.org/future-earth/).
10. M. Maron *et al.*, *Biol. Conserv.* **155**, 141 (2012).
11. R. Hobbs, *Restor. Ecol.* **15**, 354 (2007).
12. R. J. Hobbs *et al.*, *Bioscience* **61**, 442 (2011).
13. K. N. Suding, *Annu. Rev. Ecol. Evol. Syst.* **42**, 465 (2011).
14. World Resources Institute, [www.wri.org/project/forest-landscape-restoration/](http://www.wri.org/project/forest-landscape-restoration/).
15. J. F. Reynolds *et al.*, *Science* **316**, 847 (2007).
16. K. A. Wilson *et al.*, *J. Appl. Ecol.* **48**, 715 (2011).
17. K. A. Wilson *et al.*, *PLoS Biol.* **5**, e223 (2007).
18. M. L. Martinez *et al.*, *Front. Ecol. Environ.* **10**, 44 (2012).
19. C. J. Richardson *et al.*, *Science* **307**, 1307 (2005).
20. D. J. Tongway, J. A. Ludwig, *Restor. Ecol.* **4**, 338 (1996).
21. J. Harris, *Science* **325**, 573 (2009).
22. K. W. Dixon, *Science* **325**, 571 (2009).
23. M. H. M. Menz *et al.*, *Trends Plant Sci.* **16**, 4 (2011).
24. J. Aronson, *Landscape Ecol.* **26**, 457 (2011).
25. K. A. Keenleyside *et al.*, *Ecological Restoration for Protected Areas: Principles, Guidelines and Best Practices* (IUCN, Gland, Switzerland, 2012).
26. R. Arlettaz *et al.*, *Bioscience* **60**, 835 (2010).
27. W. J. Sutherland *et al.*, *Trends Ecol. Evol.* **19**, 305 (2004).
28. Biodiversity Fund, [www.cleanenergyfuture.gov.au/biodiversity-fund/](http://www.cleanenergyfuture.gov.au/biodiversity-fund/).
29. Global Restoration Network, [www.globalrestorationnetwork.org/](http://www.globalrestorationnetwork.org/).
30. A. Abreu, *Science* **336**, 1397 (2012).
31. W. Maathai, *The Green Belt Movement: Sharing the Approach and the Experience* (Lantern Books, New York, 2006).
32. A. Buch, A. B. Dixon, *Sustain. Dev.* **17**, 129 (2009).
33. B. W. van Wilgen *et al.*, *Biol. Conserv.* **148**, 28 (2012).
34. S. Cunningham, *ReWealth!* (McGraw-Hill, New York, 2008).
35. J. M. Bullock *et al.*, *Trends Ecol. Evol.* **26**, 541 (2011).
36. B. J. Cardinale *et al.*, *Nature* **486**, 59 (2012).
37. R. Biggs *et al.*, *Annu. Rev. Environ. Resour.* **37**, 421 (2012).
38. J. C. Birch *et al.*, *Proc. Natl. Acad. Sci. U.S.A.* **107**, 21925 (2010).

**Acknowledgments:** K.W.D. is supported by Australian Research Council (ARC) DP0985685 and DP1096717. R.J.H. is funded via an ARC Australian Laureate Fellowship and the ARC Centre of Excellence for Environmental Decisions.

## CANCER

# Cancer Cell Phenotypes, in Fifty Shades of Grey

Andriy Marusyk and Kornelia Polyak

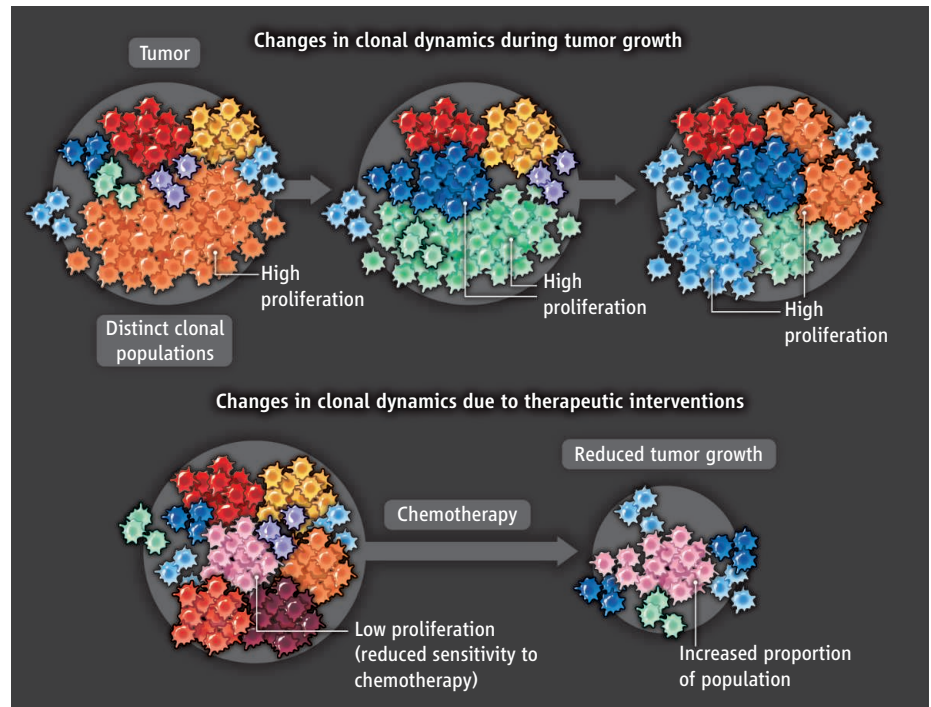
Intratumor heterogeneity refers to biological differences between malignant cells originated within the same tumor. Possible explanations for this include genetic heterogeneity (resulting from the inherent genetic instability of cancer combined with evolutionary dynamics) and cell differentiation hierarchies in tumor cell populations (1–3). However, the results of Kreso *et al.* (4) on page 543 of this issue strongly suggest that biological differences between tumor cells can be due to additional mechanisms.

To explore functional heterogeneity within tumors, Kreso *et al.* traced the fates of single cell-derived clones from 10 different human primary colorectal tumors over multiple serial transplantations in mouse xenografts. Analysis of copy number alterations and deep sequencing for mutational hotspots in 42 cancer genes revealed that a number of xenografts retained the genomic profile of the primary tumor, whereas in some cases the first transplant and the parental tumor displayed substantial genetic differences indicative of clonal selection during xenograft growth, but in subsequent transplants the tumors remained genetically fairly stable. Deep sequencing of the mutational hotspots in distinct single cell-derived clones also showed high concurrence, implying relative genetic homogeneity within xenografts.

Despite this genetic homogeneity, the different cancer clones that Kreso *et al.* observed in a tumor—made distinguishable through unique genomic integration sites of a lentiviral vector as a marker—displayed notable differences in behavior during serial transplantation. In addition to persistent clones that were observed through multiple passages and clones that became extinct with serial passages, the authors identified clones with rather unexpected behaviors. Some of these unusual clones remained below the detection threshold during the initial passages but reemerged with later transplantations; another pattern was the disappearance below threshold in mid-passages and reappearance in subsequent transplants. Although these

Department of Medical Oncology and Center for Functional Cancer Epigenetics, Dana-Farber Cancer Institute and Department of Medicine, Harvard Medical School, Boston, MA 02215, USA. E-mail: kornelia\_polyak@dfci.harvard.edu

Intratumor heterogeneity is a major obstacle in successfully eradicating tumors.



**Differences in clonal behavior.** (Top) A tumor that has not been exposed to therapies consists of clones that display distinct behaviors (shown by different colors). The tumor is generally dominated by clones with high proliferative output that can be detected through serial xenograft transplantations into immunodeficient mice. In the absence of therapy, the proportion of different types of clones can change randomly. (Bottom) By contrast, chemotherapy increases the proportion of clones with lower proliferative output, which in turn translates into reduced overall tumor growth even after the treatment is stopped. This change in clonal landscape likely reflects the reduced sensitivity of slower-proliferating clones to chemotherapy. The differences in proliferative output among clones are unlikely to be linked to genetic differences or position in differentiation hierarchies.

observations did not necessarily mean that all distinct clonal behavior patterns reflect meaningful biological diversity, mathematical modeling and statistical analyses suggested clonal differences in proliferative outputs. Notably, treatment of xenograft-bearing mice with oxaliplatin—a chemotherapeutic agent commonly used in colorectal cancer patients—preferentially eliminated persistent clones and increased the proportion of clones that were initially below the detection threshold (see the figure).

What mechanism could explain these differences in clonal behavior? Although it is formally possible that the different clones were genetically distinct, the stability of copy number alteration profiles and concordance for mutational hot spots renders this possibil-

ity unlikely, at least for the nuclear genome. Nor can the differences in proliferative outputs between the clones be explained on the basis of “traditional” distinctions between stem cells and non-stem cells, because tumor engraftment and maintenance over multiple passages fulfill the definition of cancer stem cells. Cell differentiation hierarchy is not the only type of nongenetic heterogeneity, as genetically identical cells can display phenotypic variability due to stochasticity in gene expression and signaling pathways—a phenomenon known as cellular heterogeneity (5). However, phenotypic differences associated with cellular heterogeneity are relatively transient, and it is not clear whether they could account for the apparently stable differences in clonal behavior.



A more likely explanation is the involvement of one or more distinct semistable epigenetic states that cannot be directly mapped to a differentiation hierarchy. In bacterial cell populations, a fraction of cells randomly assumes a distinct phenotype that is characterized by resistance to stress, including antibiotic treatment, at the expense of reduced proliferation rates (6). The reemergence of previously minor clones after oxaliplatin treatment and their ability to initiate new tumors (although at smaller size) suggest the presence of such slow-growing dormant clones. Similarly, a distinct phenotypic transition characterized by altered chromatin organization has been described recently as a mechanism of resistance to anti-epidermal growth factor receptor therapy in human lung cancer (7). Although the cells are locked in this epigenetic state for multiple population doublings, they can eventually revert back to their original drug-sensitive state.

Kreso *et al.* do not reveal mechanisms responsible for the variability in clonal behavior. Still, the study has several important implications. It highlights the need to adequately understand epigenetic mechanisms that underlie cancer cell phenotypes, including studies of cellular heterogeneity and more stable distinct epigenetic states (stochastic and deterministic heterogeneity).

That therapeutic resistance can be caused by distinct epigenetic states (7), which can be prevented by targeting epigenetic regulators, opens up new opportunities for improved cancer treatment. The conclusions of Kreso *et al.* also warrant more careful assessments of studies interpreted through the cancer stem cell paradigm. Quantitative analysis of such studies frequently reveals numerical inconsistencies that can invalidate the conclusions (8). Refraining from mapping the differences in cancer cell phenotypes into differentiation hierarchies would lead to more accurate scientific interpretation of the data, which is critical for clinical translation. For example, despite relatively limited experimental evidence, it is widely assumed that therapeutic resistance is fueled by the preferential survival of cancer stem cells, whereas the results of Kreso *et al.* suggest that a therapy-resistant state might be unrelated to “stemness” *per se*. Cancer cell phenotypes are not black and white but rather display a continuum of many different colors and shades.

Kreso *et al.* analyzed colorectal cancers that are fairly homogeneous for tumor-driving genetic alterations (i.e., mutations in the APC-Wnt- $\beta$ -catenin signaling pathway are observed in nearly all human colorectal cancer) and these tumors were further genetically “homogenized” by passing through a selec-

tion bottleneck created by xenotransplantation. However, phenotypic heterogeneity in the majority of human cancers is likely to be more complex, as it represents the integration of both genetic and nongenetic inputs. Therefore, adequate understanding and eradication of cancers requires a comprehensive picture that accounts for all major inputs that dictate tumor cell behaviors, including their response to current and future therapies. Technological advances that enable the complete molecular and functional profiling of individual cancer cells, as well as improved mathematical models built on actual clinical and experimental observations, will likely allow us to construct these pictures in the not-so-distant future.

#### References and Notes

1. L. I. Campbell, K. Polyak, *Cell Cycle* **6**, 2332 (2007).
2. M. Shackleton, E. Quintana, E. R. Fearon, S. J. Morrison, *Cell* **138**, 822 (2009).
3. A. Marusyk, V. Almendro, K. Polyak, *Nat. Rev. Cancer* **12**, 323 (2012).
4. A. Kreso *et al.*, *Science* **339**, 543 (2013); 10.1126/science.1226670.
5. S. J. Altschuler, L. F. Wu, *Cell* **141**, 559 (2010).
6. N. Q. Balaban, J. Merrin, R. Chait, L. Kowalik, S. Leibler, *Science* **305**, 1622 (2004).
7. S. V. Sharma *et al.*, *Cell* **141**, 69 (2010).
8. S. E. Kern, D. Shibata, *Cancer Res.* **67**, 8985 (2007).

**Acknowledgments:** Supported by the Breast Cancer Research Foundation.

10.1126/science.1234415

## CHEMISTRY

# Toward Molecular-Scale MRI

Philip Hemmer

**M**agnetic resonance imaging (MRI) is a mainstay of medical diagnostics, allowing nondestructive imaging inside opaque objects with high resolution. There have been many attempts to use MRI to image small objects such as living cells, because the resolution can be well below the optical diffraction limit. However, the detection sensitivity of conventional MRI falls rapidly for smaller feature sizes, making it impossible to resolve features smaller than a few micrometers with this method. Two reports in this issue, by Mamin *et al.* on page 557 (1) and Staudacher *et al.* on page 561 (2), demonstrate the ability to detect volumes of a few cubic nanometers, comparable to the size of large

protein molecules. These independent studies are a crucial step toward molecular-scale magnetic resonance imaging.

In conventional MRI and the related chemical diagnostic nuclear magnetic resonance (NMR), magnetic nuclei such as protons are excited by a radiofrequency field, plus a large magnetic field gradient in the case of MRI. The resulting magnetic signal emitted by the excited nuclei is collected by a magnetic induction coil, much like the antenna loop used in ultrahigh-frequency TV reception, and digitally processed to produce a spectrum or three-dimensional image. However, as the image voxel size is shrunk to allow imaging of ever smaller objects, the magnetic signal becomes too weak to be extracted from the background magnetic noise in the environment. To mitigate this noise, the antenna loop can be shrunk, but so far this approach has not

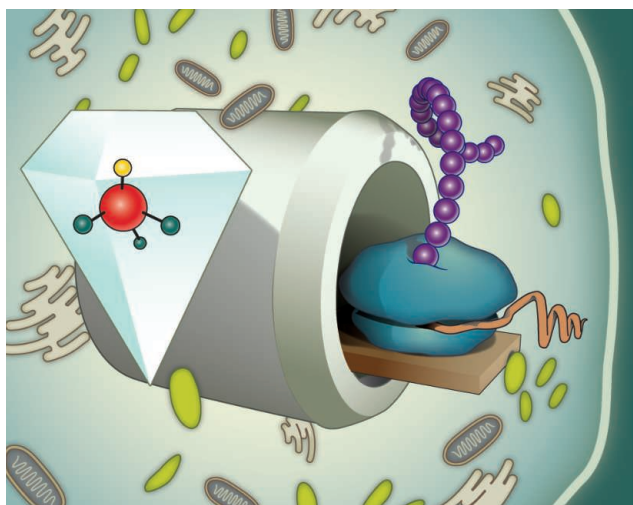
**Use of a diamond-based nanomagnetometer reduces the detection volume of MRI to the level of individual protein molecules.**

allowed MRI to achieve a resolution beyond a few micrometers.

To circumvent this problem, nonconventional detection techniques are needed. The first of these was magnetic resonance force microscopy (MRFM), developed by Rugar *et al.* nearly two decades ago (3). This approach takes advantage of the force between two magnets: the nuclear or electron spins being imaged on the one hand and a powerful nanomagnet attached to the tip of a scanning probe on the other. This approach allowed detection and imaging of single electrons (4) and imaging of ensembles of nuclei in a virus particle (5). However, it required ultralow temperatures and could therefore not be used to image dynamic samples in ambient environments, like living cells.

Another approach uses a diamond-based nanomagnetometer to sense the magnetic fields generated by small ensembles of

Texas A&M University, Electrical and Computer Engineering Department, College Station, TX 77843, USA. E-mail: prhemmer@ece.tamu.edu



**The future of live-cell imaging.** In this cartoon of a possible future application of a diamond-based nanoscale MRI-machine, a single NV inside a diamond nanocrystal is used to image a ribosome in the act of transcription inside a live cell. Mamin *et al.* and Staudacher *et al.* report a first step toward such a machine by demonstrating detection of protein-sized volumes of nuclear spins under ambient conditions.

nano-MRI, because in conventional MRI, images are acquired by recording the time evolution in the presence of applied magnetic field gradients.

The two approaches have different strengths. Mamin *et al.* manipulate the sample spins with an additional radiofrequency field; this approach allows

NVs in nanodiamonds, such processes might be observable in more interesting ambient environments like living cells (see the figure). In contrast to competing techniques like fluorescence resonance energy transfer, the NV could accomplish this task with a larger dynamic range and without the need for separate labels at each site to be monitored. Such capability would substantially enhance our understanding of structural biology and biomolecular processes, as well as numerous additional applications.

#### References

1. H. J. Mamin *et al.*, *Science* **339**, 557 (2013).
2. T. Staudacher *et al.*, *Science* **339**, 561 (2013).
3. D. Rugar *et al.*, *Science* **264**, 1560 (1994).
4. D. Rugar, R. Budakian, H. J. Mamin, B. W. Chui, *Nature* **430**, 329 (2004).
5. C. L. Degen, M. Poggio, H. J. Mamin, C. T. Rettner, D. Rugar, *Proc. Natl. Acad. Sci. U.S.A.* **106**, 1313 (2009).
6. G. Balasubramanian *et al.*, *Nature* **455**, 648 (2008).
7. J. R. Maze *et al.*, *Nature* **455**, 644 (2008).
8. B. Grotz *et al.*, *New J. Phys.* **13**, 055004 (2011).
9. P. C. Maurer *et al.*, *Science* **336**, 1283 (2012).

10.1126/science.1233222

nuclear spins. The magnetometer consists of a single nitrogen-vacancy (NV) color center in diamond; it can operate at room temperature in almost any environment (6, 7). Previously, NVs implanted just below the surface of a bulk diamond have been used to demonstrate near-single-electron spin detection and crude one-dimensional imaging for electron spins outside of the diamond crystal (8). However, imaging of nuclei will be required to observe the structure and conformations of individual molecules under ambient conditions.

By implementing different advanced noise suppression techniques, Mamin *et al.* and Staudacher *et al.* have succeeded in using near-surface NVs to detect small volumes of proton spins outside of the diamond crystal. Both authors conclude that their observed signals are consistent with a detection volume on the order of  $(5 \text{ nm})^3$  or less. This sensitivity is comparable to that of the cryogenic MRFM technique and should be adequate for detecting large individual protein molecules. Both groups also project much smaller detection volumes in the future by using NVs closer to the diamond surface. Staudacher *et al.* expect to improve sensitivity by using the NV to spin-polarize the nuclei. Mamin *et al.* project that sensitivity may eventually approach the level of single protons, provided that the NV coherence time can be kept long enough.

To confirm that the observed signals indeed arose from spins outside of the diamond, both groups cleaned the surface to verify that the magnetic proton signals disappeared. This was necessary as single nuclear spins were already detected up to a few nanometers distance inside the diamond lattice (9), but most of the envisioned applications require probing spins in the external environment.

Mamin *et al.* also observed the temporal evolution of the probed nuclear spins. This is only one small step from a fully functional

complex protocols of classic NMR to be implemented easily. In contrast, Staudacher *et al.* use passive spectroscopy, which does not require an additional radiofrequency field.

If magnetic impurities on the diamond surface can be sufficiently controlled, it should be possible to image subnanometer volumes of nuclear spins. In this case, single-molecule dynamics like protein folding or the action of catalysts in chemical reactions might be observable in real time. Furthermore, if these techniques can be extended to

#### MICROBIOLOGY

## Undernutrition—Looking Within for Answers

David A. Relman<sup>1,2</sup>

A link between the gut microbiota and conditions of undernutrition point to possible therapeutic interventions.

**U**ndernutrition—a condition resulting from inadequate intake or assimilation of nutrients—underlies more than one-third of all deaths worldwide in children younger than 5 years of age (1). Enteric infectious disease and undernutrition exacerbate and perpetuate each other by means of impaired innate and adaptive immune responses. Together they produce an insidious condition called environmental enteropathy in which damaged gut mucosal architecture and function are associated with malabsorption, dysregulation of mucosal perme-

ability, and inflammation. This vicious cycle leaves approximately one-fifth of children in the world stunted, and leads to a wide range of continuing health and developmental problems, possibly including cognitive impairment and metabolic syndrome in adulthood (2). Maternal malnutrition brings about malnutrition in their children [shockingly, nearly one-third of women in Bangladesh (3), as well as in other countries with similar levels of poverty, suffer from this condition]. These multiple, interwoven, and mutually reinforcing factors pose major challenges for efforts to address this situation. On page 548 of this issue, Smith *et al.* (4) show, with the use of an animal model, that the gut microbiota is involved in propagating a form of severe

<sup>1</sup>Departments of Medicine and of Microbiology and Immunology, Stanford University School of Medicine, Stanford, CA 94305, USA. <sup>2</sup>Veterans Affairs Palo Alto Health Care System, Palo Alto, CA 94304, USA. E-mail: relman@stanford.edu



acute undernutrition called kwashiorkor (see the figure). Like previous data linking the microbiota with obesity (5), these findings are remarkable. They also provide hope, in that by understanding the role of the gut microbiota in undernutrition, we can devise new ecologically inspired strategies for correcting this problem.

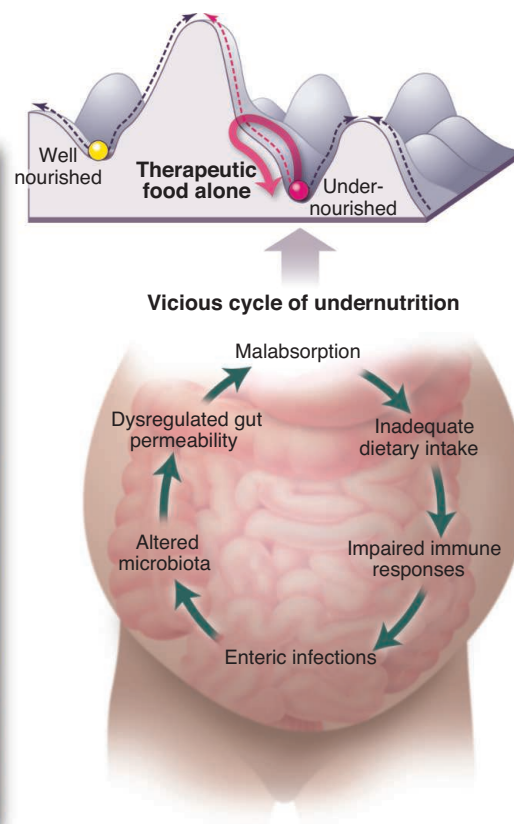
Smith *et al.* recruited 317 twin pairs in rural southern Malawi and followed them with periodic fecal sampling until they were 3 years of age. They selected 13 same-gender twin pairs that were discordant for kwashiorkor and 9 twin pairs that were well-nourished, and then characterized their fecal microbiomes. Twin pairs with kwashiorkor were treated with ready-to-use “therapeutic food” for a mean duration of 9 weeks. By relying on the same-gender mono- and dizygotic twin pairs (genetically identical twins and fraternal twins, respectively), they could isolate the impact of genetics and household environment.

A key finding of Smith *et al.* is that the overall gene content (which generally predicts functions) of the fecal microbiota in the kwashiorkor-afflicted children, in contrast to that of the well-nourished children, fails to develop with increasing age, even with the use of therapeutic food. Although there was an initial change in the gene content of the microbiota with initiation of therapeutic food, it was not sustained. The latter finding is disappointing but not surprising, given the many other determinants (besides diet) of the “fitness landscape” of the gut (that is, the likelihood of community stability under a variety of ecosystem conditions). To clarify the role of the gut microbiota in determining host nutritional state, as well as to tease apart the contributions of diet and microbiota, Smith *et al.* collected fecal microbial communities from three discordant twin pairs at the time of kwashiorkor diagnosis and transferred them into germ-free mice. The mice were fed a diet based on the typical foods of these human donors in Malawi. Two of the three groups of mice that received microbiota from a kwashiorkor-affected twin lost weight, but only if they were fed a diet based on the typical foods of these Malawian donors. Mice that received microbiota from a healthy sibling, or fed standard mouse chow, did not lose weight. A subsequent 2 weeks of treatment with therapeutic food produced weight gain in all groups of mice, and a return to the Malawian diet again led to weight loss in the recipients of the kwashiorkor microbiota. Meaningful changes in fecal taxonomic, gene, and metabolite content accompanied these transplantations and dietary shifts in the recipient mice.

Abundance of bifidobacteria and lactobacilli, as well as amounts of essential and nonessential amino acids in fecal samples, increased in mice that received kwashiorkor microbiota during administration of therapeutic food, albeit temporarily. Notably, in mice harboring a kwashiorkor microbiota that were fed a Malawian diet, analysis of urinary metabolite abundance and microbiome composition revealed inhibition of the tricarboxylic acid cycle (indicative of impaired cellular metabolism and energy production of the host). In general, the data reinforce the concept of host-microbiota cometabolism; however, additional human subjects with kwashiorkor and other forms of undernutrition should be studied to confirm these findings.

The findings of Smith *et al.* are a reminder that isolated factors, such as individual microbes or even entire microbial communities, alone cannot explain complex pheno-

types such as undernutrition, and that correction of these phenotypes will require a coordinated system-wide approach. Modification of the gut microbiota may improve the nutritional state of individuals with kwashiorkor, but accomplishing this will not be easy. Genetic determinants of the host that impact microbiota composition and function are just beginning to be identified (6, 7). For example, murine angiotensin I converting enzyme 2 (ACE2), a key regulatory enzyme of the renin-angiotensin system (which controls blood pressure and fluid balance), was unexpectedly linked with tryptophan absorption in the small intestine and activation of the signaling protein mammalian target of rapamycin (mTOR), which in turn triggered the expression of small antimicrobial peptides in the gut (8). Further, tryptophan deficiency led to diminished antimicrobial peptide expression, altered microbiota taxonomic composi-



**Nutritional state.** A child suffering from undernutrition (the condition kwashiorkor) is shown. The diagram (lower right) shows the interplay between factors that sustain a state of undernutrition. An ecological fitness landscape of the human-microbial ecosystem (upper right) illustrates how there are deep stability “domains” (or “basins of attraction”) associated with undernutrition and overnutrition; other stability domains are associated with more healthy nutritional states. Therapeutic food alone is insufficient to induce a sustained shift in the gut ecosystem state (solid red arrow) that would cause an undernourished individual to achieve a more healthy nutritional state (dashed red arrow). Correction of this self-propagating condition will require multiple, concurrent measures to remold the environmental landscape of the host gut, thereby inducing a shift toward a gut microbiome with more efficient nutrient utilization (energy harvest) and fewer intrinsic proinflammatory properties.

tion, and an enhanced propensity for inflammation in the colon. It could be that human genetic variation in ACE2 function or expression is associated with distinct physiological states of the gut epithelium as well as with distinct microbiota compositions in the gut; these variable factors may affect the absorptive function of the epithelium, with implications for the host nutritional state.

The history of environmental exposures and health status of a woman before and during pregnancy affect the intrauterine development of her child, as well as her own microbiota—which in turn is transmitted to her child at birth. In the setting of this inherited history, early postnatal exposures to enteric pathogens with subsequent inflammatory responses in the gut, altered immune system development, and damaged intestinal barrier function, as well as antibiotic use, insufficient food intake, and macro- and micronutrient deficiencies, all conspire to produce an ecological fitness landscape in the host with

strong undernutrition-associated stability domains, and high barriers preventing shifts to health-associated states. Signaling within the microbiota, and between it and the host, can perpetuate this pathologic state.

Thus, the challenge in ecological terms is to devise a strategy for altering the fitness landscape in such a manner as to favor transitions to health-associated stable states (9). Indeed, there are multiple possible points of attack. Possible therapeutic approaches include delivery of defined microbial strains—either alone or as collectives—key nutrients for host and microbiota, molecules that exploit microbiota-host signaling or trigger self-regenerative responses in the gut mucosa and epithelia, and modulators of mucosal immune function. The degree to which these approaches should be individualized for different subjects and clinical settings is not yet clear, nor are the means by which the resulting beneficial effects can be made to persist. But we are well on our

way toward the kind of detailed understanding of the human microbial ecosystem and its molecular and physiological features that will be necessary to enable the design and testing of these approaches.

#### References and Notes

1. United Nations Children's Fund, "Tracking Progress on Child and Maternal Nutrition" (UNICEF, New York, 2009).
2. R. L. Guerrant, M. D. DeBoer, S. R. Moore, R. J. Scharf, A. A. Lima, *Nat. Rev. Gastroenterol. Hepatol.* **10**, 1038/ nrgastro.2012.239 (2012).
3. T. Ahmed *et al.*, *J. Health Popul. Nutr.* **30**, 1 (2012).
4. M. I. Smith *et al.*, *Science* **339**, 548 (2013).
5. P. J. Turnbaugh *et al.*, *Nature* **444**, 1027 (2006).
6. T. Ahmed, R. Haque, A. M. Shamsir Ahmed, W. A. Petri Jr., A. Cravioto, *Nutr. Rev.* **67** (suppl. 2), S201 (2009).
7. B. W. Parks *et al.*, *Cell Metab.* **17**, 141 (2013).
8. T. Hashimoto *et al.*, *Nature* **487**, 477 (2012).
9. E. K. Costello *et al.*, *Science* **336**, 1255 (2012).

**Acknowledgments:** D.A.R. is supported by NIH Pioneer Award DP1OD000964, NIH—National Institute of General Medical Sciences 1R01GM09534-01, and by the Thomas C. and Joan M. Merigan Endowment at Stanford University. There are no conflicts of interest.

10.1126/science.1234723

## PHYSICS

# Measuring Mass in Seconds

John E. Debs, Nicholas P. Robins, John D. Close

For centuries, humans have measured time by counting oscillations of highly regular periodic motion—the Sun, a pendulum, or a quartz crystal, for example. During the past 50 years, we have chosen to use the electromagnetic oscillations, which drive absorption in an atom—a highly stable and universal frequency reference. Such atomic clocks define the SI second via an atomic resonance in cesium (1). The second is the most precisely defined physical unit. Although it may seem obvious now, making the leap from performing precise spectroscopy on the atomic structure of cesium to using its atomic structure as a precise reference to stabilize other oscillators was profound. On page 554 of this issue, Lan *et al.* (2) make an analogous distinction between performing momentum-spectroscopy on a recoiling atom, and using that spectroscopy to stabilize an oscillator, effectively locking a clock to the mass of a particle. This result has important implications for fundamental physics and precision

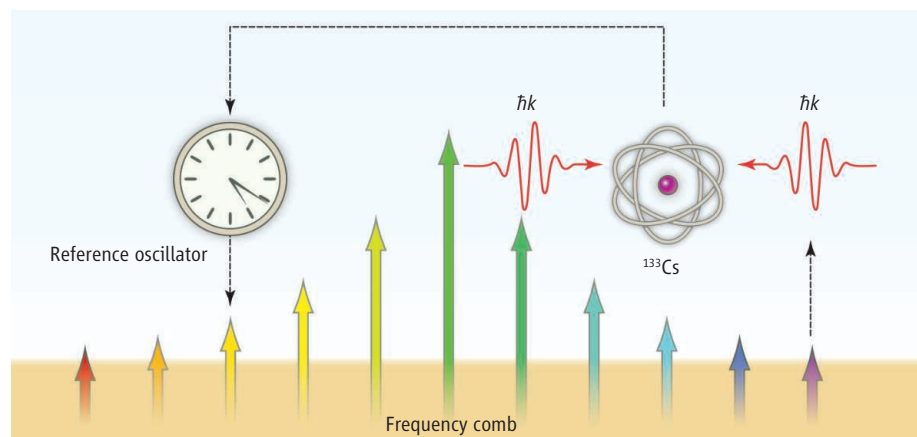
measurement, and could play a role in a new definition of the kilogram.

Einstein's theory of relativity gives us the equivalence of energy and mass, while quantum mechanics links energy and frequency. Thus, there is, at least theoretically, a direct link between a particle's rest mass and time, expressed by the Compton frequency  $\omega_c = mc^2/\hbar$ . Here,  $m$  is the rest mass of the par-

An atom interferometer and an optical frequency comb measure the Compton frequency of a cesium atom, creating a "clock" that weighs atoms.

ticle,  $c$  is the speed of light, and  $\hbar$  is Planck's constant  $h$  divided by  $2\pi$ . For an atom such as cesium,  $\omega_c$  is on the order of  $10^{25}$  Hz—an extremely high frequency to attempt to access experimentally. Strictly speaking, because a quantum state evolves at a rate directly proportional to its energy,  $\omega_c$  will contribute to its evolution.

A frequently appearing quantity in quan-



**Locking a "Compton clock."** A schematic representation of the experiment of Lan *et al.*, in which an atom interferometer measures the recoil frequency of a cesium-133 atom with lasers locked to a known frequency-comb line. This method ensures that the recoil frequency is a defined fraction of the Compton frequency of the atom. This signal stabilizes a reference oscillator, which is the reference for all frequencies in the system, including the frequency comb itself. In this way, a clock is locked to the mass of an atom.

Department of Quantum Science, Research School of Physics and Engineering, The Australian National University, Canberra, ACT 0200, Australia. E-mail: john.debs@anu.edu.au; nick.robins@anu.edu.au; john.close@anu.edu.au



tum theory is the ratio  $h/m$ , measurement of which can be thought of as a determination of  $\omega_c$  (scaled by  $c^2$ ). In recent years,  $h/m$  experiments have become an important independent measurement of the fine structure constant  $\alpha$  because  $h/m$  is the least well-known quantity in its definition:  $\alpha = (2R_\infty/c)(h/m)(m/m_e)$ , where  $m_e$  is the electron mass and  $R_\infty$  is the Rydberg constant. Independent measurements of  $\alpha$  are tests of quantum electrodynamics, and there has been substantial work on measuring  $\alpha$  with atom interferometers (3–5).

In an atom interferometer, matter waves are split and recombined by using pulses of light. Counterpropagating laser beams stimulate the absorption and emission of a photon, transferring a well-defined momentum to the atom. For two laser beams with the same frequency, the momentum transferred is  $2\hbar k$ , where  $k$  is the wave number of the light (the reciprocal of its wavelength times  $2\pi$ ) (6). Thus, the recoil energy of the atom is given by  $E = 4\hbar^2 k^2 / 2m = 4\hbar\omega_r$ , where  $\omega_r$  is the photon recoil frequency. Because the phase of the matter wave evolves according to this energy, the interferometer phase is proportional to  $\omega_r$  (5, 7, 8), and such a device can be thought of as a momentum spectrometer, provided the particle's mass is known. This simplified description of an atom-interferometric measurement of the recoil frequency is nonrelativistic. More importantly, knowledge of the laser wave number allows the value for  $h/m$  to be extracted from the measured recoil frequency.

Alternatively, in a relativistic description, the phase evolution of a matter wave is proportional to the mass-energy, and the phase shift of the interferometer is given by  $\Delta\phi = 2\omega_c T(\gamma - 1)$ . Here,  $T$  is the time it takes for the matter wave pulse to move between the beamsplitter and mirror pulses of the interferometer, and  $\gamma = (1 - v^2/c^2)^{-1/2}$  is the inverse Lorentz factor from special relativity. The recoil velocity imparted to the atoms,  $v$ , is determined by the photon wave number,  $k$ . Although atomic recoil velocities in experimentally realizable regimes are on the order of centimeters per second, well below the speed of light, the relativistic effect of time dilation can be viewed as the source of the interferometer phase shift. In the extreme relativistic limit where  $v \rightarrow c$ , the interferometer phase develops at the full Compton frequency, and the relativistic description elucidates how a measurement of  $h/m$  can be interpreted as a measurement of  $\omega_c$ . However, such a measurement still requires an independent determination of the laser wave number.

Lan *et al.* run an experiment configured similarly to an  $h/m$  measurement, the difference being that they have eliminated the laser frequency as a free variable in their system by using a frequency comb. A frequency comb is an optical “ruler” in frequency space that enables an absolute measurement of optical frequencies (9). The laser that drives the recoiling atoms is locked to a chosen comb line, and the interferometer signal becomes directly proportional to a defined fraction of the Compton frequency. A common oscillator, used to derive all frequencies for the system, is then stabilized directly to the interferometer signal (see the figure).

By defining the ratio of the laser frequency to  $\omega_r$  via the comb, all quantities in the interferometer signal are now defined except for mass. Thus, the system locks the common oscillator—a clock—to the mass of an atom. An  $h/m$  experiment measures the energy of a recoiling atom as a function of its momentum, a quantity that depends on its mass. This experiment is subtly different from that of Lan *et al.*, which uses

this measurement to stabilize an oscillator. This method is a direct analogy to stabilizing an oscillator by using the spectroscopy of cesium, in contrast to measuring the spectroscopy of cesium. By linking time to the mass of an atom, the “Compton clock” has intriguing prospects for the measurement of time and definition of the kilogram.

## References

1. T. P. Heavner, S. R. Jefferts, E. A. Donley, J. H. Shirley, T. E. Parker, *Metrologia* **42**, 411 (2005).
2. S.-Y. Lan *et al.*, *Science* **339**, 554 (2013); 10.1126/science.1230767.
3. D. S. Weiss, B. C. Young, S. Chu, *Appl. Phys. B* **59**, 217 (1994).
4. H. Müller, S. W. Chiow, Q. Long, C. Vo, S. Chu, *Appl. Phys. B* **84**, 633 (2006).
5. R. Bouchendira, P. Cladé, S. Guellati-Khélifa, F. Nez, F. Biraben, *Phys. Rev. Lett.* **106**, 080801 (2011).
6. M. A. Kasevich, S. Chu, *Phys. Rev. Lett.* **67**, 181 (1991).
7. Ch. J. Bordé, *Phys. Lett. A* **140**, 10 (1989).
8. H. Müller, S. W. Chiow, Q. Long, S. Herrmann, S. Chu, *Phys. Rev. Lett.* **100**, 180405 (2008).
9. J. L. Hall, T. W. Hänsch, *Femtosecond Optical Frequency Comb Technology: Principle, Operation and Application* (Springer Science Business Media, Dordrecht, Netherlands, 2005).

10.1126/science.1232923

## GEOCHEMISTRY

# Carbon Cycle Makeover

Donald E. Canfield<sup>1</sup> and Lee R. Kump<sup>2</sup>

Enhanced levels of anaerobic respiration processes may explain oscillations in Earth's carbon cycle.

In 1845, the French chemist and mining engineer Jacques-Joseph Ebelman figured out why Earth's atmosphere contains oxygen (1). Oxygen is produced by plants during photosynthesis, but almost all of this oxygen is used again in respiration. Ebelman reasoned that small amounts of organic matter remaining in sediments after respiration leave a residual of oxygen in the atmosphere. The source of oxygen to the atmosphere represented by organic matter burial is balanced by oxygen sinks associated with rock weathering and chemical reaction with volcanic gases. This is the long-term carbon and oxygen geochemical cycle. But Earth is an old planet, and oxygen levels have changed through time (2). On page 540 of this issue, Schrag *et al.* (3) challenge the most commonly used geochemical approach to assess long-term changes in the coupled oxygen and carbon cycles.

High on the list of factors controlling oxygen levels is the burial rate of organic carbon into sediments through time. Decades ago, geochemists began to measure the carbon isotope distributions in plant organic matter and in carbonate minerals in modern and ancient marine sediments (4). They found that the carbon isotope ratios differed between organic and inorganic carbon. To a first approximation, these differences could be explained by a preferential incorporation of  $^{12}\text{C}$  atoms over  $^{13}\text{C}$  atoms into organic matter during photosynthesis. Patterns in the isotopic compositions of both inorganic and organic carbon species through geologic time provide clues to the burial history of organic carbon.

These patterns are normally interpreted through a very simple mass balance (see the figure, panel A). Rock-weathering-derived carbon enters the ocean from rivers in inorganic form, with a  $\delta^{13}\text{C}$  usually taken as the average for Earth crust. Carbon exits into sediments in inorganic form as carbonate minerals and also as organic carbon. The

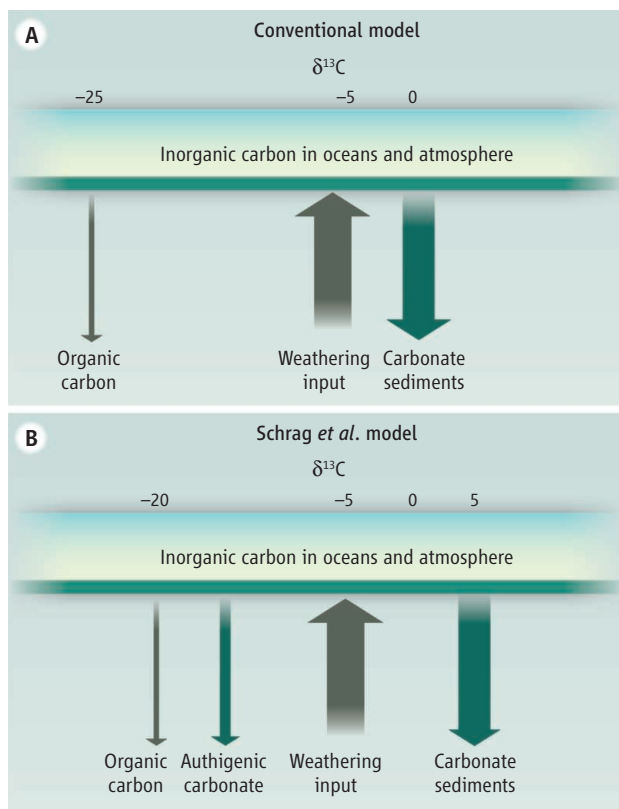
<sup>1</sup>Nordic Center for Earth Evolution, University of Southern Denmark, Odense, 5230 Denmark. <sup>2</sup>Department of Geosciences, Penn State University, University Park, PA 16802, USA. E-mail: dec@biology.sdu.dk, lrk4@psu.edu

organic carbon has a lower  $\delta^{13}\text{C}$  than the inorganic carbon by an amount depending on the fractionation of isotopes during photosynthesis. However, the combined isotopic composition of the inorganic and organic carbon leaving the oceans must equal the isotopic composition of the inorganic carbon entering it. Thus, if a large amount of organic carbon is buried, removing a lot of carbon with low  $\delta^{13}\text{C}$ , the  $\delta^{13}\text{C}$  of the inorganic carbon removed must be high. In contrast, if little organic carbon is buried, the  $\delta^{13}\text{C}$  in the inorganic carbon should approach that of the carbon entering the oceans. Using this approach, rates of organic carbon burial, and thus oxygen liberation to the atmosphere, have been inferred through geologic time.

As Schrag *et al.* highlight, however, the carbon isotope record is not always so easy to explain. This is particularly true in Precambrian rocks that show large and long-term enrichments in the  $\delta^{13}\text{C}$  of carbonate minerals. With the traditional model, these events require massive amounts of organic carbon burial, liberating huge amounts of oxygen to the atmosphere. But what triggered these extreme carbon cycling events, how were they sustained, and where is the independent geochemical evidence that they occurred?

Equally troubling are very strong depletions in the  $\delta^{13}\text{C}$  of carbonate minerals (5, 6). These depletions can extend to values less than the weathering input and are thus impossible to explain within the traditional carbon mass-balance model. Explanations for these isotope deviations have therefore focused on short-term events, such as the massive oxidation of  $^{13}\text{C}$ -depleted dissolved organic matter or methane, or the preferential weathering of  $^{13}\text{C}$ -depleted organic material from land. In another set of explanations, the carbon isotopes could have been affected by late-stage processes within Earth with no relation to ocean chemistry. None of these explanations have gained universal acceptance (6).

Schrag *et al.* provide a clever explanation for both the positive and the negative carbon isotope excursions. They argue that on an Earth with much less oxygen than today—as was likely during the Precambrian—the decomposition of organic matter in sediments by anaerobic respiration processes like sulfate and iron reduction would boost



**Carbon burial reconsidered.** In the traditional model (A), carbon loss through organic carbon and carbonate burial balances carbon input from continental weathering. Arrow sizes approximate the relative sizes of the input and output fluxes. The more carbon is lost through organic matter burial, the greater the  $\delta^{13}\text{C}$  of the carbonate output. Schrag *et al.* now propose a third output flux through authigenic carbonate formation (B). This removal pathway is  $\delta^{13}\text{C}$ -depleted compared to the weathering input, and changes in its flux can change the  $\delta^{13}\text{C}$  of carbonate sediments with no change in the organic carbon burial flux.

carbonate alkalinity to the point where carbonate minerals (known as authigenic carbonates) would readily form. Because this alkalinity was generated from oxidation of  $^{13}\text{C}$ -depleted organic matter or methane, the carbonate formed would also be  $^{13}\text{C}$ -depleted and very different in isotopic composition than carbonates formed in surface seawater, from which the carbon isotope record is mostly constructed.

In this scenario, large increases in the  $\delta^{13}\text{C}$  of inorganic carbon, as revealed from surface seawater carbonates, resulted not from high organic carbon burial rates but rather from enhanced burial of  $^{13}\text{C}$ -depleted authigenic carbonates (see the figure, panel B). Likewise, highly  $^{13}\text{C}$ -depleted inorganic carbon values were either caused by a reduced deposition rate of authigenic carbonates or are a direct record of the  $^{13}\text{C}$ -depleted authigenic carbonates themselves.

With this view of the carbon cycle, the carbon isotope record loses its link to organic carbon burial and oxygen liberation

to the atmosphere. The implications are huge.

There are, however, some important issues to consider. First, sulfate reduction and iron reduction dominate organic carbon mineralization in modern sediments where organic carbon burial is rapid (7). These sediments generate considerable carbonate alkalinity (8), but only small amounts of authigenic carbonate are formed on a global scale (3). It is not clear how these processes would have produced much more authigenic carbonate in the past, particularly because modern systems exposed to little oxygen produce only small amounts of authigenic carbonate minerals (8).

Second, if the model proposed by Schrag *et al.* is correct, authigenic carbonate production during the large positive  $\delta^{13}\text{C}$  excursions should be widely preserved in organic-rich sediments. We should actively search for these. The large negative  $\delta^{13}\text{C}$  excursions, if they record authigenic carbonates, require that enormous amounts of organic matter have been converted to inorganic carbon. However, many rocks housing these excursions contain very little organic matter (9), not obviously consistent with the large amounts of organic matter diagenesis required by Schrag *et al.*'s model.

Finally, the large negative  $\delta^{13}\text{C}$  excursions of the late Precambrian provide well-defined and globally coherent isotope events (6), yet sediment diagenetic reactions are highly variable in space and time. It remains to be shown how a globally coherent pattern can result from these processes. Nonetheless, new ideas take time to mature, and Schrag *et al.* have brought a fresh new approach to solving some puzzling problems with our understanding of the carbon cycle.

## References

1. J. J. Ebelman, *Ann. des Mines* **7**, 3 (1845).
2. L. R. Kump, *Nature* **451**, 277 (2008).
3. D. P. Schrag *et al.*, *Science* **339**, 540 (2013).
4. H. Craig, *Geochim. Cosmochim. Acta* **3**, 53 (1953).
5. L. R. Kump *et al.*, *Science* **334**, 1694 (2011).
6. J. P. Grotzinger, D. A. Fike, W. W. Fischer, *Nat. Geosci.* **4**, 285 (2011).
7. D. E. Canfield, E. Kristensen, B. Thamdrup, *Aquatic Geomicrobiology* (Academic Press, New York, 2005).
8. C. E. Reimers, K. C. Ruttenger, D. E. Canfield, M. B. Christiansen, J. B. Martin, *Geochim. Cosmochim. Acta* **60**, 4037 (1996).
9. D. T. Johnston, F. A. Macdonald, B. C. Gill, P. F. Hoffman, D. P. Schrag, *Nature* **483**, 320 (2012).

10.1126/science.1231981



# Carbon Nanotubes: Present and Future Commercial Applications

Michael F. L. De Volder,<sup>1,2,3\*</sup> Sameh H. Tawfik,<sup>4,5</sup> Ray H. Baughman,<sup>6</sup> A. John Hart<sup>4,5\*</sup>

Worldwide commercial interest in carbon nanotubes (CNTs) is reflected in a production capacity that presently exceeds several thousand tons per year. Currently, bulk CNT powders are incorporated in diverse commercial products ranging from rechargeable batteries, automotive parts, and sporting goods to boat hulls and water filters. Advances in CNT synthesis, purification, and chemical modification are enabling integration of CNTs in thin-film electronics and large-area coatings. Although not yet providing compelling mechanical strength or electrical or thermal conductivities for many applications, CNT yarns and sheets already have promising performance for applications including supercapacitors, actuators, and lightweight electromagnetic shields.

Carbon nanotubes (CNTs) are seamless cylinders of one or more layers of graphene (denoted single-wall, SWNT, or multiwall, MWNT), with open or closed ends (*1, 2*). Perfect CNTs have all carbons bonded in a hexagonal lattice except at their ends, whereas defects in mass-produced CNTs introduce pentagons, heptagons, and other imperfections in the sidewalls that generally degrade desired properties. Diameters of SWNTs and MWNTs are typically 0.8 to 2 nm and 5 to 20 nm, respectively, although MWNT diameters can exceed 100 nm. CNT lengths range from less than 100 nm to several centimeters, thereby bridging molecular and macroscopic scales.

When considering the cross-sectional area of the CNT walls only, an elastic modulus approaching 1 TPa and a tensile strength of 100 GPa has been measured for individual MWNTs (*3*). This strength is over 10-fold higher than any industrial fiber. MWNTs are typically metallic and can carry currents of up to  $10^9$  A cm<sup>-2</sup> (*4*). Individual CNT walls can be metallic or semiconducting depending on the orientation of the graphene lattice with respect to the tube axis, which is called the chirality. Individual SWNTs can have a thermal conductivity of 3500 W m<sup>-1</sup> K<sup>-1</sup> at room temperature, based on the wall area (*5*); this exceeds the thermal conductivity of diamond.

The beginning of widespread CNT research in the early 1990s was preceded in the 1980s by the first industrial synthesis of what are now known as MWNTs and documented observations of hollow carbon nanofibers as early as the 1950s. However, CNT-related commercial activity has grown most substantially during the past decade. Since 2006, worldwide CNT production capacity has increased at least 10-fold, and the annual number of CNT-related journal publications and issued patents continues to grow (Fig. 1).

<sup>1</sup>imec, 3001 Heverlee, Belgium. <sup>2</sup>Department of Mechanical Engineering, KULeuven, 3000 Leuven, Belgium. <sup>3</sup>School of Engineering and Applied Sciences, Harvard University, Cambridge, MA 02138, USA. <sup>4</sup>Department of Mechanical Engineering, University of Michigan, Ann Arbor, MI 48109, USA. <sup>5</sup>Department of Mechanical Engineering, Massachusetts Institute of Technology, Cambridge, MA 02139, USA. <sup>6</sup>The Alan G. MacDiarmid NanoTech Institute and Department of Chemistry, University of Texas at Dallas, Richardson, TX 75083, USA.

\*To whom correspondence should be addressed. E-mail: michael.devolder@imec.be (M.F.L.D.V.); ajohnh@umich.edu (A.J.H.)

Most CNT production today is used in bulk composite materials and thin films, which rely on unorganized CNT architectures having limited properties. Organized CNT architectures (fig. S1) such as vertically aligned forests, yarns, and sheets show promise to scale up the properties of individual CNTs and realize new functionalities, including shape recovery (*6*), dry adhesion (*7*), high damping (*8, 9*), terahertz polarization (*10*), large-stroke actuation (*11, 12*), near-ideal black-body absorption (*13*), and thermoacoustic sound emission (*14*).

However, presently realized mechanical, thermal, and electrical properties of CNT macrostructures such as yarns and sheets remain significantly lower than those of individual CNTs.

Meanwhile, buoyed by large-volume bulk production, CNT powders have already been incorporated in many commercial applications and are now entering the growth phase of their product life cycle. In view of these trends, this review focuses on the most promising present and future commercial applications of CNTs, along with related challenges that will drive continued research and development. Lists of known industrial activity and commercial products are given in tables S1 through S3.

## CNT Synthesis and Processing

Chemical vapor deposition (CVD) is the dominant mode of high-volume CNT production and typically uses fluidized bed reactors that enable uniform gas diffusion and heat transfer to metal catalyst nanoparticles (*15*). Scale-up, use of low-cost feedstocks, yield increases, and reduction of energy consumption and waste production (*16*) have substantially decreased MWNT prices. However, large-scale CVD methods yield contaminants that can influence CNT properties and often require costly thermal annealing and/or chemical treatment for their removal. These steps can introduce defects in CNT sidewalls and shorten CNT length. Currently, bulk purified MWNTs are sold for less than \$100 per kg, which is 1- to 10-fold greater than commercially available carbon fiber.

The understanding of CVD process conditions has enabled preferential synthesis of metallic (*17*) or semiconducting SWNTs (*18*) with selectivity of 90 to 95%, doping of CNTs with boron or nitrogen

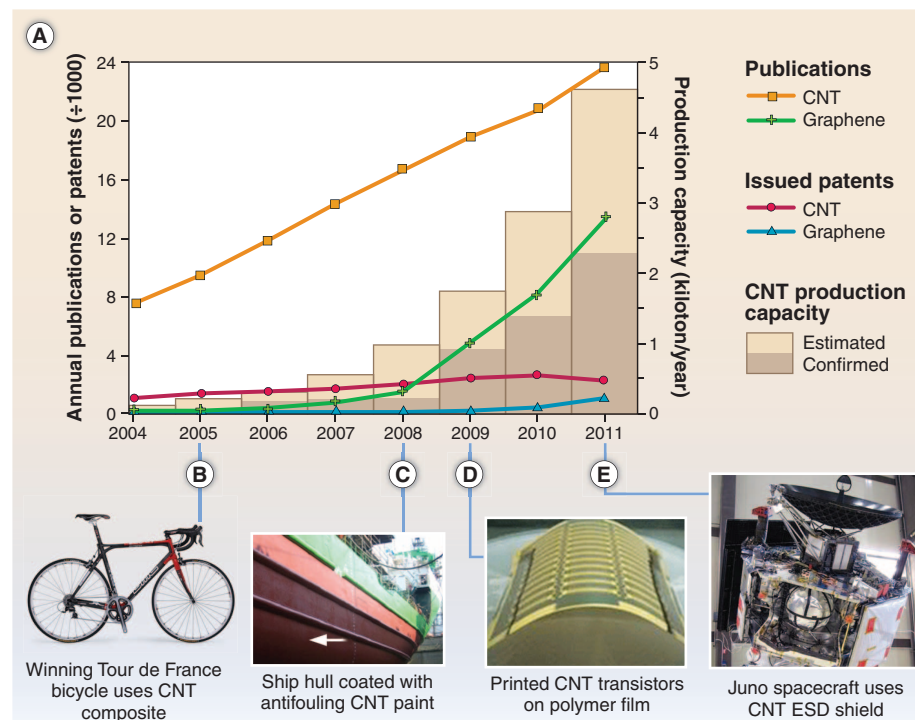


**Fig. 1.** Trends in CNT research and commercialization. (A) Journal publications and issued worldwide patents per year, along with estimated annual production capacity (see supplementary materials). (B to E) Selected CNT-related products: composite bicycle frame [Photo courtesy of BMC Switzerland AG], antifouling coatings [Courtesy of NanoCyl], printed electronics [Photo courtesy of NEC Corporation; unauthorized use not permitted]; and electrostatic discharge shielding [Photo courtesy of NanoComp Technologies, Incorporated].

(19, 20), and flow-directed growth of isolated SWNTs up to 18.5 cm long (21). However, improved knowledge is urgently needed of how CNT chirality, diameter, length, and purity relate to catalyst composition and process conditions. In situ observation of CNT nucleation (22) and molecular modeling of the CNT-catalyst interface (23) will be critical to advances in chirality-selective synthesis.

Alternatively, high-purity SWNT powders can be separated according to chirality by density-gradient centrifugation in combination with selective surfactant wrapping (24) or by gel chromatography (25). Although many CNT powders and suspensions are available commercially, the production of stable CNT suspensions requires chemical modification of the CNT surface or addition of surfactants. Washing or thermal treatment is typically needed to remove surfactants after deposition of the solution, such as by spin-coating or printing.

Moreover, because SWNT synthesis by CVD requires much tighter process control than MWNT synthesis and because of legacy costs of research and process development, bulk SWNT prices are still orders of magnitude higher than for MWNTs. Use of MWNTs is therefore favored for applications where CNT diameter or bandgap is not critical, but most emerging applications that require chirality-specific SWNTs need further price reduction for commercial viability.

Alternatively, synthesis of long, aligned CNTs that can be processed without the need for dispersion in a liquid offers promise for cost-effective realization of compelling bulk properties. These methods include self-aligned growth of horizontal (26) and vertical (27) CNTs on substrates coated with catalyst particles and production of CNT sheets and yarns directly from floating-catalyst CVD systems (28). CNT forests can be manipulated into dense solids (29), aligned thin films (30), and intricate three-dimensional (3D) microarchitectures (31) and can be directly spun or drawn into long yarns and sheets (32, 33).

### Composite Materials

MWNTs were first used as electrically conductive fillers in plastics, taking advantage of their high aspect ratio to form a percolation network at concentrations as low as 0.01 weight percent (wt %). Disordered MWNT-polymer composites reach conductivities as high as  $10,000 \text{ S m}^{-1}$  at 10 wt % loading (34). In the automotive industry, conductive CNT plastics have enabled electrostatic-assisted painting of mirror housings, as well as fuel lines and filters that dissipate electrostatic charge. Other products include electromagnetic interference (EMI)-shielding packages and wafer carriers for the microelectronics industry.

For load-bearing applications, CNT powders mixed with polymers or precursor resins can increase stiffness, strength, and toughness (35). Adding ~1 wt % MWNT to epoxy resin enhances stiffness and fracture toughness by 6 and 23%, respectively, without compromising other mechanical properties (36). These enhancements depend on CNT diameter, aspect ratio, alignment, dispersion, and interfacial interaction with the matrix.

Many CNT manufacturers sell premixed resins and master batches with CNT loadings from 0.1 to 20 wt %. Additionally, engineering nanoscale stick-slip among CNTs and CNT-polymer contacts can increase material damping (37), which is used to enhance sporting goods, including tennis racquets, baseball bats, and bicycle frames (Fig. 1C).

CNT resins are also used to enhance fiber composites (35, 38). Recent examples include strong, lightweight wind turbine blades and hulls for maritime security boats that are made by using carbon fiber composite with CNT-enhanced resin (Fig. 2A) and composite wind turbine blades. CNTs can also be deployed as additives in the organic precursors used to form carbon fibers. The CNTs influence the arrangement of carbon in the pyrolyzed fiber, enabling fabrication of 1- $\mu\text{m}$  diameter carbon fibers with over 35% increase in strength (4.5 GPa) and stiffness (463 GPa) compared with control samples without CNTs (39).

Toward the challenge of organizing CNTs at larger scales, hierarchical fiber composites have been created by growing aligned CNTs forests onto glass, SiC, alumina, and carbon fibers (35, 40, 41), creating so-called “fuzzy” fibers. Fuzzy CNT-SiC fabric impregnated with epoxy showed crack-opening (mode I) and in-plane shear interlaminar (mode II) toughnesses that are enhanced by 348 and 54%, respectively, compared with control specimens (40), and CNT-alumina fabric showed 69% improved mode II toughness (41). Multifunctional applications under investigation include lightning-strike protection, deicing, and structural health monitoring for aircraft (35, 40).

In the long run, CNT yarns and laminated sheets made by direct CVD or forest spinning or drawing methods may compete with carbon fiber for high-end uses, especially in weight-sensitive applications requiring combined electrical and mechanical functionality (Figs. 1E and 2B). In scientific reports, yarns made from high-quality few-walled CNTs have reached a stiffness of 357 GPa and a strength of 8.8 GPa but only for a gauge length that is comparable to the millimeter-long CNTs within the yarn (28). Centimeter-scale gauge lengths showed 2-GPa strength, corresponding to a gravimetric strength equaling that of commercially available Kevlar (DuPont).

Because the probability of a critical flaw increases with volume, macroscale CNT yarns may never achieve the strength of the constituent CNTs. However, the high surface area of CNTs may provide interfacial coupling that mitigates these deficiencies, and, unlike carbon fibers, CNT yarns can be knotted without degrading their strength (32). Further, coating forest-drawn CNT sheets with functional powder before inserting twist has provided weavable, braidable, and sewable yarns containing up to 95 wt % powder, which have been demonstrated as superconducting wires, battery and fuel cell electrodes, and self-cleaning textiles (42).

High-performance fibers of aligned SWNTs can be made by coagulation-based spinning of CNT suspensions (43). This is attractive for scale-up if the cost of high-quality SWNTs decreases substantially or if spinning can be extended to low-cost MWNTs. Thousands of spinnerets could operate in parallel, and CNT orientation can be achieved via liquid crystal formation, like for the spinning of Kevlar.

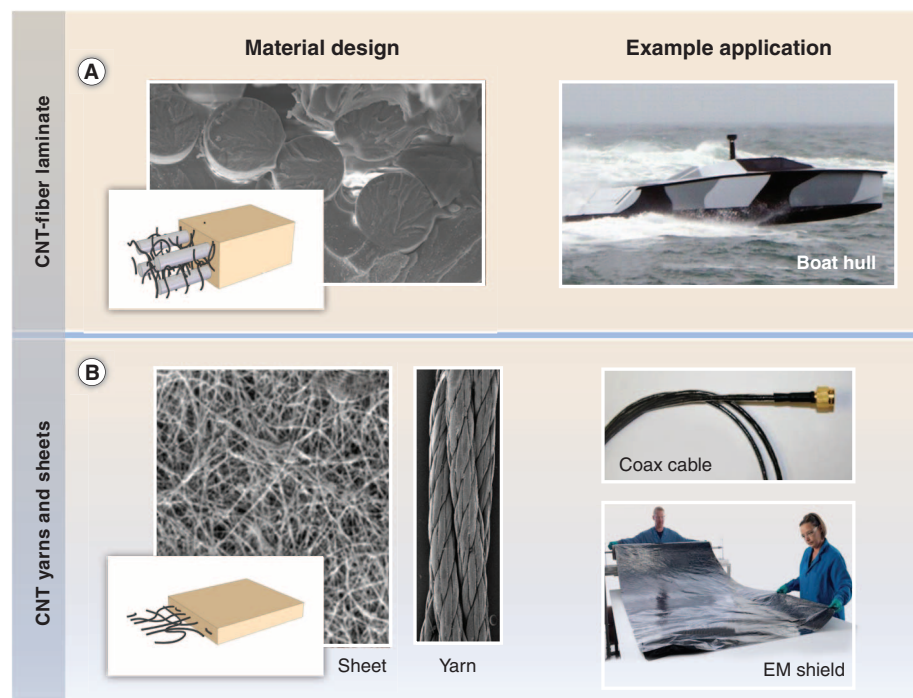


**Fig. 2.** Emerging CNT composites and macrostructures. (A) Micrograph showing the cross section of a carbon fiber laminate with CNTs dispersed in the epoxy resin and a lightweight CNT-fiber composite boat hull for maritime security boats. [Images courtesy of Zyvex Technologies] (B) CNT sheets and yarns used as lightweight data cables and electromagnetic (EM) shielding material. [Images courtesy of Nanocomp Technologies, Incorporated]



Besides polymer composites, the addition of small amounts of CNTs to metals has provided increased tensile strength and modulus (44) that may find applications in aerospace and automotive structures. Commercial Al-MWNT composites have strengths comparable to stainless steel (0.7 to 1 GPa) at one-third the density ( $2.6 \text{ g cm}^{-3}$ ). This strength is also comparable to Al-Li alloys, yet the Al-MWNT composites are reportedly less expensive.

Last, MWNTs can also be used as a flame-retardant additive to plastics; this effect is mainly attributed to changes in rheology by nanotube loading (45). These nanotube additives are commercially attractive as a replacement for halogenated flame retardants, which have restricted use because of environmental regulations.

### Coatings and Films

Leveraging CNT dispersion, functionalization, and large-area deposition techniques, CNTs are emerging as a multifunctional coating material. For example, MWNT-containing paints reduce biofouling of ship hulls (Fig. 1C) by discouraging attachment of algae and barnacles (46). They are a possible alternative to environmentally hazardous biocide-containing paints. Incorporation of CNTs in anticorrosion coatings for metals can enhance coating stiffness and strength

while providing an electric pathway for cathodic protection.

Widespread development continues on CNT-based transparent conducting films (47) as an alternative to indium tin oxide (ITO). A concern is that ITO is becoming more expensive because of the scarcity of indium, compounded by growing demand for displays, touch-screen devices, and photovoltaics. Besides cost, the flexibility of CNT transparent conductors is a major advantage over brittle ITO coatings for flexible displays. Further, transparent CNT conductors can be deposited from solution (e.g., slot-die coating, ultrasonic spraying) and patterned by cost-effective nonlithographic methods (e.g., screen printing, microplotting). Recent commercial development effort has resulted in SWNT films with 90% transparency and a sheet resistivity of 100 ohm per square. This surface resistivity is adequate for some applications but still substantially higher than for equally transparent, optimally doped ITO coatings (48). Related applications that have less stringent requirements include CNT thin-film heaters, such as for defrosting windows or sidewalks. All of the above coatings are being pursued industrially (see table S3).

### Microelectronics

High-quality SWNTs are attractive for transistors because of their low electron scattering and their

bandgap, which depends on diameter and chiral angle. Further, SWNTs are compatible with field-effect transistor (FET) architectures and high-k dielectrics (26, 49). After the first CNT transistor in 1998 (50), milestones include the first SWNT-tunneling FET with a subthreshold swing of  $<60 \text{ mV decade}^{-1}$  in 2004 (49, 51) and CNT-based radios in 2007 (52). In 2012, SWNT FETs with sub-10-nm channel lengths showed a normalized current density ( $2.41 \text{ mA } \mu\text{m}^{-1}$  at 0.5 V), which is greater than those obtained for silicon devices (53).

Despite the promising performance of individual SWNT devices, control of CNT diameter, chirality, density, and placement remains insufficient for microelectronics production, especially over large areas. Therefore, devices such as transistors comprising patterned films of tens to thousands of SWNTs are more immediately practical. The use of CNT arrays increases output current and compensates for defects and chirality differences, improving device uniformity and reproducibility (26). For example, transistors using horizontally aligned CNT arrays achieved mobilities of  $80 \text{ cm}^2 \text{ V}^{-1} \text{ s}^{-1}$ , subthreshold slopes of  $140 \text{ mV decade}^{-1}$ , and on/off ratios as high as  $10^5$  (54). These developments are supported by recent methods for precise high-density CNT film deposition methods, enabling conventional semiconductor fabrication of more than 10,000 CNT devices in a single chip (55).

CNT thin-film transistors (TFTs) are particularly attractive for driving organic light-emitting diode (OLED) displays, because they have shown higher mobility than amorphous silicon ( $\sim 1 \text{ cm}^2 \text{ V}^{-1} \text{ s}^{-1}$ ) (56) and can be deposited by low-temperature, nonvacuum methods. Recently, flexible CNT TFTs with a mobility of  $35 \text{ cm}^2 \text{ V}^{-1} \text{ s}^{-1}$  and an on/off ratio of  $6 \times 10^6$  were demonstrated (Fig. 3A) (56). A vertical CNT FET showed sufficient current output to drive OLEDs at low voltage (57), enabling red-green-blue emission by the OLED through a transparent CNT network. Promising commercial development of CNT electronics includes low-cost printing of TFTs (58), as well as radio-frequency identification tags (59). Improved understanding of CNT surface chemistry is essential for commercialization of CNT thin-film electronics; recent developments enable, for example, selective retention of semiconducting SWNTs during spin-coating (60) and reduction of sensitivity to adsorbates (61).

The International Technology Roadmap for Semiconductors suggests that CNTs could replace Cu in microelectronic interconnects, owing to their low scattering, high current-carrying capacity, and resistance to electromigration. For this, vias comprising tightly packed ( $>10^{13}$  per  $\text{cm}^2$ ) metallic CNTs with low defect density and low contact resistance are needed. Recently, complementary metal oxide semiconductor (CMOS)-compatible 150-nm-diameter interconnects (Fig. 3C) with a single CNT-contact hole resistance of 2.8 kohm were demonstrated on full 200-mm-diameter wafers (62). Also, as a replacement for solder bumps, CNTs can function both as electrical leads and heat dissipaters for use in high-power amplifiers (Fig. 3D).

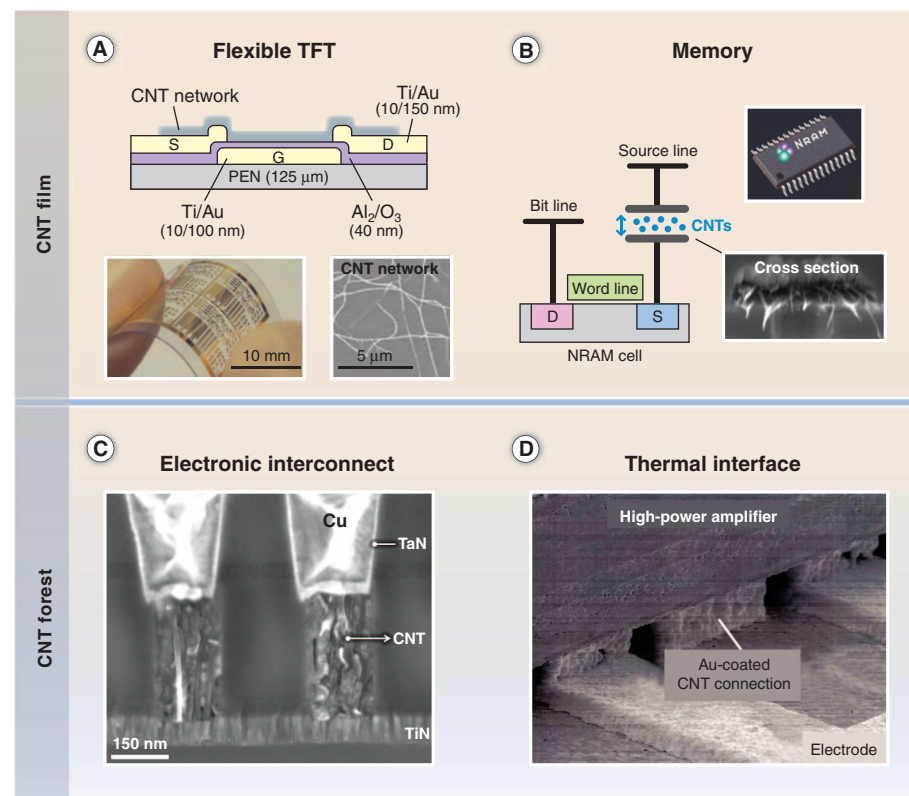


**Fig. 3.** Selected CNT applications in microelectronics. (A) Flexible TFTs using CNT networks deposited by aerosol CVD. [Schematic and photograph reprinted by permission from Macmillan Publishers Limited; scanning electron microscopy image courtesy of Y. Ohno] (B) CNT-based nonvolatile random access memory (NRAM) cell fabricated by using spin-coating and patterning of a CMOS-compatible CNT solution. [Images courtesy of Nantero, Incorporated] (C) CMOS-compatible 150-nm vertical interconnects developed by imec and Tokyo Electron Limited. [Image courtesy of imec] (D) CNT bumps used for enhanced thermal dissipation in high power amplifiers. [Image courtesy of Fujitsu Limited]

Last, a concept for a nonvolatile memory based on individual CNT crossbar electromechanical switches (63) has been adapted for commercialization (Fig. 3B) by patterning tangled CNT thin films as the functional elements. This required development of ultrapure CNT suspensions that can be spin-coated and processed in industrial clean room environments and are therefore compatible with CMOS processing standards.

### Energy Storage and Environment

MWNTs are widely used in lithium ion batteries for notebook computers and mobile phones, marking a major commercial success (64, 65). In these batteries, small amounts of MWNT powder are blended with active materials and a polymer binder, such as 1 wt % CNT loading in LiCoO<sub>2</sub> cathodes and graphite anodes. CNTs provide increased electrical connectivity and mechanical integrity, which enhances rate capability and cycle life (64, 66, 67).

Many publications report gravimetric energy storage and power densities for unpackaged batteries and supercapacitors, where normalization is with respect to the weight of active electrode materials. The frequent use of low areal densities for active materials makes it difficult to assess how such gravimetric performance metrics relate to those for packaged cells (68, 69), where high areal energy storage and power densities are needed for realizing high performance based on total cell weight or volume. In one of the few recent studies for packaged cells, remarkable performance has been obtained for supercapacitors deploying forest-grown SWNTs (62) that are binder and additive free; an energy density of 16 Wh kg<sup>-1</sup> and a power density of 10 kW kg<sup>-1</sup> was obtained for a 40-F supercapacitor with a maximum voltage of 3.5 V. On the basis of accelerated tests at up to 105°C, a 16-year lifetime was forecast. Despite these impressive metrics, the present cost of SWNTs is a major roadblock to commercialization.

For fuel cells, the use of CNTs as a catalyst support can potentially reduce Pt usage by 60% compared with carbon black (70), and doped CNTs may enable fuel cells that do not require Pt (19, 71). For organic solar cells, ongoing efforts are leveraging the properties of CNTs to reduce undesired carrier recombination and enhance resistance to photooxidation (20). In the long run, photovoltaic technologies may incorporate CNT-Si heterojunctions and leverage efficient multiple-exciton generation at p-n junctions formed within individual CNTs (72). In the nearer term, commercial photovoltaics may incorporate transparent SWNT electrodes (Fig. 4C).

An upcoming application domain of CNTs is water purification. Here, tangled CNT sheets can provide mechanically and electrochemically robust networks with controlled nanoscale porosity. These have been used to electrochemically oxidize organic contaminants (73), bacteria, and viruses (74). Portable filters containing CNT meshes have been commercialized for purification of contaminated drinking water (Fig. 4D). Moreover, membranes using aligned encapsulated CNTs with open ends permit flow through the interior of the CNTs, enabling unprece-

ded low flow resistance for both gases and liquids (75). This enhanced permeability may enable lower energy cost for water desalination by reverse osmosis in comparison to commercial polycarbonate membranes. However, very-small-diameter SWNTs are needed to reject salt at seawater concentrations (76).

### Biotechnology

Ongoing interest in CNTs as components of biosensors and medical devices is motivated by the dimensional and chemical compatibility of CNTs with biomolecules, such as DNA and proteins. At the same time, CNTs enable fluorescent (77) and photoacoustic imaging (78), as well as localized heating using near-infrared radiation (79).

SWNT biosensors can exhibit large changes in electrical impedance (80) and optical properties (81) in response to the surrounding environment, which is typically modulated by adsorption of a target on the CNT surface. Low detection limits and high selectivity require engineering the CNT surface (e.g., functional groups and coatings) (80) and appropriate sensor design (e.g., field effects, capacitance, Raman spectral shifts, and photoluminescence) (82, 83). Products under development include ink-jet-printed test strips for estrogen and progesterone detection, microarrays for DNA and protein detection, and sensors for NO<sub>2</sub> and cardiac troponin (84). Similar CNT sensors have been used for gas and toxin detection in the food industry, military, and environmental applications (82, 85).

For in vivo applications, CNTs can be internalized by cells, first by binding of their tips to receptors on the cell membrane (86). This enables transfection of molecular cargo attached to the CNT walls or encapsulated inside the CNTs (87). For example, the cancer drug doxorubicin was loaded at up to 60 wt % on CNTs compared with 8 to 10 wt % on liposomes (88). Cargo release can be triggered by using near-infrared radiation. However, for use of free-floating CNTs it will be critical to control the retention of CNTs within the body and prevent undesirable accumulation, which may result from changing CNT surface chemistry (89).

Potential CNT toxicity remains a concern, although it is emerging that CNT geometry and surface chemistry strongly influence biocompatibility, and therefore CNT biocompatibility may be engineerable (89). Early on, it was reported that injection of large quantities of MWNTs into the lungs of mice could cause asbestos-like pathogenicity (90). However, a later study reported that lung inflammation caused by injection of well-dispersed SWNTs was insignificant both compared with asbestos and with particulate matter in air collected in Washington, DC (91). Future medical acceptance of CNTs requires deeper understanding of immune response, along with definition of exposure standards for different use cases including inhalation, injection, ingestion, and skin contact. Toward use in implants, CNT forests immobilized in a polymer were studied by implantation into rats and did not show elevated inflammatory

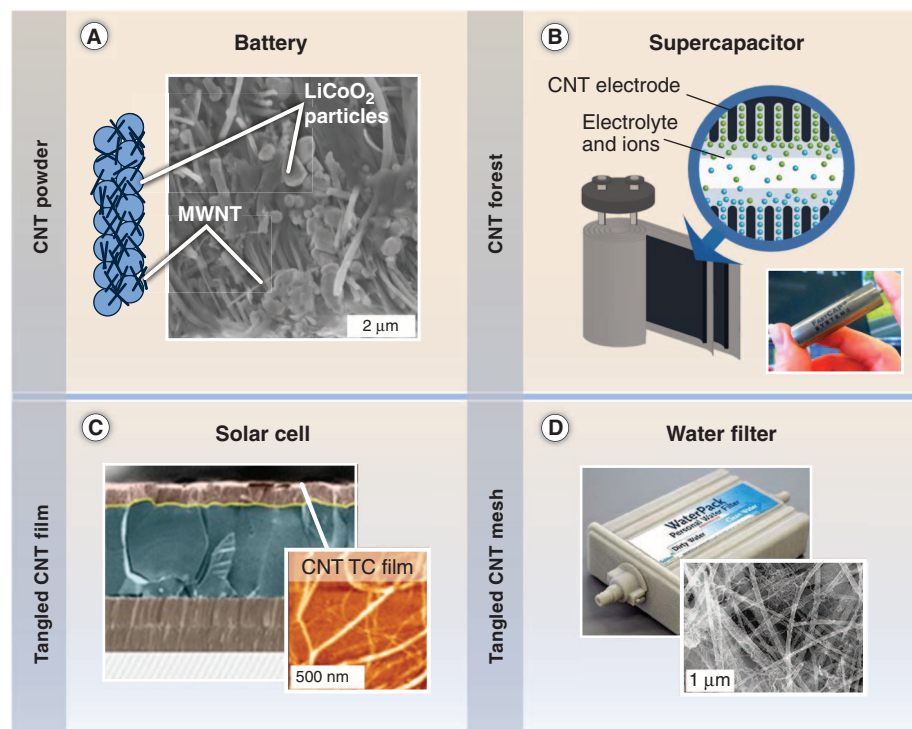


**Fig. 4.** Energy-related applications of CNTs. (A) Mixture of MWNTs and active powder for battery electrode. [Images reprinted by permission from John Wiley and Sons (67)] (B) Concept for supercapacitors based on CNT forests. [Images courtesy of FastCap Systems Corporation] (C) Solar cell using a SWNT-based transparent conductor. [Images courtesy of Eikos Incorporated] (D) Prototype portable water filter using a functionalized tangled CNT mesh in the latest stage of development. [Images courtesy of Seldon Technologies]



response relative to controls (92). This is encouraging for possible use of CNTs as low-impedance neural interface electrodes (93) and for coating of catheters to reduce thrombosis (94).

## Outlook

Most products using CNTs today incorporate CNT powders dispersed in polymer matrices or deposited as thin films; for commercialization of these products, it was essential to integrate CNT processing with existing manufacturing methods. Organized CNT materials such as forests and yarns are beginning to bridge the gap between the nanoscale properties of CNTs and the length scales of bulk engineering materials. However, understanding is needed of why the properties of CNT yarns and sheets, like thermal conductivity and mechanical strength, remain far lower than the properties of individual CNTs. At an opposite limit, placement of individual CNTs having desired structure with lithographic precision over large substrates would be a breakthrough for electronic devices and scanning probe tips.

According to press reports, many companies are investing in diverse applications of CNTs, such as transparent conductors, thermal interfaces, anti-ballistic vests, and wind turbine blades. However, often few technical details are released, and companies are likely to keep technical details hidden for a very long time after commercialization, which makes it challenging to predict market success. Hence, the increases in nanotube production capacity and sales are an especially important metric for emerging CNT applications (see Fig. 1).

Further industrial development demands health and safety standards for CNT manufacturing and use, along with improved quantitative characterization methods that can be implemented in production processes. For example, the National Institute of Standards and Technology developed a SWNT reference material in 2011; IEEE is developing standards for CNT processing in clean rooms; and in 2010 the Chinese government published standards for MWNT characterization and handling (16). Proactively, Bayer established an occupational exposure limit of  $0.05 \text{ mg m}^{-3}$  for their CNTs (95). These efforts encourage continued progress with caution, especially for CNT manufacturing operations that can potentially generate airborne particulate matter.

As larger quantities of CNT materials reach the consumer market, it will also be necessary to establish disposal and/or reuse procedures. CNTs may enter municipal waste streams, where, unless they are incinerated, cross-contamination during recycling is possible (65). Broader partnerships among industry, academia, and government are needed to investigate the environmental and societal impact of CNTs throughout their life cycle.

Lastly, continued CNT research and development will be complementary to the rise of graphene. Rapid innovations in graphene synthesis and characterization—such as CVD methods and Raman spectroscopy techniques—have leveraged findings from CNT research. Promising materials combining carbon allotropes include 3D CNT-graphene

networks for thermal interfaces (96) and fatigue-resistant graphene-coated CNT aerogels (97). The science and applications of CNTs, ranging from surface chemistry to large-scale manufacturing, will contribute to the frontier of nanotechnology and related commercial products for many years to come.

## References and Notes

1. S. Iijima, *Nature* **354**, 56 (1991).
2. P. J. F. Harris, *Carbon Nanotube Science - Synthesis, Properties, and Applications* (Cambridge Univ. Press, Cambridge, 2009).
3. B. Peng et al., *Nat. Nanotechnol.* **3**, 626 (2008).
4. B. Q. Wei, R. Vajtai, P. M. Ajayan, *Appl. Phys. Lett.* **79**, 1172 (2001).
5. E. Pop, D. Mann, Q. Wang, K. Goodson, H. J. Dai, *Nano Lett.* **6**, 96 (2006).
6. A. Y. Cao, P. L. Dickrell, W. G. Sawyer, M. N. Ghasemi-Nejhad, P. M. Ajayan, *Science* **310**, 1307 (2005).
7. L. Qu, L. Dai, M. Stone, Z. Xia, Z. L. Wang, *Science* **322**, 238 (2008).
8. M. Xu, D. N. Futaba, T. Yamada, M. Yumura, K. Hata, *Science* **330**, 1364 (2010).
9. M. F. L. De Volder, J. De Coster, D. Reynaerts, C. Van Hoof, S.-G. Kim, *Small* **8**, 2006 (2012).
10. L. Ren et al., *Nano Lett.* **9**, 2610 (2009).
11. A. E. Aliev et al., *Science* **323**, 1575 (2009).
12. M. Lima et al., *Science* **338**, 928 (2012).
13. K. Mizuno et al., *Proc. Natl. Acad. Sci. U.S.A.* **106**, 6044 (2009).
14. L. Xiao et al., *Nano Lett.* **8**, 4539 (2008).
15. M. Endo, T. Hayashi, Y.-A. Kim, *Pure Appl. Chem.* **78**, 1703 (2006).
16. Q. Zhang, J.-Q. Huang, M.-Q. Zhao, W.-Z. Qian, F. Wei, *ChemSusChem* **4**, 864 (2011).
17. A. R. Harutyunyan et al., *Science* **326**, 116 (2009).
18. L. Ding et al., *Nano Lett.* **9**, 800 (2009).
19. K. Gong, F. Du, Z. Xia, M. Durstock, L. Dai, *Science* **323**, 760 (2009).
20. J. M. Lee et al., *Adv. Mater.* **23**, 629 (2011).
21. X. Wang et al., *Nano Lett.* **9**, 3137 (2009).
22. S. Hofmann et al., *Nano Lett.* **7**, 602 (2007).
23. E. C. Neyts, A. C. T. van Duin, A. Bogaerts, *J. Am. Chem. Soc.* **133**, 17225 (2011).
24. M. S. Arnold, A. A. Green, J. F. Hulvat, S. I. Stupp, M. C. Hersam, *Nat. Nanotechnol.* **1**, 60 (2006).
25. H. Liu, D. Nishide, T. Tanaka, H. Kataura, *Nat. Commun.* **2**, 309 (2011).
26. Q. Cao, J. A. Rogers, *Adv. Mater.* **21**, 29 (2009).
27. K. Hata et al., *Science* **306**, 1362 (2004).
28. K. Kozioł et al., *Science* **318**, 1892 (2007); 10.1126/science.1147635.
29. D. N. Futaba et al., *Nat. Mater.* **5**, 987 (2006).
30. Y. Hayamizu et al., *Nat. Nanotechnol.* **3**, 289 (2008).
31. M. De Volder et al., *Adv. Mater.* **22**, 4384 (2010).
32. M. Zhang, K. R. Atkinson, R. H. Baughman, *Science* **306**, 1358 (2004).
33. K. L. Jiang, Q. Q. Li, S. S. Fan, *Nature* **419**, 801 (2002).
34. W. Bauhofer, J. Z. Kovacs, *Compos. Sci. Technol.* **69**, 1486 (2009).
35. T.-H. Chou, L. Gao, E. T. Thostenson, Z. Zhang, J.-H. Byun, *Compos. Sci. Technol.* **70**, 1 (2010).
36. F. H. Gojny, M. H. G. Wichmann, U. Kopke, B. Fiedler, K. Schulte, *Compos. Sci. Technol.* **64**, 2363 (2004).
37. J. Suhr, N. Koratkar, P. Keblinski, P. Ajayan, *Nat. Mater.* **4**, 134 (2005).
38. J. N. Coleman, U. Khan, W. J. Blau, Y. K. Gun'ko, *Carbon* **44**, 1624 (2006).
39. H. G. Chae, Y. H. Choi, M. L. Minus, S. Kumar, *Compos. Sci. Technol.* **69**, 406 (2009).
40. V. P. Veedu et al., *Nat. Mater.* **5**, 457 (2006).
41. E. J. Garcia, B. L. Wardle, A. J. Hart, N. Yamamoto, *Compos. Sci. Technol.* **68**, 2034 (2008).
42. M. D. Lima et al., *Science* **331**, 51 (2011).
43. N. Behabtu et al., *Science* **339**, 182 (2013).
44. S. R. Bakshi, A. Agarwal, *Carbon* **49**, 533 (2011).
45. T. Kashiwagi et al., *Nat. Mater.* **4**, 928 (2005).
46. A. Beigbeder et al., *Biofouling* **24**, 291 (2008).
47. Z. Wu et al., *Science* **305**, 1273 (2004).
48. S. De, J. N. Coleman, *MRS Bull.* **36**, 774 (2011).
49. A. M. Ionescu, H. Riel, *Nature* **479**, 329 (2011).

50. S. J. Tans, A. R. M. Verschueren, C. Dekker, *Nature* **393**, 49 (1998).
51. J. Appenzeller, Y. M. Lin, J. Knoch, P. Avouris, *Phys. Rev. Lett.* **93**, 196805 (2004).
52. K. Jensen, J. Weldon, H. Garcia, A. Zettl, *Nano Lett.* **7**, 3508 (2007).
53. A. D. Franklin et al., *Nano Lett.* **12**, 758 (2012).
54. Q. Cao et al., *Nature* **454**, 495 (2008).
55. H. Park et al., *Nat. Nanotechnol.* **7**, 787 (2012).
56. D. M. Sun et al., *Nat. Nanotechnol.* **6**, 156 (2011).
57. M. A. McCarthy et al., *Science* **332**, 570 (2011).
58. P. Chen et al., *Nano Lett.* **11**, 5301 (2011).
59. M. Jung et al., *IEEE Trans. Electron. Dev.* **57**, 571 (2010).
60. M. C. LeMieux et al., *Science* **321**, 101 (2008).
61. A. D. Franklin et al., *ACS Nano* **6**, 1109 (2012).
62. M. H. van der Veen et al., paper presented at the 2012 IEEE International Interconnect Technology Conference, San Jose, CA, 4 to 6 June 2012.
63. T. Rueckes et al., *Science* **289**, 94 (2000).
64. L. Dai, D. W. Chang, J.-B. Baek, W. Lu, *Small* **8**, 1130 (2012).
65. A. R. Köhler, C. Som, A. Helland, F. Gottschalk, *J. Clean. Prod.* **16**, 927 (2008).
66. K. Evanoff et al., *Adv. Mater.* **24**, 533 (2012).
67. C. Sotowa et al., *ChemSusChem* **1**, 911 (2008).
68. Y. Gogotsi, P. Simon, *Science* **334**, 917 (2011).
69. A. Izadi-Najafabadi et al., *Adv. Mater.* **22**, E235 (2010).
70. T. Matsumoto et al., *Chem. Commun.* **2004**, 840 (2004).
71. A. Le Goff et al., *Science* **326**, 1384 (2009).
72. N. M. Gabor, Z. Zhong, K. Bosnick, J. Park, P. L. McEuen, *Science* **325**, 1367 (2009).
73. G. Gao, C. D. Vecitis, *Environ. Sci. Technol.* **45**, 9726 (2011).
74. M. S. Rahaman, C. D. Vecitis, M. Elimelech, *Environ. Sci. Technol.* **46**, 1556 (2012).
75. J. K. Holt et al., *Science* **312**, 1034 (2006).
76. B. Corry, *J. Phys. Chem. B* **112**, 1427 (2008).
77. D. A. Heller, S. Baik, T. E. Eurell, M. S. Strano, *Adv. Mater.* **17**, 2793 (2005).
78. A. De La Zerda et al., *Nat. Nanotechnol.* **3**, 557 (2008).
79. N. W. S. Kam, M. O'Connell, J. A. Wisdom, H. J. Dai, *Proc. Natl. Acad. Sci. U.S.A.* **102**, 11600 (2005).
80. T. Kurkina, A. Vlandas, A. Ahmad, K. Kern, K. Balasubramanian, *Angew. Chem. Int. Ed.* **50**, 3710 (2011).
81. D. A. Heller et al., *Nat. Nanotechnol.* **4**, 114 (2009).
82. E. S. Snow, F. K. Perkins, E. J. Houser, S. C. Badescu, T. L. Reinecke, *Science* **307**, 1942 (2005).
83. Z. Chen et al., *Nat. Biotechnol.* **26**, 1285 (2008).
84. A. Star et al., *Proc. Natl. Acad. Sci. U.S.A.* **103**, 921 (2006).
85. B. Esser, J. M. Schnorr, T. M. Swager, *Angew. Chem. Int. Ed.* **51**, 5752 (2012).
86. X. Shi, A. von dem Bussche, R. H. Hurt, A. B. Kane, H. Gao, *Nat. Nanotechnol.* **6**, 714 (2011).
87. S. Y. Hong et al., *Nat. Mater.* **9**, 485 (2010).
88. Z. Liu, X. Sun, N. Nakayama-Ratchford, H. Dai, *ACS Nano* **1**, 50 (2007).
89. A. Bianco, K. Kostarelos, M. Prato, *Chem. Commun.* **47**, 10182 (2011).
90. C. A. Poland et al., *Nat. Nanotechnol.* **3**, 423 (2008).
91. G. M. Mutlu et al., *Nano Lett.* **10**, 1664 (2010).
92. D. A. X. Nayagam et al., *Small* **7**, 1035 (2011).
93. E. W. Keefer, B. R. Botterman, M. I. Romero, A. F. Rossi, G. W. Gross, *Nat. Nanotechnol.* **3**, 434 (2008).
94. M. Endo, S. Koyama, Y. Matsuda, T. Hayashi, Y. A. Kim, *Nano Lett.* **5**, 101 (2005).
95. J. Pauluhn, *Regul. Toxicol. Pharmacol.* **57**, 78 (2010).
96. S. W. Hong et al., *Adv. Mater.* **23**, 3821 (2011).
97. K. H. Kim, Y. Oh, M. F. Islam, *Nat. Nanotechnol.* **7**, 562 (2012).

**Acknowledgments:** M.F.L.D.V. was supported by the Fund for Scientific Research—Flanders, Belgium. S.H.T. and A.J.H. were supported by the Office of Naval Research (N00014101055 and N000141210815). R.H.B. was supported by the Air Force Office of Scientific Research MURI grant R17535 and Robert A. Welch grant AT-0029. The authors thank M. Endo, Y. Gogotsi, K. Hata, S. Joshi, Y. A. Kim, E. Meshot, M. Roberts, S. Suematsu, K. Tamamitsu, J. R. Von Ehr, B. Wardle, G. Yushin, and many companies for valuable input.

## Supplementary Materials

www.sciencemag.org/cgi/content/full/339/6119/535/DC1  
Materials and Methods  
Tables S1 to S3  
10.1126/science.1222453

# Authigenic Carbonate and the History of the Global Carbon Cycle

Daniel P. Schrag,<sup>1\*†</sup> John. A. Higgins,<sup>2\*</sup> Francis A. Macdonald,<sup>1</sup> David T. Johnston<sup>1</sup>

We present a framework for interpreting the carbon isotopic composition of sedimentary rocks, which in turn requires a fundamental reinterpretation of the carbon cycle and redox budgets over Earth's history. We propose that authigenic carbonate, produced in sediment pore fluids during early diagenesis, has played a major role in the carbon cycle in the past. This sink constitutes a minor component of the carbon isotope mass balance under the modern, high levels of atmospheric oxygen but was much larger in times of low atmospheric O<sub>2</sub> or widespread marine anoxia. Waxing and waning of a global authigenic carbonate sink helps to explain extreme carbon isotope variations in the Proterozoic, Paleozoic, and Triassic.

Since the observation of isotopic fractionation of carbon during photosynthesis more than 60 years ago (1), the contrast in the isotopic composition of organic carbon and calcium carbonate has been used to reconstruct the history of the global carbon cycle and its connection to the oxidation state of the planet, including the rise of atmospheric oxygen (2). The input of carbon to Earth's surface reservoirs ( $\delta^{13}\text{C}_{\text{in}}$ ) (3) is balanced by the burial of carbon either as organic carbon ( $\delta^{13}\text{C}_{\text{org}}$ ), which is depleted in  $^{13}\text{C}$  relative to dissolved inorganic carbon in seawater (DIC), or as calcium carbonate ( $\delta^{13}\text{C}_{\text{carb}}$ ), which has a similar isotopic composition to DIC. Changes in the isotopic composition of marine carbonate in the geologic record have thus been interpreted as changes in the fractional burial of organic carbon relative to carbonate carbon ( $f_{\text{org}}$ ), as described by the simple equation (4)

$$\delta^{13}\text{C}_{\text{in}} = \delta^{13}\text{C}_{\text{org}}f_{\text{org}} + \delta^{13}\text{C}_{\text{carb}}(1 - f_{\text{org}}) \quad (1)$$

For much of Earth history,  $\delta^{13}\text{C}_{\text{carb}}$  has fluctuated around a value of 0 per mil (‰), with  $\delta^{13}\text{C}_{\text{org}}$  and  $\delta^{13}\text{C}_{\text{in}}$  values at roughly -25 and -5‰ respectively, implying that 20% of total carbon burial has been as organic matter (5).

The isotopic mass balance requires a fundamental linkage between the carbon cycle and the oxidation state of Earth's surface as manifest by the amount of oxygen in the atmosphere. An increase in  $\delta^{13}\text{C}_{\text{carb}}$  implies the burial of a higher fraction of organic carbon, or alternatively a decrease in the oxidation of organic matter relative to the weathering of carbonate rocks. In either case, this would increase the amount of oxygen in the atmosphere unless other redox-sensitive elements such as sulfur or iron serve as alternative electron donors.

This basic framework has been used to interpret  $\delta^{13}\text{C}_{\text{carb}}$  variations throughout Earth history. For example, observations of  $\delta^{13}\text{C}_{\text{carb}}$  above +5‰ for more than 10 million years during the Neoproterozoic have been explained in terms of sustained periods of high fractional organic carbon burial (5). Similarly, high  $\delta^{13}\text{C}_{\text{carb}}$  values in the late Paleozoic have been attributed to high organic carbon burial after the proliferation of land plants (2). These interpretations directly inform models of atmospheric oxygen levels over the Phanerozoic (6), leading to suggestions of pulses of oxygen production and consumption throughout the geologic record (7, 8). Thus, a correct reading of carbon isotope mass balance is critical to our understanding of the accumulation of oxidizing capacity (atmospheric O<sub>2</sub> and seawater sulfate) at the Earth's surface through geologic time.

Certain aspects of the  $\delta^{13}\text{C}_{\text{carb}}$  record are challenging to explain in the simple framework described above. First, sustained high  $\delta^{13}\text{C}_{\text{carb}}$  values (>+5‰), such as what is observed throughout the Neoproterozoic (9, 10) and in the early Paleoproterozoic (7), imply very high rates of organic burial and hence accumulation of atmospheric oxygen to levels tens to hundreds times that of the present (4, 7). This is inconsistent with geological evidence for lower oxygen levels during these times (11). Second, large negative isotopic excursions of -10 to -15‰ in the Neoproterozoic are very difficult to explain either by oxidation of large amounts of organic matter (7, 12) or methane (13, 14) because both require a very large change in atmospheric oxygen as well as a very large increase in atmospheric carbon dioxide, neither of which is supported by independent geological evidence. Surveying the  $\delta^{13}\text{C}_{\text{carb}}$  record in its entirety, one is forced to conclude that our basic framework is lacking some fundamental process and that it provides a misleading basis for understanding Earth history. We suggest that authigenic carbonate, produced in sediments during early diagenetic reactions primarily associated with sulfate and iron reduction, has played a major role in the carbon isotope mass balance over Earth

history, although it represents a minor component of the modern isotope mass balance because of high levels of atmospheric oxygen in the modern world. If correct, this requires a reinterpretation of the  $\delta^{13}\text{C}_{\text{carb}}$  record.

Authigenic carbonate refers to any carbonate mineral precipitated inorganically in situ, whether at the sediment-water interface or within sediment pore waters. In the modern ocean, most authigenic carbonate is formed in sediments when alkalinity is produced from diagenetic reactions—usually those that reduce sulfate or ferric iron—resulting in supersaturation of carbonate minerals, including calcite, dolomite, or siderite. Precipitation of pyrite can also be an important source of alkalinity that enhances the precipitation of authigenic carbonate phases. Because most reduction of iron and sulfate occurs through oxidation of methane (anaerobic methane oxidation) or organic carbon, the DIC from which authigenic carbonate forms is generally depleted in  $^{13}\text{C}$ , although enrichment is possible if carbonate precipitation occurs deeper in the sediment column, where methanogenesis drives the  $\delta^{13}\text{C}$  of DIC to higher values. Authigenic carbonates composed of calcite, aragonite, and dolomite occur in continental margin sediments in North and South America and Eurasia; they are characterized by  $\delta^{13}\text{C}_{\text{carb}}$  values ranging from -60 to +26‰, with most values <0‰ (15). Authigenic carbonates ( $\delta^{13}\text{C}_{\text{carb}}$  = -18 to -55‰) are found over the entire depth range of the Gulf of Mexico slope (16); in Peru Margin sediments, the  $\delta^{13}\text{C}$  of dolomite varies between -36.1 and +11.5‰, although the majority of measurements lie between -9 and -12‰ (17). This carbonate sink is also common in sediments in anoxic basins and fjords (18, 19), as well as deltaic environments. In the mobile mudbelts of the Amazon shelf, for example, authigenic carbonate forms primarily as siderite and mixed Ca-, Mg-, Fe-, and Mn-carbonates associated with iron reduction and pyrite burial, rather than with sulfate reduction through anaerobic methane oxidation, with mass-weighted  $\delta^{13}\text{C}_{\text{carb}}$  between -15 and -19‰ (20). Approximately 30% of the total carbon burial in the Amazon fan occurs as authigenic carbonate (21). This phenomenon is not limited to modern examples; similar  $\delta^{13}\text{C}_{\text{carb}}$  values have been observed in Cenozoic sediments from the Arctic Ocean and the Norwegian-Greenland Sea (22).

Despite its widespread occurrence, authigenic carbonate does not appear to represent a substantial component (by mass) in the modern global carbon cycle. One reason is that the formation of authigenic carbonate is inhibited by the amount of O<sub>2</sub> in seawater because both oxic respiration and oxidation of reduced compounds [such as Fe(II) and H<sub>2</sub>S] lowers the saturation of carbonate phases. A recent study explored a model for the global alkalinity and carbonate cycles, proposing that changes in organic carbon cycling, electron acceptor [Fe(III), SO<sub>4</sub><sup>2-</sup>, and O<sub>2</sub>] concentrations, and the concentration of DIC would

<sup>1</sup>Department of Earth and Planetary Sciences, Harvard University, Cambridge, MA 02138, USA. <sup>2</sup>Department of Geosciences, Princeton University, Princeton, NJ 08544, USA.

\*These authors contributed equally to this work.

†To whom correspondence should be addressed. E-mail: daniel\_schrag@harvard.edu



lead to a greater importance of authigenic carbonates in marine sediments during times of low  $O_2$ , such as the Proterozoic or times of widespread anoxia in the Phanerozoic (23). More generally, environmental conditions that minimize aerobic respiration in the water column and in sediments (because this essentially acidifies the pore fluid) and maximize the production of alkalinity per unit of organic carbon respired will favor a large sink of carbon as authigenic carbonate (23).

Is there evidence for high burial rates of isotopically depleted authigenic carbonate in the geologic past? A challenge is that  $\delta^{13}C_{carb}$  records before the Jurassic are heavily biased toward shallow-water carbonate platforms because slope and deep-basin sections are typically consumed or highly deformed during subduction. One expects authigenic carbonate to be dominant in slope settings with more anaerobic respiration, rather than in shallow water carbonate platforms with low organic burial and greater oxygen availability. In addition, many studies of  $\delta^{13}C_{carb}$  have been motivated by stratigraphy by using the isotope variations to correlate across regions and even continents (10); it is possible that sections with authigenic carbonate may have been excluded from records of  $\delta^{13}C_{carb}$  variations if they were considered artifacts of postdepositional processes (7). For stratigraphic studies, such exclusions may be appropriate because the  $\delta^{13}C$  of authigenic carbonate does not necessarily capture a global change in the  $\delta^{13}C$  of DIC. From the perspective of the global carbon cycle, however, such carbonate deposition cannot be ignored because it may represent a substantial carbon sink.

A series of studies of  $\delta^{13}C_{carb}$  focused on global geochemical surveys rather than stratigraphy provides some support for the widespread occurrence of authigenic carbonates in the past

(24). Bulk carbonates from Proterozoic and Early Paleozoic continental margins from around the world record  $\delta^{13}C_{carb}$  values that range from +18 to −20‰ (Fig. 1) (24). The lowest values (<−5‰)—and perhaps some of the highest values—are most easily explained with an authigenic component, formed during early diagenesis rather than in the water column. Additional support comes from more detailed studies of Ediacaran (late Neoproterozoic) stratigraphy in China, where deeper water sections have  $\delta^{13}C_{carb}$  values as low as −16‰, compared with −2‰ for the shallowest onshore sections (25, 26). These data were originally interpreted as representing a very large  $\delta^{13}C$  gradient in DIC over hundreds of meters in the water column, which is difficult to reconcile with rates of ocean mixing; we suggest instead that these micritic carbonates in slope settings with low  $\delta^{13}C_{carb}$  values are largely composed of authigenic carbonate, formed in a similar fashion to imperfect modern analogs in the Amazon Fan, the Santa Barbara basin, or the Peru margin (17, 18, 21). Overall, observations of authigenic carbon in modern and ancient settings, as well as theoretical arguments (27), suggest a major role for authigenic carbonate in the global carbon cycle, particularly at times of lower atmospheric  $O_2$ .

If authigenic carbonate is a substantial sink for carbon burial at times in the geologic past, the isotopic mass balance described in Eq. 1 must be broadened to make explicit the fraction of carbonate burial that is authigenic ( $f_{ac}$ ), as well as the different isotopic fractionation factors for organic carbon, authigenic carbonate, and normal marine carbonate ( $\epsilon_p$ ,  $\epsilon_{ac}$ , and  $\epsilon_{mc}$ , respectively). We choose to write the isotopic fractionation between seawater and authigenic carbonate in the same manner used for the fractionation associated with photosynthesis ( $\epsilon_p$ ); like the photosynthetic frac-

tionation, it depends on the isotopic composition of a separate pool of water (pore fluid or intracellular fluid), which in turn depends on the relative rates of chemical reaction (oxidation or fixation of organic carbon) and chemical transport (diffusion in the pore fluid or across the cell membrane).

Thus,

$$\delta^{13}C_{in} = (\delta^{13}C_{DIC} - \epsilon_p)f_{org} + (1 - f_{org})[(\delta^{13}C_{DIC} - \epsilon_{ac})f_{ac} + (\delta^{13}C_{DIC} - \epsilon_{mc})(1 - f_{ac})] \quad (2)$$

or simplifying and solving for  $\delta^{13}C_{DIC}$  (27)

$$\delta^{13}C_{DIC} = \delta^{13}C_{in} + f_{org}[\epsilon_p - \epsilon_{mc} - f_{ac}(\epsilon_{ac} - \epsilon_{mc})] + f_{ac}(\epsilon_{ac} - \epsilon_{mc}) \quad (3)$$

Unfortunately, there is no easy way to empirically reconstruct  $f_{ac}$  through geologic time because the authigenic component may be broadly distributed across large volumes of sediment with relatively low carbonate content. For example, an authigenic carbonate sink of  $2.5 \times 10^{14}$  g/year—roughly one third of the modern sink related to silicate weathering—would require the addition of less than 2 weight percent carbonate to the annual flux of terrigenous sediment of  $1.7 \times 10^{16}$  g/year. Moreover, it is difficult to estimate even total carbonate accumulation through Earth's history given the incompleteness of the geologic record. However, there is an expectation that  $f_{ac}$  will be higher when there is less oxygen in bottom waters along the shelf and slope environments and when alternative electron acceptors, particularly iron, are more abundant or are more focused in the same locations where organic carbon is buried (23).

The average isotopic offset between authigenic carbonate and DIC ( $\epsilon_{ac}$ ) is determined by the balance between diffusive transport of DIC through pore fluids in the sediment column and the anaerobic oxidation of methane or organic matter, which leads simultaneously to the creation of alkalinity. Higher values of  $\epsilon_{ac}$  are expected when the reductant is  $CH_4$  ( $\delta^{13}C = -50$  to  $-90$ ‰) as compared with organic carbon ( $\delta^{13}C = -22$  to  $-26$ ‰). In modern sediments in which anaerobic methane oxidation is dominant, the maximum alkalinity occurs at the same depth as the depletion of sulfate and a minimum in the  $\delta^{13}C$  of DIC (28). In the geologic past,  $\epsilon_{ac}$  would also be affected by changes in the amount of DIC in seawater, in addition to the rate of anaerobic respiration in the sediment column. If DIC were substantially higher because of elevated atmospheric partial pressure of  $CO_2$  ( $P_{CO_2}$ ), a lower seawater  $Ca^{2+}$  concentration relative to alkalinity, or some combination of the two, then the  $\delta^{13}C$  of DIC in pore fluids would be less affected by oxidation of reduced carbon, resulting in a smaller value for  $\epsilon_{ac}$ . In contrast, increasing oxidant availability [such as  $SO_4$  or  $Fe(III)$ ] would be expected to increase both  $\epsilon_{ac}$  and  $f_{ac}$ . It is also possible to form authigenic carbonate much later in the burial history when the porosity and permeability of the

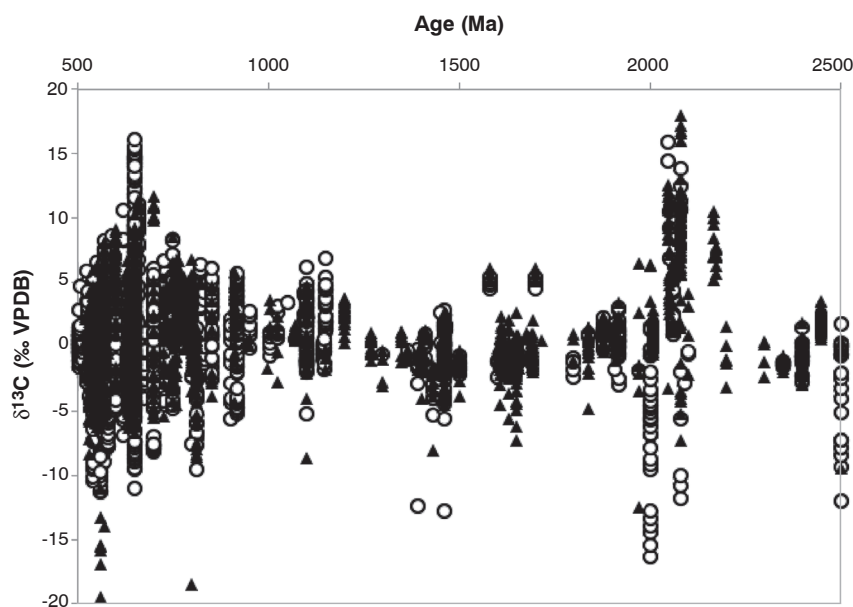


**Fig. 1.**  $\delta^{13}C_{carb}$  measurements on Early Paleozoic and Proterozoic calcites (open circles) and dolomites (triangles) from the compilation of Prokoph *et al.* (24).

sediments are lower and the distance from the sediment-water interface is large; in this case, diffusive exchange with seawater is less important in determining  $\epsilon_{ac}$ .

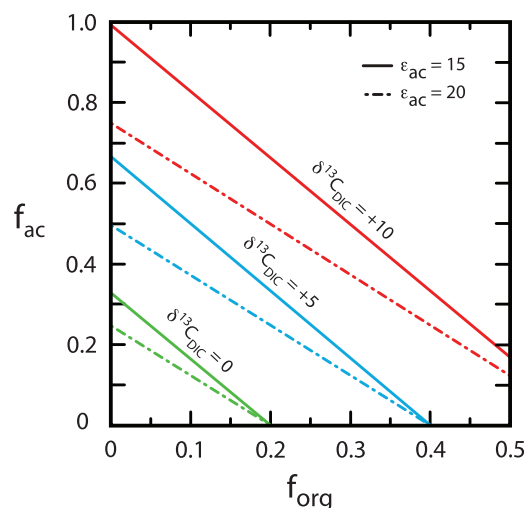
The inclusion of authigenic carbonate in the global carbon isotope mass balance adds an additional degree of freedom in explaining  $\delta^{13}\text{C}$  variations in the geologic record and complicates the connection between carbon isotopes and the redox budget of the Earth's surface. In Fig. 2, the  $\delta^{13}\text{C}$  of DIC is shown as a function of  $f_{org}$  and  $f_{ac}$  for global average values of  $\epsilon_{ac}$  of 15 and 20‰, assuming that the carbon cycle is in steady state and neglecting imbalances in other inputs (such as weathering of organic carbon and carbonate). Prolonged periods of high  $\delta^{13}\text{C}_{carb}$  in the Neoproterozoic can now be explained without invoking sustained high organic carbon burial or low organic carbon weathering fluxes (which implies the accumulation of massive amounts of atmospheric oxygen), but simply from the persistent burial of larger amounts of isotopically depleted authigenic carbonate. As an end member example, to maintain  $\delta^{13}\text{C}_{carb}$  at +5‰ without a shift from modern  $f_{org}$  values ( $f_{org} = 0.2$ ) requires that authigenic carbonate make up 29 to 37% of the global carbonate sink for global average  $\epsilon_{ac}$  values of 20 and 15‰, respectively (Fig. 2).  $\epsilon_{ac}$  is not entirely independent of  $\epsilon_p$  because the average photosynthetic fractionation is ultimately the reason for a fractionation between authigenic carbonate formed in sediments and DIC.

Applying this new framework to large, negative isotopic excursions, such as those observed in the Neoproterozoic, is more complicated because the carbon cycle during such events need not be at steady state, especially when the excursion lasts less than a few hundred thousand years. We describe two major categories of negative isotopic excursions that have fundamentally different explanations. First, some excursions can be explained through a decline in the global flux of authigenic carbonate that is due to a variety of possible factors, including the location or focusing of organic carbon burial, the carbonate saturation state of seawater, or an increase in the oxygen content of the ocean (and atmosphere). A rapid decline in authigenic carbonate deposition would drop the steady-state  $\delta^{13}\text{C}$  value of DIC and could be amplified by additional carbon feedbacks, including oxidative weathering of organic carbon. Although we expect some modest connection between  $\delta^{13}\text{C}_{carb}$  variations and the oxidation state of the Earth surface (through iron reduction, pyrite burial, or intermediate water oxygen content),  $\delta^{13}\text{C}_{carb}$  excursions created in this way need not be accompanied by a large rise in  $P\text{CO}_2$  nor a large drop in  $P\text{O}_2$ . Because such excursions result from changes in the  $\delta^{13}\text{C}$  of DIC, one would expect to see the excursion in marine organic matter as well as in marine carbonate. Moreover, one would not expect to see the  $\delta^{13}\text{C}$  values drop below the global average  $\delta^{13}\text{C}$  of the inputs (−5‰) unless there is additional carbon added from oxidation of organic carbon or methane.

A second category of negative isotope excursions results from the addition of authigenic carbonate into primary marine carbonate in slope or shelf sediments. In this case, the change in  $\delta^{13}\text{C}_{carb}$  does not represent a change in seawater DIC but rather is a local feature—although it may have a regional or global extent if it is driven, for example, by a marine transgression or changes to global redox budgets ( $\text{O}_2$ ,  $\text{SO}_4$ , or Fe); thus, the  $\delta^{13}\text{C}_{org}$  would not track the bulk rock  $\delta^{13}\text{C}_{carb}$  through the excursion. One might expect the magnitude of the apparent excursion to vary across sedimentary environments, such as from shelf to slope [as is present in Ediacaran successions in China (25, 26)] or even laterally across a sedimentary basin, depending on the distribution of authigenic carbonate production and the degree of depletion of  $\delta^{13}\text{C}$  in the pore fluid. The extent of the isotopic excursion could theoretically extend far below the  $\delta^{13}\text{C}$  of carbon inputs, limited only by the isotopic composition and mass contribution of local authigenic carbonate. This mechanism provides an explanation for large negative-isotope excursions in the carbonate record that are not observed in  $\delta^{13}\text{C}$  of organic carbon, which is a scenario that has invoked much attention and speculation (29). This scenario does not require large changes in atmospheric  $\text{O}_2$  and  $\text{CO}_2$ .

An example of the first type of excursion is possibly captured by the Tayshir anomaly from Neoproterozoic sections in Mongolia (30), which documents a covariation between the  $\delta^{13}\text{C}$  of organic carbon and carbonate carbon through an isotopic anomaly of ~15‰. With minimum  $\delta^{13}\text{C}_{carb}$  values during the excursion between −5 and −7‰, one can explain this excursion with nearly a complete shut-off of authigenic carbonate production ( $f_{ac} \rightarrow 0$ ), perhaps with some additional contribution from net oxidation of reduced carbon. The shutdown of authigenesis could be driven by a small change in the oxidation state of intermediate waters on the continental slope, perhaps related to higher atmospheric  $P\text{O}_2$ , establishing a stronger lysocline and a carbonate saturation gradient in the sediment column.

**Fig. 2.** Contours of  $\delta^{13}\text{C}$  of DIC as a function of  $f_{org}$  and  $f_{ac}$  for global average values of  $\epsilon_{ac}$  of 15 and 20‰, assuming that the carbon cycle is in steady state, and neglecting imbalances in other inputs, based on Eq. 2.



The Ediacaran Shuram anomaly is a possible example of the second category of isotope excursion. The Shuram anomaly occurs in Ediacaran sections around the world, including Namibia, China, and Oman (29). The magnitude of the isotopic excursion is variable across different locations and even within a single basin (25, 26). Important features include  $\delta^{13}\text{C}_{carb}$  values as low as −12‰ during the peak of the excursion and no parallel variations in  $\delta^{13}\text{C}_{org}$  across the excursion (31). We suggest the isotopic anomaly in this case could be explained in part by the expansion of the zone of authigenesis onto carbonate platforms during a marine transgression, effectively adding authigenic carbonate to marine carbonate precipitated from the water column.

Previous studies have attributed the large negative excursions in the Neoproterozoic—and the Shuram anomaly, in particular—to diagenetic processes (32, 33), specifically basin-scale alteration of carbonate rocks with fluids with low  $\delta^{13}\text{C}$  from oxidation of hydrocarbons, or from meteoric alteration (33). On the other hand, it has been argued that the low  $\delta^{13}\text{C}_{carb}$  values through the Shuram anomaly cannot be explained by diagenesis because they are expressed in oolitic and stromatolitic facies without evidence for secondary cements (29). Moreover, such a diagenetic explanation is difficult to reconcile with the observation of these negative excursions at precise stratigraphic intervals in geologic sections across multiple continents (10, 29). Our explanation may reconcile these views because one would expect isotopic excursions produced by mixing of marine carbonate with a depleted authigenic component to occur at broadly the same stratigraphic interval if they were produced by migration of the zone of authigenesis because of a marine transgression or drop in near-surface  $\text{O}_2$  concentration. Textures such as ooids could be preserved if authigenesis occurs on both microscales, consuming organic matter along individual laminations (34), and on mesoscales filling pore spaces with micrite on 10-m scales in mixed-carbonate siliciclastic sequences.



A prominent but transient authigenic carbonate sink may also help explain carbon isotope variations in the Paleozoic (8, 35) and Early Triassic (36). In the Triassic, for example, there is evidence for widespread anoxia in intermediate waters (37), fluctuating  $\delta^{13}\text{C}_{\text{carb}}$  values ( $-2$  to  $+8\text{‰}$ ), and gradients in the  $\delta^{13}\text{C}_{\text{carb}}$  values with depth, often with  $\delta^{13}\text{C}$  values on the slope 2 to 3‰ lighter than those on the shelf (38). We view the Early Triassic as a candidate for a period of sustained, high authigenic carbonate formation, like much of the Neoproterozoic (23). The fluctuations could be produced either from a change in the global amount of authigenic carbonate (category 1) or by migration in the zone of authigenic carbonate (category 2). In the Early Cambrian, similar fluctuations in the authigenic carbonate sink might have resulted from more modest variations in surface redox or evolutionary leaps such as the biological irrigation of sediments.

The recognition of authigenic carbonate in the sedimentary record presents a challenge for carbon isotope stratigraphy because it allows for local variations in  $\delta^{13}\text{C}_{\text{carb}}$  produced by the addition of a substantial authigenic component after burial. Until there is a clear way to quantify the amount of marine carbonate precipitated in the water column relative to authigenic carbonate precipitated in sediments, questions about the fidelity of chronostratigraphic correlations will remain. Authigenic events are likely to be broadly correlative owing to global changes in surface redox conditions, surface saturation state, and/or eustatic sea level, all of which might drive a migration of the zone of authigenesis or a change in the amount of authigenic precipitation, but detailed correlations at finer scales may prove less reliable.

Including a third major sink for carbon in sedimentary reservoirs does not sever the connection between  $\delta^{13}\text{C}_{\text{carb}}$  and the redox evolution of the Earth surface, but it does imply a more complex relationship. Rather than massive changes in atmospheric  $\text{O}_2$  and  $\text{CO}_2$ , our framework explains the large variations in  $\delta^{13}\text{C}_{\text{carb}}$  in terms of changes in the amount of authigenic carbonate driven perhaps by small changes in atmospheric  $\text{O}_2$  but potentially also by changes in the other redox budgets ( $\text{SO}_4$  and Fe), in the strength or even existence of a lysocline, or in the focusing of organic carbon burial in different sedimentary environments. With this new framework, the challenge remains to use the geologic record to understand the driving forces and events that have shaped Earth's surface.

#### References and Notes

- H. C. Urey, *Science* **108**, 489 (1948).
- W. S. Broecker, *J. Geophys. Res.* **75**, 3553 (1970).
- The inputs of carbon to Earth's surface carbon reservoirs include the return flux of  $\text{CO}_2$  from subduction or metamorphic release of carbon from carbonate and organic matter, the outgassing of mantle carbon, and the weathering of carbonate and organic matter. For a more complete discussion, see (39).
- A. H. Knoll, J. M. Hayes, A. J. Kaufman, K. Swett, I. B. Lambert, *Nature* **321**, 832 (1986).
- J. M. Hayes, H. Strauss, A. J. Kaufman, *Chem. Geol.* **161**, 103 (1999).
- R. A. Berner, *Am. J. Sci.* **309**, 603 (2009).
- L. R. Kump *et al.*, *Science* **334**, 1694 (2011).
- M. R. Saltzman *et al.*, *Proc. Natl. Acad. Sci. U.S.A.* **108**, 3876 (2011).
- F. A. Macdonald *et al.*, *Science* **327**, 1241 (2010).
- G. P. Halverson, P. F. Hoffman, D. P. Schrag, A. C. Maloof, A. H. N. Rice, *Geol. Soc. Am. Bull.* **117**, 1181 (2005).
- D. C. Catling, M. W. Claire, *Earth Planet. Sci. Lett.* **237**, 1 (2005).
- T. F. Bristow, M. J. Kennedy, *Geology* **36**, 863 (2008).
- D. P. Schrag, R. A. Berner, P. F. Hoffman, G. P. Halverson, *Geochem. Geophys. Geosyst.* **3**, 1036 (2002).
- C. J. Bjerrum, D. E. Canfield, *Proc. Natl. Acad. Sci. U.S.A.* **108**, 5542 (2011).
- T. H. Naehr *et al.*, *Deep Sea Res. Part II Top. Stud. Oceanogr.* **54**, 1268 (2007).
- H. H. Roberts, P. Aharon, *Geo-Mar. Lett.* **14**, 135 (1994).
- P. Meister *et al.*, *Sedimentology* **54**, 1007 (2007).
- C. E. Reimers, K. C. Ruttenberg, D. E. Canfield, M. B. Christiansen, J. B. Martin, *Geochim. Cosmochim. Acta* **60**, 4037 (1996).
- L. G. Anderson, D. Dyrssen, J. Skei, *Mar. Chem.* **20**, 361 (1987).
- Z. Zhu, R. C. Aller, J. Mak, *Cont. Shelf Res.* **22**, 2065 (2002).
- R. C. Aller, N. E. Blair, Q. Xia, P. D. Rude, *Cont. Shelf Res.* **16**, 753 (1996).
- N. Chow, S. Morad, I. S. Al-Aasm, *J. Sediment. Res.* **70**, 682 (2000).
- J. A. Higgins, W. W. Fischer, D. P. Schrag, *Earth Planet. Sci. Lett.* **284**, 25 (2009).
- A. Prokoph, G. A. Shields, J. Veizer, *Earth Sci. Rev.* **87**, 113 (2008).
- G. Jiang, A. J. Kaufman, N. Christie-Blick, S. Zhang, H. Wu, *Earth Planet. Sci. Lett.* **261**, 303 (2007).
- B. Shen *et al.*, *Geochim. Cosmochim. Acta* **75**, 1357 (2011).
- Bjerrum and Canfield (40) derived a similar expression for the addition of carbonate derived from carbonatization reactions in seafloor basalt. The mathematical expression is identical, but the isotopic fractionation for carbonatization is much smaller and hence provides a much smaller lever to affect the global carbon isotope mass balance. A more complete expression would include separate terms for carbonate in carbonatized basalts as well, provided that they represent removal of carbon from seawater rather than carbon from volcanic outgassing that was never counted in the surface budget.
- O. Sivan, D. P. Schrag, R. W. Murray, *Geobiology* **5**, 141 (2007).
- J. P. Grotzinger, D. A. Fike, W. W. Fischer, *Nat. Geosci.* **4**, 285 (2011).
- D. T. Johnston, F. A. Macdonald, B. C. Gill, P. F. Hoffman, D. P. Schrag, *Nature* **483**, 320 (2012).
- The absence of covariation of the  $\delta^{13}\text{C}$  of organic carbon may also be explained by contamination with a secondary component, such as detrital organic carbon (30).
- L. A. Derry, *Earth Planet. Sci. Lett.* **294**, 152 (2010).
- L. P. Knauth, M. J. Kennedy, *Nature* **460**, 728 (2009).
- S. M. A. Duguid, T. K. Kyser, N. P. James, E. C. Rankey, *J. Sediment. Res.* **80**, 236 (2010).
- A. C. Maloof *et al.*, *Geol. Soc. Am. Bull.* **122**, 1731 (2010).
- J. L. Payne *et al.*, *Science* **305**, 506 (2004).
- A. H. Knoll, J. A. Babcock, J. L. Payne, S. B. Pruss, W. W. Fischer, *Earth Planet. Sci. Lett.* **256**, 295 (2007).
- K. M. Meyer, M. Yu, A. B. Jost, B. M. Kelley, J. L. Payne, *Earth Planet. Sci. Lett.* **302**, 378 (2011).
- J. M. Hayes, J. R. Waldbauer, *Phil. Trans. R. Soc. B* **361**, 931 (2006).
- C. J. Bjerrum, D. E. Canfield, *Geochem. Geophys. Geosys.* **5**, Q08001 (2004).

**Acknowledgments:** The paper benefited from reviews from J. Hayes, R. Aller, and an anonymous reviewer. The authors acknowledge P. Hoffman for his helpful comments. This work was supported by NSF grant OCE-0961372 to D.P.S. and a Canadian Institute for Advanced Research Junior Fellowship to J.A.H. D.P.S. also thanks the Henry and Wendy Breck Foundation for support.

31 August 2012; accepted 12 December 2012  
10.1126/science.1229578

## Variable Clonal Repopulation Dynamics Influence Chemotherapy Response in Colorectal Cancer

Antonija Kreso,<sup>1,2\*</sup> Catherine A. O'Brien,<sup>1,3\*</sup> Peter van Galen,<sup>1</sup> Olga I. Gan,<sup>1</sup> Faiyaz Notta,<sup>1,2</sup> Andrew M. K. Brown,<sup>4</sup> Karen Ng,<sup>4</sup> Jing Ma,<sup>5</sup> Erno Wienholds,<sup>1</sup> Cyrille Dunant,<sup>6</sup> Aaron Pollett,<sup>7</sup> Steven Gallinger,<sup>8</sup> John McPherson,<sup>4</sup> Charles G. Mullighan,<sup>5</sup> Darryl Shibata,<sup>9</sup> John E. Dick<sup>1,2,†</sup>

Intratumoral heterogeneity arises through the evolution of genetically diverse subclones during tumor progression. However, it remains unknown whether cells within single genetic clones are functionally equivalent. By combining DNA copy number alteration (CNA) profiling, sequencing, and lentiviral lineage tracking, we followed the repopulation dynamics of 150 single lentivirus-marked lineages from 10 human colorectal cancers through serial xenograft passages in mice. CNA and mutational analysis distinguished individual clones and showed that clones remained stable upon serial transplantation. Despite this stability, the proliferation, persistence, and chemotherapy tolerance of lentivirally marked lineages were variable within each clone. Chemotherapy promoted the dominance of previously minor or dormant lineages. Thus, apart from genetic diversity, tumor cells display inherent functional variability in tumor propagation potential, which contributes to both cancer growth and therapy tolerance.

Cancer is sustained by production of aberrant cells that vary in many morphological and physiological properties. This cellular diversity remains a major challenge to our understanding of the neoplastic process and therapeutic resistance. Genetic and nongenetic processes can generate heterogeneity; however, the degree of coordination between these mechanisms and their relative contribution to tumor propagation remains unresolved.

Tumor cell diversity can arise through accrued genetic changes (1) that result in single tumors composed of many subclones that develop through complex evolutionary trajectories (2, 3). As well, tumors contain genetic subclones that vary with respect to differential growth in xenograft assays (4–6), recurrence (7), and metastatic potential (8, 9). Likewise, resistance to cancer therapies can arise through genetic mutations (10, 11).

A prominent but transient authigenic carbonate sink may also help explain carbon isotope variations in the Paleozoic (8, 35) and Early Triassic (36). In the Triassic, for example, there is evidence for widespread anoxia in intermediate waters (37), fluctuating  $\delta^{13}\text{C}_{\text{carb}}$  values ( $-2$  to  $+8\text{‰}$ ), and gradients in the  $\delta^{13}\text{C}_{\text{carb}}$  values with depth, often with  $\delta^{13}\text{C}$  values on the slope 2 to 3‰ lighter than those on the shelf (38). We view the Early Triassic as a candidate for a period of sustained, high authigenic carbonate formation, like much of the Neoproterozoic (23). The fluctuations could be produced either from a change in the global amount of authigenic carbonate (category 1) or by migration in the zone of authigenic carbonate (category 2). In the Early Cambrian, similar fluctuations in the authigenic carbonate sink might have resulted from more modest variations in surface redox or evolutionary leaps such as the biological irrigation of sediments.

The recognition of authigenic carbonate in the sedimentary record presents a challenge for carbon isotope stratigraphy because it allows for local variations in  $\delta^{13}\text{C}_{\text{carb}}$  produced by the addition of a substantial authigenic component after burial. Until there is a clear way to quantify the amount of marine carbonate precipitated in the water column relative to authigenic carbonate precipitated in sediments, questions about the fidelity of chronostratigraphic correlations will remain. Authigenic events are likely to be broadly correlative owing to global changes in surface redox conditions, surface saturation state, and/or eustatic sea level, all of which might drive a migration of the zone of authigenesis or a change in the amount of authigenic precipitation, but detailed correlations at finer scales may prove less reliable.

Including a third major sink for carbon in sedimentary reservoirs does not sever the connection between  $\delta^{13}\text{C}_{\text{carb}}$  and the redox evolution of the Earth surface, but it does imply a more complex relationship. Rather than massive changes in atmospheric  $\text{O}_2$  and  $\text{CO}_2$ , our framework explains the large variations in  $\delta^{13}\text{C}_{\text{carb}}$  in terms of changes in the amount of authigenic carbonate driven perhaps by small changes in atmospheric  $\text{O}_2$  but potentially also by changes in the other redox budgets ( $\text{SO}_4$  and Fe), in the strength or even existence of a lysocline, or in the focusing of organic carbon burial in different sedimentary environments. With this new framework, the challenge remains to use the geologic record to understand the driving forces and events that have shaped Earth's surface.

#### References and Notes

- H. C. Urey, *Science* **108**, 489 (1948).
- W. S. Broecker, *J. Geophys. Res.* **75**, 3553 (1970).
- The inputs of carbon to Earth's surface carbon reservoirs include the return flux of  $\text{CO}_2$  from subduction or metamorphic release of carbon from carbonate and organic matter, the outgassing of mantle carbon, and the weathering of carbonate and organic matter. For a more complete discussion, see (39).
- A. H. Knoll, J. M. Hayes, A. J. Kaufman, K. Swett, I. B. Lambert, *Nature* **321**, 832 (1986).
- J. M. Hayes, H. Strauss, A. J. Kaufman, *Chem. Geol.* **161**, 103 (1999).
- R. A. Berner, *Am. J. Sci.* **309**, 603 (2009).
- L. R. Kump *et al.*, *Science* **334**, 1694 (2011).
- M. R. Saltzman *et al.*, *Proc. Natl. Acad. Sci. U.S.A.* **108**, 3876 (2011).
- F. A. Macdonald *et al.*, *Science* **327**, 1241 (2010).
- G. P. Halverson, P. F. Hoffman, D. P. Schrag, A. C. Maloof, A. H. N. Rice, *Geol. Soc. Am. Bull.* **117**, 1181 (2005).
- D. C. Catling, M. W. Claire, *Earth Planet. Sci. Lett.* **237**, 1 (2005).
- T. F. Bristow, M. J. Kennedy, *Geology* **36**, 863 (2008).
- D. P. Schrag, R. A. Berner, P. F. Hoffman, G. P. Halverson, *Geochem. Geophys. Geosyst.* **3**, 1036 (2002).
- C. J. Bjerrum, D. E. Canfield, *Proc. Natl. Acad. Sci. U.S.A.* **108**, 5542 (2011).
- T. H. Naehr *et al.*, *Deep Sea Res. Part II Top. Stud. Oceanogr.* **54**, 1268 (2007).
- H. H. Roberts, P. Aharon, *Geo-Mar. Lett.* **14**, 135 (1994).
- P. Meister *et al.*, *Sedimentology* **54**, 1007 (2007).
- C. E. Reimers, K. C. Ruttenberg, D. E. Canfield, M. B. Christiansen, J. B. Martin, *Geochim. Cosmochim. Acta* **60**, 4037 (1996).
- L. G. Anderson, D. Dyrssen, J. Skei, *Mar. Chem.* **20**, 361 (1987).
- Z. Zhu, R. C. Aller, J. Mak, *Cont. Shelf Res.* **22**, 2065 (2002).
- R. C. Aller, N. E. Blair, Q. Xia, P. D. Rude, *Cont. Shelf Res.* **16**, 753 (1996).
- N. Chow, S. Morad, I. S. Al-Aasm, *J. Sediment. Res.* **70**, 682 (2000).
- J. A. Higgins, W. W. Fischer, D. P. Schrag, *Earth Planet. Sci. Lett.* **284**, 25 (2009).
- A. Prokoph, G. A. Shields, J. Veizer, *Earth Sci. Rev.* **87**, 113 (2008).
- G. Jiang, A. J. Kaufman, N. Christie-Blick, S. Zhang, H. Wu, *Earth Planet. Sci. Lett.* **261**, 303 (2007).
- B. Shen *et al.*, *Geochim. Cosmochim. Acta* **75**, 1357 (2011).
- Bjerrum and Canfield (40) derived a similar expression for the addition of carbonate derived from carbonatization reactions in seafloor basalt. The mathematical expression is identical, but the isotopic fractionation for carbonatization is much smaller and hence provides a much smaller lever to affect the global carbon isotope mass balance. A more complete expression would include separate terms for carbonate in carbonatized basalts as well, provided that they represent removal of carbon from seawater rather than carbon from volcanic outgassing that was never counted in the surface budget.
- O. Sivan, D. P. Schrag, R. W. Murray, *Geobiology* **5**, 141 (2007).
- J. P. Grotzinger, D. A. Fike, W. W. Fischer, *Nat. Geosci.* **4**, 285 (2011).
- D. T. Johnston, F. A. Macdonald, B. C. Gill, P. F. Hoffman, D. P. Schrag, *Nature* **483**, 320 (2012).
- The absence of covariation of the  $\delta^{13}\text{C}$  of organic carbon may also be explained by contamination with a secondary component, such as detrital organic carbon (30).
- L. A. Derry, *Earth Planet. Sci. Lett.* **294**, 152 (2010).
- L. P. Knauth, M. J. Kennedy, *Nature* **460**, 728 (2009).
- S. M. A. Duguid, T. K. Kyser, N. P. James, E. C. Rankey, *J. Sediment. Res.* **80**, 236 (2010).
- A. C. Maloof *et al.*, *Geol. Soc. Am. Bull.* **122**, 1731 (2010).
- J. L. Payne *et al.*, *Science* **305**, 506 (2004).
- A. H. Knoll, J. A. Babcock, J. L. Payne, S. B. Pruss, W. W. Fischer, *Earth Planet. Sci. Lett.* **256**, 295 (2007).
- K. M. Meyer, M. Yu, A. B. Jost, B. M. Kelley, J. L. Payne, *Earth Planet. Sci. Lett.* **302**, 378 (2011).
- J. M. Hayes, J. R. Waldbauer, *Phil. Trans. R. Soc. B* **361**, 931 (2006).
- C. J. Bjerrum, D. E. Canfield, *Geochem. Geophys. Geosys.* **5**, Q08001 (2004).

**Acknowledgments:** The paper benefited from reviews from J. Hayes, R. Aller, and an anonymous reviewer. The authors acknowledge P. Hoffman for his helpful comments. This work was supported by NSF grant OCE-0961372 to D.P.S. and a Canadian Institute for Advanced Research Junior Fellowship to J.A.H. D.P.S. also thanks the Henry and Wendy Breck Foundation for support.

31 August 2012; accepted 12 December 2012  
10.1126/science.1229578

## Variable Clonal Repopulation Dynamics Influence Chemotherapy Response in Colorectal Cancer

Antonija Kreso,<sup>1,2\*</sup> Catherine A. O'Brien,<sup>1,3\*</sup> Peter van Galen,<sup>1</sup> Olga I. Gan,<sup>1</sup> Faiyaz Notta,<sup>1,2</sup> Andrew M. K. Brown,<sup>4</sup> Karen Ng,<sup>4</sup> Jing Ma,<sup>5</sup> Erno Wienholds,<sup>1</sup> Cyrille Dunant,<sup>6</sup> Aaron Pollett,<sup>7</sup> Steven Gallinger,<sup>8</sup> John McPherson,<sup>4</sup> Charles G. Mullighan,<sup>5</sup> Darryl Shibata,<sup>9</sup> John E. Dick<sup>1,2,†</sup>

Intratumoral heterogeneity arises through the evolution of genetically diverse subclones during tumor progression. However, it remains unknown whether cells within single genetic clones are functionally equivalent. By combining DNA copy number alteration (CNA) profiling, sequencing, and lentiviral lineage tracking, we followed the repopulation dynamics of 150 single lentivirus-marked lineages from 10 human colorectal cancers through serial xenograft passages in mice. CNA and mutational analysis distinguished individual clones and showed that clones remained stable upon serial transplantation. Despite this stability, the proliferation, persistence, and chemotherapy tolerance of lentivirally marked lineages were variable within each clone. Chemotherapy promoted the dominance of previously minor or dormant lineages. Thus, apart from genetic diversity, tumor cells display inherent functional variability in tumor propagation potential, which contributes to both cancer growth and therapy tolerance.

Cancer is sustained by production of aberrant cells that vary in many morphological and physiological properties. This cellular diversity remains a major challenge to our understanding of the neoplastic process and therapeutic resistance. Genetic and nongenetic processes can generate heterogeneity; however, the degree of coordination between these mechanisms and their relative contribution to tumor propagation remains unresolved.

Tumor cell diversity can arise through accrued genetic changes (1) that result in single tumors composed of many subclones that develop through complex evolutionary trajectories (2, 3). As well, tumors contain genetic subclones that vary with respect to differential growth in xenograft assays (4–6), recurrence (7), and metastatic potential (8, 9). Likewise, resistance to cancer therapies can arise through genetic mutations (10, 11).



These and other studies substantiate the widely accepted view that tumors comprise genetically diverse subclones, some of which survive therapy and contribute to disease recurrence.

In the absence of differences at the level of genetic mutation, heterogeneity within a population of tumor cells can still exist, but the mechanisms remain incompletely understood. For example, the bidirectional interaction between tumor cells and the microenvironment can influence tumor phenotype (12). Other processes have also been proposed, including interconvertible activation of Rac and Rho guanosine triphosphatases (13), metastable configurations of intracellular networks (14, 15), and altered epigenetic states (16). These studies collectively indicate that in apparently homogeneous *in vitro* environments, cells of the same genotype can exist in different states that influence their behavior (17). The detection of *in vitro* cellular diversity, which is not coupled to genetic diversity, underscores the need to investigate the extent of intraclonal functional heterogeneity *in vivo* and in primary human cancers.

Arguably the most important function of any cancer clone is to maintain long-term tumor propagation. For many tumors, only a minority of cells are able to sustain tumor growth, although such cells can constitute the majority of tumor cells for some cancer types (18, 19). Whether these cells are part of one genetic clone or are derived from distinct genetic subclones remains to be determined. Moreover, whether tumor-propagating cells of a single genetic clone are all equivalent or whether there is functional variability among individual tumor cells is uncertain. Addressing these questions requires genetic analyses combined with functional assays that measure tumor propagation at the resolution of individual clones derived from single cells.

**Clonal stability is maintained through serial tumor transplantation.** To explore the relative contribution of genetic and nongenetic mechanisms to the functional heterogeneity of single human cancer cells that are capable of long-term clonal propagation, we used an *in vivo* xenotransplantation assay. The fates of single cell-derived lineages were tracked from 10 primary human colorectal cancers (CRCs; table S1). To facilitate clonal tracking, we transduced patient-

derived CRC cells with a green fluorescent protein (GFP)-expressing lentivirus and injected the cells into the renal capsule of immunodeficient mice (supplementary text and tables S2 and S3). Transduced cells efficiently generated xenografts, and GFP expression in the xenografts remained stable over serial transplantation (figs. S1 and S2). The average time to palpable tumor formation ( $99 \pm 18$  days) was stable over serial transplants (Fig. 1A), and xenografts maintained patient tumor characteristics (figs. S3 to S5). Genomic profiling of three patient tumors and corresponding xenografts using copy number alteration (CNA) analysis (Fig. 1B, figs. S6 and S7, and table S4) and targeted deep sequencing of 660 mutational hotspots in 42 genes (Fig. 1C and tables S5 to S7) established that xenografts largely retained the genomic profile of the primary tumor sample. Several CNAs and single-nucleotide variants (SNVs) were enriched in primary 1° xenografts from some samples, consistent with selection of a subclone from the patient tumor. Genomic analysis of subsequent xenograft transplants, encompassing 393 days (patient sample CT38), 341 days (CT54), and 261 days (CT59) of total tumor growth, demonstrated that the majority of genomic lesions detected in 1° xenografts were recapitulated upon serial passage (supplementary text). Exome sequencing of CT38 and its corresponding 1°, 2°, and 4° xenografts supported these findings (supplementary text, figs. S8 and S9, and tables S8 to S11). Finally, analysis of methylation pattern diversity of patient tumors and their corresponding xenografts indicated that population diversity was maintained over serial passage (supplementary text and fig. S10). Collectively, these data indicate that the CRC clones that are selected in the xenograft remain stable over sequential transplantation.

**Variation in clonal dynamics of CRC cells.** To evaluate the repopulation kinetics of multiple single cell-derived clones within a primary human tumor, we used lentiviral marking to track the progeny of single CRC cells (henceforth termed “LV clones” to distinguish them from genetic clones) over serial xenografts. To facilitate qualitative and quantitative characterization, we developed a system for establishing clonal identity and then classifying clonal behavior according to persistence, absence, or emergence across multiple recipients (see supplementary text). Rather than relying on the polymerase chain reaction, our detection strategy focused on the identification of LV clones that possessed robust clonal expansion capacity.

We observed five distinct behaviors. LV clones that were present in all serial transplants were termed type I or persistent clones (Fig. 2A, purple arrowhead). LV clones that did not persist but exhausted before reaching the final passage had less potent tumor-propagating ability relative to type I clones; these were termed type II or short-term clones (Fig. 2A, blue arrowhead). Finally, we observed LV clones that lacked tumor-propagating ability because they were only detected in the 1° recipient and were not detected in 2° and subse-

quent recipients (Fig. 2A, green arrowhead); these were termed type III or transient clones. In 10 patient samples, out of a total of 150 marked clones, we tracked 34 type I, 33 type II, and 31 type III clones (Fig. 2B), which suggests that there is substantial functional diversity with respect to clonal longevity in successive tumor transplants.

In addition to heterogeneity in longevity, we also observed dynamic behaviors in 34 of the 150 marked clones. These LV clones were initially below detection limits (approximately  $10^4$  cells/tumor) in the 1° recipients but could be identified at later transplants (Fig. 2A, red arrowhead). Because the xenograft assay monitors the output of “active” CRC cells, these type IV or resting LV clones were likely produced by CRC cells that initially were dormant or slowly proliferated but became activated in later transplants, resulting in the generation of a measurable clone. Finally, LV clones whose progeny appeared early, then became undetectable in a subsequent transplant, only to reappear at a later time point (Fig. 2A, orange arrowhead) were termed type V or fluctuating clones. Such LV clones displayed extensive but intermittent proliferation distinct from the continuous rapid proliferation of type I clones; we observed 18 examples of type V clones (Fig. 2B). Overall, these results show that not all CRC cells with the potential for tumor propagation actually function and contribute to tumor growth at any given time. Such cells can become activated at later time points.

It is noteworthy that LV clones can remain undetected for 2 to 4 months while being diluted by a factor of  $>100$  during consecutive transplants and then recur to dominate tumor growth (supplementary text and fig. S11). Whereas random growth dynamics would predict dilution of minor LV clones over multiple transplants, the frequent detection of type IV and V clones indicates that the behaviors we observe cannot be solely attributed to dilution over time or stochasticity in LV clonal behaviors. Further, mathematical modeling also predicted that LV clonal emergence correlates with changes in tumor structure and that newly appearing clones are functionally distinct from active clones, although it did raise uncertainty as to whether types I, II, and III are distinct or whether stochastic processes related to the transplantation method may contribute to clonal loss (supplementary text and fig. S12). The distinct proliferative kinetics of the five LV clonal behaviors we observed underscore the functional variability of individual cells (Fig. 2C). Each LV clone type was identified in four or more patient samples (Fig. 2D and fig. S13), establishing that the varied clonal behaviors are reproducibly found in primary CRC from a spectrum of patients. Given the absence of accompanying changes in CNAs and SNVs with serial transplantation, our data provide evidence for functional heterogeneity between individual tumor-propagating cells that share a common genetic lineage.

The genetic analysis across xenografts was carried out on bulk tumor cell populations, where clonal marking tracked the functional behavior

<sup>1</sup>Campbell Family Institute, Ontario Cancer Institute, Princess Margaret Cancer Centre, University Health Network, Toronto, Ontario M5G 1L7, Canada. <sup>2</sup>Department of Molecular Genetics, University of Toronto, Toronto, Ontario M5G 1L7, Canada. <sup>3</sup>Department of Laboratory Medicine and Pathobiology and Department of Surgery, University of Toronto, Toronto, Ontario M5L 1F4, Canada. <sup>4</sup>Ontario Institute for Cancer Research, Toronto, Ontario M5G 1L7, Canada. <sup>5</sup>St. Jude Children's Hospital, Memphis, TN 38105, USA. <sup>6</sup>Department of Civil Engineering, University of Toronto, Toronto, Ontario M5S 1A4, Canada. <sup>7</sup>Department of Pathology, Mount Sinai Hospital, Toronto, Ontario M5G 1X5, Canada. <sup>8</sup>Fred Litwin Centre for Cancer Genetics, Samuel Lunenfeld Research Institute, Mount Sinai Hospital, Toronto, Ontario M7H 2B9, Canada. <sup>9</sup>University of Southern California Keck School of Medicine, Los Angeles, CA 90089, USA.

\*These authors contributed equally to this work.

†To whom correspondence should be addressed. E-mail: jdick@uhnres.utoronto.ca

of single cells. The experimental design of genomically analyzing bulk tumor does not directly evaluate the genomic properties of each individual functionally distinct LV clone type that is present. To directly compare the genomes of distinct LV clone types from an individual tumor, we used a limiting dilution approach to isolate different LV clones and used deep sequencing of mutational hotspots to compare their mutational load. We compared the mutational hotspots between tumors generated by a type I and type V clone from CT38 and a type I and type II clone from CT59. For CT38, a linear correlation between the SNV frequencies of the type I- and type V-derived tumors was seen (fig. S14A and table S12). Likewise, for CT59, type I- and type

II-derived tumors also demonstrated similar SNV frequencies in all analyzed SNVs, including the nine somatically acquired SNVs (fig. S14B and table S13). Thus, for both CT38 and CT59, the frequency of analyzed hotspot mutations was congruent between tumors generated by single LV clones, which were derived from distinct clone types (type I and V for CT38; type I and II for CT59). Analyzing tumors generated from single cells enabled us to determine that distinct clone types within a tumor sample share similar mutational patterns as assessed by targeted sequencing. These data, together with the CNA and targeted sequencing analysis of the bulk tumor, provide further evidence for the existence of functionally distinct LV clones within a genetic lineage in CRC.

### Variable response of LV clones to oxaliplatin.

The existence of functionally heterogeneous CRC cells prompted us to investigate whether these cells might also intrinsically differ in response to therapy. We examined the effect of a commonly used chemotherapy drug, oxaliplatin, on the dynamics of LV clones. We used established xenografts of five patient samples for which the LV clone types had already been curated. In parallel with the serial transplantation of untreated recipient mice described above, three to five additional mice were transplanted with tumor cells and systemically treated with oxaliplatin once tumors were established, allowing assessment of the effects of drug treatment on steady-state clonal distribution (fig. S15A). Although oxaliplatin

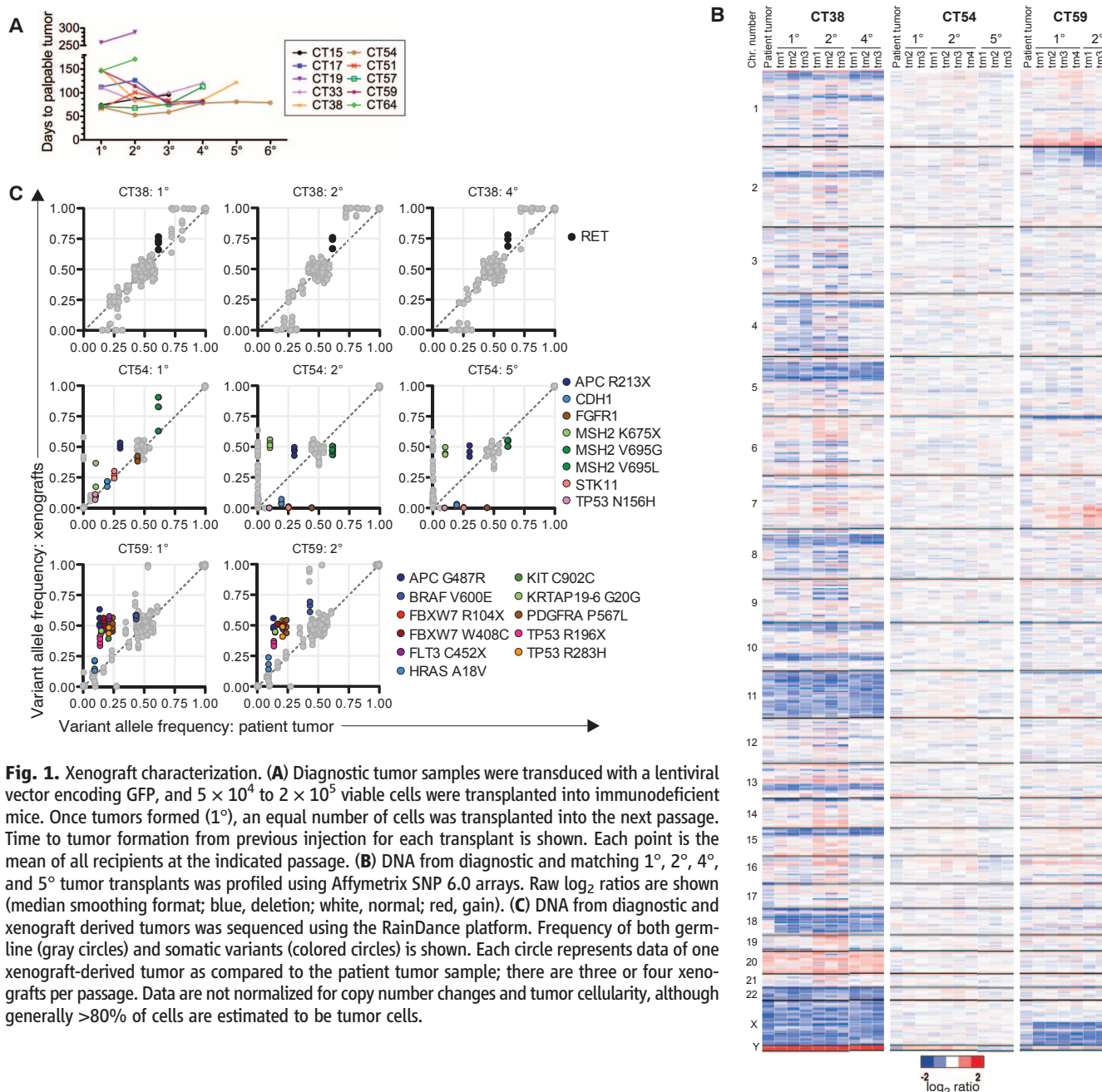


**Fig. 1. Xenograft characterization.** (A) Diagnostic tumor samples were transduced with a lentiviral vector encoding GFP, and  $5 \times 10^4$  to  $2 \times 10^5$  viable cells were transplanted into immunodeficient mice. Once tumors formed (1°), an equal number of cells was transplanted into the next passage. Time to tumor formation from previous injection for each transplant is shown. Each point is the mean of all recipients at the indicated passage. (B) DNA from diagnostic and matching 1°, 2°, 4°, and 5° tumor transplants was profiled using Affymetrix SNP 6.0 arrays. Raw log<sub>2</sub> ratios are shown (median smoothing format; blue, deletion; white, normal; red, gain). (C) DNA from diagnostic and xenograft derived tumors was sequenced using the RainDance platform. Frequency of both germline (gray circles) and somatic variants (colored circles) is shown. Each circle represents data of one xenograft-derived tumor as compared to the patient tumor sample; there are three or four xenografts per passage. Data are not normalized for copy number changes and tumor cellularity, although generally >80% of cells are estimated to be tumor cells.



treatment reduced tumor burden (figs. S15B and S16A), there was no apparent change in the absolute number of marked clones (fig. S15C), nor were the proportions of clone types significantly altered (figs. S15D and S17).

To determine whether treatment with oxaliplatin affected CRC cells with tumor propagation capability, we serially transplanted equal numbers of viable cells from both the control and treatment groups into secondary mice that were left untreated. Across five patient samples, a total of 60 secondary recipients were transplanted with tumor cells from oxaliplatin-treated xenografts (31 control and 29 oxaliplatin-treated). We observed a reduction in tumor weight (Fig. 3A and fig. S16B), as well as a trend toward a decrease in the absolute number of clones (Fig. 3B), in un-

treated secondary recipients transplanted with cells from oxaliplatin-treated xenografts versus sham-treated control cells; these results suggested that drug treatment altered the growth properties of the regrown tumor. For two samples (CT33 and CT57), GFP-expressing tumor tissue was not detected in the secondary recipients that were transplanted with oxaliplatin-treated cells, which precluded lentiviral insertion site analysis. For the remaining three patient samples (CT17, CT38, and CT54), major changes in the proportion of LV clone types occurred in xenografts derived from the oxaliplatin-treated group relative to control xenografts (Fig. 3C). The proportion of type I persistent clones was reduced, whereas LV clones that were below the detection limit in primary recipients appeared in secondary recipients transplanted with oxaliplatin-

treated tumors (Fig. 3D; Fig. 3E, arrowheads to the right). These new LV clones were classified as type IV because they were not consistently detected in control or oxaliplatin-treated tumors in preceding mice. When considering the absolute numbers of different LV clone types over the complete set of secondary mice, 84 type I clones were observed in mice transplanted with untreated control cells and 27 type I clones in mice transplanted with oxaliplatin-treated cells (Fig. 3D). By contrast, 12 type IV clones were detected in the control group versus 40 type IV clones in the oxaliplatin-treated group. These data indicate that the response of individual CRC cells to standard chemotherapy is markedly variable. Despite eradication of some persistent LV clones, resting or slowly proliferating CRC cells can endure

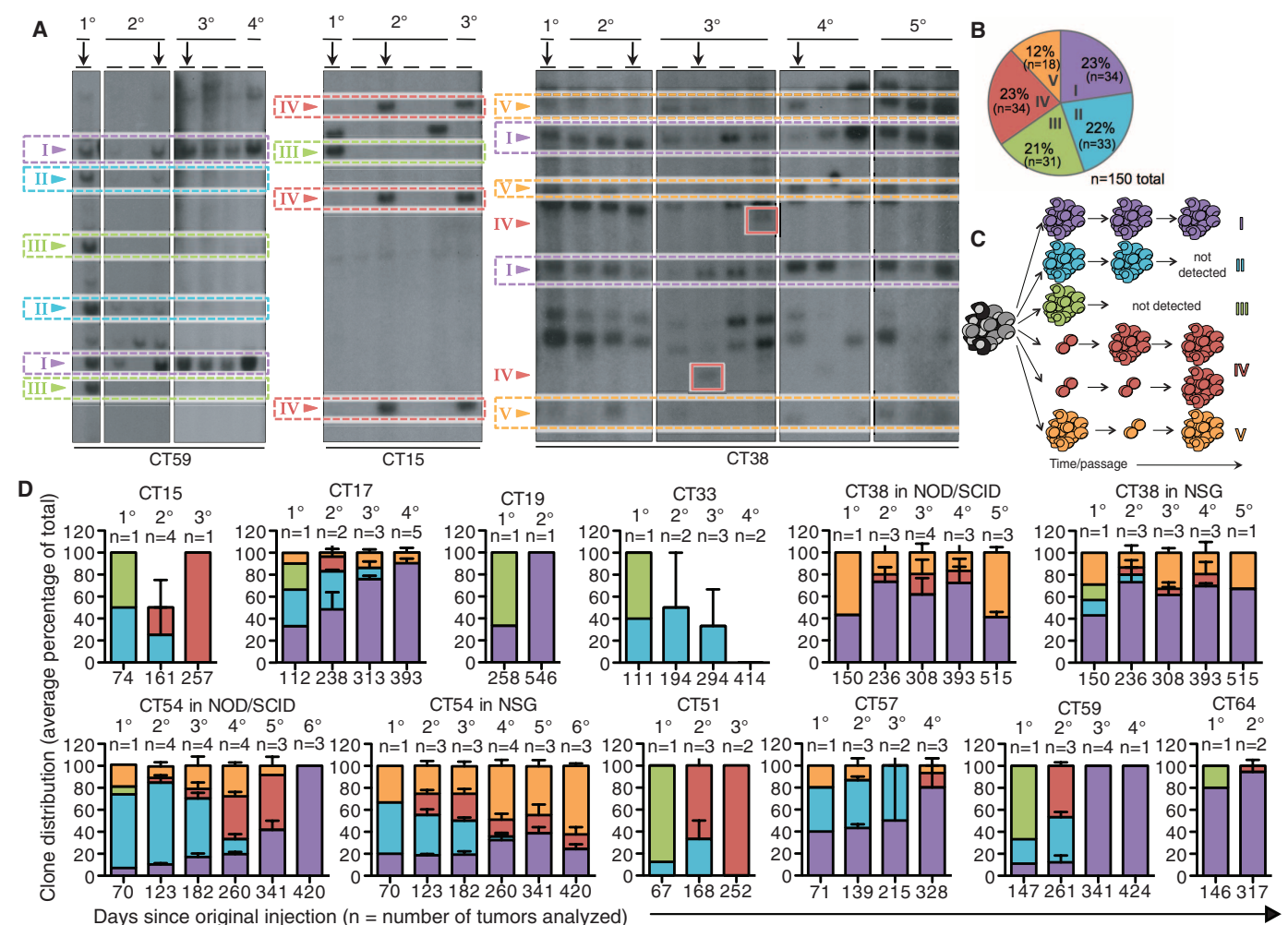


**Fig. 2.** Variation in repopulation potential of individual lentivirally-marked CRC cells. **(A)** DNA from xenografts (one tumor per lane) of various transplants (denoted by 1°, 2°, ..., 5°) was analyzed using Southern blotting with a GFP probe. Arrows above certain lanes indicate the tumor that was retransplanted into the next set of mice. Colored arrowheads indicate representative examples of different lentivirally marked (LV) clone types. **(B)** Pie chart showing the sum of each of the five LV clone types observed over all experiments. **(C)** Schematic illustrating the different types of LV clonal behaviors. LV clones were classified on the basis of detection in serial transplants; for example, a type IV clone would be below the detection limit initially and come up in later

transplants. **(D)** Charts showing the proportion of LV clone types for each patient sample, displayed as the averages of all mice per transplant. The proportion of each LV clone type was determined in every recipient mouse by dividing the number of times a particular LV clone type was observed by the total number of LV clones detected in that mouse, thereby normalizing for differential marking of samples. Next, the proportion of each LV clone type for all recipients per transplant was averaged, including recipients for which LV clones were not detected. Each bar is representative of the averaged data at a transplant, and error bars indicate SEM between the tumors; *n* denotes the number of tumors or recipients analyzed.

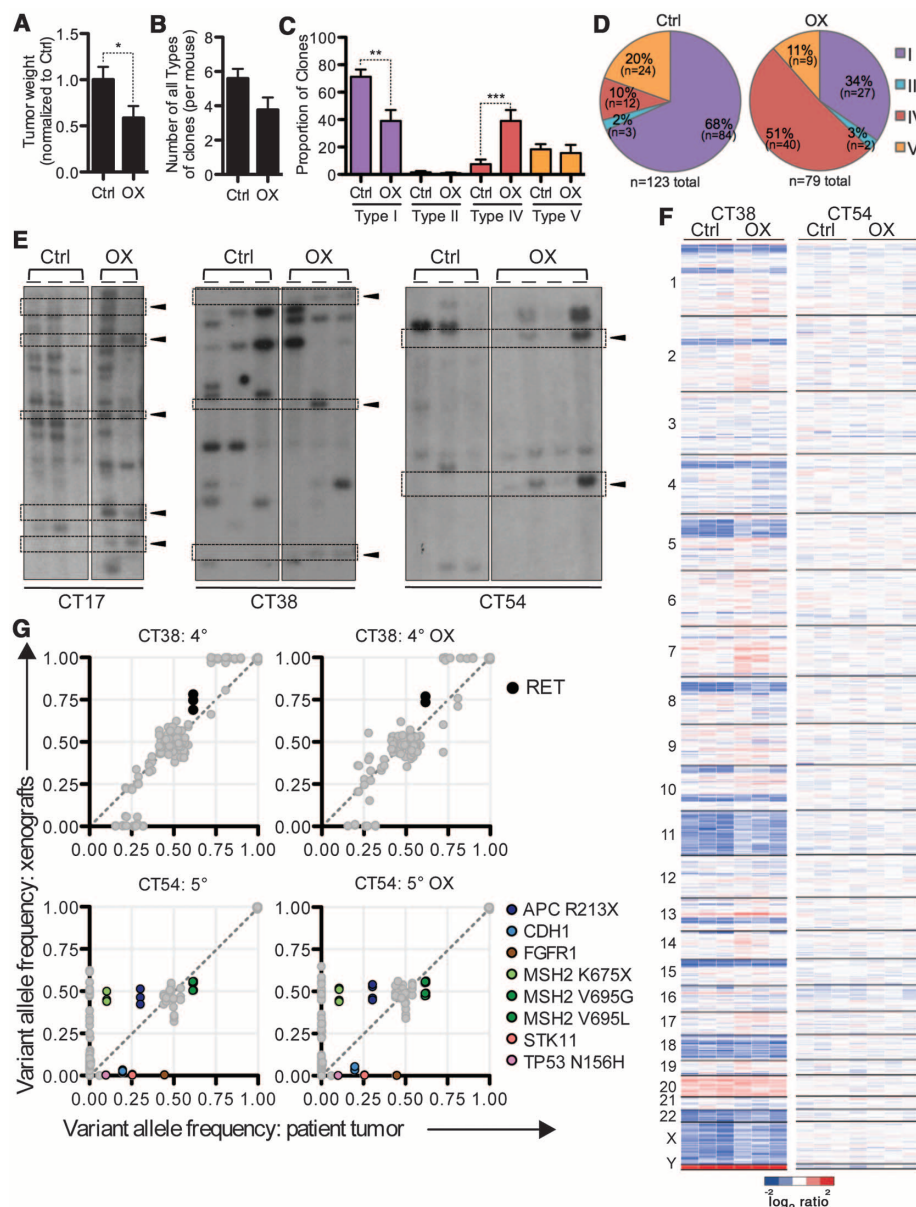


**Fig. 3.** Variable response of marked clones to oxaliplatin. Mice were either treated with phosphate-buffered saline (Ctrl) or oxaliplatin (OX) for 2 to 4 weeks and cells from these tumors were reinjected into mice, which did not receive further treatment. Once new tumors formed (about 100 days after reinjection), mice from both groups were killed and tumor weight was measured. **(A)** Previously OX-treated tumor weights were normalized to Ctrl tumor weights; data were pooled from five patient samples representing 31 Ctrl and 29 previously OX-treated samples. **(B)** Cumulative number of LV clones per mouse after transplantation of OX-treated tumors. **(C)** The proportion of LV clone types in tumors that were generated by reinjecting Ctrl and OX-treated tumors. LV clone types were assigned according to the behavior of individual clones across all transplants over the entire experiment. Data are means  $\pm$  SEM of pooled data from independent OX treatments using different patient samples; *P* values were calculated using two-tailed *t* test. **(D)** Pie chart showing the number of times the LV clone types were observed, represented as the sum of all experiments. **(E)** Southern blot showing the LV clonal makeup of tumors generated by reinjecting tumor cells from OX-treated recipients. Representative data from three patient samples are shown; solid arrowheads to the right of each experiment identify newly appearing LV clones in the previously OX-treated tumors. Each lane represents the DNA of one mouse. For comparative purposes, the Southern blot for CT38 Ctrl is the same as in Fig. 2A. **(F and G)** DNA from tumors that were generated by reinjecting Ctrl or OX-treated samples was analyzed using CNA arrays (F) or targeted deep sequencing (G). In (F), raw log<sub>2</sub> ratio copy number data are shown in median-smoothing format (blue, deletion; white, normal; red, gain). For comparative purposes, data for Ctrl in (F) and (G) are reproductions of 4° (CT38) and 5° (CT54) transplants from Fig. 1, B and C.

oxaliplatin treatment and reinitiate tumor growth, although such tumors are of smaller size. Interestingly, mathematical modeling predicted that the LV clonal landscape of post-treatment tumors was distinct from that of untreated samples (supplementary text and fig. S12).

To determine whether the altered clonal patterns after oxaliplatin treatment were due to major changes in genetic clones, we profiled DNA from control and oxaliplatin-treated tumors by genome-wide CNA analysis (Fig. 3F), targeted deep sequencing (Fig. 3G), and passenger methylation analysis (fig. S10). The results indicated that the CNAs, SNVs, and methylation pattern diversity of the oxaliplatin-treated group closely matched the control recipients (supplementary text). The absence of a detectable bottleneck or selection for novel genetic clones after chemotherapy treatment indicates that therapeutic tolerance is not always linked to the acquisition of new driver mutations. Instead, variable tumor propagation behavior of individual cells can represent a nongenetic determinant of tumor growth after therapy.

**Discussion.** Our findings establish that individual tumor cells within a uniform genetic lineage are functionally heterogeneous: They display extensive variation in growth dynamics, persistence through serial transplantation, and response to therapy. Not all functionally important cells contribute continuously to tumor growth; some are held in reserve, while others are able to oscillate between periods of dormancy and activity. This distinct intraclonal behavior affected response to conventional chemotherapy; actively proliferating progeny were preferentially eliminated, whereas the relatively dormant CRC cells became dominant during tumor reinitiation after chemotherapy. The intraclonal diversity in single-cell functional behavior of primary human CRC cells in vivo has the net effect of contributing to tumor growth during both homeostasis and therapy response.

Most tumors are expected to consist of genetically distinct subclones that contain different growth characteristics and will therefore read out differently in xenotransplantation assays (1). Similar to published work using CRC cells propagated in immunodeficient mice (20), we expanded and sequentially propagated CRC clones from different patient samples that remained stable upon serial transplantation, indicating that xenografting does not select for a significantly different tumor cell population between multiple recipients at each stage of serial transplant. Despite this stability, we observed reproducible differences in the functional fates of single marked CRC cells, indicating that in vivo dynamics of lentivirally tracked CRC clones are not driven by readily detectable genomic changes. This conclusion is supported by the genetic concordance between functionally distinct LV clone types within a single tumor isolated by limiting dilution. Thus, in addition to the widely accepted mechanism of tumor heterogeneity being driven by genetic diversity, other diversity-generating processes exist within a genetic clone. These processes endow cells with robust survival



potential, especially during stress. The contribution of diversity-generating mechanisms such as epigenetic regulation, noise in gene expression, or variability in the microenvironment (21, 22) may offer insight into CRC cell heterogeneity.

There is growing evidence of evolutionary selection for diversity-generating mechanisms in other disciplines, such as ecology (23, 24) and microbiology (25–27). For example, genetically homogeneous pools of single-cell prokaryotes display heterogeneity, where a small portion of cells naturally display drug resistance that is not caused by genetic mutation or acquisition of plasmids encoding antibiotic resistance genes. Rather, this phenomenon is due to mechanisms that reduce cell proliferation and induce a dormant nondividing state (28). We consistently observed a relatively dormant cell population in CRC, which suggests that cancer cells may take advantage of this “ancient” mechanism and use dormancy as an adaptive strategy during times of stress. We provide evidence for a relatively dormant or slowly proliferating cell population in primary human CRC cells that still retains potent tumor propagation potential, thereby preferentially driving tumor growth after chemotherapy. These findings may provide a biological basis for recurrent and metastatic disease following standard-of-care treatment (29). Our findings should focus efforts to uncover the molecular mechanisms driving chemotherapeutic tolerance in CRC cells.

The often unstated assumption in considering cellular response to stress is that cells react in a uniform manner to the inducing signal, because the classical techniques used bulk populations. However, averaging data across millions of cells has the effect of masking any heterogeneity that might exist at the single-cell level. Such con-

ventions are changing as methodological advances (30) are fueling a surge of interest in the processes governing cell-to-cell variability (14). By coupling genetic analysis to functional tumor growth assays, we find that when cells are tracked at single-cell resolution while still being part of a population of cancer cells, variable cellular behaviors can be detected. These observations set a precedent for future studies examining the basis of intracolon behavior of single cells, especially with respect to tumor propagation and other functional properties. In a broader sense, our findings reveal another layer of complexity, beyond genetic diversity, that drives the intratumoral heterogeneity of CRC. The prospect of understanding how genetic and non-genetic determinants interact to influence the functional diversity and therapy response for other cancers should drive future cancer research.

#### References and Notes

1. M. Greaves, C. C. Maley, *Nature* **481**, 306 (2012).
2. S. Nik-Zainal *et al.*; Breast Cancer Working Group of the International Cancer Genome Consortium, *Cell* **149**, 994 (2012).
3. M. Gerlinger *et al.*, *N. Engl. J. Med.* **366**, 883 (2012).
4. K. Anderson *et al.*, *Nature* **469**, 356 (2011).
5. F. Notta *et al.*, *Nature* **469**, 362 (2011).
6. E. Clappier *et al.*, *J. Exp. Med.* **208**, 653 (2011).
7. C. G. Mullighan *et al.*, *Science* **322**, 1377 (2008).
8. X. Wu *et al.*, *Nature* **482**, 529 (2012).
9. W. Liu *et al.*, *Nat. Med.* **15**, 559 (2009).
10. M. E. Gorre *et al.*, *Science* **293**, 876 (2001).
11. C. Roche-Lestienne, J. L. Lai, S. Darré, T. Facon, C. Preudhomme, *N. Engl. J. Med.* **348**, 2265 (2003).
12. M. J. Bissell, M. A. Labarge, *Cancer Cell* **7**, 17 (2005).
13. V. Sanz-Moreno *et al.*, *Cell* **135**, 510 (2008).
14. S. L. Spencer, S. Gaudet, J. G. Albeck, J. M. Burke, P. K. Sorger, *Nature* **459**, 428 (2009).
15. A. Roesch *et al.*, *Cell* **141**, 583 (2010).
16. S. V. Sharma *et al.*, *Cell* **141**, 69 (2010).
17. P. B. Gupta *et al.*, *Cell* **146**, 633 (2011).
18. K. Ishizawa *et al.*, *Cell Stem Cell* **7**, 279 (2010).
19. P. N. Kelly, A. Dakic, J. M. Adams, S. L. Nutt, A. Strasser, *Science* **317**, 337 (2007).

20. S. Jones *et al.*, *Proc. Natl. Acad. Sci. U.S.A.* **105**, 4283 (2008).
21. A. Marusyk, V. Almendro, K. Polyak, *Nat. Rev. Cancer* **12**, 323 (2012).
22. M. Kærn, T. C. Elston, W. J. Blake, J. J. Collins, *Nat. Rev. Genet.* **6**, 451 (2005).
23. M. Loreau *et al.*, *Science* **294**, 804 (2001).
24. D. F. Flynn, N. Mirotchnick, M. Jain, M. I. Palmer, S. Naeem, *Ecology* **92**, 1573 (2011).
25. H. B. Fraser, A. E. Hirsh, G. Giaever, J. Kumm, M. B. Eisen, *PLoS Biol.* **2**, e137 (2004).
26. H. L. True, S. L. Lindquist, *Nature* **407**, 477 (2000).
27. J. M. Raser, E. K. O'Shea, *Science* **304**, 1811 (2004).
28. K. Lewis, *Nat. Rev. Microbiol.* **5**, 48 (2007).
29. A. M. Abulafi, N. S. Williams, *Br. J. Surg.* **81**, 7 (1994).
30. J. M. Raser, E. K. O'Shea, *Science* **309**, 2010 (2005).

**Acknowledgments:** We thank L. Gibson, A. Khandani, and P. Penttilä for experimental support and members of the Dick lab, especially M. Doedens, J. Wang, M. Milyavsky, and E. Laurenti for technical support and critical assessment of this work, as well as UHN biobank for specimens, the Clinical Applications of Core Technology (Affymetrix) Laboratory of the Hartwell Center for Bioinformatics and Biotechnology of St. Jude Children's Research Hospital, and the American Lebanese Syrian Associated Charities of St. Jude Children's Research Hospital. Supported by Genome Canada through the Ontario Genomics Institute, Ontario Institute for Cancer Research and a Summit Award with funds from the province of Ontario, the Canadian Institutes for Health Research, the Netherlands Organisation for Scientific Research, NIH grant R21 CA149990-01, a Canada Research Chair, the Princess Margaret Hospital Foundation, and the Ontario Ministry of Health and Long Term Care (OMOHLTC). The views expressed do not necessarily reflect those of the OMOHLTC.

#### Supplementary Materials

www.sciencemag.org/cgi/content/full/science.1227670/DC1  
Materials and Methods  
Supplementary Text  
Figs. S1 to S17  
Tables S1 to S13  
References (31–56)

19 July 2012; accepted 26 November 2012  
Published online 13 December 2012;  
10.1126/science.1227670

## Gut Microbiomes of Malawian Twin Pairs Discordant for Kwashiorkor

Michelle I. Smith,<sup>1\*</sup> Tanya Yatsunenko,<sup>1\*</sup> Mark J. Manary,<sup>2,3,4</sup> Indi Trehan,<sup>2,3</sup> Rajhab Mkakosya,<sup>5</sup> Jiye Cheng,<sup>1</sup> Andrew L. Kau,<sup>1</sup> Stephen S. Rich,<sup>6</sup> Patrick Concannon,<sup>6</sup> Josyf C. Mychaleckyj,<sup>6</sup> Jie Liu,<sup>7</sup> Eric Houpt,<sup>7</sup> Jia V. Li,<sup>8</sup> Elaine Holmes,<sup>8</sup> Jeremy Nicholson,<sup>8</sup> Dan Knights,<sup>9,10†</sup> Luke K. Ursell,<sup>11</sup> Rob Knight,<sup>9,10,11,12</sup> Jeffrey I. Gordon<sup>1†</sup>

Kwashiorkor, an enigmatic form of severe acute malnutrition, is the consequence of inadequate nutrient intake plus additional environmental insults. To investigate the role of the gut microbiome, we studied 317 Malawian twin pairs during the first 3 years of life. During this time, half of the twin pairs remained well nourished, whereas 43% became discordant, and 7% manifested concordance for acute malnutrition. Both children in twin pairs discordant for kwashiorkor were treated with a peanut-based, ready-to-use therapeutic food (RUTF). Time-series metagenomic studies revealed that RUTF produced a transient maturation of metabolic functions in kwashiorkor gut microbiomes that regressed when administration of RUTF was stopped. Previously frozen fecal communities from several discordant pairs were each transplanted into gnotobiotic mice. The combination of Malawian diet and kwashiorkor microbiome produced marked weight loss in recipient mice, accompanied by perturbations in amino acid, carbohydrate, and intermediary metabolism that were only transiently ameliorated with RUTF. These findings implicate the gut microbiome as a causal factor in kwashiorkor.

**M**alnutrition is the leading cause of child mortality worldwide (1). Moderate acute malnutrition (MAM) refers to simple

wasting with a weight-for-height *z* (WHZ) score between two and three standard deviations below the median defined by World Health Organiza-

tion (WHO) Child Growth Standards (2, 3). Severe acute malnutrition (SAM) refers to either marasmus, which is extreme wasting with WHZ scores less than −3, or kwashiorkor, a virulent form of SAM characterized by generalized edema, hepatic steatosis, skin rashes and ulcerations, and anorexia (4, 5). The cause of kwashiorkor remains obscure. Speculation regarding its pathogenesis has focused on inadequate protein intake and/or excessive oxidative stress, but substantial evidence to refute these hypotheses has come from epidemiologic surveys and clinical trials (6–9). Our comparative metagenomic study of the gut microbiomes of 531 healthy infants, children, and adults living in the United States, Venezuela, and Malawi revealed a maturational program in which the proportional representation of genes encoding functions related to micro- and macronutrient biosynthesis and metabolism changes during postnatal development (10). Together, these observations give rise to the following testable hypotheses: (i) The gut microbiome provides essential functions needed for healthy postnatal growth and development; (ii) disturbances in microbiome assembly and function (for instance, those prompted by

enteropathogen infection) affect the risk for kwashiorkor; and (iii) in a self-reinforcing pathogenic cascade, malnutrition affects the gut microbiome functions involved in determining nutritional status, thus further worsening health status. To complicate matters, several gut microbiome configurations may be associated with kwashiorkor among different hosts and even within a given host over time. Moreover, microbiome configurations associated with kwashiorkor may be differentially affected by therapeutic food interventions, and features that are reconfigured during treatment may not persist after withdrawal of treatment.

To address some of these hypotheses, we performed a longitudinal comparative study of the fecal microbiomes of monozygotic (MZ) and dizygotic (DZ) twin pairs born in Malawi who became discordant for kwashiorkor. Malawi has one of the highest infant mortality rates in the world (1, 11). We reasoned that a healthy (well-nourished) co-twin in a discordant twin pair represented a very desirable control, given his or her genetic relatedness to the affected co-twin and the twins' similar exposures to diet and microbial reservoirs in their shared early environment. Ready-to-use therapeutic food (RUTF) composed of peanut paste, sugar, vegetable oil, and milk fortified with vitamins and minerals has become the international standard of treatment for SAM in community-based treatment programs (12). In Malawi, the standard of care for twins discordant for kwashiorkor is to treat both co-twins with RUTF to limit food sharing; this practice allowed us to compare and contrast their microbiomes before, during, and after treatment. Following each child in a twin pair prospectively permitted each individual to serve as his or her own control. Moreover, if there are many different routes to disrupted microbiome structure and/or function, then each discordant twin pair could provide an illustration of underlying pathology. As an additional set of controls, we defined temporal variation of the fecal

microbiomes in twin pairs who remained well nourished, lived in the same geographic locations as discordant pairs, and never received RUTF.

Regardless of their health status, a total of 317 twin pairs younger than 3 years old, from five villages in the southern region of Malawi, were enrolled in our study. We followed these children until they reached 36 months of age. Zygosity testing (13) revealed that 46 (15%) twin pairs were MZ. We used WHO criteria (3) to diagnose kwashiorkor based on the presence of bilateral pitting pedal edema, marasmus when a child had a WHZ score less than  $-3$ , and MAM when the WHZ score was between  $-2$  and  $-3$  and bilateral pitting pedal edema was absent (2, 3). We treated SAM with RUTF and MAM with a soy-peanut ready-to-use supplementary food (14). After diagnosis with SAM, we assessed anthropometry and collected a fecal sample every 2 weeks until the child recovered (defined as WHZ score greater than  $-2$  and no edema).

Fifty percent of twin pairs remained well nourished throughout the study, whereas 43% became discordant, and 7% manifested concordance for acute malnutrition. The prevalence of discordant compared with concordant phenotypes was significantly different ( $P < 10^{-15}$ , binomial and  $\chi^2$  tests). MAM was significantly more frequent than SAM, affecting 81 (60%) of the 135 discordant twin pairs ( $P = 0.02$ ,  $\chi^2$  test) (table S1A). Of the 634 children in the study, 7.4% developed kwashiorkor, 2.5% had marasmus, and 13.9% were diagnosed with MAM; 10.7% had multiple episodes of malnutrition, with the most frequent combination being marasmus and MAM (5.5% of the children) (table S1B). There was no significant relationship between concordance for acute malnutrition and zygosity, nor did we find significant differences in the number of MZ versus DZ twin pairs affected with kwashiorkor, marasmus, or MAM in our cohort ( $\chi^2$  and Fisher's exact tests). Taking all 135 discordant pairs into account, there was no statistically significant difference in the incidence of discordance for kwashiorkor, marasmus, or MAM in MZ versus DZ twin pairs (table S1A). In addition, we did not find any association between gender or geographic location and the type or incidence of malnutrition or in the discordance rate for MAM or SAM among twin pairs (table S1, B and C). For the current study, we chose to focus on children with kwashiorkor because: (i) survival of both members of a twin pair with kwashiorkor was significantly higher than with marasmus; (ii) onset occurred at a later age, allowing us to better assess the state of functional development of the gut microbiome; (iii) the duration of RUTF treatment was more uniform than in cases of marasmus; and (iv) there was a lower incidence of relapse to SAM (see supplementary text for additional details).

**Microbiomes of healthy twins and pairs discordant for kwashiorkor.** We selected nine same-gender twin pairs who remained well nourished in our study cohort and 13 of 19 same-gender twin pairs who became discordant for kwashiorkor for metagenomic analyses of their microbiomes

[ $n = 5$  MZ and 4 DZ healthy pairs and 7 MZ and 6 DZ pairs discordant for kwashiorkor; for 12 of the 13 discordant pairs, there was a single episode of kwashiorkor during the study period] (see supplementary text for the criteria used for participant selection and table S2A for additional information about participants and their samples). DNA prepared from fecal samples was subjected to multiplex shotgun pyrosequencing, and the resulting reads were annotated by comparison to the Kyoto Encyclopedia of Genes and Genomes (KEGG) database and to a database of 462 sequenced human gut microbes (table S3). To visualize the variation in this data set, we used principal coordinates analysis of Hellinger distances computed from the KEGG enzyme commission number (EC) content of fecal microbiomes (Fig. 1A and fig. S1). Principal coordinate 1 (PC1), which explained the largest amount of variation, was strongly associated with age and family membership (Fig. 1A). Because age encompasses a variety of metabolic and dietary changes, we used the positions of microbiomes along PC1 to assess functional development of the microbiomes of twin pairs who remained healthy and twin pairs who became discordant for kwashiorkor. When microbiomes from three consecutive time points from twins who remained healthy were plotted along PC1, there was a steady progression toward a configuration found in older children (Fig. 1B). We observed a similar result in healthy co-twins from discordant twin pairs. This was not the case for their siblings with kwashiorkor: Their fecal microbiomes, sampled at the time of diagnosis, as well as during and following administration of RUTF, did not show significant differences in their positions in the ordination plot (Fig. 1C). We obtained the same results for KEGG orthology groups. We used Fisher's exact test to compare the representation of KEGG ECs between a healthy and a malnourished co-twin within each family, and we identified ECs that were significantly different in as few as one and as many as six of the twin pairs (table S5).

These associations between the configurations of gut microbial communities and health status do not establish whether the microbiome is a causal factor in the pathogenesis of kwashiorkor. We reasoned that transplanting previously frozen fecal microbial communities, obtained from discordant twin pairs at the time one of the co-twins presented with kwashiorkor, into gnotobiotic mice would allow us to assess the degree to which donor phenotypes could be transmitted via their gut microbiomes and to identify features of microbial community structure, metabolism, and host-microbial cometabolism associated with donor health status and diet. In the absence of a distinct and consistent taxonomic signature of kwashiorkor (supplementary text), we selected pretreatment fecal samples from three discordant twins based on the following criteria: All twin pairs were of similar age, and neither co-twin in any pair had diarrhea or vomiting or was consuming antibiotics at the time that fecal samples were collected.

<sup>1</sup>Center for Genome Sciences and Systems Biology, Washington University in St. Louis, St. Louis, MO 63110, USA. <sup>2</sup>Department of Pediatrics, Washington University in St. Louis, St. Louis, MO 63110, USA. <sup>3</sup>Department of Community Health and Department of Pediatrics and Child Health, University of Malawi College of Medicine, Blantyre, Malawi. <sup>4</sup>U.S. Department of Agriculture Children's Nutrition Research Center, Baylor College of Medicine, Houston, TX 77030, USA. <sup>5</sup>Department of Microbiology, College of Medicine, University of Malawi, P/B 360, Chichiri, Blantyre 3, Malawi. <sup>6</sup>Center for Public Health Genomics, University of Virginia, Charlottesville, VA 22904, USA. <sup>7</sup>Division of Infectious Diseases and International Health, University of Virginia, Charlottesville, VA 22908, USA. <sup>8</sup>Biomolecular Medicine, Department of Surgery and Cancer, Faculty of Medicine, Imperial College London, London SW7 2AZ, UK. <sup>9</sup>Department of Computer Science, University of Colorado, Boulder, CO 80309, USA. <sup>10</sup>BioFrontiers Institute, University of Colorado, Boulder, CO 80309, USA. <sup>11</sup>Department of Chemistry and Biochemistry, University of Colorado, Boulder, CO 80309, USA. <sup>12</sup>Howard Hughes Medical Institute, University of Colorado, Boulder, CO 80309, USA.

\*These authors contributed equally to this work.

†Present address: Department of Computer Science and Engineering and BioTechnology Institute, University of Minnesota, Saint Paul, MN 55108, USA.

‡To whom correspondence should be addressed. E-mail: jgordon@wustl.edu



The twins selected included DZ pair 196 (aged 16.5 months), DZ pair 56 (aged 18 months), and MZ twin pair 57 (aged 21 months) (see fig. S5 and table S2A for clinical characteristics).

**Transplantation of fecal microbial communities into gnotobiotic mice.** Fecal microbiota samples from the six selected human donors were each transplanted, with a single oral gavage, into separate groups of adult 8-week-old male C57BL/6J germ-free mice. Beginning 1 week before gavage, animals were freely fed a sterilized diet based on the staple foods consumed by individuals living in rural southern Malawi (see table S6 for the composition of this low caloric density, nutrient-deficient diet and fig. S6 for experimental design) (10). In two of the three discordant twin pairs (families 196 and 57), transplantation of the kwashiorkor co-twin's microbiota resulted in significantly greater weight loss in recipient mice over the ensuing 3 weeks than in those harboring the healthy sibling's microbiota (Fig. 2A). This discordant weight loss phenotype was dependent on the combination of Malawian diet and kwashiorkor microbiota; when separate groups of animals were placed on a standard mouse chow, there were no significant differences between the weights of mice with kwashiorkor compared to healthy co-twin microbiota ( $93.6 \pm 4\%$  versus  $93 \pm 11\%$  of their starting weights after 21 days, respectively) or compared to mice with a healthy co-twin microbiota consuming a Malawian diet ( $102.4 \pm 11.1\%$ ).

Three weeks after gavage, mice consuming the Malawian diet were switched to the RUTF given to children with SAM. At the time of the diet switch, all recipients of kwashiorkor microbiota from families 196 and 57 had become severely anorectic. All mice in each treatment group rapidly gained weight while consuming RUTF. In the case of the most discordant set of recipients (from family 196), mice with the kwashiorkor co-twin's microbiota did not achieve the same body weight as recipients of the healthy sibling's microbiota, but these mice did reach  $96.8 \pm 2.8\%$  of their pre-gavage weight. After 2 weeks on RUTF, all mice in all treatment groups were returned to the Malawian diet. Whereas all recipients of microbiota transplants lost weight, this re-exposure did not produce the profound weight loss that mice colonized with the kwashiorkor microbiota had experienced during their first exposure (Fig. 2A). These results indicate that the gut microbiota from two of the three discordant pairs are able to transmit a discordant malnutrition phenotype, manifested by weight loss, to recipient gnotobiotic mice. Given that the most discordant weight loss phenotype was produced by microbiota from twin pair 196, we initiated a detailed time-series analyses of the organismal, gene, and metabolite content of the transplanted microbial communities as a function of co-twin donor and diet (fig. S6 and table S2, B and C).

Transplantation was efficient: (i) 62 of 72 species-level taxa present in the input community

from the healthy co-twin and 58 of 67 species-level taxa from the kwashiorkor co-twin were detected in fecal microbiota collected from all transplant recipients across time points and diets (table S7); (ii) 90.6 and 89.6% of the 859 ECs detected in each of the healthy and kwashiorkor input communities were identified in the fecal microbiota of transplant recipients after 3 weeks on the Malawian diet; and (iii) the proportional representation of ECs in input versus output fecal communities was highly correlated (correlation coefficient  $R^2 = 0.893$  to  $0.936$ ) (fig. S7, A and B). Polymerase chain reaction–Luminex assays (15–18) for 22 common bacterial, parasitic, and viral enteropathogens in the input human microbiota, as well as in recipient mouse fecal samples, indicated that the markedly discordant weight loss phenotype in recipients of these microbiota was not due to transfer and/or subsistence of any of the surveyed pathogens (fig. S8, A and B, and supplementary text).

Comparison of the two groups of gnotobiotic recipients while they consumed a Malawian diet showed significant differences in the proportional representation of 37 species-level taxa. Organisms with the most statistically significant differences, and whose relative proportions were higher in mice with the kwashiorkor microbiota, were (i) *Bilophila wadsworthia*, a hydrogen-consuming, sulfite-reducing organism that is related to members of *Desulfovibrio* (phylum Proteobacteria) and has been linked to inflammatory bowel disease (IBD) in humans and induces a proinflammatory T helper 1 response in a mouse model of IBD (19), and (ii) *Clostridium innocuum*, a gut symbiont that can function as an opportunist in immunocompromised hosts (table S8B) (20). *B. wadsworthia* and members of the order Clostridiales were also overrepresented in the fecal microbiota of the kwashiorkor co-twin from family 196 compared with his healthy co-twin at the time he presented with kwashiorkor (table S8B).

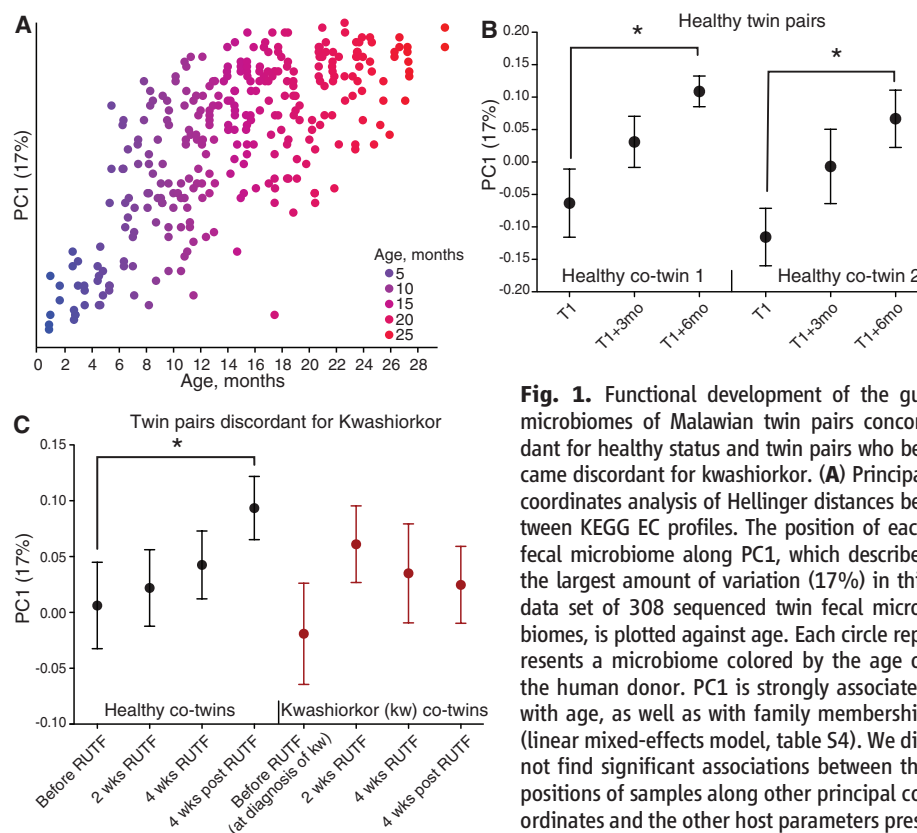


**Fig. 1.** Functional development of the gut microbiomes of Malawian twin pairs concordant for healthy status and twin pairs who became discordant for kwashiorkor. **(A)** Principal coordinates analysis of Hellinger distances between KEGG EC profiles. The position of each fecal microbiome along PC1, which describes the largest amount of variation (17%) in this data set of 308 sequenced twin fecal microbiomes, is plotted against age. Each circle represents a microbiome colored by the age of the human donor. PC1 is strongly associated with age, as well as with family membership (linear mixed-effects model, table S4). We did not find significant associations between the positions of samples along other principal coordinates and the other host parameters presented in table S2A. On average, the degree

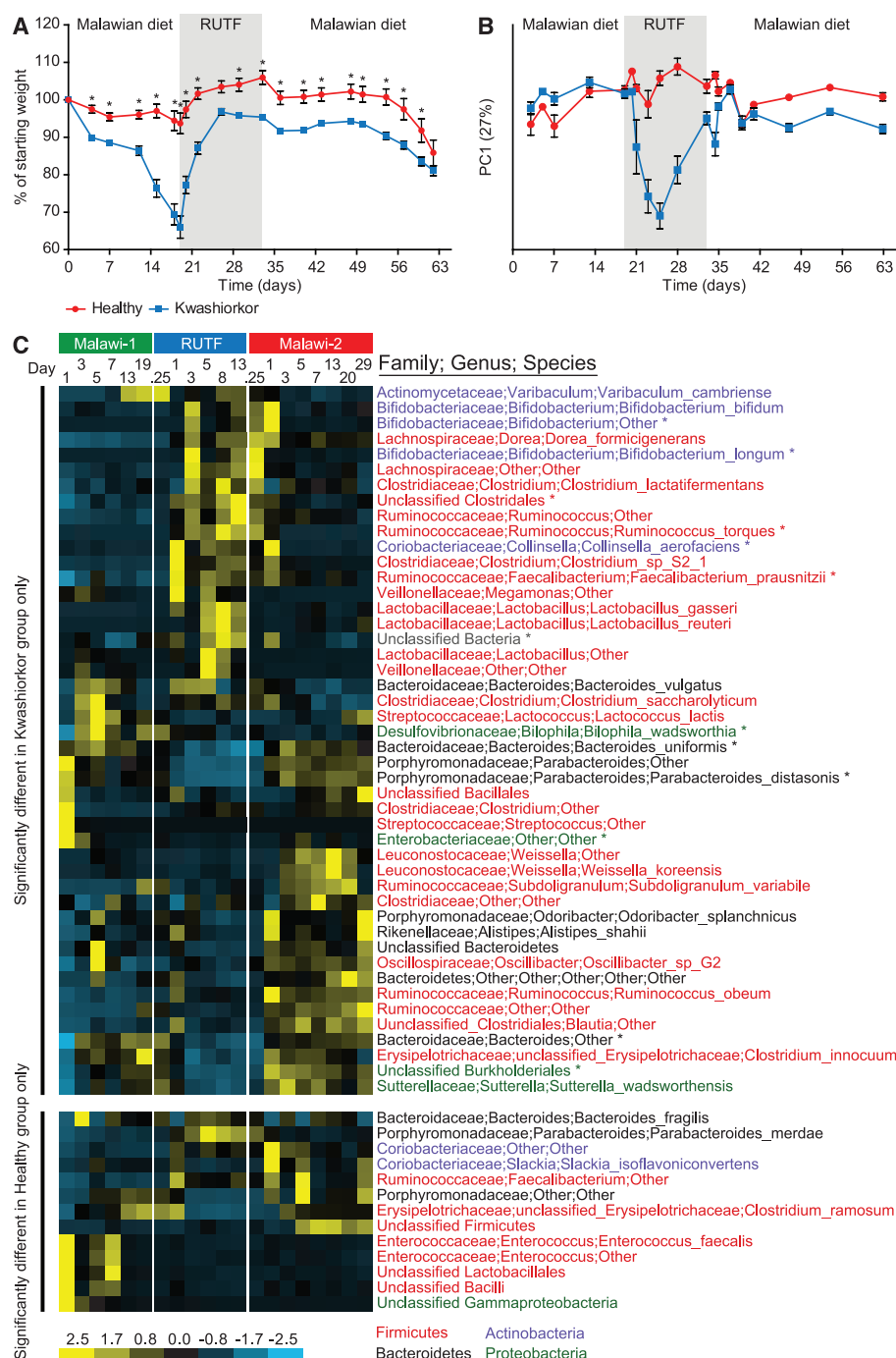
of intrapersonal variation in a co-twin was not smaller than the variation between co-twins (fig. S2). Similar to twins who remained healthy, the temporal variation within a co-twin member of a discordant twin pair was equal to the variation between co-twins, but still smaller compared with unrelated children (fig. S2). **(B)** Average  $\pm$  SEM (error bars) PC1 coordinate obtained from the data shown in (A) for microbiomes sampled at three consecutive time points from nine twin pairs who remained well nourished (healthy) during the study (participants surveyed between 3 weeks and 24.5 months of age). **(C)** Average  $\pm$  SEM (error bars) PC1 coordinate obtained from (A) for microbiomes sampled before, during, and after RUTF treatment from co-twins discordant for kwashiorkor.  $*P < 0.05$ , Friedman test with Dunn's post-hoc test applied to data shown in (B) and (C). Similar results were obtained using other distance metrics [Bray Curtis, Euclidian, and Kulczynski (fig. S3)]. (See also fig. S4, which shows how changes in the relative proportion of Actinobacteria parallel the patterns observed with the changes along PC1. Children with kwashiorkor manifested a statistically significant decrease in Actinobacteria with the introduction of RUTF, unlike their healthy co-twins).

Switching from a Malawian diet to RUTF produced a rapid change in configuration of the fecal microbiota that was most pronounced in recipients of the kwashiorkor co-twin's community (Fig. 2B and fig. S9, A and B). Thirty species-level taxa exhibited statistically significant changes in their representation in kwashiorkor microbiota transplant recipients (Fig. 2C and tables S7B and S8A), with prominent increases in *Bifidobacteria* (*B. longum*, *B. bifidum*, plus another unclassified taxon), two *Lactobacilli* [*L. reuteri* and *L. gasseri*, which can produce bac-

teriocins and stimulate the innate immune system to inhibit the growth and eliminate various enteropathogens (21–23)], and two members of *Ruminococcus* [*R. torques*, a mucus degrader (24), and *Faecalibacterium prausnitzii*, a member of the order Clostridiales that exhibits anti-inflammatory activity in a mouse model of colitis and whose decreased representation is associated with increased risk of ileal Crohn's disease (25)]. We observed statistically significant decreases in the representation of members of the Bacteroidales (*B. uniformis*, *Parabacteroides distasonis*, plus

an unclassified *Parabacteroides* taxon) (see Fig. 2C and legend for time courses). Twenty-eight bacterial species-level taxa also exhibited significant changes in their representation in gnotobiotic mice harboring the healthy co-twin's microbiota in response to RUTF. The pattern of change of 13 different taxa—including the two *Ruminococcus* spp., *B. uniformis*, *P. distasonis*, *B. longum*, and an unclassified *Bifidobacterium* taxon—was shared by both recipient groups (healthy and kwashiorkor), although the *Bifidobacterium* response was less pronounced in the healthy microbiota

**Fig. 2.** Transplantation of fecal microbiota from kwashiorkor and healthy co-twins from family 196 into gnotobiotic mice fed Malawian and RUTF diets. **(A)** Discordant weight loss in recipient mice ( $n = 10$  mice per group,  $*P < 0.05$ , Student's  $t$  test). Data points are colored by recipient group: blue, kwashiorkor co-twin fecal microbiota recipients; red, healthy co-twin fecal microbiota recipients. Error bars indicate SEM. **(B)** Average  $\pm$  SEM (error bars) PC1 coordinate obtained from the weighted UniFrac distances shown in fig. S9, A and B, for fecal microbiota sampled from mice over time. Same color key as in (A). **(C)** Heatmap of phylotypes assigned to species-level taxa whose representation in the fecal microbiota of gnotobiotic mice changed significantly ( $P < 0.05$ , Student's  $t$  test with Bonferroni correction) as a function of donor microbiota and Malawian versus RUTF diets. Asterisks indicate taxa that changed significantly in both healthy and kwashiorkor microbiota transplant recipients. Species level taxa are colored by phylum: red, Firmicutes; blue, Actinobacteria; black, Bacteroidetes; and green, Proteobacteria. Switching from a Malawian diet to RUTF produces a rapid change in the configuration of the transplanted kwashiorkor microbiota. A bloom in *Lactobacilli* occurs early during treatment with RUTF but regresses by the end of this diet period and remains unchanged when animals are returned to the Malawian diet. *Bifidobacterium* spp. also bloom early during administration of RUTF. Unlike the *Lactobacilli*, the increase of *Bifidobacterium* is sustained into the early phases of M2, after which they diminish. Like the members of *Bifidobacterium*, *R. torques* increases its representation during RUTF and then rapidly diminishes when mice returned to a Malawian diet. The increase in *F. prausnitzii* is sustained into and through M2. The responses of the Bacteroidales were opposite to that of the other three groups: Bacteroidales decrease with the administration of RUTF and re-emerge with M2. The response of the *Lactobacilli* observed in the kwashiorkor transplant recipients is not seen in gnotobiotic mice containing the healthy co-twin's microbiota. The pattern of change of the two *Ruminococcus* spp., *B. uniformis*, *P. distasonis*, *B. longum*, and an unclassified *Bifidobacterium* taxon is shared by both recipient groups (healthy and kwashiorkor), although the *Bifidobacterium* response is more diminutive in the healthy microbiota treatment group. *Parabacteroides merdae*, an unclassified taxon from the genus *Faecalibacterium*, as well as a member of the *Coriobacteriaceae*, are specifically elevated in the healthy co-twin's microbiota when mice switch to a RUTF diet. Of these, only *P. merdae* does not persist when animals are returned to the Malawian diet (also see tables S7A and S8A).





treatment group (Fig. 2C and tables S7A, S7B, and S8A). These changes were representative of those that occurred in the human donors; the change in *Bifidobacterium* was unique to the kwashiorkor co-twin (table S9).

Metabolic profiles associated with kwashiorkor.

Gas chromatography–mass spectrometry analyses of short-chain fatty acids and 69 other products of carbohydrate, amino acid, nucleotide, and lipid (fatty acid) metabolism in cecal and fecal samples collected during the different diet periods ( $n = 4$  to 5 mice per family-196 microbiota donor) showed that levels of the majority of these metabolites increased when mice were switched to RUTF. In contrast, levels of several di- and monosaccharides (maltose, gentibiose, and tagatose) decreased (fig. S10). There were a number of significant differences between the two groups of mice while they were consuming the different diets (Fig. 3). Although switching to RUTF produced a significant increase in fecal levels of six essential amino acids (valine, leucine, isoleucine, methionine, phenylalanine, and threonine) and three nonessential amino acids (alanine, tyrosine, and serine) in both groups, the response was initially greater in the kwashiorkor group. Four weeks after returning to a Malawian diet, levels of six of these amino acids remained higher in the healthy microbiota recipient group than before consumption of RUTF, but in the kwashiorkor group, these values fell to pre-RUTF-treatment levels (fig. S11, A and B). We observed the same pattern of transient response with urea cycle intermediates in the kwashiorkor group (fig. S11C). RUTF-associated increases in levels of propionate, butyrate, lactate, and succinate were generally greater in mice harboring the healthy co-twin’s microbiota (fig. S12A). Similarly, acetate levels were elevated early on during RUTF in the healthy but not the kwashiorkor microbiota (fig. S12A). Increases in these end products of fermentation were accompanied by reductions in the levels of a number of mono- and disaccharides (fig. S12B). The observed differences in metabolic profiles were not attributable to differences in microbial community biomass: There were no statistically significant differences in fecal DNA content between recipients of the healthy and kwashiorkor co-twin microbiota when assayed at the midpoint of RUTF treatment [ $986.5 \pm 108.3$  (mean  $\pm$  SEM) versus  $903.2 \pm 97.7$  ng DNA/mg feces, respectively;  $P = 0.22$ , Student’s  $t$  test] or 4 weeks after cessation of treatment ( $559.7 \pm 62.2$  versus  $651.6 \pm 98.9$  ng DNA/mg feces, respectively;  $P = 0.44$ ). (For characterization of gnotobiotic recipients of family-57 transplants, including taxonomic and metabolic responses to the different diets that they share with family-196 recipients, see supplementary text; fig. S7, C and D; and tables S7C, S7D, S8C, S8D, S9, and S10.)

Microbial-host cometabolism as a function of donor microbiota and host diet. We used standard  $^1\text{H}$  nuclear magnetic resonance (NMR) spectroscopy to generate urine metabolite pro-

files (Table 1, fig. S15, and supplementary text) (26). A pronounced metabolic shift seen in response to RUTF was not sustained on reintroduction of the Malawian diet; urinary metabolic profiles at the end of the second Malawian diet period (M2) resembled those from the first period (M1), with renewed differentiation between healthy and kwashiorkor microbiota transplant groups. The kwashiorkor microbiota-associated metabolic phenotype was not as distinctive in M2 as it was during M1. When we reanalyzed the data after excluding the RUTF samples, the metabolic differentiation was more apparent between the two Malawian dietary periods (fig. S15, A to C).

Among the notable results, we found that levels of urinary taurine were affected by both donor microbiota and diet. Mice colonized with microbiota from a healthy donor excreted more taurine while consuming both the Malawian diet and RUTF compared with mice with a kwashiorkor microbiota; in both recipient groups, urinary taurine levels were higher when mice consumed a

Malawian diet (Table 1). *B. wadsworthia* grows well on bile acids and uses taurine from taurine-conjugated bile acids as a terminal electron acceptor, converting it to ammonia, acetate, and sulfide (27). In agreement with this property, fecal levels of *B. wadsworthia* showed an inverse relationship with urinary taurine levels. Levels were higher in the kwashiorkor group; even when the mice were consuming RUTF, recipients of the kwashiorkor microbiota exhibited significantly lower urinary taurine levels and significantly higher fecal levels of *B. wadsworthia* (Table 1 and table S8, A and B). In addition to urinary taurine levels, fecal methionine and cysteine concentrations were significantly lower in mice harboring kwashiorkor compared with those carrying healthy co-twin microbiota when consuming a Malawian diet (Fig. 3). Dietary methionine and cysteine meet most of the human body’s needs for sulfur; these amino acids are more abundant in animal and cereal proteins than in vegetable proteins. The Malawian diet is

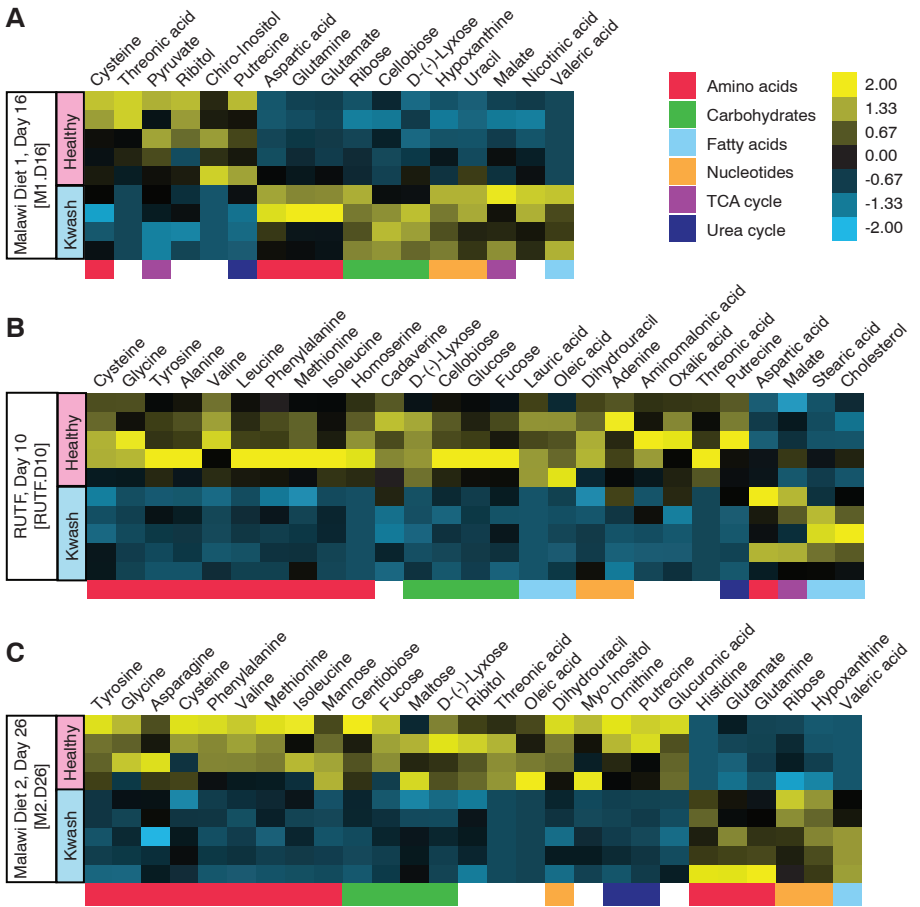


**Fig. 3.** Metabolites with significant differences in their fecal levels in gnotobiotic mice colonized with microbiota from discordant twin pair 196 as a function of diet. Data are from fecal samples collected 3 days before the end of (A) the first period of consumption of the Malawian diet (M1, day 16; abbreviated M1.D16), (B) RUTF treatment (RUTF.D10), and (C) the second period of Malawian diet consumption (M2, D26). Significant differences are defined as  $P < 0.05$ , according to Student’s  $t$  test. Procrustes analysis of data obtained from the transplanted microbiota from discordant co-twins in family 196 (fig. S13) revealed a significant correlation between metabolic and taxonomical profiles on each diet with an overall goodness of fit ( $M^2$  value) of 0.380 ( $P < 0.0001$ ; 1000 Monte Carlo label permutations) for all diets and microbiota.

**Table 1.** Metabolite analysis of urine samples obtained from mice with transplanted healthy or kwashiorkor co-twin microbiota from family 196 at each diet phase.  $R^2X$  represents the variation in  $^1H$  NMR spectral data explained by the O-PLS-DA model, where a value of 1 would indicate that 100% of the variation in the spectral data set is explained by the model.  $Q^2Y$  represents the predictive ability of the model and is calculated by leaving a percentage of the data out (15%) while calculating the ability of the model to discriminate between classes in any pairwise comparison (e.g., kwashiorkor versus healthy). Additionally,  $Q^2Y$  indicates the level of robustness or significance of the metabolic differences between two classes. The numbers in each column are obtained from median fold normalized O-PLS-DA models and represent the correlation between the NMR data (relative concentration of urinary metabolite) and a given class (e.g., healthy versus kwashiorkor co-twin microbiota or Malawi diet 1 versus RUTF diet). The greater the  $Q^2Y$  or predictive value for the O-PLS-DA comparison of two classes, the stronger or more reliable the composite metabolic differences are between two classes (e.g., dietary periods). The closer to 1.0 the correlation value is for any given metabolite, the more weight that metabolite has in discriminating between those two classes. Metabolites are colored according to their overrepresentation in a treatment group. **(A)** Urinary metabolites with differences in their levels in mice transplanted with the healthy co-twin versus the kwashiorkor co-twin microbiota within a given diet. Color code: blue, higher in kwashiorkor co-twin microbiota recipients; red, higher in healthy co-twin microbiota recipients; white, no significant difference between kwashiorkor and healthy. **(B)** Urinary metabolites with differences in their representation of mice transplanted with healthy or kwashiorkor co-twin microbiota between diets. Color code: red, higher during the M1 diet phase relative to RUTF or relative to M2; orange, higher on RUTF relative to M1 or M2; blue, higher on M2 compared to RUTF or M1; white, no significant differences in the indicated diet comparison.

<b>A</b>		M1	RUTF	M2	
$R^2X$		0.38	0.49	0.36	
$Q^2Y$		0.62	0.8	0.78	
2-oxoadipate		0.8747	0.9069	0.6603	Higher metabolite concentration in recipients of kwashiorkor co-twin microbiota
taurine			0.8578	0.6236	
lactate				0.4618	Higher metabolite concentration in recipients of healthy co-twin donor microbiota
creatine		0.9303			
creatinine		0.7692			
methylamine		0.6755	0.8338	0.7646	
dimethylamine		0.7732			
trimethylamine		0.8469			
trimethylamine <i>N</i> -oxide					
phenylacetylglutamate		0.8522	0.8816		
indoxyl sulfate		0.6591	0.8138		
hippurate		0.6301	0.9485	0.9786	
allantoin		0.7662			

<b>B</b>		Recipients of healthy co-twin donor microbiota		Recipients of kwashiorkor co-twin donor microbiota	
		M1 vs RUTF	RUTF vs M2	M1 vs RUTF	RUTF vs M2
$R^2X$		0.66	0.58	0.61	0.74
$Q^2Y$		0.57	0.94	0.31	0.87
2-oxoglutarate		0.7448	0.8538	0.9062	0.8761
citrate		0.7065	0.7921	0.827	0.7137
succinate		0.6794	0.6841	0.8348	0.846
fumarate		0.7439	0.7553		
acetate				0.7	
2-oxoadipate		0.8382	0.6198		
taurine		0.632	0.7469		0.5998
lactate		0.5558			0.4733
creatine			0.7432	0.9474	0.759
creatinine				0.8297	0.7051
methylamine					0.7562
dimethylamine			0.7469		
trimethylamine		0.7149	0.6639		0.8534
trimethylamine <i>N</i> -oxide					0.799
phenylacetylglutamate			0.8447	0.5716	0.6616
indoxyl sulfate		0.8021	0.8699	0.9593	
hippurate			0.8602		
allantoin			0.8203	0.9133	0.93
1-methylnicotinamide					0.769

Higher metabolite concentration during Malawian diet phase 1	Higher metabolite concentration during RUTF	Higher metabolite concentration during Malawian diet phase 2
--	---	--

deficient in total protein and in animal protein. Studies have found a decrease of serum methionine levels and urinary sulfate excretion in patients with kwashiorkor (28–33). Moreover, cysteine or methionine deficiency in experimental animals can produce weight loss (correctable by sulfate supplementation) (34–36). Our findings suggest that the combination of a kwashiorkor microbiota and a Malawian diet may contribute to abnormal sulfur metabolism, thereby affecting the pathogenesis and manifestations of this form of SAM.

For mice containing the healthy co-twin's microbiota, urinary excretion of tricarboxylic acid (TCA) cycle intermediates 2-oxoglutarate, citrate, succinate, and fumarate were closely coupled together. These mitochondrial metabolites typically follow similar reabsorption control mechanisms in the renal tubule that are closely linked to tubular pH. In mice containing kwashiorkor microbiota, urinary fumarate excretion was effectively decoupled from the other TCA intermediates (fig. S15, D to G). Differential excretion rates of TCA intermediates can occur where there is selective enzymatic inhibition of the TCA cycle (37). The TCA cycle also appears to be disrupted in the kwashiorkor microbiota itself (threefold increase in cecal levels of succinate;  $P < 0.05$ , unpaired Student's *t* test), and an increased succinate-to-fumarate ratio (0.58 versus 0.23,  $P < 0.05$ , unpaired Student's *t* test while on the Malawian diet) suggests inhibition of succinate dehydrogenase, the enzyme responsible for converting succinate to fumarate. Taken together, these observations suggest that the kwashiorkor microbiota examined in these gnotobiotic mice may generate chemical products that result in a selective inhibition of one or more TCA cycle enzymes, making energy metabolism a bigger challenge for these children when they are exposed to a micro- and macronutrient-deficient, low-calorie diet.

**Prospectus.** The discordance rate for kwashiorkor is high for both MZ and DZ twins in our study population. Our results illustrate the value of using twins discordant for nutritional phenotypes to characterize the interrelationship between the functional development of the gut microbiome in children and their nutritional status. Linking metagenomic analyses with dietary experiments in gnotobiotic mice that have received gut microbiota transplants from twins discordant for kwashiorkor allowed us to gain insights into pathogenesis by identifying transmissible features associated with healthy versus diseased donors. By replicating a human donor's gut community in multiple recipient mice, we have been able to mimic a clinical intervention and identify community characteristics, including differences in taxonomic composition and in taxonomic and metabolic responses to RUTF. The resulting data provide biomarkers of community metabolism and of microbial-host cometabolism that delineate and discriminate diet and microbiota effects, including biomarkers indicative of the more labile, short-lived nature of the responses of microbiota from kwashiorkor donors to RUTF. The



interrelationships between diet, microbiota, and many facets of host physiology can be explored in detail in these “personalized” gnotobiotic mouse models. These models may be useful for developing new and more effective approaches for treatment and/or prevention. In addition, studies of other forms of malnutrition that take an approach analogous to that described here could also provide insights about the contribution of the gut microbiome to this global health problem.

## References and Notes

1. United Nations (UN) Inter-Agency Group for Child Mortality Estimation, *Levels & Trends in Child Mortality Report* (2011); [www.childinfo.org/files/Child\\_Mortality\\_Report\\_2011.pdf](http://www.childinfo.org/files/Child_Mortality_Report_2011.pdf).
2. WHO Multicentre Growth Reference Study Group, *Acta Paediatr. Suppl.* **450**, 76 (2006).
3. WHO, UN Children's Fund, *WHO Child Growth Standards and the Identification of Severe Acute Malnutrition in Infants and Children* (2009); [www.who.int/nutrition/publications/severemalnutrition/9789241598163/en/index.html](http://www.who.int/nutrition/publications/severemalnutrition/9789241598163/en/index.html).
4. C. D. Williams, B. M. Oxon, H. Lond, *Lancet* **226**, 1151 (1935).
5. T. Ahmed, S. Rahman, A. Cravioto, *Indian J. Med. Res.* **130**, 651 (2009).
6. C. Gopalan, in *Calorie Deficiencies and Protein Deficiencies: Kwashiorkor and Marasmus: Evolution and Distinguishing Features*, R. A. McCance, E. M. Widdowson, Eds. (Churchill, London, 1968), pp. 48–58.
7. M. H. Golden, *Lancet* **319**, 1261 (1982).
8. H. Ciliberto *et al.*, *BMJ* **330**, 1109 (2005).
9. C. A. Lin *et al.*, *J. Pediatr. Gastroenterol. Nutr.* **44**, 487 (2007).
10. T. Yatsunenko *et al.*, *Nature* **486**, 222 (2012).
11. R. E. Black *et al.*, *Lancet* **371**, 243 (2008).
12. WHO, World Food Programme, UN System Standing Committee on Nutrition, UN Children's Fund, *Community-Based Management of Severe Acute Malnutrition* (2007); [www.who.int/nutrition/topics/statement\\_commbased\\_malnutrition/en/index.html](http://www.who.int/nutrition/topics/statement_commbased_malnutrition/en/index.html).
13. Materials and methods are available as supplementary materials on Science Online.
14. L. Lagrone, S. Cole, A. Schondelmeyer, K. Maleta, M. J. Manary, *Ann. Trop. Paediatr.* **30**, 103 (2010).
15. J. Liu *et al.*, *J. Clin. Microbiol.* **50**, 98 (2012).
16. M. Taniuchi *et al.*, *Diagn. Microbiol. Infect. Dis.* **71**, 386 (2011).
17. M. Taniuchi *et al.*, *Am. J. Trop. Med. Hyg.* **84**, 332 (2011).
18. M. Taniuchi *et al.*, *Diagn. Microbiol. Infect. Dis.* **73**, 121 (2012).
19. S. Devkota *et al.*, *Nature* **487**, 104 (2012).
20. N. Crum-Cianflone, *Am. J. Med. Sci.* **337**, 480 (2009).
21. T. Itoh, Y. Fujimoto, Y. Kawai, T. Toba, T. Saito, *Lett. Appl. Microbiol.* **21**, 137 (1995).
22. M. F. Fernández, S. Boris, C. Barbés, *J. Appl. Microbiol.* **94**, 449 (2003).
23. Y. Kato-Mori *et al.*, *J. Med. Food* **13**, 1460 (2010).
24. A. A. Salyers, S. E. West, J. R. Vercellotti, T. D. Wilkins, *Appl. Environ. Microbiol.* **34**, 529 (1977).
25. H. Sokol *et al.*, *Proc. Natl. Acad. Sci. U.S.A.* **105**, 16731 (2008).
26. O. Beckonert *et al.*, *Nat. Protoc.* **2**, 2692 (2007).
27. H. Laue, K. Dengler, A. M. Cook, *Appl. Environ. Microbiol.* **63**, 2016 (1997).
28. J. C. Edozien, E. J. Phillips, W. R. F. Collis, *Lancet* **275**, 615 (1960).
29. R. G. Whitehead, R. F. Dean, *Am. J. Clin. Nutr.* **14**, 313 (1964).
30. S. Awwaad, E. A. Eisa, M. El-Essawy, *J. Trop. Med. Hyg.* **65**, 179 (1962).
31. G. Arroyave, D. Wilson, C. DeFunes, M. Béhar, *Am. J. Clin. Nutr.* **11**, 517 (1962).
32. T. R. Ittyerah, S. M. Pereira, M. E. Dumm, *Am. J. Clin. Nutr.* **17**, 11 (1965).
33. T. R. Ittyerah, *Clin. Chim. Acta* **25**, 365 (1969).
34. D. H. Baker, *Prog. Food Nutr. Sci.* **10**, 133 (1986).
35. N. Orentreich, J. R. Matias, A. DeFelice, J. A. Zimmerman, *J. Nutr.* **123**, 269 (1993).
36. M. Mori, S. Manabe, K. Uenishi, S. Sakamoto, *Tokushima J. Exp. Med.* **40**, 35 (1993).
37. J. K. Nicholson, J. A. Timbrell, P. J. Sadler, *Mol. Pharmacol.* **27**, 644 (1985).

**Acknowledgments:** We thank S. Wagoner, J. Manchester, and M. Meier for superb technical assistance; J. Manchester, S. Deng, and J. Hoisington-López for assistance with DNA sequencing; M. Karlsson, D. O'Donnell, and S. Wagoner for help with gnotobiotic mouse husbandry; W. Van Treuren for writing several scripts, B. Mickelson (Teklad Diets) and H. Sandige for assistance with the design of the mouse diets; and members of the Gordon lab for valuable suggestions during the course of this work. This work was supported by

grants from the Bill & Melinda Gates Foundation, and the NIH (DK30292, DK078669, T32-HD049338). M.I.S. was the recipient of a postdoctoral fellowship from the St. Louis Children's Discovery Institute (MD112009-201). J.V.L. was the recipient of an Imperial College Junior Research Fellowship. Illumina V4-16S rRNA and 454 shotgun pyrosequencing data sets have been deposited with the European Bioinformatics Institute. Specifically, human: V4-16S rRNA data sets (ERP001928) and shotgun sequencing data sets (ERP001911). Mouse: gnotobiotic recipients of discordant twin pair 196: V4-16S rRNA data sets (ERP001861); gnotobiotic recipients of discordant twin pair 196: shotgun sequencing data sets (ERP001819); gnotobiotic recipients of discordant twin pair 57: V4-16S rRNA data sets (ERP001871); gnotobiotic recipients of discordant twin pair 57: shotgun sequencing data sets (ERP001909). Twin pairs were recruited through health centers located in Makhwira, Mitondo, M'biza, Chamba, and Mayaka. Recruitment of participants for the present study, clinical protocols, sample collection procedures, and informed consent documents were all reviewed and approved by the College of Medicine Research Ethics Committee of the University of Malawi and by the Human Research Protection Office of Washington University in St. Louis. All experiments involving mice were performed using protocols approved by the Washington University Animal Studies Committee. Author contributions: M.I.S., T.Y., and J.I.G. designed the experiments; M.J.M. designed and implemented the clinical monitoring and sampling for the trial; R.M. and I.T. participated in patient recruitment, sample collection, sample preservation, and clinical evaluations; M.I.S. performed experiments involving gnotobiotic mice, whereas T.Y. characterized microbiota obtained from twins; M.I.S., T.Y., J.C., A.L.K., S.S.R., P.C., J.C.M., J.L., E. Houpt, J.V.L., E. Holmes, and J.N. generated data; M.I.S., T.Y., E. Holmes, J.N., D.K. L.K.U., R.K., and J.I.G. analyzed the results; and M.I.S., T.Y., and J.I.G. wrote the paper.

## Supplementary Materials

[www.sciencemag.org/cgi/content/full/339/6119/548/DC1](http://www.sciencemag.org/cgi/content/full/339/6119/548/DC1)  
Materials and Methods  
Supplementary Text  
Figs. S1 to S15  
Tables S1 to S10  
References (38–54)

17 August 2012; accepted 10 December 2012  
10.1126/science.1229000

## REPORTS

# A Clock Directly Linking Time to a Particle's Mass

Shau-Yu Lan,<sup>1</sup> Pei-Chen Kuan,<sup>1</sup> Brian Estey,<sup>1</sup> Damon English,<sup>1</sup> Justin M. Brown,<sup>1</sup> Michael A. Hohensee,<sup>1</sup> Holger Müller<sup>1,2\*</sup>

Historically, time measurements have been based on oscillation frequencies in systems of particles, from the motion of celestial bodies to atomic transitions. Relativity and quantum mechanics show that even a single particle of mass  $m$  determines a Compton frequency  $\omega_0 = mc^2/\hbar$ , where  $c$  is the speed of light and  $\hbar$  is Planck's constant  $h$  divided by  $2\pi$ . A clock referenced to  $\omega_0$  would enable high-precision mass measurements and a fundamental definition of the second. We demonstrate such a clock using an optical frequency comb to self-reference a Ramsey-Bordé atom interferometer and synchronize an oscillator at a subharmonic of  $\omega_0$ . This directly demonstrates the connection between time and mass. It allows measurement of microscopic masses with  $4 \times 10^{-9}$  accuracy in the proposed revision to SI units. Together with the Avogadro project, it yields calibrated kilograms.

A particle with mass-energy  $E = mc^2$  is represented by a wave oscillating at the Compton frequency  $\omega_0 = mc^2/\hbar$  in the particle's rest frame, where  $c$  is the speed of light

and  $\hbar$  is Planck's constant  $h$  divided by  $2\pi$  (1). This is the basis of de Broglie's theory of matter waves (2) and underpins modern quantum mechanics and field theory: The time evolution of

states is given by wave equations whose plane-wave solutions are proportional to

$$e^{-i\phi} = \exp(-ip_\mu x^\mu/\hbar) = \exp(-i\omega_0\tau) \quad (1)$$

where  $p_\mu = (-m\gamma, m\gamma\mathbf{v})$  and  $x^\mu$  are the momentum and position four-vector,  $\tau = t/\gamma$  is the proper time,  $\gamma$  is the Lorentz factor, and  $\mathbf{v}$  and  $t$  are the laboratory-frame velocity and time. Much has been theorized about the physical reality of quantum states as “oscillators” (3–7), but surprisingly few experiments have been proposed to address this topic (8). Here, we directly address a consequence of Eq. 1 that has deep physical and perhaps even cosmological implications: Because the oscillations of a wave packet accumulate phase  $\omega_0\tau$  just like a clock following the same

<sup>1</sup>Department of Physics, 366 Le Conte Hall MS7300, University of California, Berkeley, CA 94720, USA. <sup>2</sup>Lawrence Berkeley National Laboratory, One Cyclotron Road, Berkeley, CA 94720, USA.

\*To whom correspondence should be addressed. E-mail: hm@berkeley.edu

trajectory, it has been suggested that the passage of time is observable as soon as the universe contains massive particles ( $I$ ). It ought to be possible to build a Compton clock: a clock referenced to the mass of a single particle.

Advances in timekeeping (9–12) have followed the use of references with higher frequency, increased quality factor  $Q$ , and lowered instability from systematic influences. The Compton frequency of a stable particle is high ( $\omega_0/2\pi = 3 \times 10^{25}$  Hz for a cesium atom), has virtually infinite quality factor  $Q = \omega_0/T$ , where  $1/T$  is the particle's  $1/e$  lifetime, and is one of the most stable quantities in nature. In principle, a Compton-frequency clock could be built by annihilating a particle-antiparticle pair and counting the frequencies of the generated photons. However, this frequency is far beyond modern counting techniques; to access it, we require a method of dividing it into a technically accessible range.

Here, we present a Compton clock by combining an atom interferometer with an optical frequency comb. In a Ramsey-Bordé atom interferometer (Fig. 1) (7, 13), a quantum wave packet initially at rest interacts with a pulse of two counterpropagating laser beams having laboratory-frame frequencies of  $\omega_{\pm}$  and wavenumbers of  $k_{\pm}$ , respectively. The wave packet absorbs  $n$  photons from the first beam while being stimulated to emit  $n$  photons into the second beam, without modifying its internal state through multiphoton Bragg diffraction (14, 15). By appropriate choice of the laser intensity and pulse duration, the process occurs with a probability of 50%, splitting the wave packet. While the first partial wave packet remains at rest, the second moves away with a laboratory-frame momentum  $p = n\hbar(k_+ + k_-)$ . It is convenient to introduce a rapidity parameter  $\rho$  so that  $p = mc \sinh(\rho)$  and the Lorentz factor  $\gamma = [1 - v^2/c^2]^{-1/2} = \cosh(\rho)$ . Energy-momentum conservation (the Bragg condition) provides the relation

$$\omega_{\pm} = \omega_L e^{\pm \rho/2} \quad (2)$$

where  $\omega_L = \omega_0 \sinh(\rho/2)/n$ . [In the nonrelativistic limit,  $\omega_L \approx (\omega_+ + \omega_-)/2 \approx kc$  and  $\omega_{\pm} \approx \omega_L(1 \pm n\hbar k/mc)$ .] Interaction with four laser pulses (Fig. 1) brings the wave packets together for interference.

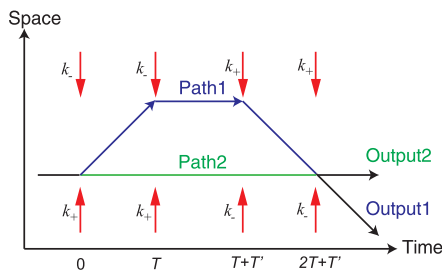


**Fig. 1.** Paths of the matter waves in a Ramsey-Bordé interferometer versus time; red arrows denote laser beams. Additional paths that do not interfere are not shown. The diagram is drawn in a freely falling inertial frame, and does not show the free fall of the atoms.

The probability of detecting the particle at the outputs (Fig. 1) is given by  $\cos^2(\Delta\phi/2)$ , where  $\Delta\phi$  is the relative phase of the wave packets. In a relativistic, semiclassical treatment, Eq. 1 shows that the wave packets acquire a relative phase of  $\Delta\phi_{\text{free}} = \omega_0[\tau^{(1)} - \tau^{(2)}] = 2\omega_0 T(\gamma^{-1} - 1)$  (non-relativistically,  $\Delta\phi_{\text{free}} \approx -4n^2 \hbar k^2 T/m$ ) during their free evolution between the laser pulses (3), where  $\tau^{(1,2)}$  are the proper times on paths 1 and 2. Their difference  $\tau^{(1)} - \tau^{(2)}$  is related to the laboratory-frame time by a factor  $\gamma^{-1} - 1$ , which is determined by the laser frequencies by Eq. 2 and can be used to divide the Compton frequency into a technically accessible range. Synchronizing an oscillator to the divided Compton frequency is accomplished as follows: In the experiment, this oscillator sets the frequency difference  $\omega_m \equiv \omega_+ - \omega_-$  between the counterpropagating laser beams. Whenever the particle absorbs a photon, the phase of the photon is added to the wave packet's phase and subtracted for stimulated emission. It can be shown (16) that the sum  $\Delta\phi_{\text{laser}}$  of these phases (eq. S2) cancels the free evolution phase  $\Delta\phi_{\text{free}}$  exactly if, and only if,  $\omega_{\pm}$  satisfy Eq. 2, so that

$$\omega_m = \frac{2n\omega_L^2}{\omega_0} \quad (3)$$

The phase cancellation  $\Delta\phi = \Delta\phi_{\text{laser}} + \Delta\phi_{\text{free}} = 0$  is verified by observing the interference fringes of the particle at the interferometer output and maintained by feedback to the oscillator.

Ramsey-Bordé interferometers are routinely used to measure  $\hbar/m$  (17), but such measurements of  $\hbar/m$  are not themselves clocks because they are reliant upon an external frequency reference to measure  $\omega_L$ . We use an optical frequency comb

to set  $\omega_L = N\omega_m$ , eliminating the laser frequency as a free parameter. Combined with Eq. 3, we obtain

$$\omega_m = \frac{\omega_0}{(2nN^2)} \quad (4)$$

which is an exact result in this relativistic and semiclassical picture, showing that  $\omega_m$  is determined solely by the Compton frequency. Corrections from nonclassical paths are negligible here. We are free to choose any value for  $n$  and  $N$  and lock the oscillator directly to the Compton frequency or a subharmonic without changing the underlying physics. For example,  $n = 2$  and  $N = 1/2$  yields  $\omega_0 = \omega_m = 2\omega_L$  and  $\omega_{\pm} = \omega_L(1 \pm \sqrt{2})^{\pm 1}$ . In practice,  $N$  is chosen so that  $\omega_L$  and  $\omega_m$  are accessible to existing technologies. The experiment is a Compton clock by virtue of the fact that it self-references the laser frequency through the optical frequency comb, which ensures that the output frequency  $\omega_m$  is fully determined by the Compton frequency and known ratios. It is independent of any external standards. The self-referenced atom interferometer serves as a clockwork that links the frequency of our master oscillator to the Compton frequency of the matter wave packets.

Our experiment uses cesium-133 atoms because they are amenable to the techniques of atom optics and are electrically neutral, which reduces systematic effects. Because their internal structure is not relevant to  $\omega_m$ , the atoms approximate noninteracting point masses. Our atom interferometer has been described in detail elsewhere (15). The clock's operation is illustrated in Fig. 2. A voltage-controlled 10-MHz crystal oscillator O1 [FTS 1050A (Symmetricom, Beverly, MA)] with frequency  $\omega_{\text{cryst}}$  is the master oscillator for all

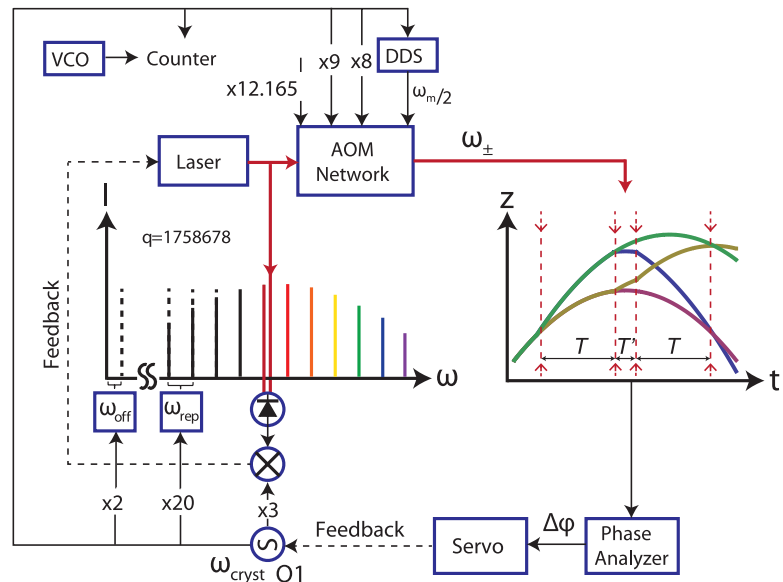


**Fig. 2.** Schematic. Oscillator O1 is the frequency reference for all signal generators and the optical frequency comb. The laser used to address the atom interferometer is phase-locked to the comb. Shown in the diagram is the freely falling atomic trajectories versus time for the simultaneous conjugate interferometers (the lower of which being shown in Fig. 1) used to cancel the gravity-induced phase. The phase measurement from the atom interferometer provides an error signal to O1 in order to close the feedback loop.



frequency sources, pulse generators, and lasers involved in the experiment. The frequency comb stabilizes the laser frequency to  $N_c\omega_{\text{cryst}}$ , where  $N_c = 35,173,594.165$  (16). A direct digital synthesizer (DDS) generates  $\omega_m/2 = N_{\text{DDS}}\omega_{\text{cryst}}$  at  $\sim 82$  kHz, and acousto-optical modulators (AOMs) generate  $\omega_{\pm}$  by applying the relation  $\omega_{\pm} = \omega_L \pm \omega_m/2$  (valid in the nonrelativistic limit), where  $N_{\text{DDS}} = 2,326,621,801,616/2^{48}$ . The factor  $N$  is thus  $N = N_c/N_{\text{DDS}} = 4,255,305,521.31286$ . Another AOM shapes the time domain profile of the laser pulses. Our signal to noise is optimal for 5th-order Bragg diffraction ( $n = 5$ ) with a pulse separation time (Fig. 1)  $T = 160$  ms. The atomic population at the interferometer output is determined by means of fluorescence detection and then processed to yield the interferometer phase  $\Delta\phi = \Delta\phi_{\text{laser}} + \Delta\phi_{\text{free}}$ .

A feedback loop adjusts  $\omega_{\text{cryst}}$  so as to maintain  $\Delta\phi = 0$ . Its operation is demonstrated in Fig. 3: The first 10 data points are taken during normal operation. At the 11th data point, we briefly disable the feedback, so that  $\omega_{\text{cryst}}$  is free-running, and the experiment performs a Ramsey-Bordé photon recoil measurement. The measured signal is then proportional to  $\omega_L^2 = (N_c\omega_{\text{cryst}})^2$  (Eq. 3).

Increasing  $N_c$  by 100 parts per billion (ppb) increases  $\omega_L$  and produces a 200-ppb increase in  $\Delta\phi_{\text{free}}$  (Fig. 3, shaded area). At the 13th data point, the feedback is restored. Because the feedback stabilizes  $\omega_{\text{cryst}}$  to a value inversely proportional to  $N_c^2$  (Eq. 4), the signal frequency decreases by 400 ppb, equilibrating 200 ppb lower than the first 10 data points (Fig. 3), which is opposite to the observed shift for a recoil measurement.

Quantitative agreement is demonstrated by comparing the rest-mass stabilized frequency  $\omega_{\text{cryst}}$  with a rubidium frequency standard [SRS FS725 (Stanford Research Systems, Sunnyvale, CA)] over 6 hours (Fig. 4A). It averages to 9,999,998.127 Hz with a SD of the mean of 0.015 Hz. A  $\chi^2$  test (Fig. 4B) yields a normalized  $\chi^2 = 1.4$ . Our statistical uncertainty is  $0.015 \text{ Hz} \times (\chi^2)^{1/2} = 0.018 \text{ Hz}$ , or 1.8 ppb. Using Eq. 4 and correcting for systematic effects (16), we obtain the Compton frequency  $\omega_0/2\pi = (2,993,486,252 \pm 12) \times 10^{16} \text{ Hz}$ . The deviation from the expected values (16, 18) is  $-5.2 \pm 4.0$  ppb and is consistent with zero within  $2\sigma$ . The Allan variance (Fig. 4C) is below  $10^{-8}/[\tau/(1000 \text{ s})]^{1/2}$ , where  $\tau$  is the integration time.

Although this accuracy is modest, similar to the first cesium atomic clocks (9), the resolution and accuracy of atom interferometry is advancing rapidly (19). Up to 100-fold improvement in resolution could be obtained by approaching the shot noise limit of our interferometer. Use of higher laser frequencies (which is possible without changing the reference particle), lighter particles, and/or longer interrogation times can possibly lead to a Compton clock that can serve as a primary time standard. The intrinsic stability and  $Q$  factor of a stable particle's Compton frequency is unmatched by any other frequency reference. Mass, frequency, time, and length could all be derived from one fundamental unit, defined by a specific particle.

The clock can also be used for the opposite purpose, measuring mass by measuring the Compton frequency. In 2011, the General Conference on Weights and Measures (CGPM-2011) considered a revision to the SI units that would assign an exact value to the Planck constant  $h$  (20). The kilogram would then be referenced to the second through the defined values of the Planck constant and the speed of light. Microscopic masses could be related to the fine structure constant (21, 22) or  $h/M$  (17); macroscopic masses could be measured by using the Watt balance (23, 24). These methods, however, require auxiliary measurements and/or intricate theory (16). The Compton clock would provide an absolute measurement of the cesium atom's mass to an accuracy of 4.0 ppb, which is competitive with other methods and greater than 10 times more accurate than in the present SI (18). Other microscopic masses can be related to the cesium mass by means of mass spectroscopy.

The link to macroscopic masses can be made by Avogadro spheres: silicon crystals of accurately measured volume  $V$  and lattice constant  $a$  (25). In theory, the number of atoms contained in such a crystal is  $N_{\text{at}} = 8V/a^3$ , where 8 is the number of atoms in the unit cell. Because binding energies are negligible, the Compton frequency of the sphere is  $\omega_M = [m(\text{Si})/m(^{133}\text{Cs})]N_{\text{at}}\omega_{\text{Cs}}$ , given by the measured Compton frequency of

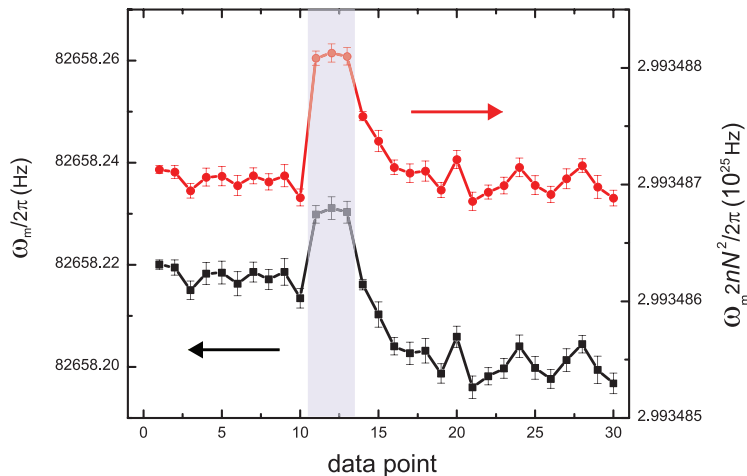


**Fig. 3.** Measured frequency  $\omega_m$  (lower trace; left axis) as well as  $\omega_m(2nN^2)$  (upper trace; right axis) shows the action of the feedback loop. During the shaded interval, the feedback is disabled.

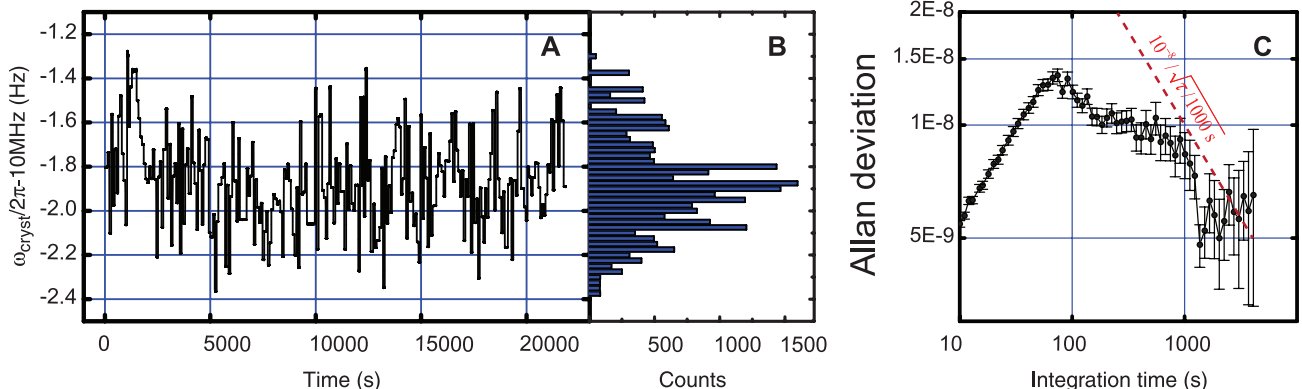


**Fig. 4.** Compton clock performance. (A) Frequency minus 10 MHz versus time plotted over  $\sim 6$  hours. (B) Histogram of data (bin size = 0.025 Hz). (C) Root Allan variance (RAV) of the data in (A). It is  $<10^{-8}/(\tau/1000 \text{ s})^{1/2}$  between integration times  $\tau$  of  $\sim 100$  s and  $\sim 1$  hour. The slope between  $\tau = 10$  and 100 s is an artifact of the 80-s update cycle of the experiment.

cesium atoms  $\omega_{\text{Cs}}$ . This yields its mass as  $M = \omega_{\text{M}} h/c^2$ . The ratio  $m(\text{Si})/m(^{133}\text{Cs})$  is between the effective molar mass of the sphere's material and cesium-133. According to (25), present data yields the spheres' mass with an overall accuracy of 30 ppb so that they would constitute the most accurately calibrated macroscopic masses under the proposed CGPM-2011 redefinition—a testament to the precision achieved in constructing Avogadro spheres.

Although any method for measuring microscopic mass can be used, the Compton clock offers a transparent connection between the second and a microscopic mass on the basis of simple physical principles without requiring auxiliary measurements. It directly realizes a long-standing proposal to measure mass in terms of the Compton frequency (6). The method outlined here offers a different set of systematic effects as compared with Watt balances (23, 24), thus serving as an important test of the overall consistency of the laws of physics and experimental methods. It is based on a body's inertial rather than gravitational mass. In the context of the present SI, the combination of the Avogadro project and the Compton clock serves as a measurement of the Planck constant.

Looking forward, the rapidly developing field of optomechanics (26) might enable measurements of the single-photon recoil energy of a nanomechanical mirror. This could result in a clock referenced to the mass of a mesoscopic object, or a mesoscopic mass standard. Because Bragg diffraction of electrons has already been demonstrated (27), a clock using elementary par-

ticles or even antiparticles is possible. Such clocks would be useful for testing CPT symmetry or the Einstein Equivalence Principle for antimatter.

We have demonstrated a clock stabilized to the rest mass of a particle. It highlights the intimate connection between frequency and mass. It proves that massive particles can serve as a frequency reference without requiring their mass to be converted to energy as an explicit illustration of a key principle of quantum mechanics. Furthermore, we have shown that a single massive particle is sufficient to measure time.

#### References and Notes

1. R. Penrose, *Cycles of Time: An Extraordinary View of the Universe* (Knopf, New York, 2011), sec. 2.3.
2. L. De Broglie, thesis, University of Paris, Paris, France (1924).
3. H. Müller, A. Peters, S. Chu, *Nature* **463**, 926 (2010).
4. M. A. Hohensee, S. Chu, A. Peters, H. Müller, *Phys. Rev. Lett.* **106**, 151102 (2011).
5. P. Wolf *et al.*, *Class. Quantum Gravity* **28**, 145017 (2011).
6. J. W. G. Wignall, *Phys. Rev. Lett.* **68**, 5 (1992).
7. Ch. J. Bordé, *Eur. Phys. J. Spec. Top.* **163**, 315 (2008).
8. M. A. Hohensee, B. Estey, P. Hamilton, A. Zeilinger, H. Müller, *Phys. Rev. Lett.* **108**, 230404 (2012).
9. L. Essen, J. V. L. Parry, *Nature* **176**, 280 (1955).
10. T. E. Parker, *Metrologia* **47**, 1 (2010).
11. A. D. Ludlow *et al.*, *Science* **319**, 1805 (2008).
12. C. W. Chou, D. B. Hume, J. C. J. Koelemeij, D. J. Wineland, T. Rosenband, *Phys. Rev. Lett.* **104**, 070802 (2010).
13. A. D. Cronin, J. Schmiedmayer, D. E. Pritchard, *Rev. Mod. Phys.* **81**, 1051 (2009).
14. H. Müller, S.-W. Chiow, Q. Long, S. Herrmann, S. Chu, *Phys. Rev. Lett.* **100**, 180405 (2008).
15. S.-Y. Lan, P.-C. Kuan, B. Estey, P. Haslinger, H. Müller, *Phys. Rev. Lett.* **108**, 090402 (2012).
16. Materials and methods are available as supplementary materials on Science Online.
17. R. Bouchendira, P. Cladé, S. Guellati-Khélifa, F. Nez, F. Biraben, *Phys. Rev. Lett.* **106**, 080801 (2011).

18. P. J. Mohr, B. N. Taylor, D. B. Newell, *The 2010 CODATA Recommended Values of the Fundamental Physical Constants* (Web Version 6.0); <http://physics.nist.gov/constants>.
19. S. Dimopoulos, P. W. Graham, J. M. Hogan, M. A. Kasevich, *Phys. Rev. Lett.* **98**, 111102 (2007).
20. "Resolution 1: On the possible future revision of the International System of Units, the SI," General Conference on Weights and Measures, Sèvres, France, 17 to 21 October 2011.
21. D. Hanneke, S. Fogwell, G. Gabrielse, *Phys. Rev. Lett.* **100**, 120801 (2008).
22. T. Aoyama, M. Hayakawa, T. Kinoshita, M. Nio, *Phys. Rev. Lett.* **109**, 111807 (2012).
23. I. A. Robinson, B. P. Kibble, *Metrologia* **44**, 427 (2007).
24. R. L. Steiner, E. R. Williams, R. Liu, D. B. Newell, *IEEE Trans. Instrum. Meas.* **56**, 592 (2007).
25. B. Andreas *et al.*, *Phys. Rev. Lett.* **106**, 030801 (2011).
26. T. J. Kippenberg, K. J. Vahala, *Science* **321**, 1172 (2008).
27. D. L. Freimund, H. Batelaan, *Phys. Rev. Lett.* **89**, 283602 (2002).

**Acknowledgments:** We thank S. Chu, P. Hamilton, and M. Kasevich for stimulating discussions; D. Budker, P. Kehaiyas, G. Kim, M. Xu, E. Ronayne Sohr, and D. Schlippert for experimental assistance; and A. Brachmann, R. Falcone, and W. E. White for providing a laser. J.M.B. acknowledges support by the Miller Institute for Basic Research in Science. This work was supported by the Alfred P. Sloan Foundation, the David and Lucile Packard Foundation, the National Institute of Standards and Technology, the National Science Foundation, and the National Aeronautics and Space Administration.

#### Supplementary Materials

[www.sciencemag.org/cgi/content/full/science.1230767/DC1](http://www.sciencemag.org/cgi/content/full/science.1230767/DC1)

Materials and Methods

Supplementary Text

Figs. S1 and S2

Table S1

References (28–32)

26 September 2012; accepted 20 November 2012

Published online 10 January 2013;

10.1126/science.1230767

# Nanoscale Nuclear Magnetic Resonance with a Nitrogen-Vacancy Spin Sensor

H. J. Mamin,<sup>1</sup> M. Kim,<sup>1,2</sup> M. H. Sherwood,<sup>1</sup> C. T. Rettner,<sup>1</sup> K. Ohno,<sup>3</sup> D. D. Awschalom,<sup>3</sup> D. Rugar<sup>1\*</sup>

Extension of nuclear magnetic resonance (NMR) to nanoscale samples has been a longstanding challenge because of the insensitivity of conventional detection methods. We demonstrated the use of an individual, near-surface nitrogen-vacancy (NV) center in diamond as a sensor to detect proton NMR in an organic sample located external to the diamond. Using a combination of electron spin echoes and proton spin manipulation, we showed that the NV center senses the nanotesla field fluctuations from the protons, enabling both time-domain and spectroscopic NMR measurements on the nanometer scale.

Both nuclear magnetic resonance (NMR) spectroscopy and magnetic resonance imaging (MRI) have become indispensable

tools in many diverse fields of research, including analytical chemistry, materials science, structural biology, neuroscience, and medicine (1). The one major deficiency of NMR is the low sensitivity of the conventional coil-based induction method of detection, which prevents its application to samples at the nanometer scale (2). Much improved detection sensitivity has been achieved with magnetic resonance force microscopy, which is based on detecting weak magnetic forces in

the presence of a strong field gradient and has demonstrated nanometer-scale NMR imaging at cryogenic temperatures (3). Here, we present an alternative nanoscale detection method that works in the absence of a magnetic field gradient, thus preserving spectroscopic information, and is operable over a wide range of temperatures, including room temperature. A single near-surface nitrogen-vacancy (NV) center in diamond is used as an atomic-size sensor to detect weak magnetic fields originating from nuclear spins external to the diamond. In an initial demonstration, we detected randomly polarized hydrogen nuclei (protons) in an organic polymer. Both time domain and spectroscopic information were obtained by appropriately manipulating the protons so as to affect the precession phase of the highly coherent NV electron spin. The results suggest that NV-based NMR detection may provide a path toward three-dimensional nanoscale magnetic resonance imaging (nanoMRI) under ambient conditions (4, 5).

NV centers are proving to be particularly useful for both quantum information processing and nanoscale magnetic sensing (6–11). The negatively charged center has a spin state with a long coherence time, especially in isotopically purified crystals (12, 13), and an electronic-level structure

<sup>1</sup>IBM Research Division, Almaden Research Center, San Jose, CA 95120, USA. <sup>2</sup>Center for Probing the Nanoscale, Stanford University, Stanford, CA 94305, USA. <sup>3</sup>Center for Spintronics and Quantum Computation, University of California, Santa Barbara, CA 93106, USA.

\*To whom correspondence should be addressed. E-mail: [rugar@us.ibm.com](mailto:rugar@us.ibm.com)



that enables a convenient optical initialization and readout of the spin state. Much previous work has concentrated on the interactions of NV centers with nuclear spins internal to the diamond lattice (14–17), but nanoMRI requires the detection of external nuclear spins.

The key to effective external spin sensing is to have the NV center positioned near the diamond surface while maintaining a long spin coherence time (18–20). The spin coherence in diamond can be adversely affected by magnetic fluctuations from  $^{13}\text{C}$  nuclear spins and various paramagnetic centers, such as nitrogen P1 centers and surface dangling bonds (21). In our experiments, the NV center was embedded in a layer of isotopically pure  $^{12}\text{C}$  diamond grown epitaxially on top of an electronic grade (001)-oriented diamond substrate by plasma-enhanced chemical vapor deposition (Fig. 1A). NV centers were formed ~20 nm below the surface by briefly introducing  $^{15}\text{N}_2$  gas during the growth process, followed by electron irradiation to create vacancies and annealing at 850°C to mobilize the vacancies and mitigate lattice damage (13, 22). Despite their proximity to the surface, the resulting NV centers (Fig. 1B) had long electron spin coherence times  $T_{2e}$ , on the order of 600  $\mu\text{s}$  as determined by Hahn spin echo measurements (Fig. 1D). This long spin coherence is critical for achieving the sensitivity required for these experiments.

The experimental apparatus consisted of a home-built scanning confocal microscope that uses 532-nm laser radiation to probe the NV center. Fluorescence from the NV center in the wavelength range of 600 to 800 nm was detected with an avalanche photodiode and gated photon counter. The fluorescence intensity is indicative of the NV spin state because the  $m_s = 0$  spin state fluoresces with ~30% greater brightness than the  $m_s = \pm 1$  states. To manipulate the spins in both the diamond and the polymer, a 3.6- $\mu\text{m}$ -wide microwire was lithographically fabricated on the diamond surface and driven by a programmable microwave (MW) synthesizer for NV spin control and a radiofrequency (RF) function generator for proton spin control. The proton-containing sample was a 60-nm-thick layer of poly(methyl methacrylate) (PMMA) with proton density  $\rho_N \approx 57 \text{ nm}^{-3}$  formed by spin casting on the diamond surface. A background magnetic field  $B_0$  of 70 to 80 mT from a permanent magnet was accurately aligned [111] axis).

Several different protocols are possible for detecting weak magnetic signals from relatively distant nuclear spins. For the detection of internal  $^{13}\text{C}$  nuclear spins, multipulse sequences, such as the Carr-Purcell-Meiboom-Gill (CPMG) sequence, have been used to selectively couple the NV center to the Larmor-frequency magnetic field emanating from freely precessing nuclei (15–17). This approach is effective when the nuclear spin precession has a  $T_{2n}^*$  correlation time comparable

to or exceeding the electron spin coherence time  $T_{2e}$  of the NV center. By contrast, for a typical solid-state organic sample, the nuclear spin correlation time is greatly reduced by strong dipolar interactions among the densely packed protons. Conventional proton NMR measurements on our PMMA material found  $T_{2n}$  and  $T_{2n}^*$  to be 18 and 14  $\mu\text{s}$ , respectively, much shorter than the 600- $\mu\text{s}$  coherence time of the NV center. Thus, there is a mismatch in the time scales, and the nuclear spin precession will not remain coherent for the full duration of a long multipulse sequence (20). Rather than sensing the Larmor precession of the protons, we coupled the NV center to the longitudinal magnetization, which has a correlation time given by the spin-lattice relaxation time  $T_{1n}$ , on the order of seconds at room temperature.

As evident in Fig. 1C, the effective sample volume probed by the NV center was small, on the order of  $(24 \text{ nm})^3$ . Because of the small volume and low polarizing magnetic field, the proton polarization was dominated by  $\sqrt{N}$  statistical fluctuations, where the number of protons  $N$  was of order  $10^6$  (23). Although the mean proton polarization was negligible, statistical fluctuations of the longitudinal polarization were detected by their effect on the phase of the NV spin precession (20, 24–27). We started by polarizing the NV center to the  $m_s = 0$  spin state with a 4- $\mu\text{s}$  laser pulse (Fig. 2A). The NV center was then driven with MW pulses in a spin echo sequence with total echo time  $\tau$  in the range of 300 to 440  $\mu\text{s}$ . Synchronous with the spin echo sequence, we applied two identical RF pulses separated in time by  $\tau/2$ , with each pulse consisting of exactly 30 sine wave cycles (approximating NMR  $\pi$  pulses). The first RF pulse set up an initial random longitudinal polarization for the first half of the echo sequence. The second RF pulse inverted this polarization for the second half. The inversion of proton polarization reversed the proton dipolar magnetic field  $B_N(t)$  acting on the NV center and upset the equivalence of the NV spin precession for the two halves of the spin echo, thus reducing the spin echo amplitude. The identical nature of the RF pulses minimized any spurious effect they might have on the NV spin echo because identical disturbances during the two halves of the echo sequence should cancel. The spin echo sequence was typically repeated several million times to accumulate sufficient photon counting

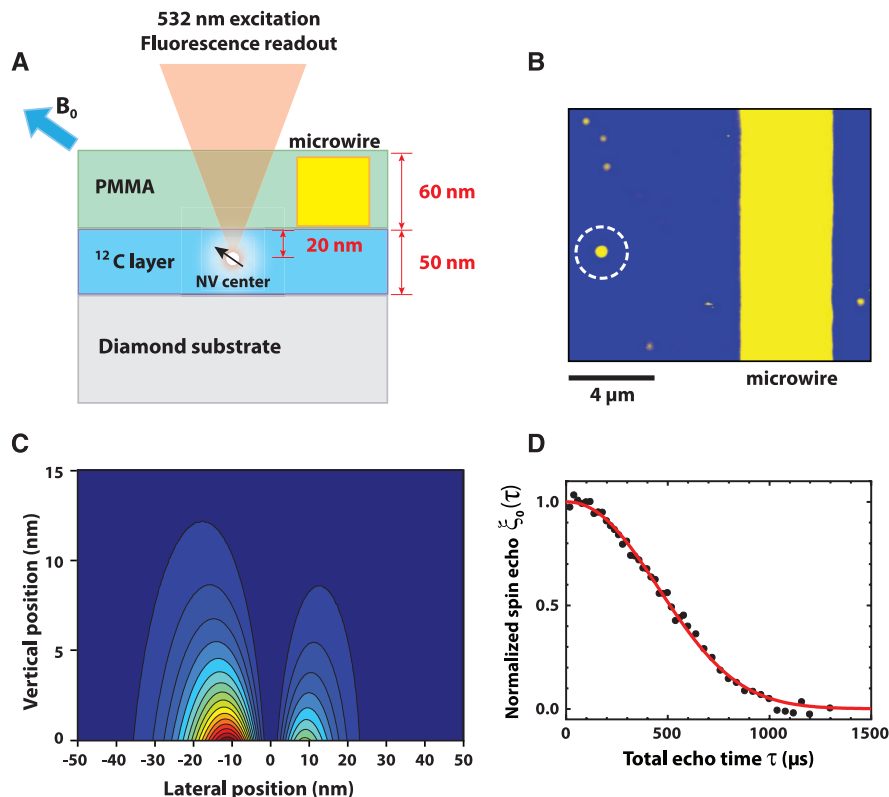


**Fig. 1.** Basic configuration of NV-NMR detection. (A) Sample geometry with [111]-oriented NV spin embedded 20-nm deep within  $^{12}\text{C}$  diamond layer. The NV center detects NMR of protons in the PMMA polymer layer. (B) Fluorescence image of sample surface showing microwire and NV center (circled). (C) Cross-section of the PMMA layer showing calculated spatial dependence of proton detection sensitivity. Half of the proton signal originates from a volume of  $(24 \text{ nm})^3$ . The two lobes are a consequence of the  $54.7^\circ$  tilt angle of the NV axis with respect to the surface normal. (D) Normalized spin echo response versus total echo time. Solid curve is a fit of measured data points using the model  $\xi_0(\tau) = \exp[-(\tau/T_{2e})^n]$ . Fit parameters give  $n = 2.17$  and  $T_{2e} = 606 \mu\text{s}$ .

statistics and to ensure that many different random polarization states of the sample protons were probed.

The spin echo response as a function of the frequency of the RF pulses (Fig. 2B) displayed distinct dips when the RF frequency matched

the proton NMR frequency. As expected, the RF frequency for the dip depended on the magnitude of the applied static field  $B_0$ . The dip frequency as a function of field was well fit by a line with slope  $42.6 \text{ MHz} \cdot \text{T}^{-1}$  (Fig. 2C), which matches the gyromagnetic ratio for protons. When the PMMA layer was removed from the diamond, the signal disappeared, indicating that the proton signal does indeed originate from the polymer and not from hydrogen contamination within the diamond (bottom curve in Fig. 2B).

The amplitude of the proton magnetic field fluctuations can be estimated from the depth of the dips in Fig. 2. The precession phase imbalance accumulated during the spin echo is given by  $\delta\phi = \gamma_0^{1/2} B_N(t) dt - \gamma_{1/2}^{1/2} B_N(t) dt$ , where  $\gamma = 2\pi \times 28 \text{ GHz} \cdot \text{T}^{-1}$  is the NV electron spin gyromagnetic ratio. Assuming  $\delta\phi$  is a normally distributed random variable with zero mean, the resulting spin echo amplitude is  $\xi(\tau) = \xi_0(\tau) \langle \cos \delta\phi \rangle = \xi_0(\tau) \exp(-\langle (\delta\phi)^2 \rangle / 2)$ . Here,  $\xi_0(\tau)$  is the normalized spin echo amplitude in the absence of proton reversals (Fig. 1D),  $\langle \dots \rangle$  indicates mean value, and  $\langle (\delta\phi)^2 \rangle$  is the variance of the accumulated phase, which depends on both the magnitude and correlation properties of the proton field fluctuations (20). For  $T_{1n} \gg \tau$ , where  $B_N(t)$  is essentially static for the duration of an individual echo sequence (except for the RF-induced inversion),  $\langle (\delta\phi)^2 \rangle = \gamma^2 \tau^2 \langle B_N^2 \rangle$ . Combining this equation with the expression for  $\xi(\tau)$ , we find  $\langle B_N^2 \rangle = (2/\gamma^2 \tau^2) \log(\xi_0(\tau)/\xi(\tau))$ , which simplifies for small fields to  $\langle B_N^2 \rangle = (2/\gamma^2 \tau^2) \Delta\xi/\xi_0(\tau)$ , where  $\Delta\xi/\xi_0(\tau) = [\xi_0(\tau) - \xi(\tau)]/\xi_0(\tau)$  is the fractional change in spin echo amplitude.

The dips in Fig. 2B had depths that were roughly  $\Delta\xi/\xi_0(\tau) = 0.20$ , which from the above expressions

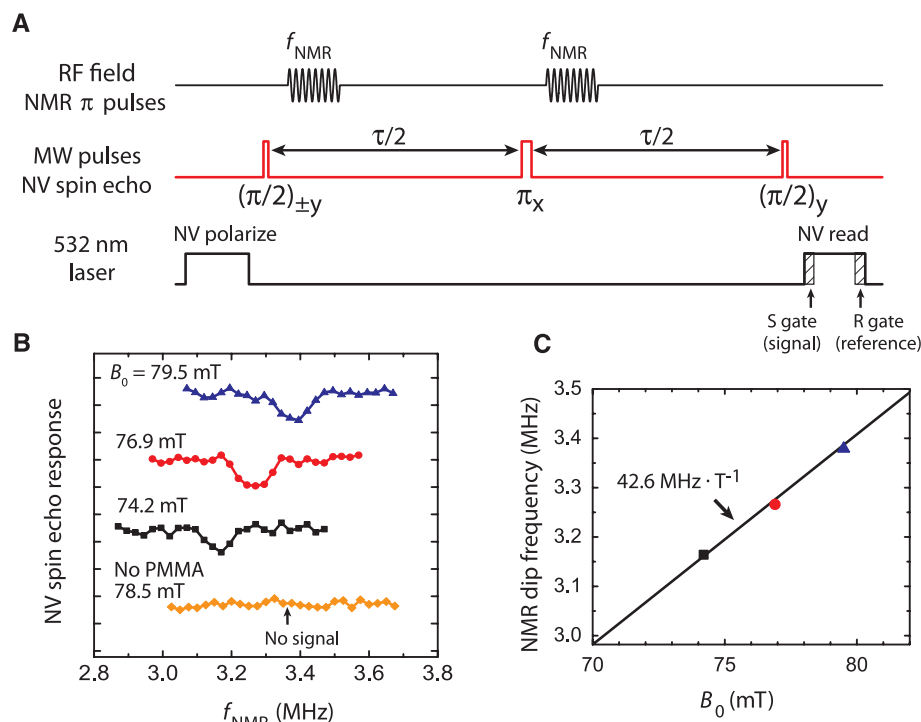
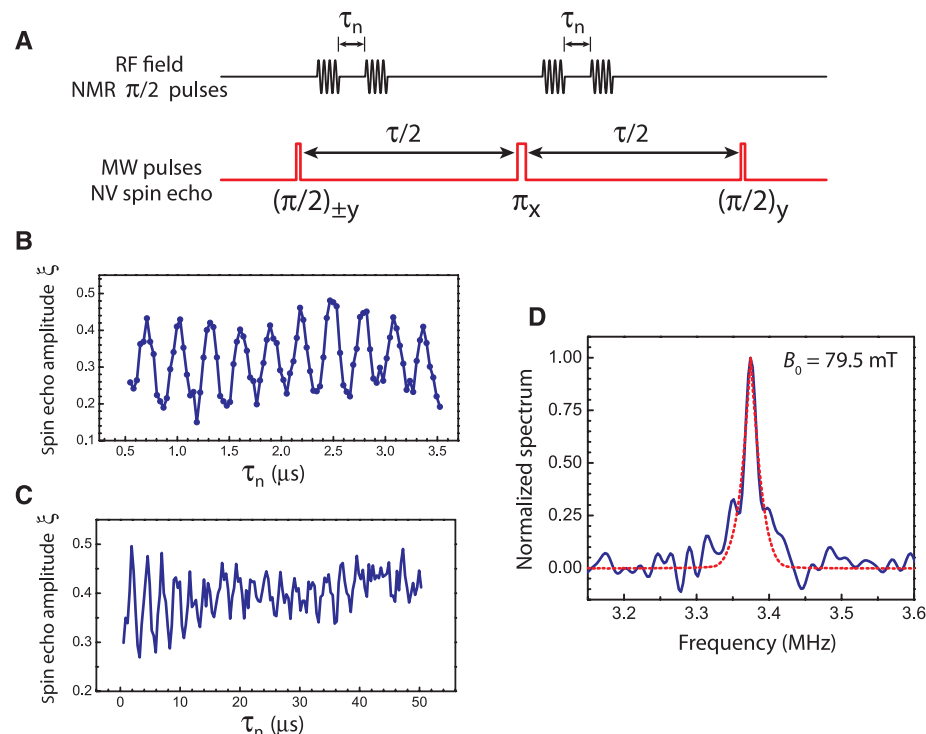


**Fig. 2.** Nanoscale NMR detection. **(A)** Pulsing scheme in which RF pulses serve to invert sample protons during the NV spin echo. Measurements are made with two different initial  $\pi/2$  pulse phases. **(B)** Relative spin echo response as a function of RF frequency. With the PMMA sample present, clear dips are seen when the RF frequency matches the proton Larmor frequency. No dip is evident after PMMA has been removed. Curves are offset vertically for clarity. Total echo time was  $300 \mu\text{s}$ . **(C)** Center frequency of dips versus external field  $B_0$ . Line shows expected dependence based on the proton gyromagnetic ratio.

**Fig. 3.** Time domain measurements and NMR spectrum taken at  $B_0 = 79.5 \text{ mT}$ . **(A)** Spin echo sequence with an RF pulsing scheme similar to a Ramsey fringe. The effectiveness of proton inversion depends on evolution time  $\tau_n$ . RF pulses consist of 15 sine wave cycles and approximate NMR  $\pi/2$  pulses. **(B)** Proton-induced oscillation of spin echo response  $\xi$  as a function of  $\tau_n$  measured in steps of  $32 \text{ ns}$ . The oscillation frequency matches the expected  $3.38\text{-MHz}$  proton precession frequency. **(C)** Proton-induced oscillation of spin echo signal for a longer record where the sampling period is  $336 \text{ ns}$ . Undersampling of the waveform causes the apparent frequency to be shifted to  $396 \text{ kHz}$  due to aliasing. Initial decay during the first  $15 \mu\text{s}$  is evident. **(D)** Solid curve: NV-based NMR spectrum obtained by cosine transform of data in (C). Frequencies have been shifted upward by  $2.976 \text{ MHz}$  to compensate for the aliasing effect. Dashed curve: Conventional  $500\text{-MHz}$  NMR proton spectrum of PMMA that has been plotted to overlay the NV-based spectrum.





gives the root-mean-square magnetic field  $B_{\text{rms}} \equiv \langle B_N^2 \rangle^{1/2} = 12$  nT-rms, a value substantially less than expected. For a thick polymer layer, the field was expected to be  $B_{\text{rms}} \approx C \mu_0 \mu_p \rho_N^{1/2} / d^{3/2}$ , where  $C = 1/8\sqrt{2\pi} \approx 0.050$ ,  $\mu_0$  is the permeability of free space,  $\mu_p$  is the proton magnetic moment, and  $d$  is the depth of the NV center (22, 24). Assuming a NV depth of 20 nm gives  $B_{\text{rms}} = 75$  nT-rms, substantially greater than the experimental value. The cause of this discrepancy is not presently understood, but could be the result of greater-than-expected NV depth or inefficiency in the proton inversions by less-than-ideal RF field amplitude (estimated to be about 1 mT).

The signal-versus-frequency curves in Fig. 2B represent a crude form of NMR spectroscopy, but the dips are broadened by the amplitude of the RF pulses. To obtain higher spectral resolution, we implemented a Fourier transform technique resembling that used in conventional high-resolution NMR spectroscopy, where a time domain “free induction decay” (FID) is Fourier transformed to obtain the NMR frequency spectrum (1). We modified our pulse sequence by splitting each RF  $\pi$  pulse into a pair of  $\pi/2$  pulses (Fig. 3A). We then incremented the spacing  $\tau_n$  of the  $\pi/2$  pulses in a manner similar to a Ramsey fringe experiment while monitoring the effect on the NV spin echo. This pulsing scheme differed from a conventional Ramsey experiment in that the frequency of the RF pulses was at the proton frequency and not at an offset frequency, and the RF pulses were not gated from a continuous-wave oscillator, but were triggered waveforms consisting of exactly 15 sine wave cycles.

As the pulse spacing  $\tau_n$  was scanned, the NV spin echo response oscillated with a period that matched the proton Larmor frequency (Fig. 3B). This time domain response is roughly equivalent to a conventional FID in NMR, but is based on the correlation of the precession of the statistical proton polarization. No oscillations were seen if the RF frequency was far off the NMR resonance (e.g., by 600 kHz) or if the PMMA was removed (fig. S2).

To obtain a longer time record, we recorded the spin echo response using coarser steps in  $\tau_n$  (Fig. 3C). The coarser steps allowed faster acquisition of a long time record, but undersampled the Larmor frequency oscillation, resulting in an “aliasing” effect where the Larmor precession frequency appeared to have shifted to a lower frequency. Despite the undersampling, the precession oscillations were clearly seen and decayed substantially during the first 15  $\mu\text{s}$ , similar to the  $T_{2n}^*$  time scale expected for PMMA. After the initial decay, some oscillations persisted to the end of the 50- $\mu\text{s}$ -long record, which was unexpected for a solid-state polymer given the short  $T_{2n}^*$ . This unexpected persistence of the apparent proton coherence is not understood, although it suggests that some component of the sample, perhaps residual solvent, has a longer than expected  $T_{2n}^*$ .

By applying a cosine transform to the time domain data, we obtained the frequency spectrum shown in Fig. 3D. The spectrum shows a single narrow peak at the proton Larmor frequency (after correcting for aliasing) with full width at half-maximum of  $\sim 20$  kHz. Some broadening at the base of the peak is also evident. For comparison, we overlay a conventional NMR spectrum taken at 11.7 T, which also shows just a single central peak with a width that closely matches that of the NV-based spectrum.

The detection of external nuclear spins using a single NV center represents an important first step toward NV-based nanoMRI. Looking forward, it is instructive to evaluate current sensitivity levels and project possible improvements in the context of future imaging experiments. For the detection of the random fields with our protocol, the minimum detectable mean-square magnetic field [i.e., with unity signal-to-noise ratio (SNR)] is given by  $B_{\text{min}}^2 = A/\gamma^2 \tau^3 T_a^{1/2}$ , where  $T_a$  is the total acquisition time (22). The parameter  $A$  characterizes the photon-counting rate and spin-dependent contrast and is given by  $A = 2\sqrt{2}(\alpha_0 + \beta_0)^{1/2}/(\alpha_0 - \beta_0)\xi_0(\tau)$ , where  $\alpha_0$  and  $\beta_0$  are the average number of photons detected per echo for the NV in the  $m_s = 0$  and  $\pm 1$  states, respectively. Under the present conditions of  $\alpha_0 = 0.02$ ,  $\beta_0 = 0.014$ ,  $\tau = 440$   $\mu\text{s}$ , and  $\xi_0(\tau) = 0.60$ , and assuming the longest practical dwell time for an imaging application to be  $T_a = 60$  s, we find that  $B_{\text{min}} = 8$  nT-rms.

Using the results of numerical calculations, we can interpret the minimum detectable field in terms of the volume of protons needed to produce such a field (22). Assuming a cubic volume element (voxel) located 20 nm above the NV center on the diamond surface, we find that the voxel size producing 8 nT-rms is  $(4.3 \text{ nm})^3$ . Here, we have taken into account the  $54.7^\circ$  angle between the [111]-oriented spins and the (001) surface normal and assumed optimal lateral placement of the voxel. If we require a signal-to-noise ratio of 10, the corresponding volume element would be  $(12 \text{ nm})^3$ . Many technical improvements in NV signal detection have been previously demonstrated that would enhance the spin sensitivity even further. For example, if we assume a fivefold improvement of fluorescence detection using microfabricated photonic structures (18, 28) and a reduction of NV center depth to 5 nm with  $T_{2e} = 200$   $\mu\text{s}$  (13), we find that  $B_{\text{min}} = 15$  nT-rms for a 60-s acquisition time. The reduced NV depth would greatly improve the sensitivity to the protons on the surface, yielding unity SNR for a volume element of only  $(0.2 \text{ nm})^3$ , essentially single-proton sensitivity, if a (111)-oriented diamond surface is assumed. If we demand a SNR of 10 and require the ability to image at least 5 nm deep into the sample, the corresponding volume element is  $(1.8 \text{ nm})^3$ . Although many technical issues still remain, the potential for three-dimensional nanoscale imaging with room-temperature operation, elemental selectivity, and no radiation damage suggests that NV-based nanoMRI could become

an important complement to current state-of-the-art molecular imaging techniques, such as cryo-electron tomography (29) and noncontact atomic force microscopy (30).

## References and Notes

1. R. R. Ernst, G. Bodenhausen, A. Wokaun, *Nuclear Magnetic Resonance in One and Two Dimensions* (Oxford Univ. Press, Oxford, 1987).
2. P. Glover, S. P. Mansfield, *Rep. Prog. Phys.* **65**, 1489 (2002).
3. C. L. Degen, M. Poggio, H. J. Mamin, C. T. Rettner, D. Rugar, *Proc. Natl. Acad. Sci. U.S.A.* **106**, 1313 (2009).
4. C. L. Degen, *Appl. Phys. Lett.* **92**, 243111 (2008).
5. B. M. Chernobrod, G. P. Berman, *J. Appl. Phys.* **97**, 014903 (2005).
6. A. Gruber *et al.*, *Science* **276**, 1202 (1997).
7. R. J. Epstein, F. M. Mendoza, Y. K. Kato, D. D. Awschalom, *Nat. Phys.* **1**, 94 (2005).
8. M. S. Grinolds *et al.*, *Nat. Phys.* **7**, 687 (2011).
9. F. Jelezko *et al.*, *Phys. Rev. Lett.* **93**, 130501 (2004).
10. J. R. Maze *et al.*, *Nature* **455**, 644 (2008).
11. G. Balasubramanian *et al.*, *Nature* **455**, 648 (2008).
12. G. Balasubramanian *et al.*, *Nat. Mater.* **8**, 383 (2009).
13. K. Ohno *et al.*, *Appl. Phys. Lett.* **101**, 082413 (2012).
14. P. Neumann *et al.*, *Science* **329**, 542 (2010).
15. N. Zhao *et al.*, *Nat. Nanotechnol.* **7**, 657 (2012).
16. T. H. Taminiau *et al.*, *Phys. Rev. Lett.* **109**, 137602 (2012).
17. S. Kolkowitz, Q. P. Unterreithmeier, S. D. Bennett, M. D. Lukin, *Phys. Rev. Lett.* **109**, 137601 (2012).
18. P. Maletinsky *et al.*, *Nat. Nanotechnol.* **7**, 320 (2012).
19. B. Grotz *et al.*, *New J. Phys.* **13**, 055004 (2011).
20. H. J. Mamin, M. H. Sherwood, D. Rugar, *Phys. Rev. B* **86**, 195422 (2012).
21. A. Laraoui, J. S. Hodges, C. A. Meriles, *Nano Lett.* **12**, 3477 (2012).
22. See supplementary materials on Science Online.
23. C. L. Degen, M. Poggio, H. J. Mamin, D. Rugar, *Phys. Rev. Lett.* **99**, 250601 (2007).
24. C. A. Meriles *et al.*, *J. Chem. Phys.* **133**, 124105 (2010).
25. A. Laraoui, J. S. Hodges, C. Ryan, C. Meriles, *Phys. Rev. B* **84**, 104301 (2011).
26. J. M. Taylor *et al.*, *Nat. Phys.* **4**, 810 (2008).
27. L. T. Hall, J. H. Cole, C. D. Hill, L. C. L. Hollenberg, *Phys. Rev. Lett.* **103**, 220802 (2009).
28. J. P. Hadden *et al.*, *Appl. Phys. Lett.* **97**, 241901 (2010).
29. E. I. Tocheva, Z. Li, G. J. Jensen, *Cold Spring Harb. Perspect. Biol.* **2**, a003442 (2010).
30. L. Gross, F. Mohn, N. Moll, P. Liljeroth, G. Meyer, *Science* **325**, 1110 (2009).

**Acknowledgments:** We thank F. Reinhard, J. Wrachtrup, P. Hemmer, and A. Bleszynski Jayich for helpful discussions. This work was supported by the Defense Advanced Research Projects Agency QuASAR program, the Air Force Office of Scientific Research, and the Center for Probing the Nanoscale at Stanford University (NSF grant PHY-0830228).

## Supplementary Materials

www.sciencemag.org/cgi/content/full/339/6119/557/DC1  
Materials and Methods  
Supplementary Text  
Figs. S1 to S3

15 October 2012; accepted 3 December 2012  
10.1126/science.1231540

# Nuclear Magnetic Resonance Spectroscopy on a (5-Nanometer)<sup>3</sup> Sample Volume

T. Staudacher,<sup>1,2</sup> F. Shi,<sup>3</sup> S. Pezzagna,<sup>4</sup> J. Meijer,<sup>4</sup> J. Du,<sup>3</sup> C. A. Meriles,<sup>5</sup>  
F. Reinhard,<sup>1\*</sup> J. Wrachtrup<sup>1</sup>

Application of nuclear magnetic resonance (NMR) spectroscopy to nanoscale samples has remained an elusive goal, achieved only with great experimental effort at subkelvin temperatures. We demonstrated detection of NMR signals from a (5-nanometer)<sup>3</sup> voxel of various fluid and solid organic samples under ambient conditions. We used an atomic-size magnetic field sensor, a single nitrogen-vacancy defect center, embedded ~7 nanometers under the surface of a bulk diamond to record NMR spectra of various samples placed on the diamond surface. Its detection volume consisted of only 10<sup>4</sup> nuclear spins with a net magnetization of only 10<sup>2</sup> statistically polarized spins.

**N**uclear magnetic resonance (NMR) spectroscopy (1, 2) provides a label-free method for chemical analysis, provided that

there is sufficient sample for detection. Much effort has been directed to applying NMR to nanoscale samples. Indeed, NMR detection of a (4 nm)<sup>3</sup> voxel of protons has been achieved with magnetic resonance force microscopy, a challenging experimental technique operating at ultralow temperature in vacuum (3, 4). Under ambient conditions, microcoil detectors have enabled the detection of liquid samples of (3000 nm)<sup>3</sup> volume, but further miniaturization of this technique is not straightforward (5, 6).

Recently, single nitrogen-vacancy (NV) centers in diamond (7, 8) have been proposed as a novel atomic-size magnetic field sensor for de-

tecting nanoscale nuclear spin ensembles or even single nuclear spins (9). This center is a joint defect in the carbon lattice of diamond, consisting of a substitutional nitrogen atom and an adjacent vacancy. Its spin triplet (spin 1) ground state can be polarized and read out optically, so that electron spin resonance experiments can be performed on a single spin. A single center can be used as a nanoscale magnetic field sensor, able to detect a magnetic field in the nanotesla range in an integration time of 1 s (10). This corresponds to the field of a single nuclear spin at a distance of a few nanometers (9). Indeed, detection of single <sup>13</sup>C nuclear spins has recently been reported, located inside the diamond lattice a few nanometers from the NV center (11–13).

Here we demonstrate detection of proton (<sup>1</sup>H) nuclear spins in various liquid and solid samples placed on the diamond surface. This is a key milestone toward achieving nanoscale magnetic resonance imaging based on scanning NV centers (14, 15). The technique additionally allows one to perform NMR on an arbitrary sample in the regime of ultralow and zero magnetic field, because it is based on statistical rather than thermal polarization of the nuclei. Further, our results are an initial step toward efficient hyperpolarization of any organic sample by the coherent transfer of polarization from the optically and fully polarized NV center.

We used the experimental setup sketched in Fig. 1A. Single NV centers were created 2.5 to

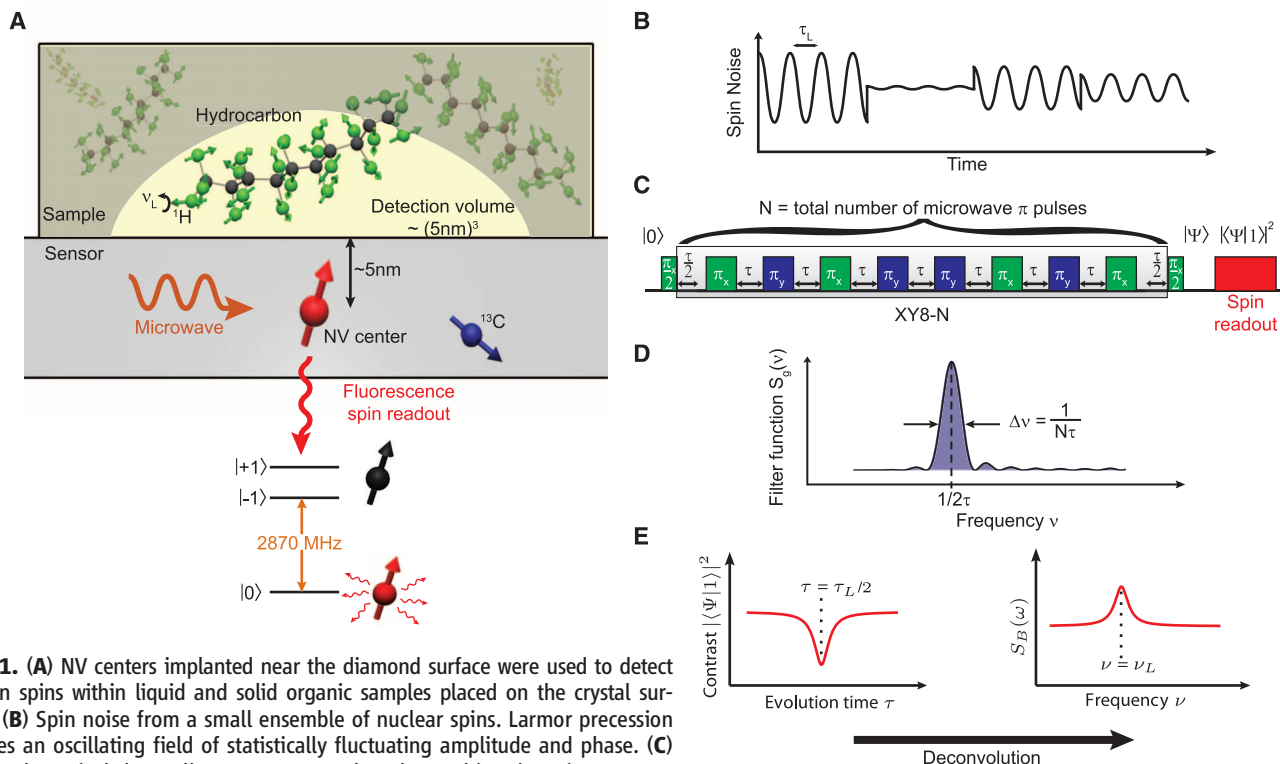


**Fig. 1.** (A) NV centers implanted near the diamond surface were used to detect proton spins within liquid and solid organic samples placed on the crystal surface. (B) Spin noise from a small ensemble of nuclear spins. Larmor precession creates an oscillating field of statistically fluctuating amplitude and phase. (C) XY8-N dynamical decoupling sequence used to detect this spin noise. Ramsey interferometry by an initial and final  $\pi/2$  pulse measures the magnetic field. A train of  $N$   $\pi$  pulses acts as a filter to select a specific frequency component of the noise. (D) Filter function of the pulse sequence, peaking at one specific frequency  $1/2\tau$ . (E) Repeating the sequence for varying pulse spacing  $\tau$  yields a spectrum of the spin noise.

<sup>1</sup>3rd Physics Institute and Research Center SCoPE, University of Stuttgart, 70569 Stuttgart, Germany. <sup>2</sup>Max Planck Institute for Solid State Research, 70174 Stuttgart, Germany. <sup>3</sup>Hefei National Laboratory for Physics Sciences at Microscale and Department of Modern Physics, University of Science and Technology of China, Hefei, 230026, China. <sup>4</sup>RUBION, Ruhr-Universität Bochum, 44801 Bochum, Germany. <sup>5</sup>Department of Physics, The City College of New York, CUNY New York, NY 10031, USA.

\*To whom correspondence should be addressed. E-mail: f.reinhard@physik.uni-stuttgart.de



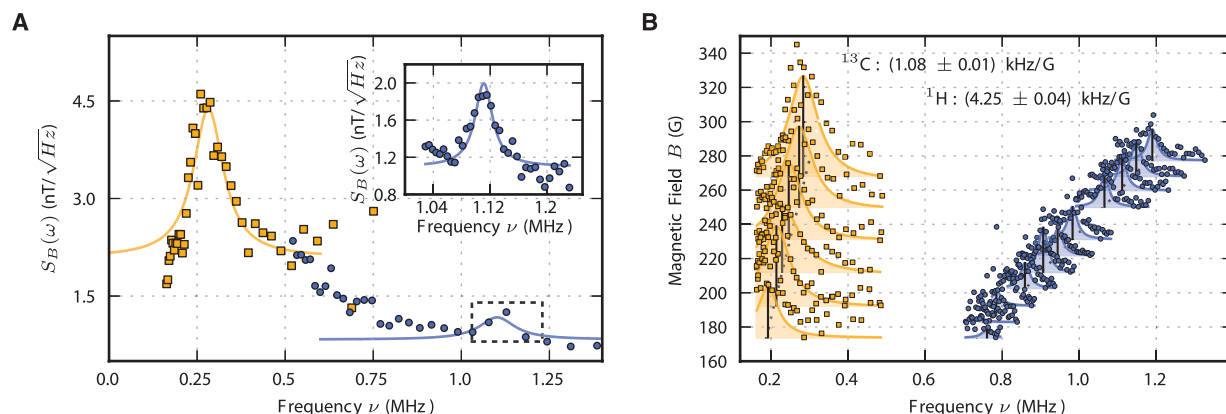


**Fig. 2. (A)** NMR spectrum of statistically polarized nuclei in the vicinity of a shallow implanted NV center. A strong contribution of  $^{13}\text{C}$  nuclei inside the diamond [yellow, acquired by a CPMG6 sequence (20)] was accompanied by a

weaker component of  $^1\text{H}$  nuclei of the sample (blue, acquired using a XY8-160 sequence and a sample of microscopy immersion oil). **(B)** Both components shifted with the magnetic field at the gyromagnetic ratios of the respective species.

10 nm below the surface of the diamond by ion implantation (16) with a sample of organic material placed on the diamond surface [see supplementary material (17)].

Our technique for detecting the magnetic field of protons in the sample is based on measuring the statistical polarization of the spin population near the NV center with a dynamical decoupling method (Fig. 1, B to E). The magnetic field at the NV center is dominated by a small number of nearest protons (on the order of  $10^4$ ). The net magnetization of this small set of randomly oriented spins is zero but has a sizable standard deviation equivalent to  $\sqrt{N} = 10^2$  protons. Equivalently, this excess amount of protons can be considered to be statistically polarized along a random direction (18, 19). In particular, this statistical polarization will lead to a random magnetization  $\langle M_x \rangle, \langle M_y \rangle$  in the transverse plane, which undergoes Larmor precession under the applied magnetic field and leads to an oscillating field component  $B_z = B(\langle M_x \rangle, \langle M_y \rangle) \cos(2\pi t/\tau_{\text{Larmor}} + \phi)$  along the axis of the NV center.

We detected this oscillating component using dynamical decoupling ac magnetometry based on the XY8-N pulse sequence (20–26) (Fig. 1C). Here, an initial  $\pi/2$  microwave pulse places the NV center into a coherent superposition  $(|0\rangle + e^{i\phi}|1\rangle)/\sqrt{2}$  of two spin states. Its phase  $\phi$  is sensitive to the fluctuating magnetic field and evolves from  $\phi = 0$  at the beginning of the sequence to a nonzero random phase  $\phi = \Delta\phi$ , which is converted into a population difference of the states by a final  $\pi/2$  pulse and subsequently read out. For a fluctuating magnetic field, this phase is a random variable with variance  $\langle \Delta\phi^2 \rangle$ , which, when averaged over many repetitions, reduces the read-out contrast obtained after the final  $\pi/2$  pulse to

$$C = 2|\langle |\psi \rangle|^2 - 1 = e^{-\langle \Delta\phi^2 \rangle / 2}$$

The phase  $\langle \Delta\phi^2 \rangle$  is made sensitive to specific frequency components by periodically flipping the NV spin by a train of  $N$  equidistant  $\pi$  pulses between the initial and final  $\pi/2$  pulse.

This “quantum lock-in detection” (23) enhances sensitivity to all fields oscillating synchronously with the pulse spacing  $\tau$ , while it suppresses the effect of field fluctuations at every other frequency. More precisely

$$\langle \Delta\phi^2 \rangle = \gamma^2 \sum_{n=-\infty}^{\infty} S_g(\nu_n) S_B(\nu_n)$$

where  $\gamma = g\mu_B/\hbar$  is the NV spin’s gyromagnetic ratio,  $\nu_n = n/N\tau$ ,  $S_B(\nu_n)$  is the power spectral density of magnetic field fluctuations, and the filter function  $S_g(\nu_n)$  is a function sharply peaked around the frequency  $1/2\tau$  encoding the effect of the  $\pi$ -pulse train (Fig. 1D). Repeating the experiment for varying pulse spacings  $\tau$ , we can sample the entire spectrum  $S_B(\nu_n)$  and hence record a NMR spectrum of statistically polarized nuclei in the vicinity of the center.

A typical spectrum obtained from such an experiment (Fig. 2A) is dominated by a strong peak at the  $^{13}\text{C}$  Larmor frequency, corresponding to spin noise from intrinsic nuclei of the diamond lattice. Under high-order dynamical decoupling, sensitivity increased sufficiently to reveal an additional smaller peak (blue line in Fig. 2A) that we attribute to protons from the sample placed on the diamond surface. Its frequency scales linearly with magnetic field (Fig. 2B) with a slope of  $4.25 \pm 0.04$  kHz/G, the gyromagnetic ratio of  $^1\text{H}$ .

We could reversibly switch the signal seen by a given NV center by coating the surface with different solid and liquid compounds (Fig. 3A). The signal was visible under a coating of immersion oil (yellow circles), but it completely vanished under a coating of a deuterated polymer ( $^2\text{H}$ -PMMA, blue triangles) and subsequently reappeared when the surface was coated with its natural-abundance equivalent (green squares). We also demonstrated basic spectroscopy by recording several high-resolution spectra (Fig. 3B). Under a PMMA coating, we measured a broadened linewidth of  $46.3 \pm 1.5$  kHz (obtained from a Lorentzian fit), which agrees well with reported data (27). Spectroscopy under a

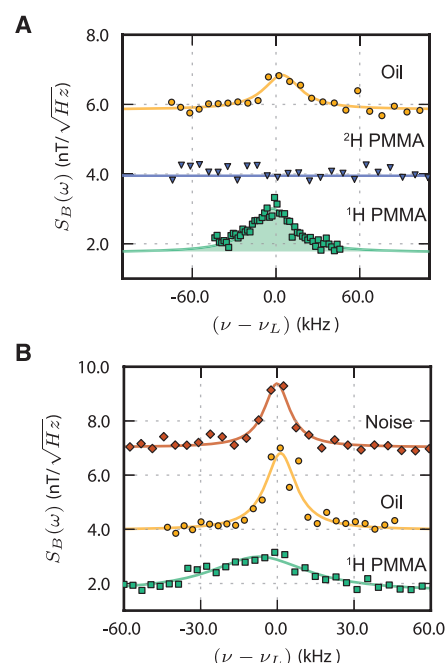
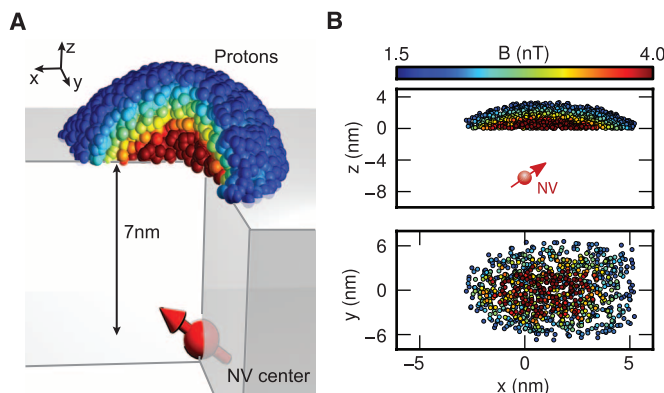


**Fig. 3. (A)** NMR spectra obtained successively on the same center with an XY8-80 sequence under coatings of a liquid sample (immersion oil, yellow points), a deuterated solid ( $^2\text{H}$  PMMA, blue triangles), and a protonated solid sample ( $^1\text{H}$  PMMA, green squares). **(B)** High-resolution spectra (XY8-112). Green squares: Spectrum under a polymer coating ( $^1\text{H}$  PMMA). Yellow circles: Spectrum under immersion oil, obtained on the same NV. Tilted red squares: Spectral resolution of our scheme, obtained on a different NV by applying externally generated magnetic field noise of fixed frequency. Spectra are offset along the  $y$  axis to enhance readability.

liquid sample reveals a narrow line (oil, Fig. 3B), as expected from rotational narrowing. Its linewidth of  $14.4 \pm 0.4$  kHz was still four orders of magnitude greater than typical values for bulk liquid NMR, which can be explained by two effects. First, diffusion through the nanoscale sample volume can randomize polarization on a fast

**Fig. 4.** Numerical simulation of the detection volume. (A) Three-dimensional visualization of the  $10^4$  closest protons (spheres), generating 70% of the signal. Protons are color-coded by their contribution to the total signal. (B) Two-dimensional projections of (A).



time scale and broaden the line. Second, the line was substantially broadened by our spectral resolution ( $12.2 \pm 0.3$  kHz, upper curve of Fig. 3B). This experimental resolution could be improved by increasing  $N$ , the order of dynamical decoupling, which should allow for an ultimate resolution of  $\Delta\nu/\nu \approx (T_{1,NV}\Omega_{R,NV})^{-1} \approx 1$  ppm, with  $T_{1,NV}\Omega_{R,NV}$  denoting the relaxation time and Rabi frequency of the NV, respectively (28, 29).

The integrated, background-corrected field strength experienced under a coating of PMMA by a typical NV center is  $B_{\text{rms}} = 390 \pm 60$  nT (green shaded area in Fig. 3A). According to an analytical model of the proton magnetic field (30), assuming a homogeneous proton density of  $5 \times 10^{28} \text{ m}^{-3}$ , this field strength corresponds to an NV center located  $6.4 \pm 0.7$  nm below the surface. Numerical simulations of the ion implantation predict a similar value (17). This suggests that our result can yield a nondestructive method to measure the depth of an individual center with nanometer statistical uncertainty.

We confirmed the signal magnitude by a numerical simulation, which explicitly computes the field of  $4 \times 10^5$  protons, placed at random locations in a cube of 20-nm width. We found that 70% of the signal was generated by the  $10^4$  closest protons, corresponding to a detection volume of only  $(5 \text{ nm})^3$  (Fig. 4), which is comparable to that of a medium-size (100-kD) protein.

An important extension of our results will be the combination with scanning NV centers (14, 15) to implement NMR imaging at the nanoscale. Being based on statistical rather than thermal polarization, our approach enables the acquisition of NMR spectra of an arbitrary substance at low magnetic fields, down to and including zero field, without the need for prepolarization (31). In this regime, magic angle spinning can be realized by rotating the external field rather than the sample. This allows for higher rotation frequencies than at high field, which is potentially of great benefit for solid-state NMR. Finally, we anticipate that our technique can yield a new method of hyperpolarization for arbitrary samples by coherently transferring the polarization of the NV spin to the sample. We estimate that full polarization of the detection volume might be achievable. The transfer of one quan-

tum of angular momentum would occur on the time scale of our detection ( $\sim 20 \mu\text{s}$ ), and hence  $10^4$  transfers can be completed on a time scale faster than the protons' longitudinal relaxation time  $T_1$  (typically on the order of seconds).

#### References and Notes

1. F. Bloch, *Phys. Rev.* **70**, 460 (1946).
2. E. M. Purcell, H. C. Torrey, R. V. Pound, *Phys. Rev.* **69**, 37 (1946).
3. D. Rugar, R. Budakian, H. J. Mamin, B. W. Chui, *Nature* **430**, 329 (2004).
4. C. L. Degen, M. Poggio, H. J. Mamin, C. T. Rettner, D. Rugar, *Proc. Natl. Acad. Sci. U.S.A.* **106**, 1313 (2009).
5. L. Ciobanu, D. A. Seeber, C. H. Pennington, *J. Magn. Reson.* **158**, 178 (2002).
6. A. Blank, J. H. Freed, *Isr. J. Chem.* **46**, 423 (2007).
7. A. Gruber *et al.*, *Science* **276**, 2012 (1997).
8. F. Jelezko, T. Gaebel, I. Popa, A. Gruber, J. Wrachtrup, *Phys. Rev. Lett.* **92**, 076401 (2004).
9. J. M. Taylor *et al.*, *Nat. Phys.* **4**, 810 (2008).
10. G. Balasubramanian *et al.*, *Nat. Mater.* **8**, 383 (2009).
11. T. H. Taminiau *et al.*, *Phys. Rev. Lett.* **109**, 137602 (2012).
12. S. Kolkowitz, Q. P. Unterreithmeier, S. D. Bennett, M. D. Lukin, *Phys. Rev. Lett.* **109**, 137601 (2012).
13. N. Zhao *et al.*, *Nat. Nanotechnol.* **7**, 657 (2012).
14. G. Balasubramanian *et al.*, *Nature* **455**, 648 (2008).
15. P. Maletinsky *et al.*, *Nat. Nanotechnol.* **7**, 320 (2012).
16. J. Meijer *et al.*, *Appl. Phys. Lett.* **87**, 261909 (2005).

17. Supplementary materials are available on Science Online.
18. C. L. Degen, M. Poggio, H. J. Mamin, D. Rugar, *Phys. Rev. Lett.* **99**, 250601 (2007).
19. F. Reinhard *et al.*, *Phys. Rev. Lett.* **108**, 200402 (2012).
20. L. Cywiński, R. M. Lutchyn, C. P. Nave, S. Das Sarma, *Phys. Rev. B* **77**, 174509 (2008).
21. G. de Lange, D. Ristè, V. V. Dobrovitski, R. Hanson, *Phys. Rev. Lett.* **106**, 080802 (2011).
22. A. Laraoui, J. S. Hodges, C. A. Meriles, *Appl. Phys. Lett.* **97**, 143104 (2010).
23. S. Kotler, N. Akerman, Y. Glickman, A. Keselman, R. Ozeri, *Nature* **473**, 61 (2011).
24. J. Bylander *et al.*, *Nat. Phys.* **7**, 565 (2011).
25. L. T. Hall, J. H. Cole, C. D. Hill, L. C. L. Hollenberg, *Phys. Rev. Lett.* **103**, 220802 (2009).
26. N. Bar-Gill *et al.*, *Nat. Commun.* **3**, 858 (2012).
27. K. M. Sinnott, *J. Polym. Sci., Polym. Phys. Ed.* **42**, 3 (1960).
28. E. C. Reynhardt, G. L. High, J. A. van Wyk, *J. Chem. Phys.* **109**, 8471 (1998).
29. G. D. Fuchs, V. V. Dobrovitski, D. M. Toyli, F. J. Heremans, D. D. Awschalom, *Science* **326**, 1520 (2009).
30. C. A. Meriles *et al.*, *J. Chem. Phys.* **133**, 124105 (2010).
31. M. P. Ledbetter *et al.*, *Proc. Natl. Acad. Sci. U.S.A.* **105**, 2286 (2008).

**Acknowledgments:** We thank L. Häussler, D. Antonov, A. Denisenko, and A. Aird for sharing cTRIM and molecular dynamics simulation data and G. Majer and T. Bräuninger for bulk NMR measurements, as well as H. J. Mamin, D. Rugar, and P.-G. Reinhard for helpful discussions. This work was supported by the European Union (SQUETEC, DIAMANT), the Max Planck Society, Deutsche Forschungsgemeinschaft (SFB/TR21, Research groups 1493 and 1482, SPP1601), Defense Advanced Research Projects Agency (QUASAR program), Volkswagen Foundation, contract research of the Baden-Württemberg foundation ("Methoden für die Lebenswissenschaften"), the 973 Program (2013CB921800), NNSFC (11227901, 91021005, 10834005), and Chinese Academy of Sciences. T.S. acknowledges financial support from the IMPRS-AM and C.A.M. from the Humboldt Foundation and the NSF (NSF-1111410).

#### Supplementary Materials

[www.sciencemag.org/cgi/content/full/339/6119/561/DC1](http://www.sciencemag.org/cgi/content/full/339/6119/561/DC1)  
Materials and Methods  
Supplementary Text  
Figs. S1 to S7  
References (32, 33)

17 October 2012; accepted 3 December 2012  
10.1126/science.1231675

## Detecting Ozone- and Greenhouse Gas–Driven Wind Trends with Observational Data

Sukyoung Lee<sup>1\*</sup> and Steven B. Feldstein<sup>1</sup>

Modeling studies suggest that Antarctic ozone depletion and, to a lesser degree, greenhouse gas (GHG) increase have caused the observed poleward shift in the westerly jet during the austral summer. Similar studies have not been performed previously with observational data because of difficulties in separating the two contributions. By applying a cluster analysis to daily ERA-Interim data, we found two 7- to 11-day wind clusters, one resembling the models' responses to GHG forcing and the other resembling ozone depletion. The trends in the clusters' frequency of occurrence indicate that the ozone contributed about 50% more than GHG toward the jet shift, supporting the modeling results. Moreover, tropical convection apparently plays an important role for the GHG-driven trend.

Throughout the late 20th century, the Southern Hemisphere (SH) westerlies have undergone a poleward shift (1–3), especially

during the austral summer (December through February; DJF hereafter) (Fig. 1A). This change affects weather and climate not only by altering the



location of storms but also by influencing the rate of carbon uptake in the Southern Ocean (4, 5) and by decreasing Antarctic snow melt (6). This poleward jet shift is commonly described as a trend toward the positive phase of the Southern Annular Mode (SAM), a pattern that is often defined as the first empirical orthogonal function of the zonal-mean zonal wind (7). Modeling studies found that a positive SAM trend can be simulated either by increasing the atmospheric greenhouse gas (GHG) concentration (8) or by decreasing stratospheric ozone, with the ozone having a greater impact (9, 10). It is unclear to what extent the model-based attributions are valid in nature; similar attribution studies have not been performed with observational data because of the perception that the circulation responses cannot be separated. However, the continuum perspective (11, 12) suggests that the responses to the two forcings may be sufficiently different from each other that a cluster analysis would find them to be distinctive. Although this approach has its own uncertainties, if the response to the forcings inferred from observational data resemble those from model experiments, we can be reasonably confident that the impacts of the individual forcings are being accurately evaluated.

This possibility was explored by applying the method of self-organizing maps (SOMs) (12, 13) to daily DJF zonal-mean zonal wind data from the European Center for Medium-Range Weather Forecasts ERA-Interim reanalysis data set (14). The method partitions the data into a specified number of patterns, referred to as SOM patterns, organized on an ( $m \times n$ ) SOM grid. The SOM patterns are determined by minimizing the euclidean distance (12) between the SOM patterns and the observed fields, yielding patterns that closely resemble the observations. The number of SOM patterns chosen has its basis in two criteria: the number must be large enough to accurately capture the observed daily fields but small enough to conveniently describe the zonal wind anomalies. We quantified this accuracy by calculating pattern correlations between the observed daily fields and the particular SOM pattern for each day that has the smallest euclidean distance from the observed field. From this calculation (summarized in Table 1), we conclude that a ( $4 \times 1$ ) grid meets these two criteria.

The four SOM patterns (Fig. 2, left column) express various degrees of zonal wind variability: The first pattern (first row, referred to as SOM1) corresponds to an equatorward shift of the mid-latitude westerlies; the second pattern (second row, SOM2) also describes an equatorward shift but includes a strong tropical signal; the third pattern (third row, SOM3) coincides with a poleward shift of the westerlies with a weakening in the maximum strength of the jet; and the fourth pattern (fourth row, SOM4) corresponds to a smaller poleward jet shift with a strong tropical component.

Three of the four SOM patterns (except SOM2) coincide with a large-amplitude composite (15) SAM signal (fig. S1). The frequency of occurrence (for brevity, “frequency”) of each SOM pattern was measured by counting the number of days on which the euclidean distance between a particular SOM pattern and the observed pattern is smallest. This yielded a time series of the frequency (Fig. 2, right column). For SOM3, there is a statistically significant ( $P < 0.05$ ) positive linear trend (see the red dashed line). The SOM1 frequency also shows a noticeable trend (the black dashed line), although it is not statistically significant.

The extent to which the trend of individual SOM patterns contributes to the actual observed linear trend can be quantified by multiplying each SOM pattern by the corresponding frequency trend normalized by 90 (DJF) days (16). The result (Fig. 2, middle column) shows that the poleward shift in the westerlies is dominated by contributions from both SOM1 and SOM3, with the latter being roughly 50% greater. The sum of all four SOM-derived trends (Fig. 1B) compares well with the actual trend (Fig. 1A) in most

regions. Because the composite (15) time scales of SOM1 and SOM3 are 11 and 7 days (measured as the average of the time scales over which the composite SOM1 and SOM3 amplitudes grow and decay by a factor of  $e$ ), respectively (fig. S2), our finding indicates that most of the observed poleward jet shift can be explained by the decadal trends in the frequencies of SOM1 and SOM3.

The spatial structures suggest that SOM1 may be linked to GHG warming and SOM3 to stratospheric ozone depletion. Figure 2 shows that SOM1 has a node at the jet center, with one dominant extremum on the equatorward side of the jet that has virtually no vertical tilt. In contrast, SOM3 has a node located slightly poleward of the jet center and three extrema on the equatorward side of the jet, with the two nodes on the equatorward side tilting poleward with height. These characteristics of SOM1 and SOM3 are present in the model responses to GHG forcing [e.g., figure 5b in (8), figure 4b in (10), and figure 3a in (17)] and ozone forcing [figure 3a in (18), figure 4a in (10), and figure 4B in (19)], respectively [figure 4b in (10) is reproduced as fig. S3].

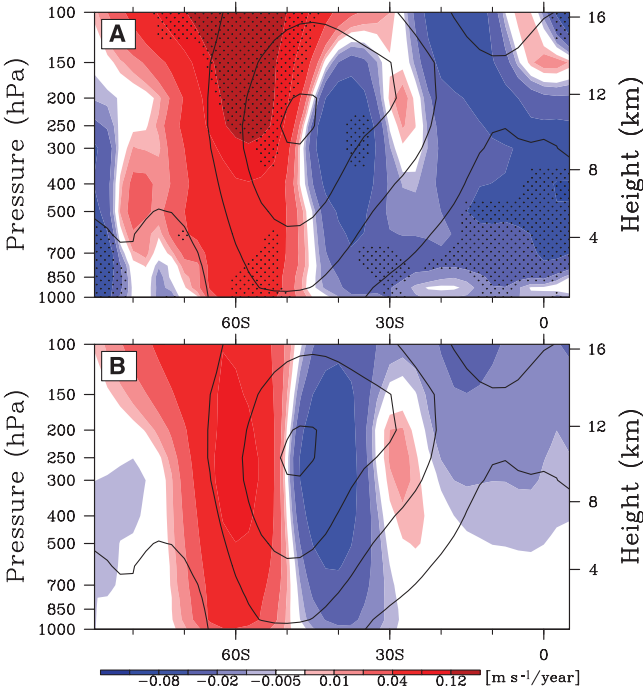


**Fig. 1.** The 1979 to 2008 DJF zonal-mean zonal wind trend: (A) total trend and (B) the sum of the four SOM trends shown in Fig. 2. The solid contours show the climatological zonal-mean zonal wind.

**Table 1.** Pattern correlations between the daily zonal-mean zonal wind and the corresponding SOM pattern for each day, weighted by the corresponding SOM frequency (second column). The third column shows correlations (corr) for SOM1 for the ( $4 \times 1$ ) grid, and SOM1-like patterns for all other grids. When there are more than one SOM1-like patterns, multiple correlations are shown. Similarly, the fourth column shows correlations for SOM3 and SOM3-like patterns.

SOM grid	Mean corr for all SOMs	Corr for SOM1-like pattern	Corr for SOM3-like pattern
(4 × 1)	0.48	0.59	0.66
(5 × 1)	0.51	0.61	0.67
(6 × 1)	0.52	0.69	0.70
(7 × 1)	0.54	0.68	0.73
(8 × 1)	0.55	0.68	0.63/0.75
(9 × 1)	0.58	0.73/0.63	0.75

<sup>1</sup>Department of Meteorology, The Pennsylvania State University, University Park, PA 16802, USA.  
\*To whom correspondence should be addressed. E-mail: sxl31@meteo.psu.edu

Figure 3A shows the time series of both DJF global mean temperature [from the National Oceanic and Atmospheric Administration (NOAA) Climatic Data Center], defined here as the deviation from the 1901 to 2000 average, and the SOM1 frequency. (The former time series is used as an indicator of the response to GHG forcing.) At time scales longer than 7 years (low pass), the upper limit of the El Niño–Southern Oscillation (ENSO) time scale, these time series are correlated at  $-0.52$ , whereas for shorter time scales (raw minus low pass; simply “high pass”

hereafter), their correlation is  $0.50$ . Both correlations are significant ( $P < 0.05$ ). The high-pass SOM1 frequency and global mean temperature are correlated with the Niño 3.4 index (Fig. 3B) at values of  $0.75$  and  $0.64$ , respectively, indicating that the positive correlation between the high-pass SOM1 frequency and global mean temperature is likely due to the driving of both quantities by ENSO. Indeed, as indicated by the blue lines in Fig. 2, ENSO influences the SOM1 frequency, whereas its impact is negligible for the remaining SOMs.

How do we then interpret the negative correlation at the low frequencies? We suggest that the answer lies in the fact that GHG driving not only increases the global mean temperature, it also causes a La Niña-like trend in tropical sea surface temperature (20, 21) and convection (22), with both variables exhibiting an increase over Indonesia and a decrease over the central tropical Pacific. This is supported by SOM1 exhibiting both a downward decadal trend in its frequency of occurrence (Fig. 2) and on intra-seasonal time scales by its being associated with

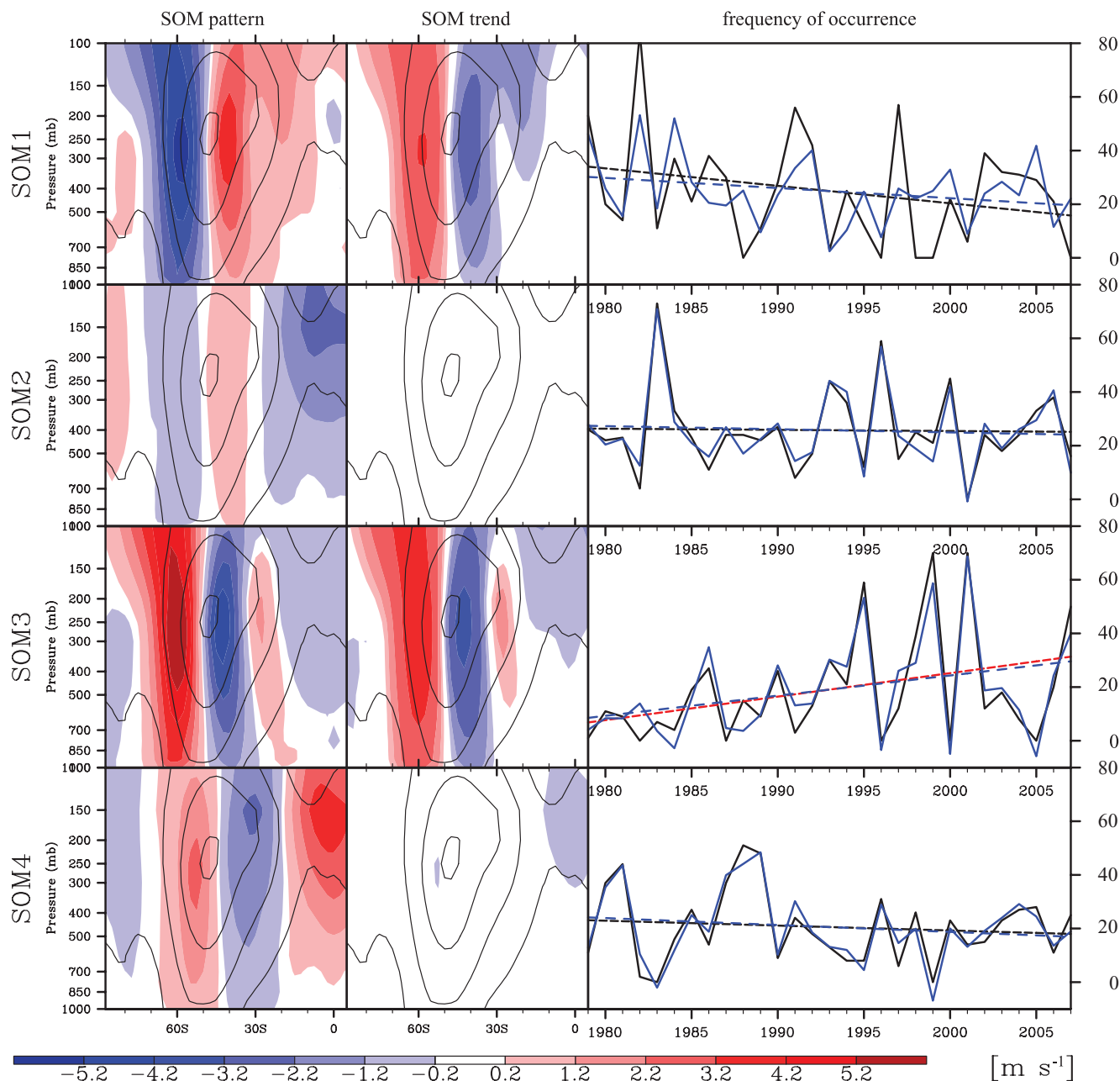


**Fig. 2.** The SOM patterns of the DJF zonal-mean zonal wind for a  $(4 \times 1)$  grid. The left column shows the SOM patterns, the middle column is the 1979 to 2008 trend for each SOM, and the right column shows the frequency time series (solid black line) shown as the number of days for each DJF season. The solid contours in the first two columns show the climatological zonal-mean zonal wind. In the third column, the solid blue lines

are ENSO-removed frequency time series. The dashed black (blue) lines are the least square linear fit of the frequency (ENSO-removed frequency) time series. If the linear fit is statistically significant ( $P < 0.05$ ) based on a Student's  $t$  test, the dashed black line is replaced by a dashed red line. The color bar is for the first column. The scale for the second column is shown in the color bar of Fig. 1.



an El Niño-like outgoing long-wave radiation (OLR; a proxy of tropical convection intensity) anomaly pattern (fig. S4a) that is opposite in sign to that for La Niña. [If the OLR composite is confined to ENSO neutral years, the La Niña-like convection anomalies remain intact, except in the eastern Pacific (fig. S4b).] The trend in tropical OLR associated with the SOM patterns is dominated by SOM1, and consistently the 1979 to 2008 OLR trend exhibits a La Niña-like OLR structure (fig. S5). This connection between the La Niña-like convection and the poleward jet shift is consistent with previous studies (23, 24). The SOM3 frequency is not correlated with the global mean temperature and is instead sig-

nificantly correlated at  $-0.45$  ( $P < 0.05$ ) with a November Antarctic ozone index, which we define as the integrated total column ozone anomaly (from ERA-Interim data) poleward of  $75^{\circ}\text{S}$  (with area weighting), where the reference state for the anomaly is the 1979 to 2008 DJF mean total column ozone. (The SOM1 frequency is uncorrelated with the ozone index.) To facilitate comparison with the SOM3 frequency, we plotted the ozone index with its sign reversed (Fig. 3C). Moreover, the SOM3 frequency time series closely resembles the yearly time series of the calendar date of the stratospheric final warming (25), whose trend toward later dates is attributed to ozone depletion. The final warming occurs most-

ly during December. Consistently, we found that for this month SOM3 occurs most frequently and its trend is positive. A separate SOM analysis for each of the three months, which yields similar patterns, also found that the frequency time series for SOM3-like patterns exhibits the highest correlations with the Antarctic ozone index during December. In contrast, the correlations between SOM1-like frequency series and the global mean temperature were found to be largest during January and February, indicating that the influence of GHG is strongest during the late summer. The composite temperature structure provides further support for these relationships between the SOM patterns and the external forcings (Fig. 4).

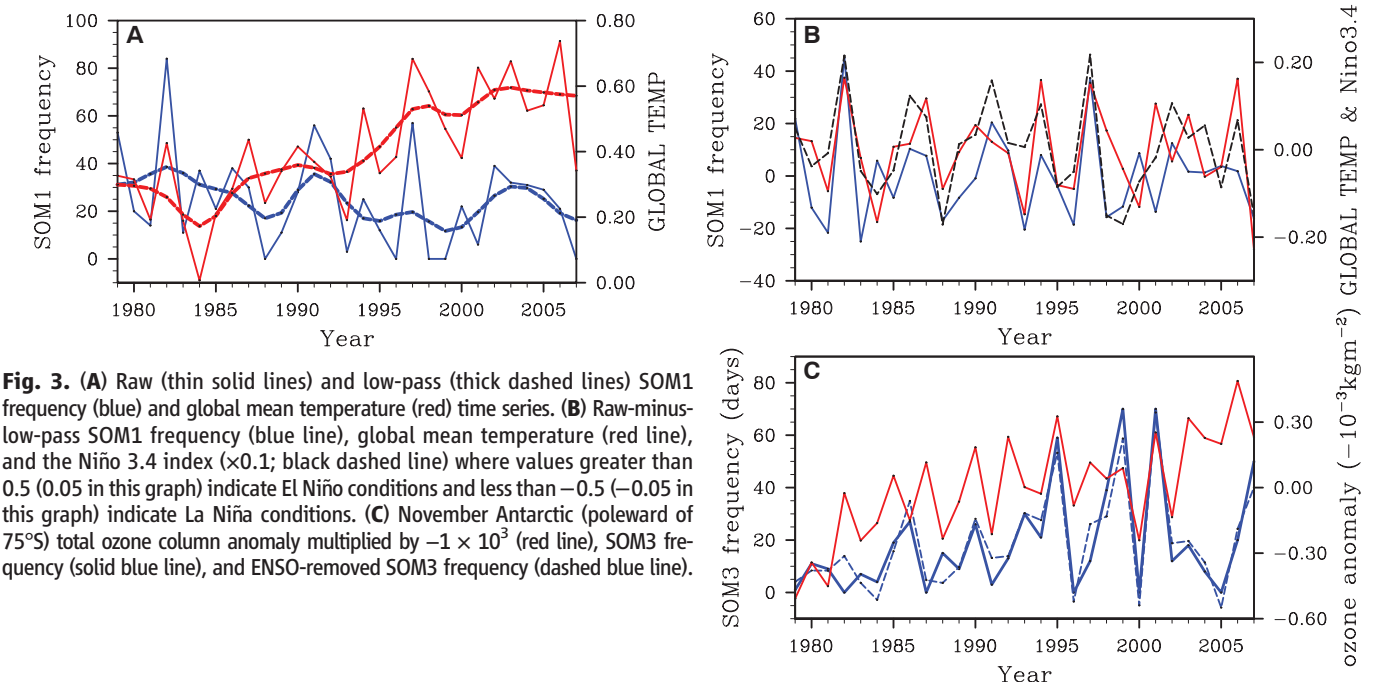


**Fig. 3.** (A) Raw (thin solid lines) and low-pass (thick dashed lines) SOM1 frequency (blue) and global mean temperature (red) time series. (B) Raw-minus-low-pass SOM1 frequency (blue line), global mean temperature (red line), and the Niño 3.4 index ( $\times 0.1$ ; black dashed line) where values greater than 0.5 (0.05 in this graph) indicate El Niño conditions and less than  $-0.5$  ( $-0.05$  in this graph) indicate La Niña conditions. (C) November Antarctic (poleward of  $75^{\circ}\text{S}$ ) total ozone column anomaly multiplied by  $-1 \times 10^3$  (red line), SOM3 frequency (solid blue line), and ENSO-removed SOM3 frequency (dashed blue line).

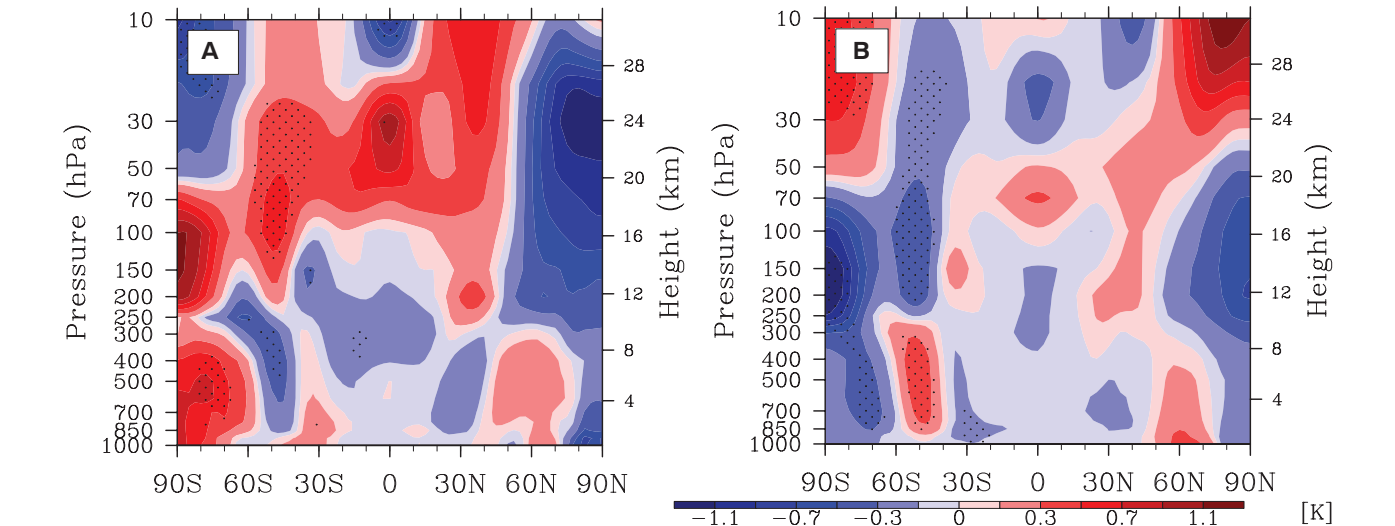


**Fig. 4.** Time-averaged (lag  $-10$  days to  $+10$  days) composite zonal-mean temperature based on (A) SOM1 and (B) SOM3. The dots indicate statistical significance ( $P < 0.05$ ) based on a Student's  $t$  test. For SOM1, the days are chosen only from ENSO neutral years. Because of the negative SOM1 frequency trend, multiplication of the SOM1 composites by  $-1$  yields the canonical GHG-induced pattern of widespread stratospheric cooling and tropospheric warming.

The SOM1 composite, which is confined to ENSO neutral years (supplementary text; to isolate the influence of non-ENSO processes), shows that in the tropics and mid-latitudes there is widespread warming in the stratosphere and cooling in the troposphere. Because the decadal SOM1 frequency trend is negative, this spatial structure indicates that the long-term temperature trend associated with SOM1 is stratospheric cooling and tropospheric warming. This is indeed consistent with the canonical temperature response to an increased atmospheric loading of GHG. The GHG-induced polar stratospheric temperature changes also match with the findings of modeling studies (26) (supplementary text). For SOM3, there is cooling in the Antarctic lower stratosphere, which is consistent with ozone depletion. All of the above evidence collectively suggests that SOM1 is driven by GHG, whereas SOM3 is driven by ozone.

Although a number of different theories for the jet shift have been proposed (27–30), the mechanism is still a subject of debate because it is difficult to tease apart the proposed causalities. The finding here that the trends are realized through fundamentally short time processes provides an avenue to test the theories in the future. One mechanism that has received limited attention is the impact of tropical convection on the poleward jet shift. Such a mechanism is appealing because it would link two robust trends seen in climate models: (i) intensification of tropical precipitation minus evaporation (hence tropical convection) and (ii) a positive SAM trend (poleward jet shift). Indeed, the SOM1 zonal wind anomalies are established about 10 days after the El Niño-like convection strengthens (figs. S4B and S6), and we found evidence that this connection involves convectively excited Rossby waves. The remaining three SOM patterns are also asso-

ciated with significant ( $P < 0.05$ ) tropical convection anomalies reminiscent of the eastward-propagating convective complex in the tropics known as the Madden-Julian Oscillation. However, a more detailed description of the role of the convection will be reported elsewhere, as doing so is beyond the scope of this report.

The zonal wind evolution (fig. S6) indicates that from lag –5 to lag +5 days SOM1 is accompanied by significant zonal wind anomalies with features close to being symmetric about the equator, particularly within the tropics and subtropics. This quasi-hemispheric symmetry further suggests that tropical convection plays an important role for enabling GHG forcing to influence the mid-latitude jets. For SOM3, extratropical anomalies are first established by lag –15 days. The signal extends into the tropical troposphere by the lag-0 day, and 5 days later it reaches the Arctic troposphere and stratosphere. This picture of a tropical conduit helps to explain the fact that the model responses to Antarctic ozone depletion also produce a substantial response in the Northern Hemisphere (19).

This study shows evidence that the atmospheric response to GHG and stratospheric ozone changes can be distinguished by applying cluster analysis to daily data. We found that the ozone forcing had a greater effect on the jet shift, supporting the modeling results (9, 10). Moreover, this method allows us to estimate the trends caused by each of the forcings. Given the debate over the uncertainty in the ozone recovery (31), we make estimates of the year 2040 1000-hPa zonal-mean zonal wind for the following two limiting scenarios: the first based on the assumption that the ozone concentration will remain at its current value (scenario 1) and the second based on the assumption that the ozone will recover by 2040 (32) (scenario 2). In both scenarios,

we assume that the GHG-driven zonal wind trend will remain at its 1979 to 2008 value. As Table 2 shows, the greatest fractional changes occur between 60° and 67.5°S. At 65°S, close to the coastline of Antarctica where the wind stress change can have a great impact on coastal upwelling, the wind speed would increase by 126% under scenario 1, whereas under scenario 2, the wind speed would decrease to almost zero.

## References and Notes

1. J. W. Kidson, *J. Clim.* **12**, 2808 (1999).
2. D. W. J. Thompson, J. M. Wallace, G. C. Hegerl, *J. Clim.* **13**, 1018 (2000).
3. G. J. Marshall, *J. Clim.* **16**, 4134 (2003).
4. J. R. Toggweiler, J. L. Russell, S. R. Carson, *Paleoceanography* **21**, PA2005 (2006).
5. R. F. Anderson *et al.*, *Science* **323**, 1443 (2009).
6. M. Tedesco, A. J. Monaghan, *Geophys. Res. Lett.* **36**, L18502 (2009).
7. V. Limpasuvan, D. L. Hartmann, *Geophys. Res. Lett.* **26**, 3133 (1999).
8. P. J. Kushner, I. M. Held, T. L. Delworth, *J. Clim.* **14**, 2238 (2001).
9. J. M. Arblaster, G. A. Meehl, *J. Clim.* **19**, 2896 (2006).
10. L. M. Polvani, D. W. Waugh, G. J. P. Correa, S.-W. Son, *J. Clim.* **24**, 795 (2011).
11. C. Franzke, S. B. Feldstein, *J. Atmos. Sci.* **62**, 3250 (2005).
12. N. C. Johnson, S. B. Feldstein, B. Tremblay, *J. Clim.* **21**, 6354 (2008).
13. T. Kohonen, *Self-Organizing Maps: Information Science* (Springer, Berlin, 2001).
14. B. C. Dee *et al.*, *Q. J. R. Meteorol. Soc.* **137**, 553 (2011).
15. Materials and methods are available as supplementary materials on Science Online.
16. M. E. Higgins, J. J. Cassano, *J. Geophys. Res.* **114**, D16107 (2009).
17. D. J. Lorenz, E. T. DeWeaver, *J. Geophys. Res.* **112**, D10119 (2007).
18. A. Y. Karpechko, N. P. Gillett, L. J. Gray, M. Dall'Amico, *J. Geophys. Res.* **115**, D22117 (2010).
19. S. M. Kang, L. M. Polvani, J. C. Fyfe, M. Sigmond, *Science* **332**, 951 (2011); 10.1126/science.1202131.
20. A. C. Clement, R. Seager, M. A. Cane, S. E. Zebiak, *J. Clim.* **9**, 2190 (1996).
21. M. A. Cane *et al.*, *Science* **275**, 957 (1997).
22. S. Lee, T. Gong, N. Johnson, S. B. Feldstein, D. Pollard, *J. Clim.* **24**, 4350 (2011).
23. M. L. L'Heureux, D. W. J. Thompson, *J. Clim.* **19**, 276 (2006).
24. T. Gong, S. B. Feldstein, D. Luo, *J. Atmos. Sci.* **67**, 2854 (2010).
25. R. X. Black, B. A. McDaniel, *J. Atmos. Sci.* **64**, 2968 (2007).
26. B. Grassi, G. Redaelli, G. Visconti, *Geophys. Res. Lett.* **33**, L23704 (2005).
27. W. A. Robinson, *J. Clim.* **10**, 176 (1997).
28. L. M. Polvani, P. J. Kushner, *Geophys. Res. Lett.* **29**, 1114 (2002).
29. S.-W. Son, S. Lee, *J. Atmos. Sci.* **62**, 3741 (2005).
30. G. Chen, I. M. Held, *Geophys. Res. Lett.* **34**, L21805 (2007).
31. E. C. Weatherhead, S. B. Andersen, *Nature* **441**, 39 (2006).
32. A. Tabazadeh, E. Cordero, *Atmos. Environ.* **38**, 647 (2004).

**Acknowledgments:** This research was supported by NSF grants AGS-1036858 and AGS-1139970. The authors acknowledge N. Johnson for providing the Matlab codes used for the SOM analysis and two anonymous reviewers for their helpful suggestions and comments.

## Supplementary Materials

www.sciencemag.org/cgi/content/full/339/6119/563/DC1  
Materials and Methods  
Figs. S1 to S6  
References (33, 34)

24 May 2012; accepted 27 November 2012  
10.1126/science.1225154

**Table 2.** Projected 1000-hPa zonal-mean zonal wind changes (relative to 1979 to 2008 climatological values) in the year 2040, based on two scenarios: the Antarctic ozone concentration remaining at the current level (scenario 1); the ozone concentration recovering to the pre-1980 value (scenario 2). In both scenarios, it is assumed that the rate of zonal wind change caused by the GHG increase remains at its 1979 to 2008 value.

Latitude (°S)	Scenario 1 (m/s)	Scenario 2 (m/s)	Climatology (m/s)
30.0	–0.13	–0.04	–2.39
32.5	–0.17	0.01	–1.29
35.0	–0.21	0.07	0.13
37.5	–0.22	0.12	2.02
40.0	–0.20	0.15	3.85
42.5	–0.14	0.15	5.42
45.0	–0.06	0.14	6.68
47.5	0.05	0.11	7.40
50.0	0.17	0.06	7.64
52.5	0.27	–0.01	7.42
55.0	0.37	–0.08	6.73
57.5	0.44	–0.15	5.65
60.0	0.47	–0.23	4.07
62.5	0.44	–0.27	2.20
65.0	0.33	–0.23	0.26
67.5	0.18	–0.15	–1.55
70.0	0.08	–0.09	–2.31



# Uncovering the Protein Translocon at the Chloroplast Inner Envelope Membrane

Shingo Kikuchi,<sup>1</sup> Jocelyn Bédard,<sup>1\*</sup> Minako Hirano,<sup>2</sup> Yoshino Hirabayashi,<sup>1</sup> Maya Oishi,<sup>1</sup> Midori Imai,<sup>1†</sup> Mai Takase,<sup>1</sup> Toru Ide,<sup>2</sup> Masato Nakai<sup>1‡</sup>

Chloroplasts require protein translocons at the outer and inner envelope membranes, termed TOC and TIC, respectively, to import thousands of cytoplasmically synthesized preproteins. However, the molecular identity of the TIC translocon remains controversial. Tic20 forms a 1-megadalton complex at the inner membrane and directly interacts with translocating preproteins. We purified the 1-megadalton complex from *Arabidopsis*, comprising Tic20 and three other essential components, one of which is encoded by the enigmatic open reading frame *ycf1* in the chloroplast genome. All four components, together with well-known TOC components, were found stoichiometrically associated with different translocating preproteins. When reconstituted into planar lipid bilayers, the purified complex formed a preprotein-sensitive channel. Thus, this complex constitutes a general TIC translocon.

Translocation of nuclear-encoded preproteins across the double envelope membranes of chloroplasts is mediated by two protein translocons, the TOC and TIC complexes (1–5). Tic20, an integral inner membrane protein with four predicted transmembrane helices, has been proposed to form part of a general protein-conducting channel (6, 7). Recombinant Tic20 has further been reported to have the capacity to form a channel (8). A 1-megadalton (MD) translocation intermediate complex has been recently identified at the inner membrane, in which Tic20 is in close contact with a translocating preprotein (9). Whereas Tic20 forms a stable 1-MD complex in the inner membrane, Tic21 interacts only weakly with the complex, and other known Tic proteins such as Tic110 and Tic40 are not involved in the complex (9). Thus, detailed organization of this 1-MD complex has remained elusive.

Here, we generated transgenic *Arabidopsis* plants expressing a protein A-tagged Tic20-I (the major Tic20 isoform in *Arabidopsis*), and the tagged Tic20-I-containing complexes were purified (fig. S1). Three proteins with molecular masses of 214, 100, and 56 kD were specifically copurified with Tic20-I, which were confirmed to form a stable 1-MD complex together with Tic20-I (Fig. 1A). Subsequent mass spectrometric analysis revealed three previously uncharacterized *Arabidopsis* proteins (fig. S2A).

Surprisingly, the 214-kD protein, AtCg01130, is encoded by the previously enigmatic chloroplast gene *ycf1* (hypothetical chloroplast open

reading frame 1) (10–12). The deduced protein, here renamed Tic214, is 1786 amino acids in length with a calculated relative molecular mass  $M_r$  of 213,742 and is predicted to contain six N-terminal transmembrane domains (figs. S2B and S3). The 100-kD protein, At5g22640, is a nuclear-encoded protein of 871 amino acids with

a calculated  $M_r$  of 99,954 (fig. S4). This protein likely has no cleavable transit peptide (fig. S2A) and thus was named Tic100. The 56-kD protein, At5g01590, is also a nuclear-encoded protein of 527 amino acids with a calculated  $M_r$  of 61,625 (fig. S5). This protein is most likely synthesized as a preprotein and processed to form a mature protein upon import (fig. S6A) and thus was designated Tic56. Tic100 and Tic56 are highly conserved among most land plants, but show no remarkable overall sequence similarity to any proteins of known function and have no predicted transmembrane segment.

In wild-type chloroplasts, Tic214, Tic100, Tic56, and Tic20-I appeared to form stable 1-MD TIC complexes (Fig. 1, B and C, and fig. S6, B and C), which were shown to associate with preproteins (fig. S7). If we assume that the stoichiometry of the components in the 1-MD complex is 1:1:1:1 (fig. S8), we would expect that the complex represents a trimeric assembly of Tic214, Tic100, Tic56, and Tic20-I (1170 kD). The stoichiometry of Tic20-I:Tic75 (the channel protein of the TOC complex) in the envelope membranes was roughly estimated to be 1:2.5 (fig. S8). Tic20-I and Tic214 likely constitute the membrane-integral part of the 1-MD TIC complex; Tic20-I is entirely buried in the core of the complex, whereas Tic214

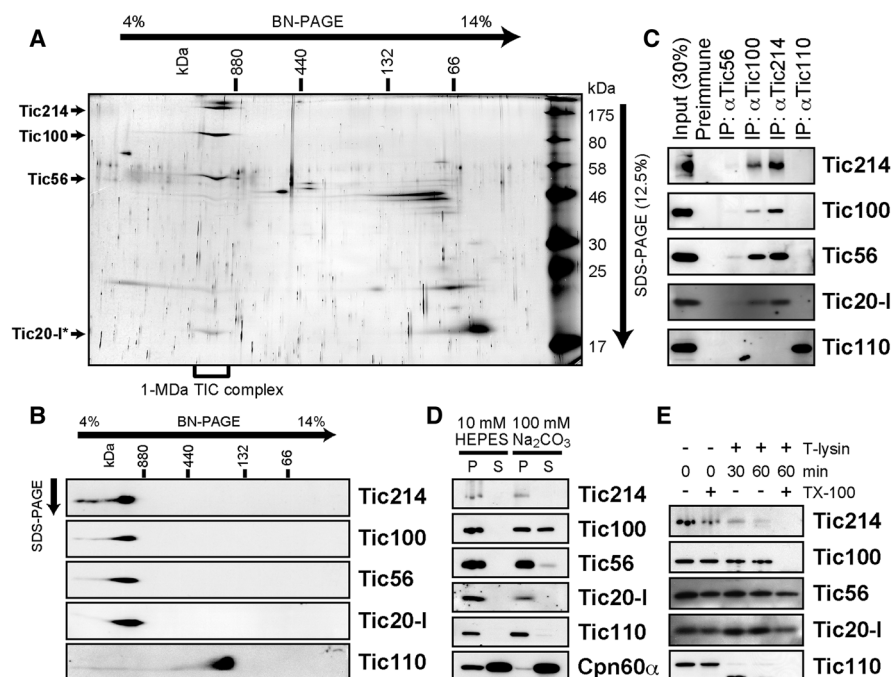


**Fig. 1.** The 1-MD complex is composed of Tic20-I and three other Tic proteins. (A) Tic214, Tic100, and Tic56 were copurified with protein A-tagged Tic20-I (PA2-Tic20-I). The purified fraction was separated by two-dimensional blue native (2D-BN) SDS-PAGE followed by silver staining. Tic20-I\*, tobacco etch virus (TEV) protease-cleaved PA2-Tic20-I. (B) Wild-type *Arabidopsis* chloroplasts were solubilized with 1% digitonin in the presence of 1 M NaCl and then separated by 2D-BN SDS-PAGE followed by immunoblotting. (C) Co-immunoprecipitation of the 1-MD TIC complex components. (D and E) The localization and topology of the different TIC complex components were analyzed by alkaline (D) and protease (E) treatment. (D) Chloroplasts were treated with either 10 mM HEPES-KOH, pH 7.5 (hypotonic lysis), or 100 mM Na<sub>2</sub>CO<sub>3</sub> on ice for 30 min, followed by centrifugation to obtain supernatant (S) and membrane pellet (P) fractions. (E) Inverted inner envelope membrane vesicles (26) were treated with or without thermolysin (T-lysin; 100 μg/ml) and with or without Triton X-100 [TX-100; 0.1% (w/v)] on ice for the indicated time periods.

<sup>1</sup>Laboratory of Regulation of Biological Reactions, Institute for Protein Research, Osaka University, 3-2 Yamadaoka, Suita, Osaka 565-0871, Japan. <sup>2</sup>Graduate School for the Creation of New Photonics Industries, 1955-1 Kurematsu Nishi-ku, Hamamatsu, Shizuoka 431-1202, Japan.

\*Present address: Department of Biology, University of Leicester, Leicester LE1 7RH, UK.

†Present address: Department of Plastic Surgery, Kobe University Graduate School of Medicine, Kobe, Japan.

‡To whom correspondence should be addressed. E-mail: nakai@protein.osaka-u.ac.jp

is exposed to both sides of the inner membrane (Fig. 1, D and E, and fig. S6D). Tic100 is associated peripherally in the complex at the intermembrane space side, whereas Tic56 is mostly embedded in the complex.

In a search for evidence of direct involvement of the 1-MD TIC complex as a general protein translocation machinery at the inner membrane, we used purified model preproteins in import experiments *in vitro* to isolate translocation intermediate-associated proteins from *Arabidopsis* chloroplasts (Fig. 2 and fig. S9) (13–15). Almost all major isolated proteins could be assigned to either the well-known TOC compo-

nents (including Toc159, Toc75, and Toc33) or the 1-MD TIC complex components (including Tic214, Tic100, Tic56, and Tic20-I) (Fig. 2). Association of these TOC and TIC components with preproteins absolutely required adenosine triphosphate (ATP) in the import reactions that could drive preprotein translocation across the envelope membranes (fig. S9B). Tic214, Tic100, Tic56, and Tic20-I were purified at levels comparable to those of TOC components and preproteins (Fig. 2 and fig. S9B). Two different model preproteins, pSTEV and pFdTEV, resulted in essentially similar profiles of associated proteins (Fig. 2), which supports the direct involvement of

the 1-MD TIC complex in protein translocation as a general import machinery in concert with the well-established TOC complex.

By contrast, we observed hardly any specific association of Tic110 or Tic40 with the translocation intermediate complexes (Fig. 2 and fig. S9B). This is surprising because Tic110, an abundant inner membrane protein, was initially identified by a similar method (15) and has long been considered to be a central player (5), together with Tic40, in preprotein translocation across the inner membrane (16). The migration of Tic110 upon SDS–polyacrylamide gel electrophoresis (PAGE) was almost the same as that of Tic100. However,

**Fig. 2.** Association of the 1-MD TIC complex components with two distinct model preproteins. *Arabidopsis* chloroplasts were incubated with 100 nM urea-denatured protein A-tagged preproteins pSTEV or pFdTEV in the presence of 0.5 mM ATP for 10 min at 25°C. As a control, incubation without preprotein (–) was also performed. Reisolated chloroplasts were directly solubilized with 1% digitonin, and insoluble material was removed by ultracentrifugation. The resulting supernatant was incubated with immunoglobulin G–sepharose for 2 hours at 4°C. After the beads were washed thoroughly, bound protein complexes were eluted under nondenaturing conditions by TEV cleavage. The denatured samples were separated by 12.5% SDS-PAGE followed by silver staining (left) or immunoblotting (right). ENV, *Arabidopsis* mixed envelope fraction; TIC, the 1-MD TIC complex purified from PA2-Tic20-I plants; \*1, unidentified protein currently under investigation; \*2, unknown contaminating protein; AcTEV, TEV protease; pFd and pS, TEV-cleaved preproteins; Tic20-I\*, TEV-cleaved PA2-Tic20-I.

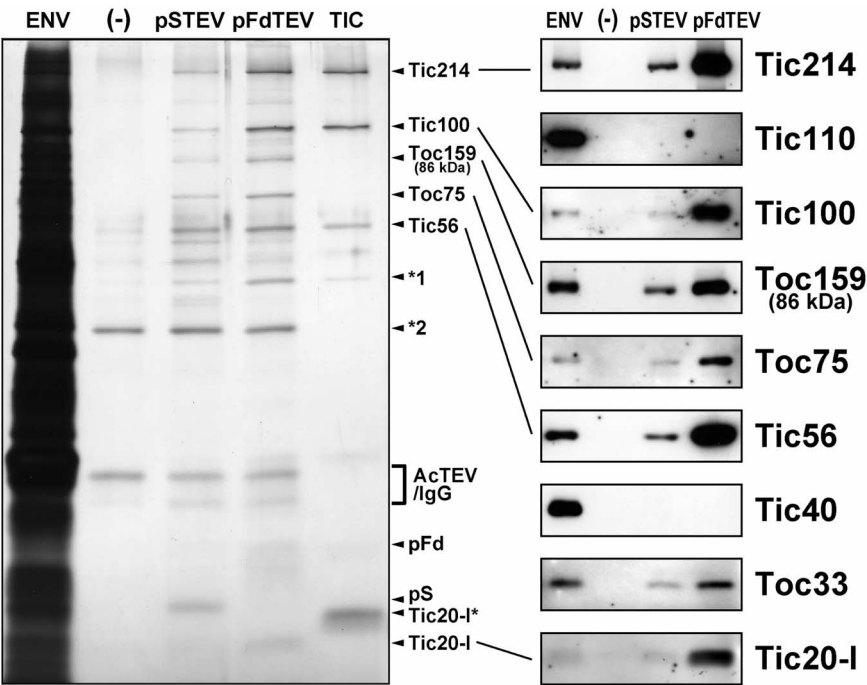
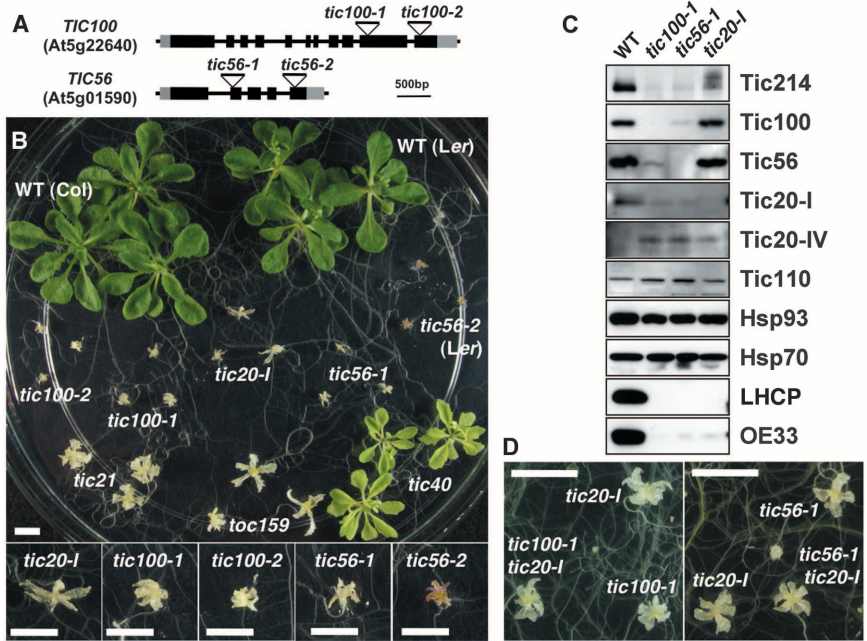


**Fig. 3.** Characterization of *tic100* and *tic56* *Arabidopsis* knockout mutants. (A) Schematic representation of the genes encoding Tic100 and Tic56. Triangles, T-DNA insertions; solid boxes, exons; thin lines, introns; shaded boxes, untranslated regions. (B) Visible phenotypes of various *tic* and *toc* mutants (16, 19–22, 27) grown on sucrose-containing media for 3 weeks. Scale bars, 5 mm. (C) Total proteins were extracted from 3-week-old wild-type *Arabidopsis* and from homozygous albino *tic100-1*, *tic56-1*, and *tic20-1* mutants; 24 µg of total protein was subjected to SDS-PAGE and immunoblotting. Hsp93 and Hsp70, stromal molecular chaperones; LHCP, light-harvesting chlorophyll-binding protein; OE33, 33-kD protein of the oxygen-evolving complex of photosystem II. (D) Double and single knockouts were identified in the progeny derived from a +/*tic20-1* +/*tic100-1* heterozygous plant (left) and from a +/*tic20-1* +/*tic56-1* heterozygous plant (right). Scale bars, 1 cm.





they are completely different proteins, and Tic110 exists as a very distinct 200- to 300-kD entity in the inner membrane (Fig. 1B) (9) most probably without any stably associated proteins (fig. S10). Physical interaction between Tic110 and any component of the 1-MD TIC complex was hardly observed even after chemical cross-linking (Fig. 1C and fig. S11). Thus, although Tic110 might act as a scaffold for stromal molecular chaperones at a later stage during import (17, 18), direct participation of these Tic proteins in preprotein translocation is unclear.

The null mutant of *Arabidopsis* *TIC20-I* displays developmental defects during embryogenesis and results in an albino, seedling-lethal phenotype due to a strong defect in protein import into chloroplasts (19–21). Null mutants of *TIC100* (22) and *TIC56* showed very similar

phenotypes (Fig. 3, A and B, and figs. S12 and S13). Absence of either Tic100 or Tic56 led to marked reductions of the remaining 1-MD TIC complex components, indicating that they are important for assembly of the complex (Fig. 3C and fig. S12E). Furthermore, chloroplasts isolated from a viable *tic56-3* pale green mutant had a notable protein import defect (figs. S14 and S15).

Like the *tic20-I* mutant (20), no photosynthetic proteins accumulated in the albino seedlings of the *tic100-I* and *tic56-I* mutants, although some housekeeping proteins did accumulate (Fig. 3C). This residual import ability in the *tic20-I* mutant can be attributed to partial compensation by the elevated expression of the minor, partially redundant homolog Tic20-IV (Fig. 3C) (20), because a *tic20-I tic20-IV* double-knockout mutant exhibits more severe embryo lethality

(20, 21). The *tic20-I tic56-I* and *tic20-I tic100-I* double-knockout mutants showed phenotypes similar to those of the single-knockout mutants, *tic20-I*, *tic56-I*, or *tic100-I*, indicating that neither Tic56 nor Tic100 contributes to the compensation provided by Tic20-IV (Fig. 3D and fig. S12). By contrast, neither a *tic20-IV tic56-I* nor a *tic20-IV tic100-I* double-knockout mutant could be identified, which suggests that such double-knockout mutants are also embryo-lethal. Hence, there seems to be a residual import pathway for some housekeeping proteins in which Tic20-IV but neither Tic20-I, Tic56, nor Tic100 is involved (Fig. 3C), and impairment of both pathways causes embryo lethality (20).

The chloroplast gene initially called *ycf1* was reported to be an essential gene in tobacco (11) and in *Chlamydomonas* (12). Thus, one can anticipate that Tic214 is an essential *Arabidopsis* protein. Overall, like Tic20-I, both Tic100 and Tic56 (and most likely Tic214) are indispensable components of the 1-MD TIC complex required for photosynthetic protein import, and are therefore essential for plant viability.

When reconstituted into planar lipid bilayers, the purified 1-MD TIC complexes showed ion channel activity (Fig. 4 and fig. S16). In most cases, three identical channels appeared to be simultaneously incorporated into the bilayer as a unit (fig. S16C). This also suggests a trimeric assembly of Tic214, Tic100, Tic56, and Tic20-I to form the 1-MD complex. The single-channel current-voltage (*I-V*) curve (Fig. 4B) indicates weak rectification, because current was slightly larger at negative voltages than at positive voltages. The average slope conductance at 0 mV was  $266 \pm 18$  pS ( $N = 10$ ), a value comparable to those obtained with other protein translocators (23–25). Channel gating had a weak dependence on the membrane voltage, as spike-like short closures were frequently observed at negative high voltages (Fig. 4A). Because they always showed rectifying and voltage-dependent gating properties, we concluded that TIC channels incorporated into planar bilayers had the same orientation (fig. S16B).

In the presence of 0.1  $\mu$ M preprotein (pS-protA) in the physiological intermembrane space side of the membrane (fig. S16B), TIC channels were blocked at positive voltage but open at negative voltage (Fig. 4C). At high positive voltages, the open probability decreased with an increase in preprotein concentration (fig. S16D). In contrast, TIC currents were only slightly affected, even by a high concentration (1  $\mu$ M) of mature protein (mS-protA) lacking a transit peptide (Fig. 4D and fig. S16D). When preproteins were added to the opposite (stromal) side of the membrane, TIC channels were not blocked either at positive or negative voltage (fig. S16E). Thus, the TIC complex forms membrane channels, where preproteins specifically interact with and plug the channel pore.

Although homologs of Tic20 have been identified in cyanobacteria and are well conserved among virtually all plastid-containing lineages (21), phylogenetic analysis (fig. S17) revealed

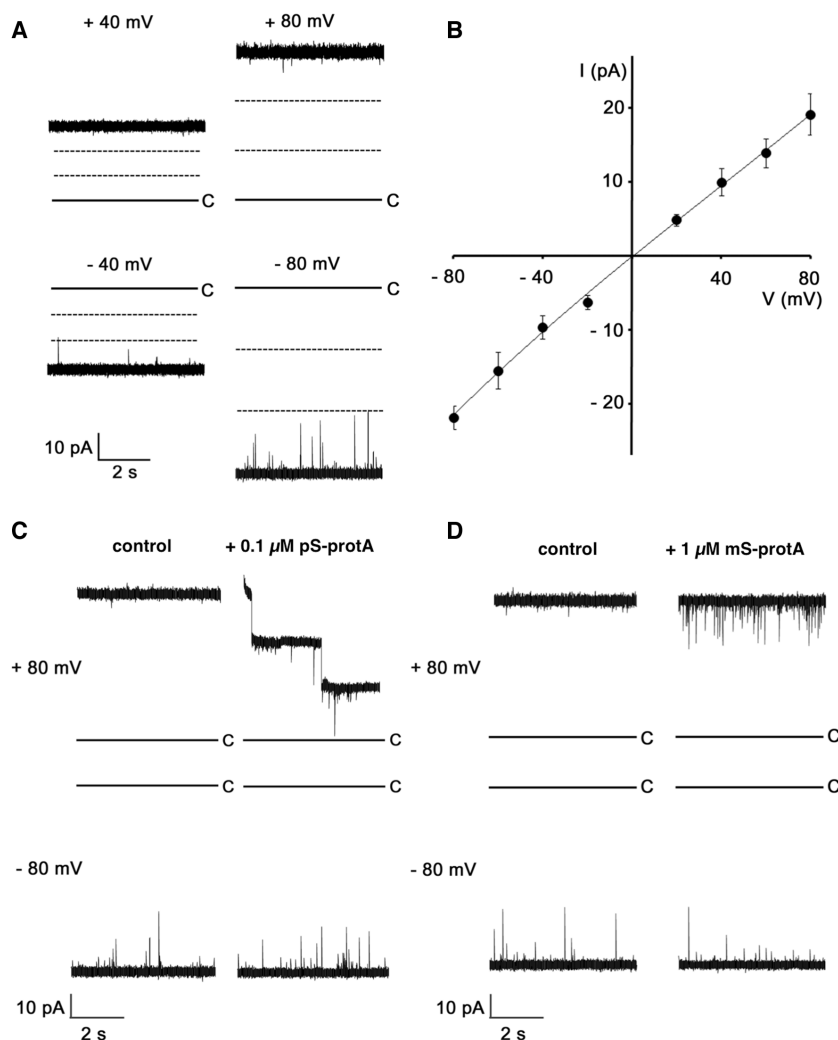


**Fig. 4.** Reconstituted 1-MD TIC complexes form preprotein-sensitive channels in planar bilayer membranes. (A) Representative current fluctuations in reconstituted 1-MD TIC complexes at different membrane voltages. Solid line labeled C indicates zero current. The distance between dashed lines corresponds to a unitary step. (B) The single-channel current-voltage (*I-V*) relationship. Data are means  $\pm$  SD ( $N = 8$  to 19). (C) Representative current recordings in the absence (control) and presence of 0.1  $\mu$ M pS-protA in the intermembrane space side at the indicated membrane voltage. (D) Representative current recordings in the absence (control) and presence of 1  $\mu$ M mS-protA in the intermembrane space side at the indicated membrane voltage.

no direct homologs for Tic214, Tic100, or Tic56 in extant cyanobacteria, Glaucophyta, or Rhodophyta, indicating that this TIC transport system evolved largely after the initial endosymbiotic event. Thus, the chloroplast inner membrane protein translocon that we describe here has changed markedly during evolution through modifications of both nuclear and chloroplast genomes.

## References and Notes

1. K. Cline, C. Dabney-Smith, *Curr. Opin. Plant Biol.* **11**, 585 (2008).
2. P. Jarvis, *New Phytol.* **179**, 257 (2008).
3. F. Kessler, D. J. Schnell, *Curr. Opin. Cell Biol.* **21**, 494 (2009).
4. H. M. Li, C.-C. Chiu, *Annu. Rev. Plant Biol.* **61**, 157 (2010).
5. S. Schwenkert, J. Soll, B. Bölter, *Biochim. Biophys. Acta* **1808**, 901 (2011).
6. A. Kouranov, X. Chen, B. Fuks, D. J. Schnell, *J. Cell Biol.* **143**, 991 (1998).
7. X. Chen, M. D. Smith, L. Fitzpatrick, D. J. Schnell, *Plant Cell* **14**, 641 (2002).
8. E. Kovács-Bogdán, J. P. Benz, J. Soll, B. Bölter, *BMC Plant Biol.* **11**, 133 (2011).
9. S. Kikuchi *et al.*, *Plant Cell* **21**, 1781 (2009).
10. S. Sato, Y. Nakamura, T. Kaneko, E. Asamizu, S. Tabata, *DNA Res.* **6**, 283 (1999).
11. A. Drescher, S. Ruf, T. J. Calsa Jr., H. Carrer, R. Bock, *Plant J.* **22**, 97 (2000).
12. E. Boudreau *et al.*, *Mol. Gen. Genet.* **253**, 649 (1997).
13. D. J. Schnell, F. Kessler, G. Blobel, *Science* **266**, 1007 (1994).
14. F. Kessler, G. Blobel, H. A. Patel, D. J. Schnell, *Science* **266**, 1035 (1994).
15. F. Kessler, G. Blobel, *Proc. Natl. Acad. Sci. U.S.A.* **93**, 7684 (1996).
16. M.-L. Chou *et al.*, *EMBO J.* **22**, 2970 (2003).
17. T. Inaba, M. Li, M. Alvarez-Huerta, F. Kessler, D. J. Schnell, *J. Biol. Chem.* **278**, 38617 (2003).
18. M.-L. Chou, C.-C. Chu, L.-J. Chen, M. Akita, H. M. Li, *J. Cell Biol.* **175**, 893 (2006).
19. Y.-S. Teng *et al.*, *Plant Cell* **18**, 2247 (2006).
20. Y. Hirabayashi, S. Kikuchi, M. Oishi, M. Nakai, *Plant Cell Physiol.* **52**, 469 (2011).
21. A. R. Kasmati, M. Töpel, R. Patel, G. Murtaza, P. Jarvis, *Plant J.* **66**, 877 (2011).
22. Q. Liang *et al.*, *Physiol. Plant.* **140**, 380 (2010).
23. K. Hill *et al.*, *Nature* **395**, 516 (1998).
24. K. N. Truscott *et al.*, *Nat. Struct. Biol.* **8**, 1074 (2001).
25. P. Kovermann *et al.*, *Mol. Cell* **9**, 363 (2002).
26. D. T. Jackson, J. E. Froehlich, K. Keegstra, *J. Biol. Chem.* **273**, 16583 (1998).
27. J. Bauer *et al.*, *Nature* **403**, 203 (2000).

**Acknowledgments:** We thank K. Iwasaki, N. Miyazaki, S. Thompson, T. Takao, C. Awada, H. Mori, and J. Mima for helpful suggestions and valuable discussions; P. Jarvis, D. Schnell, and I. Nishimura for vectors; the Arabidopsis Biological Resource Center, Institut National de la Recherche Agronomique, and Cold Spring Harbor Laboratory for the T-DNA lines; and RIKEN Bioresource Center for the full-length cDNAs. Supported by grants-in-aid for scientific research from the Ministry of Education, Culture, Sports, Science and Technology, Japan (20059022, 22020024, 24117511, and 24657073, M.N.; 21107518 and 22370059, T.I.; 23770190 and 23113519, M.H.) and by a Japan Society for the Promotion of Science postdoctoral fellowship for foreign researchers (J.B.). S.K., J.B., Y.H., M.O., M.I., M.T., and M.N. performed biochemical and genetic analyses; M.H. and T.I. performed electrophysiological analyses; M.N. conceived and supervised the whole project and wrote the paper.

## Supplementary Materials

www.sciencemag.org/cgi/content/full/339/6119/571/DC1  
Materials and Methods  
Figs. S1 to S17  
Table S1  
References (28–48)

24 August 2012; accepted 30 November 2012  
10.1126/science.1229262

# Emergent Sensing of Complex Environments by Mobile Animal Groups

Andrew Berdahl,<sup>1,\*†</sup> Colin J. Torney,<sup>1,\*</sup> Christos C. Ioannou,<sup>1,2</sup> Jolyon J. Faria,<sup>1</sup> Iain D. Couzin<sup>1†</sup>

The capacity for groups to exhibit collective intelligence is an often-cited advantage of group living. Previous studies have shown that social organisms frequently benefit from pooling imperfect individual estimates. However, in principle, collective intelligence may also emerge from interactions between individuals, rather than from the enhancement of personal estimates. Here, we reveal that this emergent problem solving is the predominant mechanism by which a mobile animal group responds to complex environmental gradients. Robust collective sensing arises at the group level from individuals modulating their speed in response to local, scalar, measurements of light and through social interaction with others. This distributed sensing requires only rudimentary cognition and thus could be widespread across biological taxa, in addition to being appropriate and cost-effective for robotic agents.

Research on collective intelligence has demonstrated how organisms, including humans, can improve decision-making accuracy by appropriately pooling individual estimates (1–8). In the earliest study, in 1907, Sir Francis Galton made a near-perfect estimate of the weight of an ox by using 787 guesses made by others (9). Pooling of information is not exclusive to the human domain; for example, it has also been suggested that aggregating imperfect esti-

mates may help organisms, or cells, navigate weak or noisy environmental gradients (2–5). If each individual makes an error-prone estimate of the local gradient, it may benefit by also basing its movement decisions on the direction of motion of others, termed the “many wrongs” hypothesis (3).

Despite the importance of collective sensing to the ecology of many social species (10, 11) and the value to bio-inspired technological applications [such as particle swarm optimization (12), or swarm robotics (13)], with the exception of the social insects (8), we do not know how grouping enhances sensing capabilities in animal groups. Here, we use an integrated experimental and theoretical approach to address this deficit. We use schooling fish (golden shiners, *Notemigonus crysoleucas*) as our model experimental system and take advantage of their natural preference for a shaded (darker) habitat (14). Thus, our ex-

periments do not require training and are not susceptible to confounding factors relating to competition for, or consumption of, a preferred resource. Shiners school naturally in shallow water (15) and remain highly cohesive (14), which allowed us to explore the role of group size during a gradient detection task.

Our experiments were conducted with juvenile fish (body length  $4.9 \pm 0.5$  cm) in a shallow tank (213 cm by 122 cm, 8-cm water depth). Dynamic light fields were projected onto the tank. These fields consisted of a circular patch that was darkest at its center and transitioned smoothly (as an exponential) to the brightest light levels. Noise was added to this gradient to generate local variability in space and time. Furthermore, the circular patch itself moved at a constant speed between a series of randomly selected locations within the tank. See (16) for further details. The task for the fish was to track the preferred, darker regions of this dynamic environment.

We investigated the performance of single fish and groups of 2, 4, 8, 16, 32, 64, 128, and 256 individuals. Three levels of environmental noise were employed. For the lowest value, the light field was dominated by the simple circular patch; for the highest level of noise, the field largely consisted of ephemeral, local peaks. Measured light levels at the surface of the tank ranged from 4.2 lux (approximately twilight) to 150 lux (overcast day), corresponding to their natural environment in the morning or evening. We stress, however, that light is used as a proxy for any important environmental cue (such as temperature or salinity), with the circular patch representing large-scale features and the noise recreating fine-scale structure.

Because golden shiners are highly cryptic when in dark regions, the tank was lit with infrared light. The level of the projected light field, with respect to their positions, was then used to calculate a

<sup>1</sup>Department of Ecology and Evolutionary Biology, Princeton University, Princeton, NJ 08544, USA. <sup>2</sup>School of Biological Sciences, University of Bristol, Woodland Road, Bristol BS8 1UG, UK.

\*These authors contributed equally to this work.

†To whom correspondence should be addressed. E-mail: aberdahl@princeton.edu (A.B.); icouzin@princeton.edu (I.D.C.)



**Fig. 1. (A)** The positions of a group of 32 fish as they negotiate the light field, superimposed on that field. Medium noise level (0.25) is shown. Note that the frame only includes a small region of the larger tank. The snapshots are 2 s apart, with time increasing to the right. **(B)** Performance,  $\Psi$ , as a function of group size. The data points show the mean  $\Psi$  over experimental trials, and the error bars show twice the standard error. The solid blue line is the statistical model's fit to the data, and the shaded region is its 95% confidence interval. The red line is the equivalent performance measure for a numerical schooling model that incorporates a simple speed-differential algorithm. The quantitative values of this curve are dependent on model parameters, but the qualitative trend is independent of implementation details (16).

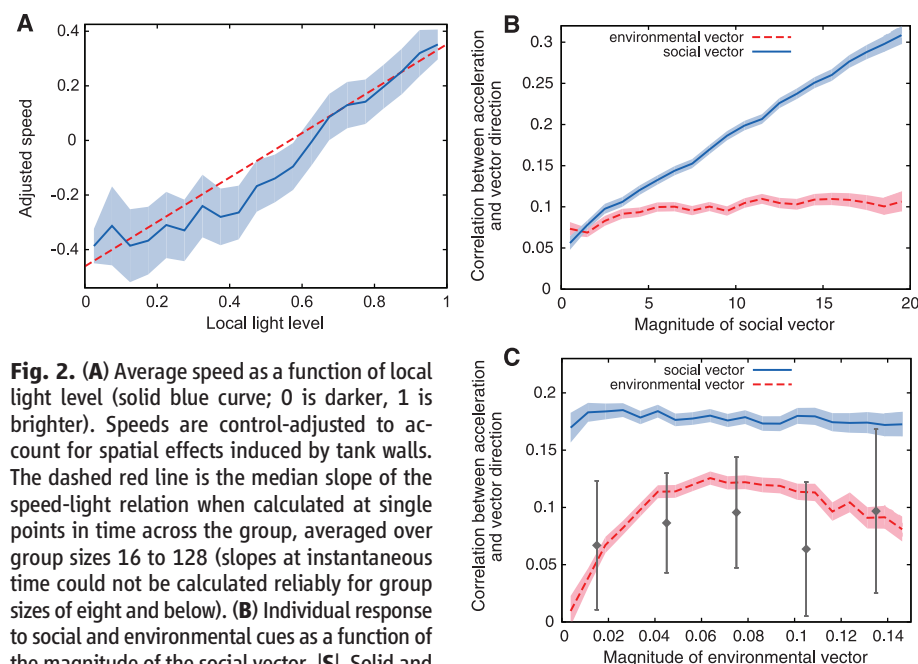
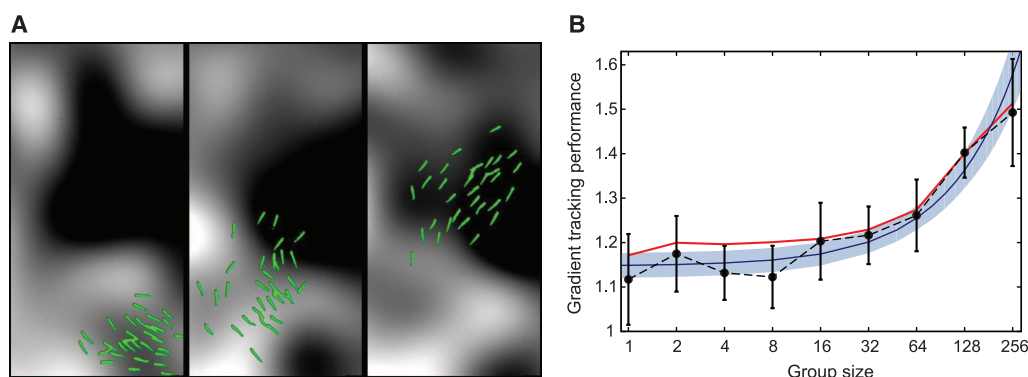


**Fig. 2. (A)** Average speed as a function of local light level (solid blue curve; 0 is darker, 1 is brighter). Speeds are control-adjusted to account for spatial effects induced by tank walls. The dashed red line is the median slope of the speed-light relation when calculated at single points in time across the group, averaged over group sizes 16 to 128 (slopes at instantaneous time could not be calculated reliably for group sizes of eight and below). **(B)** Individual response to social and environmental cues as a function of the magnitude of the social vector,  $|S|$ . Solid and dashed lines show the correlation between the direction of acceleration and the direction of the social vector and environmental vector, respectively. **(C)** Individual response to social and environmental cues as a function of the magnitude of the environmental vector,  $|G|$ . Legend as (B). Gray diamonds show solitary fish and demonstrate that the response to the environmental vector is approximately the same for individuals and those in groups. All shaded regions and error bars denote twice the standard error, data in (A) is down-sampled to remove any spatial correlations in speed and light level. See (16) for details and group sizes shown separately.

performance metric,  $\Psi$ : the time-averaged darkness level at the locations of the fish. This was normalized by a null performance value such that  $\Psi = 1$  in the absence of an environmental response. The value of  $\Psi$  increases above unity as performance increases, up to a theoretical maximum of  $\Psi_{\max} = 3.2 \pm 0.5$  (16).

The level of performance,  $\Psi$ , increased greatly as a function of group size (Fig. 1B). The value of  $\Psi$  was marginally above 1 for the smallest group sizes and for single fish; thus, fish always sought darker regions, regardless of group size. However, larger groups were significantly more effective at doing so [ $\chi^2_1 = 67$ ,  $P = 3.3 \times 10^{-16}$ , linear mixed

model (LMM)]. Results were not dependent on the level of noise in the projected light field (noise main effect:  $\chi^2_1 = 0.016$ ,  $P = 0.97$ , noise  $\times$  group size:  $\chi^2_1 = 0$ ,  $P = 1$ , LMM). The strategy is therefore robust, as it is unaffected by the structure and complexity of the light field.

In order to investigate the mechanism underlying the observed collective response to light gradients, fish were tracked individually to obtain trajectories (16). For all group sizes, we found a strong positive relation between individual speed and the light level at the location of that fish; fish tended to travel more slowly in dark regions and more quickly in light regions, as shown in Fig. 2A.

Using the accelerations of each fish, we assessed the degree to which the motion of individuals may be explained by environmental and social influences. On the basis of attraction to conspecifics, we estimated a social vector,  $S_i$ , for each individual,  $i$ , by taking into account the positions of neighbors within a fixed distance. We used seven body lengths, or 34.3 cm, for this distance; however, results are not dependent on the specific range (16). In addition, we measured the environmental vector,  $G_i$ , for each fish, which points in the direction of steepest ascent in the darkness level with a magnitude proportional to the rate of increase (the gradient of the light field measured from the perspective of the focal fish). We then measured the actual response of individual fish to these potential cues ( $S_i$  and  $G_i$ ) as the correlation between the direction of these influences and the direction of their acceleration (16).

The relation between the predicted influence (x axis) and the observed response (y axis) to  $S_i$  and  $G_i$ , respectively, is shown in Fig. 2, B and C. Acceleration was much more strongly influenced by the location of conspecifics than by environmental gradients (Fig. 2, B and C). When the magnitude of the social vector was high (near-neighbors were located in a consistent direction from the focal individual), the social influence was entirely dominant (Fig. 2B). Groups and solitary fish responded similarly to gradients (Fig. 2C). The slight dip in the response of groups to very high gradients can be attributed to the fact that such steep changes in light level are contributed predominantly by local, ephemeral noise (fig. S17), not by the longer-range feature to be tracked.

Although there is an interdependence between social and environmental effects, because of the increased likelihood of a fish being located in darker regions, these results show that the location of near-neighbors is a far better predictor of an individual's motion than the direction of the nearest dark region. Thus, when making movement decisions, fish more strongly respond to social cues than they do to the environment.

We isolate two complementary processes that result in effective gradient tracking by larger groups.

To illustrate the first mechanism, consider a scenario where a polarized group is travelling perpendicular to a gradient in light level. Individuals within the group, if located on the brighter side of the environment, will travel more quickly. This, in conjunction with interindividual attraction, induces rotation and turning toward the darker region. We find that, for a single instance in time, variation in speed among fish within a group corresponds to the variation in light level at their locations (Fig. 2A, dashed line). This speed differential across a group causes turning toward those who move more slowly (fig. S10). Second, as individuals slow down, the distance between them is reduced (see fig. S14), which increases the local density of animals in darker regions. Social influence results in acceleration tending to be in this direction (Fig. 2B).

To demonstrate the generic nature of these results, we performed simulations of grouping individuals (17, 18) that moderate their speed according to their local light level. Simulated individuals move within the same light fields that were presented to the real fish, yet lack any explicit gradient detection capacity. As in the experiments, greater group-level responsiveness to the environment arises spontaneously as group size increases (Fig. 1B). Further, we show that, although increased group numbers reduce measurement error, the key determinant of performance is the spatial extent of the group in relation to the length scale of the environment; groups that span a larger area are more likely to capture the variation in cue required to elicit a speed differential across the group (16).

Motion toward darker regions (taxis), therefore, results from social interactions among individuals, each of whom exhibits a rudimentary, nondirectional response to their environment (kinesis). Thus, the collective dynamics create a

group-level responsiveness to the environment that is absent at the individual level (19). The resulting increase in gradient-tracking ability for larger groups agrees with previous hypotheses (20, 21) and could explain empirical studies showing that grouping facilitates the detection of chemical cues (22–24) and improves the accuracy of migrations that rely on such cues (25, 26).

The simple algorithm revealed here may allow groups to respond to environmental gradients that occur over long length scales, for instance during the seasonal migration of fish tracking a single isotherm (27). If the mechanism we observed here is found to be widespread, as would be suggested by its robust nature and ease of implementation (in evolutionary terms), there are important ramifications for ecosystem conservation and management. Our results demonstrate that the ability to respond to environmental information may decline as populations are fragmented and average group sizes decrease.

#### References and Notes

1. A. W. Woolley, C. F. Chabris, A. Pentland, N. Hashmi, T. W. Malone, *Science* **330**, 686 (2010).
2. D. Grünbaum, *Evol. Ecol.* **12**, 503 (1998).
3. A. M. Simons, *Trends Ecol. Evol.* **19**, 453 (2004).
4. E. A. Codling, J. W. Pitchford, S. D. Simpson, *Ecology* **88**, 1864 (2007).
5. P. A. Larkin, A. Walton, *J. Fish. Res. Board Can.* **26**, 1372 (1969).
6. C. W. Clark, M. Mangel, *Theor. Popul. Biol.* **30**, 45 (1986).
7. I. D. Couzin *et al.*, *Science* **334**, 1578 (2011).
8. N. R. Franks, S. C. Pratt, E. B. Mallon, N. F. Britton, D. J. Sumpter, *Phil. Trans. R. Soc. B* **357**, 1567 (2002).
9. F. Galton, *Nature* **75**, 450 (1907).
10. S. Bauer *et al.*, in *Animal Migration: A Synthesis*, E. J. Milner-Gulland, J. M. Fryxell, A. R. E. Sinclair, Eds. (Oxford Univ. Press, New York, 2011), pp. 68–87.
11. T. J. Pitcher, J. K. Parrish, *Behaviour of Teleost Fishes* (Springer, New York, 1993), vol. 2, pp. 369–439.
12. R. Poli, J. Kennedy, T. Blackwell, *Swarm Intell.* **1**, 33 (2007).
13. P. Ogren, E. Fiorelli, N. E. Leonard, *IEEE Trans. Automat. Contr.* **49**, 1292 (2004).

14. S. G. Reeb, *Anim. Behav.* **59**, 403 (2000).
15. D. J. Hall *et al.*, *J. Fish. Board Can.* **36**, 1029 (1979).
16. Materials and methods are available as supplementary materials on Science Online.
17. I. D. Couzin, J. Krause, N. R. Franks, S. A. Levin, *Nature* **433**, 513 (2005).
18. M. Camperi, A. Cavagna, I. Giardina, G. Parisi, E. Silvestri, *Interface Focus* **2**, 715 (2012).
19. C. J. Torney, Z. Neufeld, I. D. Couzin, *Proc. Natl. Acad. Sci. U.S.A.* **106**, 22055 (2009).
20. A. Huth, C. Wissel, *Ecol. Modell.* **75–76**, 135 (1994).
21. U. Kils, thesis, University of Kiel, Germany (1987).
22. R. E. McNicol, E. Scherer, J. H. Gee, *Environ. Biol. Fishes* **47**, 311 (1996).
23. L. W. Hall Jr., D. T. Burton, S. L. Margrey, W. C. Graves, *J. Toxicol. Environ. Health* **10**, 1017 (1982).
24. C. W. Steele, A. D. Scarfe, D. W. Owens, *J. Fish Biol.* **38**, 553 (1991).
25. T. P. Quinn, K. Fresh, *Can. J. Fish. Aquat. Sci.* **41**, 1078 (1984).
26. J. J. Hard, W. R. Heard, *Can. J. Fish. Aquat. Sci.* **56**, 578 (1999).
27. K. Schaefer, D. Fuller, B. Block, *Mar. Biol.* **152**, 503 (2007).

**Acknowledgments:** We thank J. Herbert-Read for experimental assistance, N. O. Handegard for providing code and advice for track linking, and A. Haenssen for technical support. Suggestions from members of the Couzin laboratory and two anonymous reviewers greatly improved this manuscript. Funded by NSF awards PHY-0848755, EAGER-1251585, and CNH-1211972; U.S. Office of Naval Research award N00014-09-1-1074; U.S. Army Research Office grant W911NG-11-1-0385; Leverhulme Early Career Fellowship; Natural Sciences and Engineering Research Council of Canada Postgraduate Scholarship Fellowship; and the Yukon Foundation. All experiments were conducted in accordance with federal and state regulations and were approved by the Princeton University Institutional Animal Care and Use Committee. Code freely available at <http://icouzin.princeton.edu>.

#### Supplementary Materials

[www.sciencemag.org/cgi/content/full/339/6119/574/DC1](http://www.sciencemag.org/cgi/content/full/339/6119/574/DC1)  
Materials and Methods  
Supplementary Text  
Figs. S1 to S17  
Tables S1 and S2  
References (28–30)

11 June 2012; accepted 12 December 2012  
10.1126/science.1225883

## The Bacteriophage T7 Virion Undergoes Extensive Structural Remodeling During Infection

Bo Hu,<sup>1</sup> William Margolin,<sup>2</sup> Ian J. Molineux,<sup>3\*</sup> Jun Liu<sup>1\*</sup>

Adsorption and genome ejection are fundamental to the bacteriophage life cycle, yet their molecular mechanisms are not well understood. We used cryo-electron tomography to capture T7 virions at successive stages of infection of *Escherichia coli* minicells at ~4-nm resolution. The six phage tail fibers were folded against the capsid, extending and orienting symmetrically only after productive adsorption to the host cell surface. Receptor binding by the tail triggered conformational changes resulting in the insertion of an extended tail, which functions as the DNA ejection conduit into the cell cytoplasm. After ejection, the extended phage tail collapsed or disassembled, which allowed resealing of the infected cell membrane. These structural studies provide a detailed series of intermediates during phage infection.

**A**fter encountering a cell, a bacteriophage delivers its genetic material into the host cytoplasm via an orchestrated series of

conformational changes (1). T7 is a member of the *Podoviridae*, having short, noncontractile tails that are too short to span a bacterial cell en-

velope (2). The icosahedral 2-nm-thick T7 capsid is 60 to 61 nm in diameter, and inside, coaxial to the dodecameric head-tail connector, is a 26- by 21-nm internal core, which is thought to consist of three proteins: gp14, gp15, and gp16 (2, 3). The core is essential for both virion morphogenesis and ejection of the 40-kb genome. Near the head-proximal end of the 23-nm tail are six fibers, trimers of gp17. Each fiber has an N-terminal domain that attaches the fiber to the tail, followed by proximal and distal half-fibers. The latter interact with the cell surface (4, 5). After adsorption, the core proteins are ejected through the portal-tail

<sup>1</sup>Department of Pathology and Laboratory Medicine, University of Texas Medical School at Houston, Houston, TX 77030, USA.

<sup>2</sup>Department of Microbiology and Molecular Genetics, University of Texas Medical School at Houston, Houston, TX 77030, USA.

<sup>3</sup>Molecular Genetics and Microbiology, Institute for Cell and Molecular Biology, University of Texas at Austin, Austin, TX 78712, USA.

\*To whom correspondence should be addressed. E-mail: [molineux@austin.utexas.edu](mailto:molineux@austin.utexas.edu) (I.J.M.); [jun.liu.1@uth.tmc.edu](mailto:jun.liu.1@uth.tmc.edu) (J.L.)



complex into the infected cell, and it has been hypothesized that they extend the tail, creating a trans-envelope channel used for DNA transport (6–8). Here, we used cryo-electron tomography (cryo-ET) to provide three-dimensional (3D) structures of infected cell complexes in near-native, frozen-hydrated states at ~4-nm resolution (fig. S1).

We infected small ( $\leq 0.3 \mu\text{m}$  in diameter) *Escherichia coli* minicells (9) to achieve maximum resolution. The T7-infected minicells produced infective centers at normal efficiencies, and the parent skinny cells were good hosts for the phage, which suggested that our structures reflected the normal infection pathway (10). The 3D reconstructions revealed adsorbed virions at three stages of infection (Fig. 1 and movie S1) and supported the hypothesis (6–8) that T7 internal core proteins form a trans-envelope channel (Fig. 1, B and E). Dual-axis tomography confirmed the presence of various conformations (movie S2). In order to obtain better structural details, we used subvolume averaging to determine the 3D structures during infection (10).

Asymmetric reconstructions of a fiberless gene 17 mutant (Fig. 2, A and D) and wild-type (Fig. 2, B and E) virions were derived from 1945 and 6116 subvolumes, respectively. The overall structure of wild-type T7 (Fig. 2B) is similar to that reported (3), but our tomographic reconstruction resolved the tail fibers (Fig. 2, B, C, E, and F). Placing a known structure of part of the distal half-fiber (5) into the cryo-ET density revealed a good fit (Fig. 2F). Each fiber

was folded back onto the capsid with the proximal half-fiber rising across the face of a capsomer. The  $\sim 90^\circ$  kink between proximal and distal half-fibers was visible in 3D surface renderings (Fig. 2, E and F). Fibers retained a conformation similar to that of isolated tail complexes (fig. S2) (4).

The T7 tail exhibited 6-fold symmetry, but the distal half-fibers were bound to the capsid, which is 5-fold symmetrical at the connector. To better understand the symmetry mismatch and the fiber-capsid interactions, we classified each fiber independently by correspondence analysis (figs. S3 and S4). Class I fibers exhibited only a short fragment corresponding to the N-terminal domain that is bound to the tail (4), which indicated that neither half-fiber was bound to the capsid. Proximal and distal half-fibers were visible in class II and were subdivided into subclasses by their different orientations on the capsid (Fig. 2, H and I). Projecting all distal half-fiber conformations onto the same surface showed that there is no specific binding site (fig. S4).

Phage tail fibers are normally depicted extending away from the capsid, poised for adsorption. However, we found that ~50% of mature T7 virions had five fibers bound to the capsid and ~30% had four; very few had no bound fibers (Fig. 2J). Most published electron microscopy (EM) images of T7 do not resolve fibers; they were visible in a tomogram of negatively stained T7 particles only as short projections from the capsid (fig. S2). More than 95% of the wild-type T7 prepared for this study

made infective centers in exponentially growing cells within 2 to 3 min, which suggested that extended fibers were not required for rapid adsorption (10). Proximal half-fibers of the T7-related phage P-SSP7 also appear bound in mature virions but are extended in spontaneously emptied free particles (11). Furthermore, cryo-EM reconstructions of T4 virions show fibers wrapped around the tail sheath, not pointing away from the capsid (12). Maintaining tail fibers on the body of free virions may thus be typical of many phages.

Adsorbed T7 virions were generally oriented perpendicular to the cell surface with the tail slightly indenting the outer membrane (Fig. 3, A and B; fig. S5; and movie S3), similar to adsorbed phage P-SSP7 (11). Proximal half-fibers extended horizontally, whereas distal half-fibers were vertical; bound fibers exhibited the same 6-fold symmetry as the tail, covering  $\sim 3000 \text{ nm}^2$  of the cell surface. During adsorption, fibers underwent a large rotation, which was probably due to the N-terminal domain pivoting on its connection to the tail (fig. S6). Two-thirds (3352) of adsorbed phages analyzed were captured at this intermediate stage, with the internal core remaining intact within the capsid, which suggests that recognition of the cell surface by all six fibers is insufficient to trigger later steps of infection.

About one-third (1886) of adsorbed particles displayed a tubelike extension of the tail that penetrated both cell membranes (Fig. 3, C and D; figs. S5 and S7; and movie S3). A functional extension of the T7 tail is essential for genome delivery into the host (2). The energy required for this dramatic change in structure must be stored in the virion, because cellular energy sources will not yet be accessible. The interaction between the tail and the outer membrane also changed, which presumably reflects the conformational changes that signal ejection of the internal core, which was no longer visible (Fig. 3, A and C). However, the head still appeared full, which suggested that the encapsidated DNA had expanded to occupy the volume originally occupied by the core.

The extended tail is probably composed of ejected core proteins, which have been found in the infected cell envelope (7, 8). Gp14 localizes to the infected cell outer membrane, whereas gp15 and gp16 span the periplasm and cytoplasmic membrane. Various mutant gp16-containing virions change the kinetics of genome ejection or prevent DNA from entering the cytoplasm; the latter defect can be suppressed by virions also harboring a mutant gp15 (8, 13–16). After infection by 16E37F mutant virions, which are defective in cell wall hydrolysis and which exhibit delayed DNA entry into the cytoplasm (14, 17), the extended tail took  $\sim 20$  times as long to form (fig. S8). The estimated volume of the internal core (3) is sufficient to form the entire extension. The overall tail extension was  $\sim 45 \text{ nm}$ , and the tube had an outer diameter of

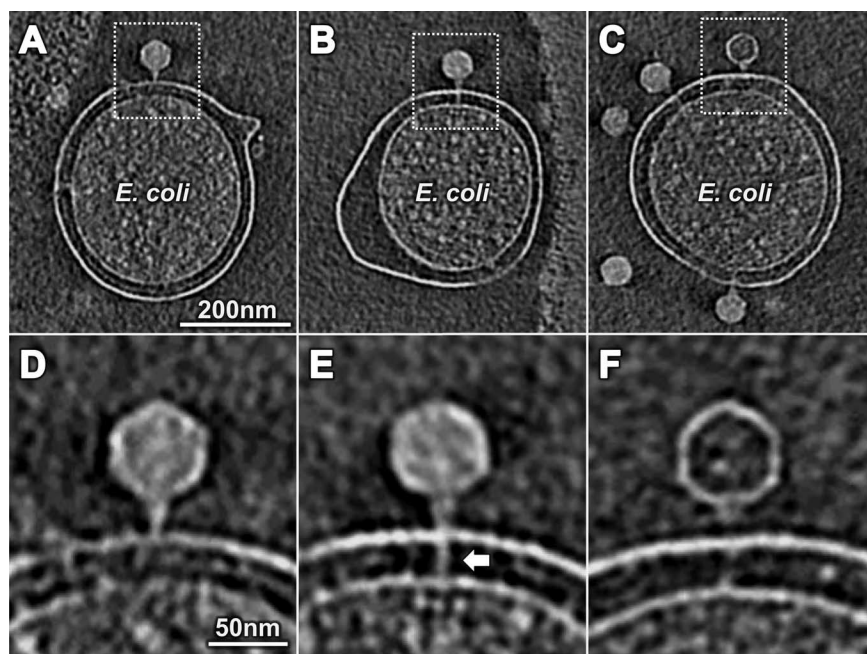


**Fig. 1.** Three stages of T7 infection. (A and D) T7 adsorbed to the outer membrane. The density spanning the cell envelope at  $270^\circ$  in (A) was derived from fiducial gold markers (shown explicitly in movie S1 as a series of slices across the cell in (A)). (B and E) An extended tail (arrow) spanned the cell envelope. (C and F) After DNA ejection, the extended tail was not apparent.

**Fig. 2.** Asymmetric reconstructions of virions. (A) A central slice of a fiberless virion revealed the tail, capsid, and internal core. Fibers were visible in a central slice (B) and a cross section of wild-type virions (C). Surface rendering of fiberless (D) and wild-type virions in side (E) and bottom (F) views. A crystal structure of the receptor-binding domain of T7 fibers (5) was placed into three fiber densities. Residues A518, D520, and V544, known to affect phage host range (5), are highlighted in red (F). Classification revealed different conformations of fibers not bound (G) or bound to the capsid (H and I). (J) Distribution of the number of bound fibers on free virions; few had either six or zero fibers bound.

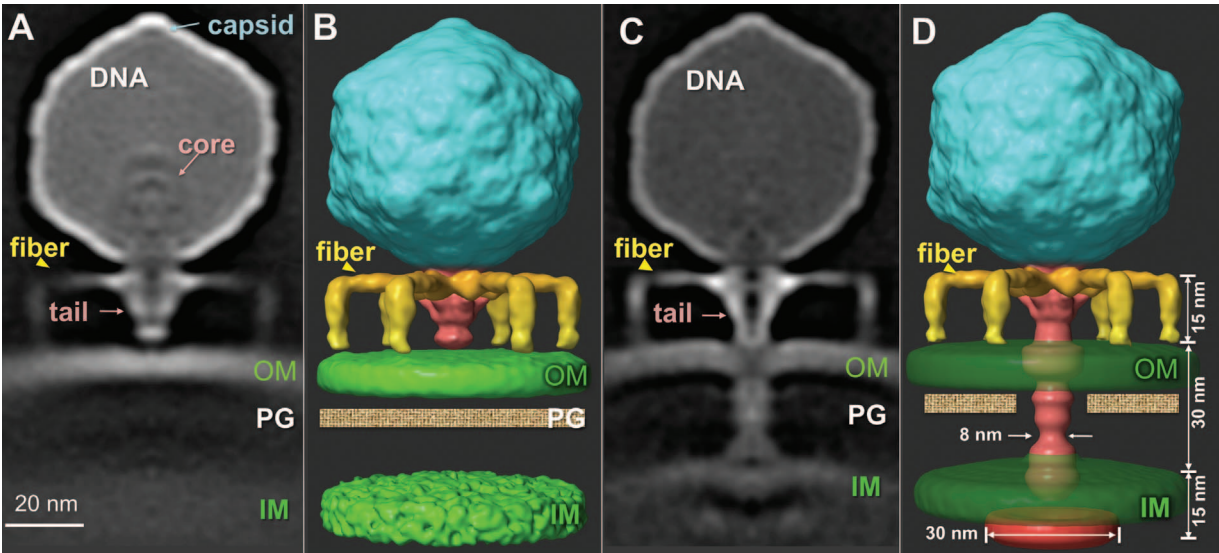
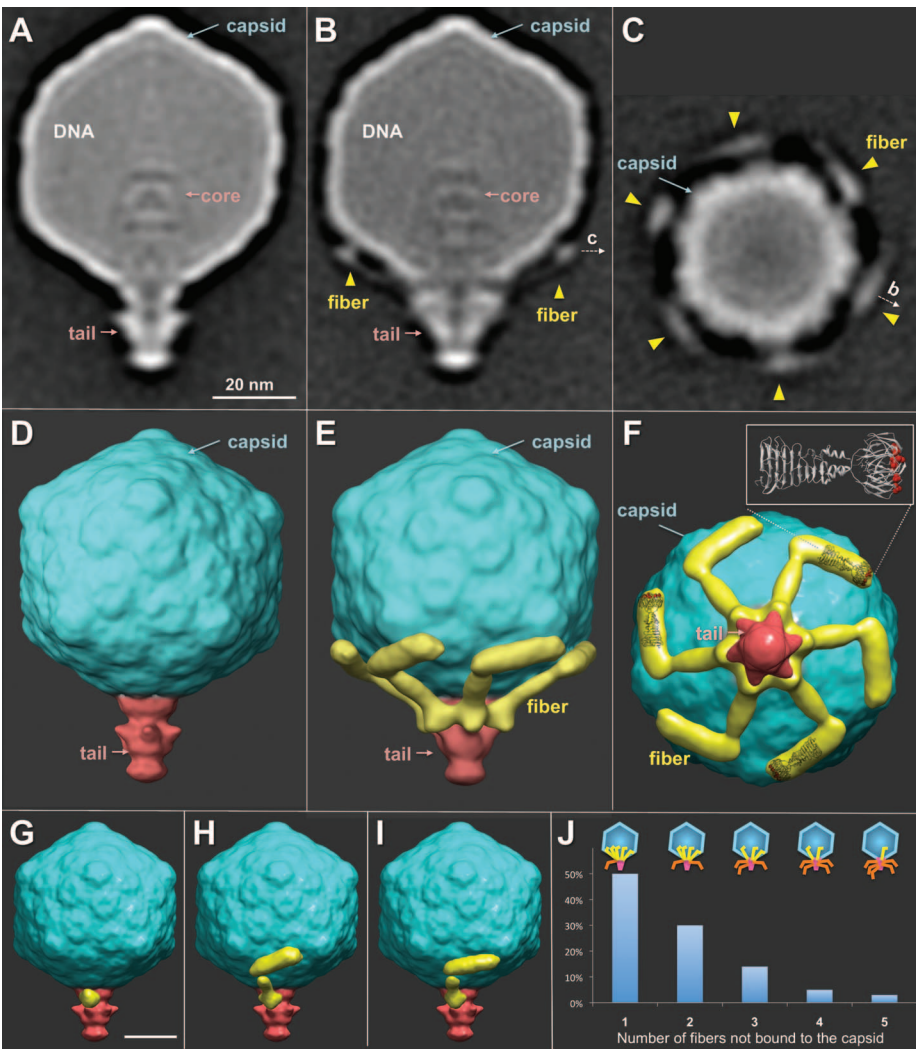
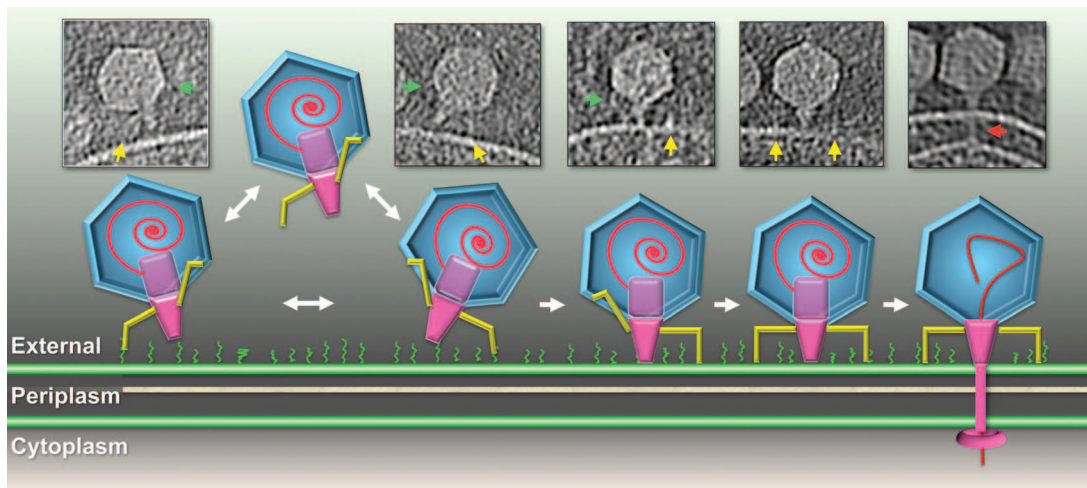


**Fig. 3.** Adsorption structures. (A) Central slice and (B) 3D surface view of a subvolume average derived from 3352 virions. All six fibers were bound to the cell, and the tail made a small indentation in the outer membrane (OM); the internal core and DNA were still in the capsid. (C) Central slice

and (D) 3D surface view of a subvolume average derived from 1886 virions. The internal core had been ejected from the virion, forming an extended tail that penetrated the cell cytoplasm. PG, peptidoglycan cell wall; IM, inner membrane.



**Fig. 4.** Schematic model of T7 infection. The insert tomograms show the different orientations of tail fibers. Fibers bound to the cell are highlighted with yellow arrows, unbound fibers with green arrows. After “walking” across the cell surface to find the receptor for the tail, all fibers rotate downward to contact the outer membrane. Commitment to infection occurs after internal core proteins are ejected from the virion and the extended tail (red arrow) forms.



$\geq 8$  nm, sufficient to accommodate double-stranded DNA in its lumen. As the tube approached the cytoplasmic membrane, density broadened (Fig. 3, C and D), probably because the extended tail was flexible (movie S4). Density associated with the tube was less distinct inside the cytoplasm, but  $\sim 12$  nm below the center of the membrane a  $\sim 30$  by 6 nm toroid with a  $\sim 4$ -nm central cavity was clearly present (fig. S9 and movie S4). The toroid may be part of the molecular motor that has been hypothesized to pull the leading genome end into the cell (6, 8, 16).

About 3% (162) of adsorbed phages had completely ejected their genome. Virion structure at this stage of infection was thus determined only at relatively low resolution (fig. S10 and movie S3). The cytoplasmic toroid was not visible, and the tube traversing the periplasm had collapsed or disassembled, which presumably prevented dissipation of the membrane potential, which would inhibit phage development. We tested whether an energized membrane was required for channel formation by treating minicells with carbonyl cyanide *m*-chlorophenyl hydrazone (CCCP) before infection. Of the 244 virions observed, 14% did not adsorb, 55% adsorbed without tail extension, 31% formed a trans-envelope structure, but none ejected their genome (fig. S11). An energized membrane was thus not necessary for adsorption or ejection of internal proteins, but, as expected (16, 18), it is essential for genome translocation.

The combination of technical advances in cryo-ET and a reduction in *E. coli* cell size has allowed us to describe detailed features of the mature T7 virion and structural changes during infection. Tail fibers, usually depicted extending away from the virion, were mostly bound to the capsid. Our data suggest a dynamic equilibrium between bound and unbound states. Maintaining fibers in a folded-back configuration would allow a higher rate of virion dif-

fusion, whereas transient extension could still permit the phage to explore a large volume in search of a cell. Binding of fibers to bacterial receptors is weak, but transient binding could reduce the dimensional space for finding a suitable site for infection from three to two (19). Weak binding could potentially achieve the necessary specificity of adsorption by cooperative binding among fibers or by a second component, i.e., the tail, binding with high specificity (2, 7, 20). We propose that the transition to a stably adsorbed state occurs following a random walk after an initial interaction between a fiber and the cell; e.g., bound fiber no. 1 is directly replaced by binding of fiber no. 2 without virion release (Fig. 4 and movie S5). Alternatively, in a quasi-2D diffusion process, fiber no. 1 may dissociate, followed rapidly by fiber no. 2 detaching from the capsid and binding to the cell. Note that the common lab strain of phage  $\lambda$ , which lacks side tail fibers, has been suggested to move across the cell surface in a quasi-1D process (21). At a preferred site of infection, the tail interacts specifically with its receptor, which prevents further lateral movement and allows all fibers to bind. The fibers of phage T7 may thus function primarily to facilitate interaction of the tail with its specific receptor. After stable adsorption, infection is triggered by ejection of the internal core proteins into the cell envelope and the formation of an extended tail, which may protect the entering genome from periplasmic nucleases.

#### References and Notes

1. J. E. Johnson, W. Chiu, *Curr. Opin. Struct. Biol.* **17**, 237 (2007).
2. S. R. Casjens, I. J. Molineux, *Adv. Exp. Med. Biol.* **726**, 143 (2012).
3. X. Agirrezabala *et al.*, *EMBO J.* **24**, 3820 (2005).
4. A. C. Steven *et al.*, *J. Mol. Biol.* **200**, 351 (1988).
5. C. Garcia-Doval, M. J. van Raaij, *Proc. Natl. Acad. Sci. U.S.A.* **109**, 9390 (2012).
6. I. J. Molineux, *Mol. Microbiol.* **40**, 1 (2001).

7. P. Kemp, L. R. Garcia, I. J. Molineux, *Virology* **340**, 307 (2005).
8. C. Y. Chang, P. Kemp, I. J. Molineux, *Virology* **398**, 176 (2010).
9. J. Liu *et al.*, *Proc. Natl. Acad. Sci. U.S.A.* **109**, E1481 (2012).
10. See supplementary materials on Science Online.
11. X. Liu *et al.*, *Nat. Struct. Mol. Biol.* **17**, 830 (2010).
12. P. G. Leiman *et al.*, *Viol. J.* **7**, 355 (2010).
13. L. R. Garcia, I. J. Molineux, *J. Bacteriol.* **178**, 6921 (1996).
14. M. Moak, I. J. Molineux, *Mol. Microbiol.* **37**, 345 (2000).
15. J. S. Struthers-Schlinke, W. P. Robins, P. Kemp, I. J. Molineux, *J. Mol. Biol.* **301**, 35 (2000).
16. P. Kemp, M. Gupta, I. J. Molineux, *Mol. Microbiol.* **53**, 1251 (2004).
17. M. Moak, I. J. Molineux, *Mol. Microbiol.* **51**, 1169 (2004).
18. A. Z. Zimkus, S. K. Zavriev, L. L. Grinius, *Mol. Biol. (Mosk)* **20**, 185 (1986).
19. G. Adam, M. Delbrück, in *Structural Chemistry and Molecular Biology*, R. Rich, N. Davidson, Eds. (Freeman, San Francisco, 1968), pp. 198–215.
20. U. Qimron, B. Marintcheva, S. Tabor, C. C. Richardson, *Proc. Natl. Acad. Sci. U.S.A.* **103**, 19039 (2006).
21. E. Rothenberg *et al.*, *Biophys. J.* **100**, 2875 (2011).

**Acknowledgments:** We thank P. Leiman, S. Norris, and Y. W. Yin for comments. B.H. and J.L. were supported in part by grants R01AI087946 from the National Institute on Allergy and Infection, NIH, and AU-1714 from the Welch Foundation. W.M. was supported by NIH grant R01GM61074 and a grant from the Human Frontier Science Program. EM maps have been deposited in the EM Data Bank ([www.ebi.ac.uk/pdbe/emdb/](http://www.ebi.ac.uk/pdbe/emdb/)) with accession nos. EMD-5534, 5535, 5536, and 5537. J.L. and I.J.M. designed research; B.H. and W.M. constructed the *E. coli* mutants; B.H. and J.L. collected and analyzed data; and B.H., W.M., J.L., and I.J.M. wrote the paper.

#### Supplementary Materials

[www.sciencemag.org/cgi/content/full/science.1231887/DC1](http://www.sciencemag.org/cgi/content/full/science.1231887/DC1)  
Materials and Methods  
Figs. S1 to S11  
Table S1  
References (22–30)  
Movies S1 to S5

23 October 2012; accepted 13 December 2012  
Published online 10 January 2013;  
10.1126/science.1231887

# Circulating Breast Tumor Cells Exhibit Dynamic Changes in Epithelial and Mesenchymal Composition

Min Yu,<sup>1,6\*</sup> Aditya Bardia,<sup>1,3\*</sup> Ben S. Wittner,<sup>1</sup> Shannon L. Stott,<sup>1,2</sup> Malgorzata E. Smas,<sup>1</sup> David T. Ting,<sup>1</sup> Steven J. Isakoff,<sup>1,3</sup> Jordan C. Ciciliano,<sup>1</sup> Marissa N. Wells,<sup>1</sup> Ajay M. Shah,<sup>2</sup> Kyle F. Concannon,<sup>1</sup> Maria C. Donaldson,<sup>1</sup> Lecia V. Sequist,<sup>1,3</sup> Elena Brachtel,<sup>1,4</sup> Dennis Sgroi,<sup>1,4</sup> Jose Baselga,<sup>1,3</sup> Sridhar Ramaswamy,<sup>1,3</sup> Mehmet Toner,<sup>2,5</sup> Daniel A. Haber,<sup>1,3,6†</sup> Shyamala Maheswaran<sup>1,5†</sup>

Epithelial-mesenchymal transition (EMT) of adherent epithelial cells to a migratory mesenchymal state has been implicated in tumor metastasis in preclinical models. To investigate its role in human cancer, we characterized EMT in circulating tumor cells (CTCs) from breast cancer patients. Rare primary tumor cells simultaneously expressed mesenchymal and epithelial markers, but mesenchymal cells were highly enriched in CTCs. Serial CTC monitoring in 11 patients suggested an association of mesenchymal CTCs with disease progression. In an index patient, reversible shifts between these cell fates accompanied each cycle of response to therapy and disease progression. Mesenchymal CTCs occurred as both single cells and multicellular clusters, expressing known EMT regulators, including transforming growth factor (TGF)- $\beta$  pathway components and the FOXC1 transcription factor. These data support a role for EMT in the blood-borne dissemination of human breast cancer.

Most cancer-related deaths are caused by metastasis, the dissemination of cancer cells from the primary tumor through the blood to new organ sites (1). Aberrant activation of epithelial-mesenchymal transition (EMT) has been implicated in this process, based on

studies with human cancer cell lines and mouse models (2, 3). Immunohistochemical approaches to identify EMT in tumors is complicated by the presence of reactive mesenchymal stromal cells (4, 5), and analysis of circulating tumor cells (CTCs) has been hampered by reliance on epithelial markers

to separate cancer cells from surrounding hematopoietic cells of mesenchymal origin (6, 7). To address these technical challenges, we optimized microfluidic capture of CTCs with epithelial- and tumor-specific antibodies, and we then used this technology to analyze EMT in CTCs from breast cancer patients.

We established a quantifiable, dual-colorimetric RNA-in situ hybridization (ISH) assay to examine tumor cells for expression of seven pooled epithelial (E) transcripts [keratins (KRT) 5, 7, 8, 18, and 19; EpCAM (epithelial cell adhesion molecule); and CDH1 (cadherin 1)] and three mesenchymal (M) transcripts [FN1 (fibronectin 1), CDH2 (cadherin 2), and SERPINE1/PAI1 (serpin peptidase inhibitor, clade E)]. These probes were validated in cell lines to confirm differential expression in epithelial versus mesenchymal cancer cells and the absence of expression in blood cells that contaminate CTC preparations (table S1 and fig. S1A). After validating the

<sup>1</sup>Massachusetts General Hospital Cancer Center, Harvard Medical School, Charlestown, MA 02129, USA. <sup>2</sup>Center for Bioengineering in Medicine, Harvard Medical School, Charlestown, MA 02129, USA. <sup>3</sup>Department of Medicine, Harvard Medical School, Charlestown, MA 02129, USA. <sup>4</sup>Department of Pathology, Harvard Medical School, Charlestown, MA 02129, USA. <sup>5</sup>Department of Surgery, Harvard Medical School, Charlestown, MA 02129, USA. <sup>6</sup>Howard Hughes Medical Institute, Chevy Chase, MD 20815, USA.

\*These authors contributed equally to this work.

†To whom correspondence should be addressed. E-mail: haber@helix.mgh.harvard.edu (D.A.H.); maheswaran@helix.mgh.harvard.edu (S.M.)

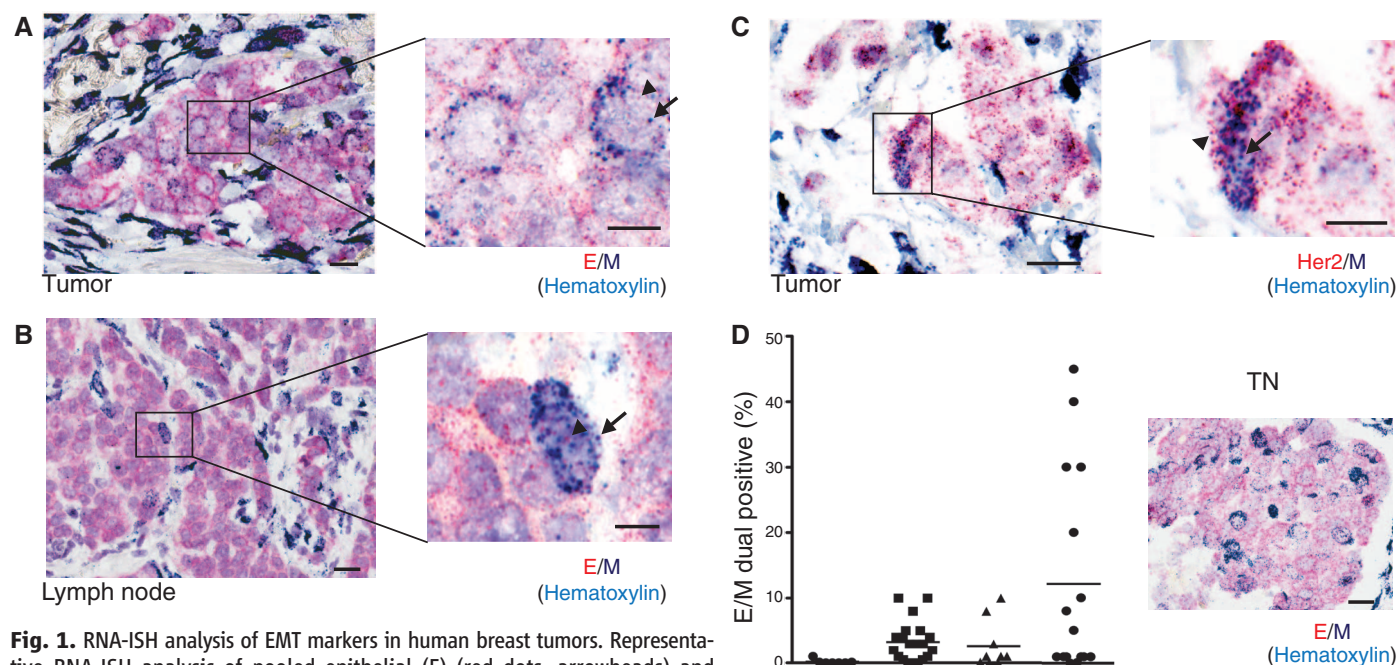


**Fig. 1.** RNA-ISH analysis of EMT markers in human breast tumors. Representative RNA-ISH analysis of pooled epithelial (E) (red dots, arrowheads) and mesenchymal (M) (dark blue dots, arrows) markers in (A) primary tumor and (B) tumor-infiltrated lymph node of a patient with ductal ER<sup>+</sup>/PR<sup>+</sup> type breast cancer. (C) RNA-ISH analysis of HER2 (red dots, arrowheads) and M (dark blue dots, arrows) expression in a HER2<sup>+</sup> primary breast tumor. (D) Quantitation of E and M dual-positive tumor cells (percentage of total tumor cells) in a TMA consisting of premalignant DCIS (*N* = 7 cases) and ER<sup>+</sup>/PR<sup>+</sup> (*N* = 20 cases), HER2<sup>+</sup> (*N* = 9 cases), and TN (*N* = 16 cases) breast cancers. A representative image from a TN case is shown on the right. E, red dots; M, dark blue dots; nuclei are stained with hematoxylin, light blue. Scale bars: (A) to (D), 20  $\mu$ m; inserts, 10  $\mu$ m.



E/M RNA-ISH analysis in mouse xenografts of epithelial or mesenchymal breast cancer cells (fig. S1B), we applied the assays to primary human breast cancer specimens.

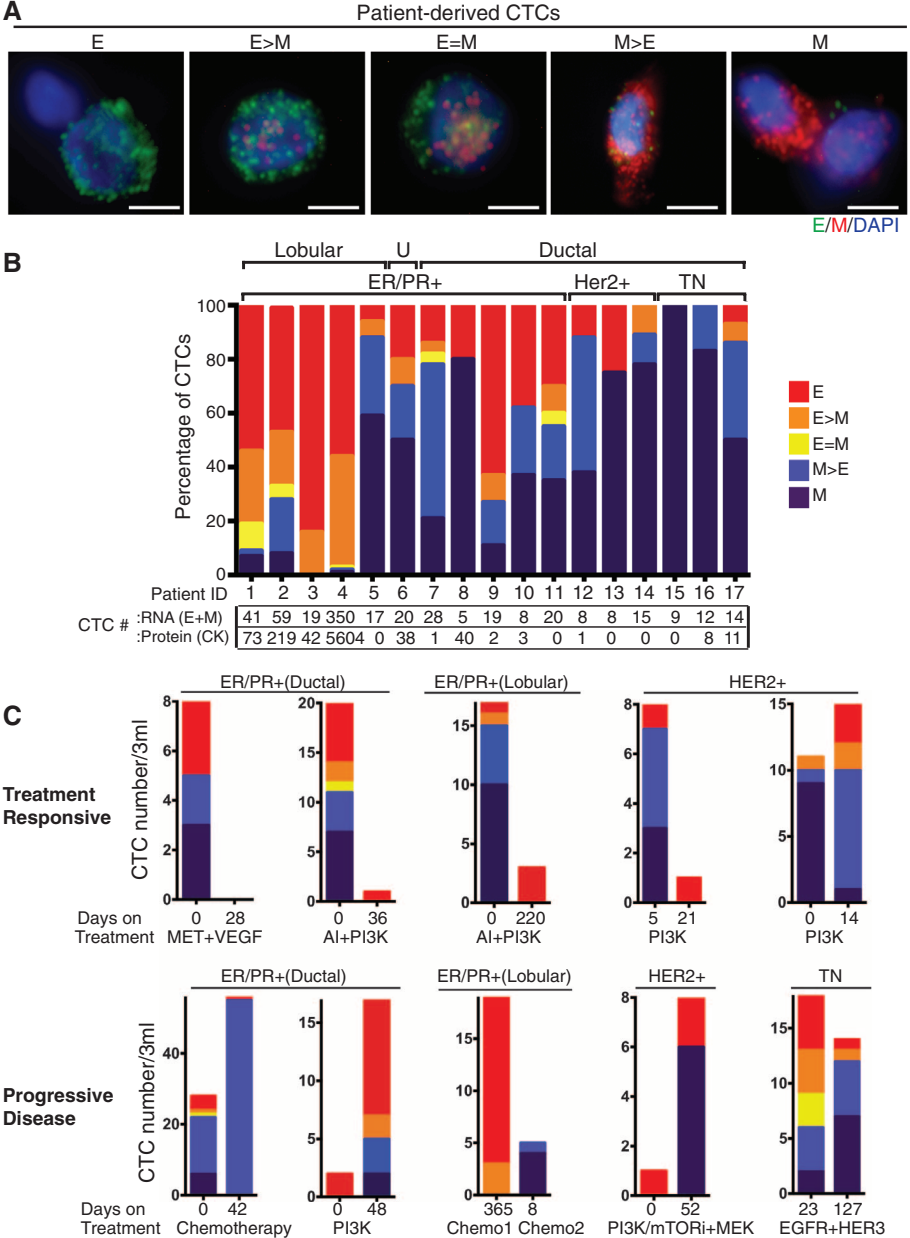
Among the majority of E<sup>+</sup> cancer cells, and distinct from the M<sup>+</sup> stromal cells, we detected a small number of biphenotypic E<sup>+</sup>/M<sup>+</sup> cells with clear epithelial histology, both in primary tumors and in draining lymph nodes (Fig. 1, A and B). Dual-RNA-ISH staining for M markers and a tumor-specific marker (HER2) confirmed the identity of such mesenchymal cells as tumor-derived (Fig. 1C). We scored tissue microarrays (TMAs) containing multiple primary breast cancers of various histological subtypes for the number of dual E<sup>+</sup>/M<sup>+</sup> cells. Using this assay, we found that benign breast tissue (*N* = 6 cases) and tumor cells in pre-invasive ductal carcinoma in situ

(DCIS) lesions (*N* = 7 cases) were exclusively epithelial, whereas reactive stromal cells were exclusively mesenchymal. In contrast, we found that all three major histological subtypes of invasive breast cancer contained rare tumor cells with epithelial morphology that stained with both E and M markers: ER/PR<sup>+</sup> subtype (mean = 3.3%, range 0 to 10%, *N* = 20 cases); HER2<sup>+</sup> subtype (mean = 2.7%, range 0 to 10%, *N* = 9 cases); and the triple negative (TN) (ER<sup>-</sup>/PR<sup>-</sup>/HER2<sup>-</sup>) subtype (mean = 12.1%, range 0 to 45%, *N* = 16 cases) (Fig. 1D). The higher number of M<sup>+</sup> tumor cells in primary TN breast cancer is consistent with this type of breast cancer being enriched for mesenchymal markers, including vimentin (8, 9). Some TN cases contained clusters of cells in the middle of the tumor mass that were strongly positive for both E and M markers, yet were histo-

logically indistinguishable from the neighboring E<sup>+</sup> tumor cells (Fig. 1D). Thus, human primary breast tumors contain rare cancer cells that co-express mesenchymal and epithelial markers.

To extend our EMT analysis to CTCs, we used the microfluidic HB (herringbone)-chip (10) to capture CTCs from blood with an antibody cocktail directed against EpCAM, EGFR (epithelial growth factor receptor), and HER2 (human epithelial growth factor receptor 2) (fig. S2). Human breast cancer cell lines exhibiting epithelial (MCF7 and SKBR3) and mesenchymal (MDA-MB-231) characteristics were spiked into blood and captured on the triple-antibody cocktail-coated CTC-chip to ensure capture efficiencies of 80 to 90%. MCF10A cells expressing the EMT-inducing transcription factor Lbx1 (11) were used to optimize the quantitative immunofluorescence-based

**Fig. 2.** RNA-ISH analysis of EMT markers in CTCs from patients with metastatic breast cancer. **(A)** Representative images of five types of CTCs isolated from patients with metastatic breast cancer, based on RNA-ISH staining of E (green dots) and M (red dots) markers. Scale bar, 5  $\mu$ m **(B)** Quantitation of EMT features in CTCs based on E and M RNA-ISH staining of histological subtypes of breast cancer [lobular, ductal, and U (unknown)], along with molecular classification (ER/PR, HER2, TN). CTC numbers per 3 ml of blood based on RNA (E<sup>+</sup>/M<sup>+</sup>) or protein (CK) staining are listed below. **(C)** Fractionation of CTCs according to E/M ratios in five patients who were clinically responding to treatment (top) and five patients who had progressive disease on treatment (bottom). The subtype of breast cancer, each patient's treatment regimen, and the number of days on treatment are shown. The drugs used to inhibit the signaling pathways shown on the figure are as follows: MET + VEGF (vascular endothelial growth factor), cabozantinib; AI (aromatase inhibitor), letrozole; PI3K (phosphatidylinositol 3-kinase), BKM120, INK1117, and BYL719; PI3K/mTOR (mammalian target of rapamycin), SAR245409; MEK (MAP kinase kinase), MSC193639B; EGFR/HER3 (human epidermal growth factor receptor 3), MEHD7945A. The chemotherapeutic drugs used were cisplatin, taxol, and adriamycin. Tumor genotypes are given in table S2.



E and M RNA-ISH detection of cells captured on the CTC-chip (fig. S3). Using this assay, we defined five categories of cells ranging from exclusively epithelial (E) to intermediate ( $E > M$ ,  $E = M$ ,  $M > E$ ) and exclusively mesenchymal (M) (fig. S3 and Fig. 2A).

To determine the cutoff for a positive CTC score, we first analyzed samples from five healthy blood donors. Two mesenchymal cells were identified in one of the five specimens (median 0, range 0 to 2 cells per 3 ml). To set a conservative threshold, we established 5 cells per 3 ml as cutoff for a positive CTC score. We next analyzed blood samples from 41 patients at various stages of treatment for metastatic breast cancer. Seventeen patients (41%) scored positive for CTCs, with EMT features varying according to histological subtype (Fig. 2, A and B). CTCs from patients with lobular type cancers (typically  $ER^+/PR^+$ ) were predominantly epithelial, whereas those from the TN subtype were predominantly mesenchymal. Interestingly, CTCs from patients with  $HER2^+$  breast cancer, whose primary tumors typically contain few  $E^+/M^+$  cells, were also predominantly mesenchymal (Fig. 2B). Of note, standard cytokeratin-based protein staining of CTCs was comparable to RNA-

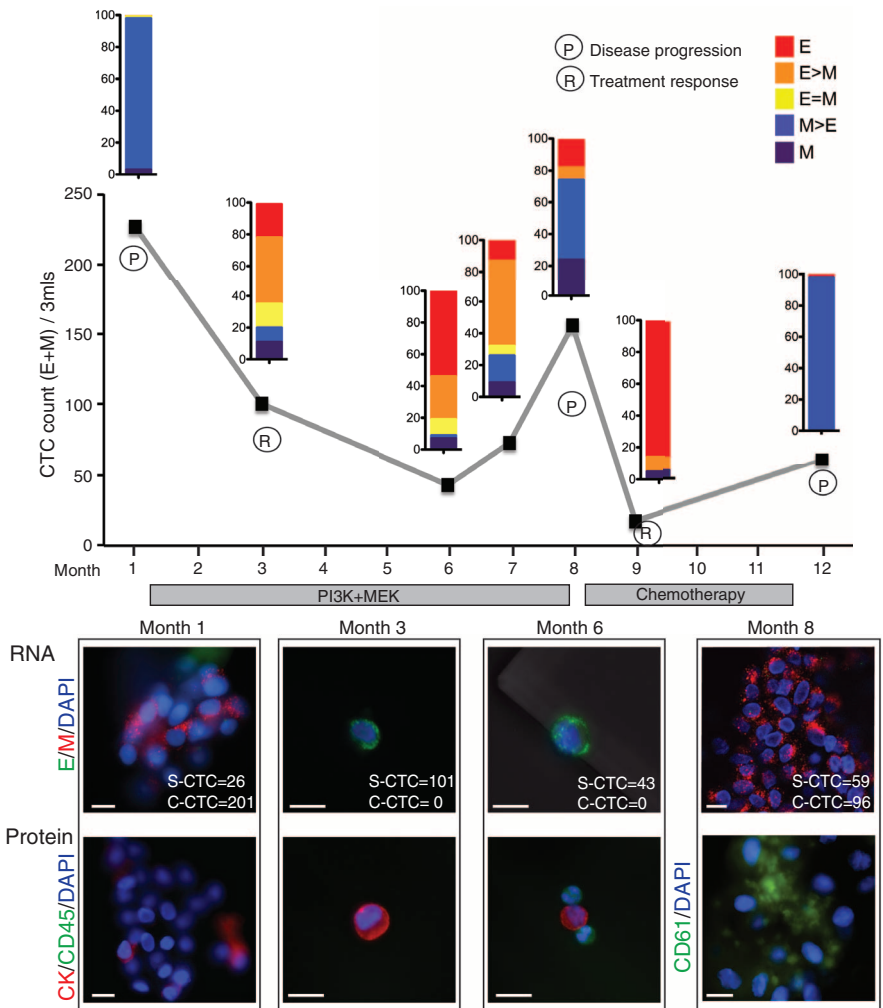
ISH for scoring epithelial CTCs but dramatically undercounted cases with mesenchymal CTCs (12).

We next compared CTC features in pre- and posttreatment blood samples from 10 of these cases. Five patients who responded to therapy showed a decrease in CTC numbers and/or a proportional decrease in  $M^+$  compared with  $E^+$  CTCs in the posttreatment sample (Fig. 2C). In contrast, five patients who had progressive disease while on therapy showed an increased number of  $M^+$  CTCs in the posttreatment sample. We obtained serial specimens from one index patient with  $ER/PR^+$  lobular carcinoma. This patient had initially responded to an experimental regimen, developed resistance, and then responded transiently to standard chemotherapy (Fig. 3). A high number of  $M^+$  CTCs was evident at the first time point. The first clinical response to the experimental regimen was accompanied by declining CTC numbers and a switch to predominantly  $E^+$  cells. After 7 months of this therapy, the patient showed disease progression, which was associated with an increase in  $M^+$  CTCs. These cells declined in number again and switched to an  $E^+$  phenotype during a second response to the chemotherapy regimen. After 3 months, the

patient again showed disease progression, along with a switch to  $M^+$  CTCs (Fig. 3).

The increase in  $M^+$  CTCs in the index patient was accompanied by the appearance of multicellular CTC clusters, ranging from 4 to 50 cells, with one cluster having ~100 tumor cells (Fig. 3, fig. S4, and movie S1). These clusters were absent from specimens with predominantly  $E^+$  CTCs. CTC clusters are seen in patients with advanced cancer (10) and can be detected with different CTC isolation platforms (13, 14). The CTC clusters were strongly positive for M markers and weakly positive for E markers by ISH and were stained weakly with epithelial cytokeratin antibodies (Fig. 3). This observation is at odds with the prevailing hypothesis that EMT results in highly migratory single cells rather than clusters of cells bearing mesenchymal markers (2, 3). However, consistent with the recent observation that platelets bound to tumor cells release transforming growth factor  $\beta$  (TGF- $\beta$ ), potentially inducing EMT within the circulation (15), staining of CTC clusters showed an abundance of attached (CD61-positive) platelets (Fig. 3). We detected  $M^+$  CTC clusters of 2 to 20 cells not only in the index patient but in two additional patients, both with  $ER/PR^+$  breast cancer (fig. S5).

**Fig. 3.** Longitudinal monitoring of EMT features in CTCs from an index patient. Plot of CTC counts per 3 ml of blood based on RNA (E and M markers) detection methods in a patient with KRAS- and PIK3CA-mutant  $ER/PR^+$  lobular breast cancer, who was serially sampled during treatment with inhibitors targeting the PI3K (GDC0941) and MEK (GDC0973) pathways, followed by adriamycin chemotherapy. Color-coded quantitation of EMT features based on RNA-ISH staining is shown above each time point. Treatment history and clinical responses are noted on the chart. P, disease progression; R, treatment response).  $M^+$  clusters were detected at time points 1, 8, and 12. Images of CTCs staining for E (green) and M (red) markers and protein staining for CK (red), CD45 (green), or platelet marker CD61 (green) from different time points are shown below the chart. The number of single CTCs (S-CTC) detected on the entire CTC-chip upon processing 3 ml of blood and the number of CTCs within the CTC clusters (C-CTC) are indicated. Nuclei are stained with 4',6-diamidino-2-phenylindole (DAPI) (blue). Scale bar, 10  $\mu$ m. Criteria for disease progression (P) or treatment response (R) are described in the supplementary materials.





To identify signaling pathways within CTCs that contribute to EMT in breast cancer patients, we subjected these to RNA sequencing, using a single-molecule platform to avoid amplification bias associated with rare templates (16, 17). Because captured CTCs are contaminated with abundant leukocytes, we processed each specimen through paired anti-EpCAM-capture and mock-capture CTC-chips, allowing us to subtract digital gene expression (DGE) profiles of adherent blood cells from the CTC-enriched cells. DGE profiles for CTC-enriched cell populations from the index patient at five serial time points identified 45 enriched genes, compared with similarly processed blood samples from 10 healthy donors used to measure anti-EpCAM-capture background [permutation-based statistical model applied to each of five time points with a false discovery rate (FDR) threshold of 0.15] (Fig. 4 and table S3). Enriched transcripts included epithelial keratins KRT 8 and 19, and breast tumor markers, mammaglobins (SCGB2A2 and SCGB2A1), and trefoil factors 1 and 3 (TFF1 and TFF3), the most abundant of which (TFF1) was highly expressed in both primary tumor and metastatic lymph node from this patient (fig. S6). CTC-associated transcripts identified 12 signatures in the Gene Set Enrichment Analysis (GSEA) database, with an FDR < 0.25 (Fig. 4

and table S4). The strongest association was with a gene signature up-regulated in bone relapse of breast cancer ( $P = 1.32 \times 10^{-7}$ ; FDR = 0.000767), which is noteworthy because the patient had metastatic bone lesions at the time of CTC analysis.

An additional set of 170 transcripts was enriched in CTCs captured at a mesenchymal predominant time point, characterized by multiple (>18)  $M^+$  CTC clusters (Fig. 4 and table S5). SERPINE1/PAI1 and FN1, two mesenchymal probes used in the RNA-ISH panel, were the most and third most abundant CTC cluster-associated transcripts. The GSEA database identified 717 gene signatures (FDR of 0.25) (Fig. 4 and table S6) with dramatic enrichment for EMT-related expression changes, including significant overlap with a core EMT signature (18) (table S7) (11 out of 90;  $P = 8.1 \times 10^{-8}$ ; odds ratio = 9.8). In addition, enrichment for extracellular matrix (ECM) and ECM-related membrane receptors (including integrin and interleukin receptors) were potentially associated with the clustering phenomenon. Signatures reported in invasive ductal and lobular carcinomas, therapy resistance, and TGF- $\beta$ , interleukin-6, and WNT (LEF1) signaling pathways were also noted. Among these, the most significant was TGF- $\beta$  ( $P = 2.96 \times 10^{-11}$ ), a potent initiator of mesenchymal trans-

formation (2), directly implicated in platelet-induced EMT (15). Expression of Snail, Slug, or other well-established transcriptional regulators of EMT was not detected in the  $M^+$  CTC clusters, but Forkhead box protein C1 (FOXC1) (Fig. 4), a transcription factor that induces EMT in cell culture models (19, 20), was detected. RNA-ISH revealed FOXC1 expression in CTCs and within localized regions of primary breast cancer and a tumor-infiltrated lymph node from the index patient and other cases (fig. S7). Thus, along with TGF- $\beta$  activation, aberrant expression of FOXC1 may contribute to EMT in human breast cancer.

In summary, we have provided evidence of EMT in human breast cancer specimens, both in rare cells within primary tumors and more abundantly in CTCs. These findings are consistent with results derived from mouse tumor models, including recent studies using lineage tracing in Kras/Tp53 pancreatic and Her2-transgenic breast cancers (21, 22) and with the detection of vimentin-stained and/or CK<sup>+</sup> CTCs in patients with cancer (23–25). Notably, we found a striking association between expression of mesenchymal markers and clusters of CTCs, rather than single migratory cells. The expression of mesenchymal markers by these adherent cells could result from proliferation of a single cell

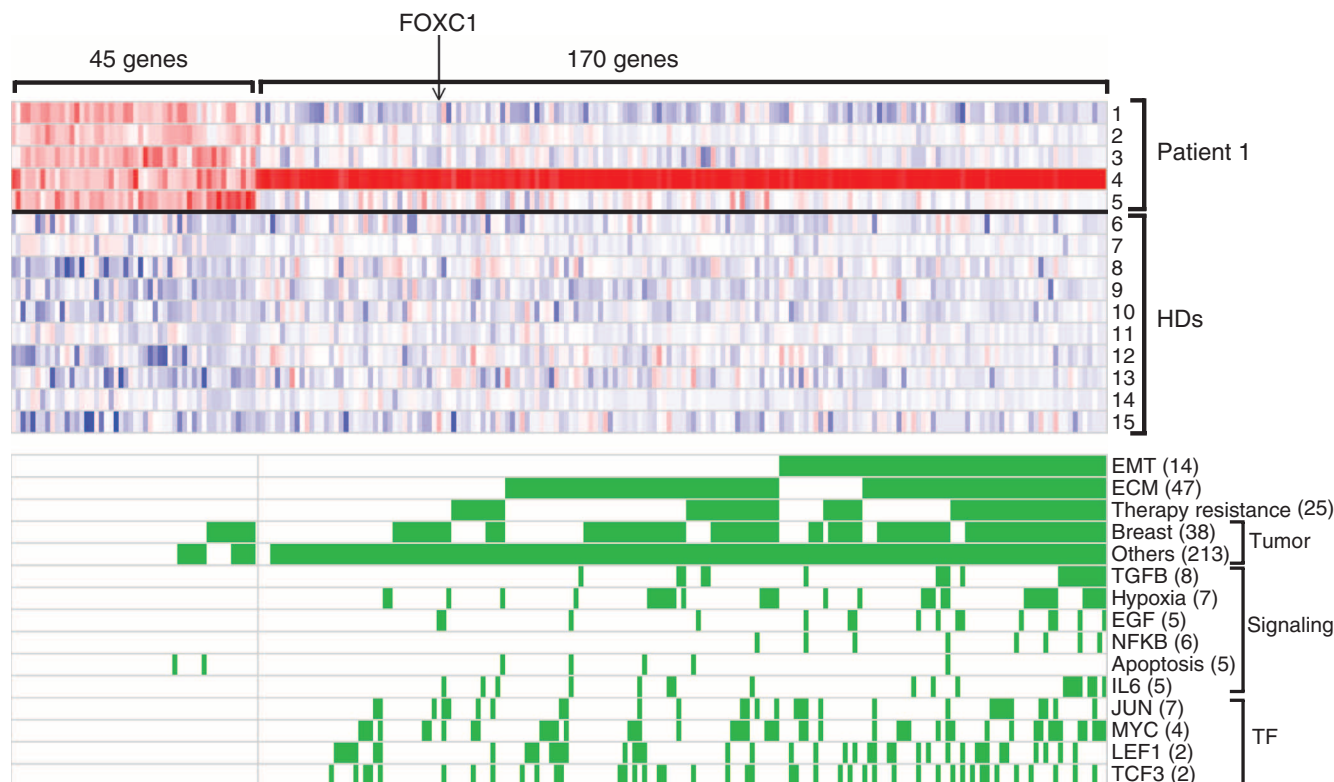


**Fig. 4.** RNA-sequence analysis of transcripts enriched in CTCs. Heat map representing transcripts enriched in CTCs captured from the index patient, who was sampled at multiple time points during treatment. A CTC signature of 45 genes was derived by comparing 5 time points from the patient (rows 1 to 5) with identically processed blood specimens from 10 healthy donors (HDs) (rows 6 to 15). An EMT-specific signature of 170 genes was derived

from comparing  $M^+$  cluster-enriched CTCs (row 4) with  $E^+$  CTCs. Red and blue colors indicate relative high and low gene expression, respectively. Categories of gene signatures in the GSEA database are shown for both the 45 gene CTC signature and the 170 gene EMT-cluster CTC signature, with genes contributing to the enrichment highlighted in green. The number of enriched signatures within each category is given in parentheses.

that has undergone EMT into a cluster of such cells or, alternatively, from the mesenchymal transformation of preexisting CTC clusters within the bloodstream. The proposal that mesenchymal transformation of epithelial cells is mediated by TGF- $\beta$  released from platelets (15) is supported by our observation of strong TGF- $\beta$  signatures in mesenchymal CTC clusters, many of which carry attached platelets. Collective migration of grouped cells that maintain their cell-cell and cell-matrix connections has been implicated in cancer metastasis (26, 27), and may involve increased survival signals as CTC clusters circulate in the blood (17, 28, 29). The clinical importance of EMT as a potential biomarker of therapeutic resistance and as a potential drug target in breast cancer warrants further investigation.

#### References and Notes

1. D. X. Nguyen, P. D. Bos, J. Massagué, *Nat. Rev. Cancer* **9**, 274 (2009).
2. J. P. Thiery, *Nat. Rev. Cancer* **2**, 442 (2002).
3. R. Kalluri, R. A. Weinberg, *J. Clin. Invest.* **119**, 1420 (2009).
4. T. Brabletz, *Nat. Rev. Cancer* **12**, 425 (2012).
5. H. Ledford, *Nature* **472**, 273 (2011).

6. K. Pantel, R. H. Brakenhoff, B. Brandt, *Nat. Rev. Cancer* **8**, 329 (2008).
7. M. Yu, S. Stott, M. Toner, S. Maheswaran, D. A. Haber, *J. Cell Biol.* **192**, 373 (2011).
8. H. Jeong, Y. J. Ryu, J. An, Y. Lee, A. Kim, *Histopathology* **60**, E87 (2012).
9. Z. Jiang *et al.*, *Cell Cycle* **10**, 1563 (2011).
10. S. L. Stott *et al.*, *Proc. Natl. Acad. Sci. U.S.A.* **107**, 18392 (2010).
11. M. Yu *et al.*, *Genes Dev.* **23**, 1737 (2009).
12. R. E. Payne *et al.*, *Br. J. Cancer* **106**, 1790 (2012).
13. M. G. Krebs *et al.*, *J. Thorac. Oncol.* **7**, 306 (2012).
14. E. H. Cho *et al.*, *Phys. Biol.* **9**, 016001 (2012).
15. M. Labelle, S. Begum, R. O. Hynes, *Cancer Cell* **20**, 576 (2011).
16. F. Ozsolak *et al.*, *Nat. Methods* **7**, 619 (2010).
17. M. Yu *et al.*, *Nature* **487**, 510 (2012).
18. J. H. Taube *et al.*, *Proc. Natl. Acad. Sci. U.S.A.* **107**, 15449 (2010).
19. K. Polyak, R. A. Weinberg, *Nat. Rev. Cancer* **9**, 265 (2009).
20. N. Bloustain-Qimron *et al.*, *Proc. Natl. Acad. Sci. U.S.A.* **105**, 14076 (2008).
21. Y. Hüsemann *et al.*, *Cancer Cell* **13**, 58 (2008).
22. A. D. Rhim *et al.*, *Cell* **148**, 349 (2012).
23. A. J. Armstrong *et al.*, *Mol. Cancer Res.* **9**, 997 (2011).
24. A. Lecharpentier *et al.*, *Br. J. Cancer* **105**, 1338 (2011).
25. C. V. Pecot *et al.*, *Cancer Discov.* **1**, 580 (2011).
26. O. Iliina, P. Friedl, *J. Cell Sci.* **122**, 3203 (2009).
27. D. G. Duda *et al.*, *Proc. Natl. Acad. Sci. U.S.A.* **107**, 21677 (2010).
28. Y. N. Kim, K. H. Koo, J. Y. Sung, U. J. Yun, H. Kim, *Int. J. Cell Biol.* **2012**, 306879 (2012).
29. J. M. Hou *et al.*, *J. Clin. Oncol.* **30**, 525 (2012).

**Acknowledgments:** We are grateful to all the patients who participated in this study; we thank D. Juric, C. Koris, and the Massachusetts General Hospital (MGH) clinical research coordinators for help with clinical studies; A. Gilman, B. Brannigan, and M. Zeinali for technical support; F. Ozsolak and P. Milos (Helicos) for RNA sequencing; A. Forrest-Hay and Q. Nguyen (Affymetrix) for RNA-ISH reagents; L. Libby for mouse studies; and J. Walsh for expertise with microscopy. This work was supported by grants from the Breast Cancer Research Foundation (D.A.H.), Stand Up To Cancer (D.A.H., M.T., and S.M.), Susan G. Komen for the Cure KG090412 (S.M.), NIBIB EB008047 (M.T., D.A.H.), NCI CA129933 (D.A.H.), the National Cancer Institute–MGH Federal Share Program (S.M.), and the Howard Hughes Medical Institute (M.Y. and D.A.H.). The MGH and M.T. have filed a patent for the HB (Herringbone) microchip (U.S. patent 09816815.4). Sequencing data have been deposited in the Gene Expression Omnibus database (accession no. GSE41245).

#### Supplementary Materials

www.sciencemag.org/cgi/content/full/339/6119/580/DC1  
Materials and Methods  
Figs. S1 to S7  
Tables S1 to S7  
References (30–36)  
Movie S1

7 August 2012; accepted 6 December 2012  
10.1126/science.1228522

# Systematic Identification of Signal-Activated Stochastic Gene Regulation

Gregor Neuert,<sup>1,2\*</sup> Brian Munsky,<sup>3\*</sup> Rui Zhen Tan,<sup>1,5,6</sup> Leonid Teytelman,<sup>1</sup> Mustafa Khammash,<sup>4,7†</sup> Alexander van Oudenaarden<sup>1,8,†‡</sup>

Although much has been done to elucidate the biochemistry of signal transduction and gene regulatory pathways, it remains difficult to understand or predict quantitative responses. We integrate single-cell experiments with stochastic analyses, to identify predictive models of transcriptional dynamics for the osmotic stress response pathway in *Saccharomyces cerevisiae*. We generate models with varying complexity and use parameter estimation and cross-validation analyses to select the most predictive model. This model yields insight into several dynamical features, including multistep regulation and switchlike activation for several osmosensitive genes. Furthermore, the model correctly predicts the transcriptional dynamics of cells in response to different environmental and genetic perturbations. Because our approach is general, it should facilitate a predictive understanding for signal-activated transcription of other genes in other pathways or organisms.

A central goal of systems biology is to understand and predict the complex, stochastic dynamics of gene regulation (1–3). Although biochemical studies have identified many regulatory proteins in these processes, this typically does not enable construction of quantitatively predictive models of transcriptional dynamics. One challenge lies in the fact that gene regulation is a dynamic multistate process with largely unknown reaction rates. For example, a two-state system may represent closed and open chromatin (4–6) or the presence or absence of a transcription factor (7–9). Including more states or regulatory reactions results in a combinatorial increase in the

number of possible model structures (10) and leads to a complicated trade-off between overfitting and predictive power.

We propose a data-driven comprehensive approach to identify and validate predictive, quantitative models of transcriptional dynamics through the integration of single-cell experiments and discrete stochastic analyses within a system identification framework. We apply this approach to the well-characterized high-osmolarity glycerol (HOG) mitogen-activated protein kinase (MAPK) pathway in *Saccharomyces cerevisiae* and focus on the regulation of *STL1*, *CTT1*, and *HSP12* (11, 12) genes. Upon osmotic shock, the Hog1p kinase

quickly enters the nucleus (Fig. 1A, and figs. S2 to S4, and S6) (13–16) and activates *STL1*, *CTT1*, and *HSP12* gene expression (figs. S6 and S9) (17). We find that the Hog1p translocation dynamics is homogeneous (14, 15, 17), yet downstream gene activation is heterogeneous among cells (17). To quantify *STL1* expression directly, we developed a single-molecule fluorescent in situ hybridization (smFISH) (18, 19, 20) assay, which captures the stochastic nature of mRNA transcription with high temporal and single-molecule resolution (Fig. 1B) (21, 22, 23).

In addition to the kinase Hog1p, we consider the effects of the transcription factor Hot1p and the chromatin modifiers Arp8p and Gcn5p that modulate *STL1* transcription (17, 24). For this system, we seek to find and validate a model that predicts the system's dynamic mRNA expression

<sup>1</sup>Departments of Physics and Biology and Koch Institute for Integrative Cancer Research, Massachusetts Institute of Technology, Cambridge, MA 02139, USA. <sup>2</sup>Department of Molecular Physiology and Biophysics, School of Medicine, Vanderbilt University, Nashville, TN 37232, USA. <sup>3</sup>Center for Nonlinear Studies and the Information Sciences Group, Los Alamos National Laboratory, Los Alamos, NM 87545, USA. <sup>4</sup>Department of Biosystems Science and Engineering, ETH-Zuerich, 4058 Basel, Switzerland. <sup>5</sup>Bioinformatics Institute, A\*STAR, Singapore 138671, Singapore. <sup>6</sup>Harvard University Graduate Biophysics Program, Harvard Medical School, Boston, MA 02115, USA. <sup>7</sup>Center for Control, Dynamical Systems and Computation and Department of Mechanical Engineering, University of California, Santa Barbara, CA 93106, USA. <sup>8</sup>Hubrecht Institute, Royal Netherlands Academy of Arts and Sciences and University Medical Center Utrecht, Uppsalalaan 8, 3584 CT, Utrecht, Netherlands.

\*These authors contributed equally to this work.

†Co-senior authors.

‡To whom correspondence should be addressed. E-mail: a.vanoudenaarden@hubrecht.eu



for several genes (*STL1*, *CTT1*, and *HSP12*) in response to environmental and genetic perturbations. We propose a range of model structures, each with a discrete number of states,  $\{S_1, S_2, \dots, S_N\}$  (Fig. 2A). Each haploid cell occupies one state at a time, and transitions among states are discrete, stochastic events. At least two states are required to explain bimodality, but additional states allow for more complex mechanisms, such as chromatin remodeling or transcription factor binding or release (7–9, 17). Because activated mRNA transcription and degradation rates are constant throughout different conditions (fig. S5), only transition rates can be variable and are as-

sumed to be constant or linearly dependent on the kinase. After identifying the model structure and Hog1p dependency, we validate the model structure for several mutants and different Hog1p-dependent genes.

To choose the best number of states needed to match *STL1* gene expression dynamics, we allow every state transition rate to be Hog1p-dependent. For two-, three-, four-, and five-state model structures with any parameter set, we use the finite state projection (FSP) approach (25) to formulate a finite set of linear ordinary differential equations that predicts the time-varying probability distributions. We adjust the model parameters

until the FSP analysis fits the bimodal mRNA distributions at all times (26). As expected, the fit improves as the model complexity increases (Fig. 2B, red line, and fig. S11). However, increased complexity leads to greater parametric uncertainty and may diminish predictive power. Applying cross-validation analyses to replicate experiments at 0.4 M NaCl (27), we score all models according to their estimated predictive power (Fig. 2B, blue line). This prediction estimate is validated with additional experiments conducted at 0.2 M NaCl, and we find that cross-validation provides an excellent estimate of predictive power (Fig. 2B, compare blue and green lines, and figs. S11 and S12). We find that the two- and three-state models are too simple, whereas the more complex five-state model structure is prone to overfitting (Fig. 2B and figs. S11 and S12).

We now concentrate on the four-state model structures and determine which reactions depend upon Hog1p. To identify a Hog1p-model structure with enough flexibility to match the data while avoiding overfitting, we allow one or two Hog1p dependencies. We then rank the corresponding maximum likelihoods and cross-validate the top ranked Hog1p-model structures. The fit improves with increasing complexity (Fig. 2B, red line, and fig. S11), while constraining the number of Hog1p dependencies reduces uncertainty (Fig. 2B and fig. S11). One notable feature of the identified model structure and its corresponding parameters is that in the absence of Hog1p, a fast reaction from  $S_2 \rightarrow S_1$  keeps all cells in the inactive  $S_1$  state (fig. S8, red

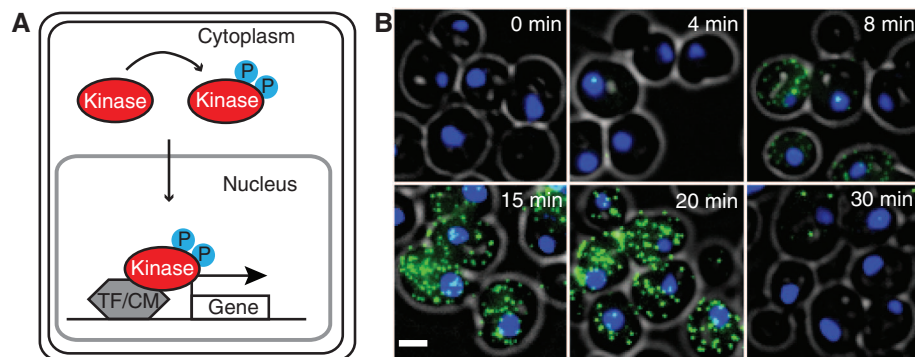


**Fig. 1.** Quantitative analysis of single-cell stochastic gene regulation. **(A)** Schematic of a generic signaling cascade in which a kinase enters the nucleus and interacts with transcription factors (TF) and chromatin modifiers (CM) to regulate gene expression. **(B)** Rapid, stochastic, and bimodal activation of endogenous *STL1* mRNA expression is detected with single-molecule RNA-FISH [yeast cell: gray circle; DAPI (4',6-diamidino-2-phenylindole)-stained nucleus: blue; *STL1* mRNA: green dots]. Scale bar: 2 μm.

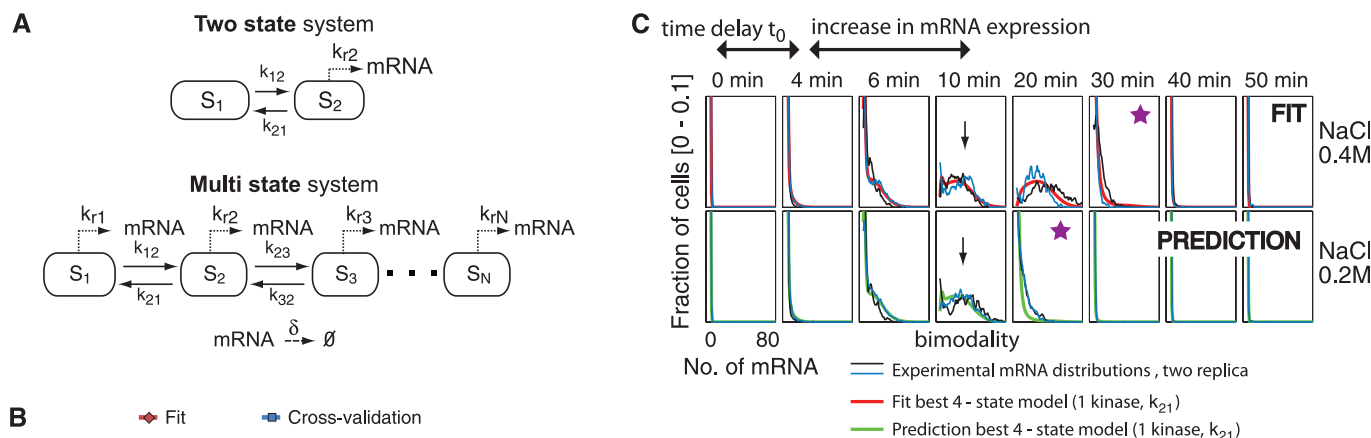


**Fig. 2.** Identifying a maximally predictive model structure. **(A)** Two- and multistate model structures that allow for kinase, transcription factor, and chromatin modifier-dependent activation of gene expression. **(B)** Relative likelihoods of best fit for different model structures at 0.4 M NaCl (red, left axis) and the resulting predictions at 0.2 M NaCl (green, right axis). Cross-validation at 0.4 M NaCl (27) is used to quantify predictive uncertainty (gray region, left axis) and yields excellent a priori knowledge of predictive power (compare blue and green lines). **(C)** mRNA expression distributions at two NaCl concentrations (black and blue lines) and best fit at 0.4 M (red line) and the corresponding prediction at 0.2 M NaCl (green line). The fit and predictions correspond to the four-state structure with one Hog1p dependency identified at 0.4 M NaCl in (fig. S7). The black arrow indicates the similar mRNA expression levels after an osmotic shock of 0.2 and 0.4 M NaCl. The purple star indicates the time point of gene expression deactivation.

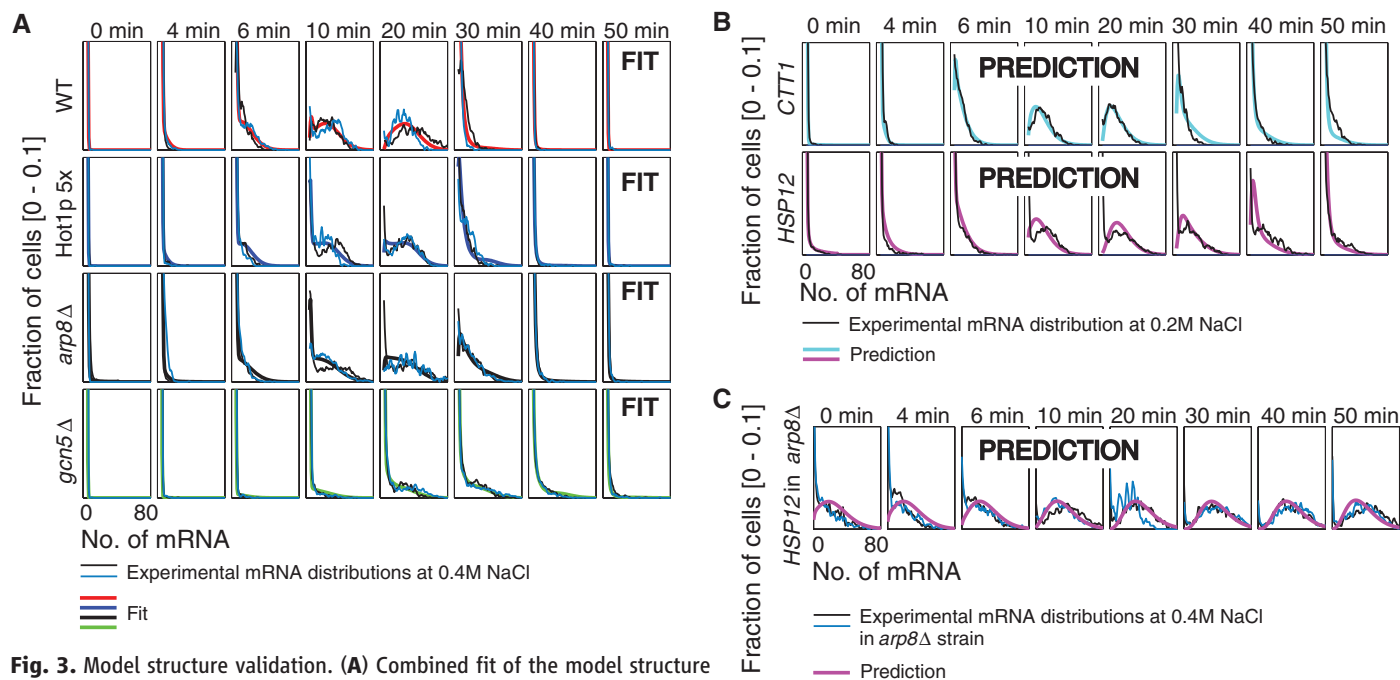


**Fig. 3. Model structure validation.** (A) Combined fit of the model structure identified (fig. S7) to different genetic mutations affecting *STL1* expression at 0.4 M NaCl: wild-type (WT) (red), Hot1p 5× (blue), *arp8*Δ (black), and *gcn5*Δ (green). (B) Model prediction of *CTT1* (cyan) and *HSP12* (magenta) expression at 0.2 M NaCl. (C) Model prediction for *HSP12* expression at 0.4 M in the *arp8*Δ strain.

line). When Hog1p exceeds a certain threshold, the gene can transition among the active *S*<sub>2</sub>, *S*<sub>3</sub>, and *S*<sub>4</sub> states (fig. S8, blue, green, and black lines). Our final model captures all qualitative and quantitative features of *STL1* mRNA expression dynamics after a 0.4 M NaCl osmotic shock (Fig. 2C, top). These features include a constant time delay, *t*<sub>0</sub>, between Hog1p translocation and mRNA expression; slow activation of gene expression; transient bimodality in RNA populations; conserved maximal mRNA expression between different conditions; and Hog1p-dependent modulation of gene expression duration. In addition, the model makes the best predictions for the mRNA expression after osmotic shock with 0.2 M NaCl (Fig. 2C, bottom).

To test the generality of this model’s predictive power, we collect new data sets at 0.4 M NaCl for several different mutant strains and for different Hog1p-activated genes. The different mutant strains include a fivefold Hot1p-overexpression strain and gene knockouts of the chromatin modifiers *ARP8* or *GCN5*. We also consider two additional stress response genes: *CTT1* and *HSP12*. The model identified above fits equally well to the mRNA expression dynamics for *STL1* in the Hot1p-overexpression strain as well as the *arp8*Δ and *gcn5*Δ mutants (Fig. 3A and figs. S15, S18, and S19). The same structure also fits the *CTT1* and *HSP12* mRNA expression dynamics (figs. S9, S15, S18, and S19) with relatively few parameter changes between the different genes and mutations (table S2) (27). The resulting model makes excellent predictions for the dynamics of *CTT1* and *HSP12* mRNA

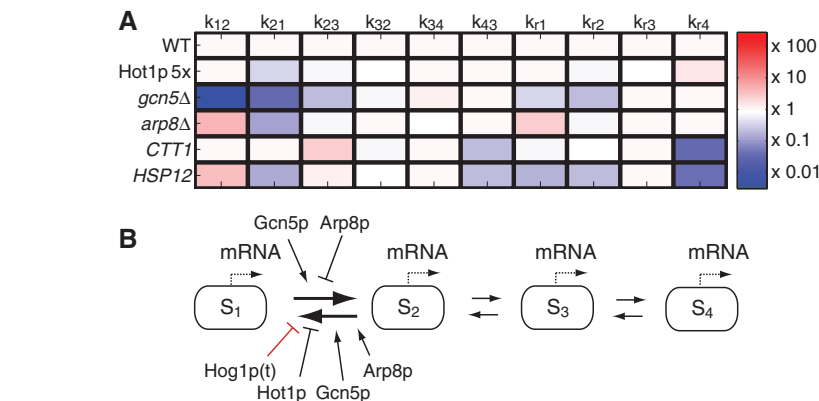


**Fig. 4. Relating model structure to biological function.** (A) Mutant and gene-specific rate changes relative to *STL1*. (B) Final model, in which Hog1p, Hot1p, Gcn5p, and Arp8p regulate transitions between states *S*<sub>1</sub> and *S*<sub>2</sub>.

expression at 0.2 M NaCl (Fig. 3, B and C, and figs. S16, S18, and S19). Combining the relative changes in the rates measured for *STL1* in the mutant *ARP8* strain with the rate changes for the *CTT1* and *HSP12* expression measured in wild-type strain results in a very good prediction of the *CTT1* and *HSP12* mRNA expression in the *ARP8* mutant strain (Fig. 3C and figs. S17 to S19) (27).

Having determined that the model structure identified above can fit and predict *STL1*, *CTT1*, and *HSP12* mRNA expression dynamics in different mutant strains, we examine which rates vary most for each mutant and gene in comparison to wild-type *STL1* (Fig. 4A and table S2). The most variable rates between different mutations are the *k*<sub>12</sub> and *k*<sub>21</sub> transition rates, which indicate

that Hot1p, Gcn5p, and Arp8p all modulate the transition rates into and out of the *S*<sub>1</sub> state but result in different Hog1p-activation and -deactivation thresholds (fig. S10). Other transition rates are affected to a much lower degree.

The identified model structure and parameters quantitatively capture and/or predict all of the observed experimental data (Figs. 2 to 4 and figs. S15 to S19). The model also yields several qualitative and quantitative insights, including (i) a switchlike mechanism that activates each gene and stabilizes its activity when Hog1p exceeds a gene-specific threshold and (ii) gene-specific production and degradation rates that are independent of the Hog1p-kinase dynamics. The four-state model structure is essential to explain the temporal dynamics in gene expression observed in



all of the experiments. This structure describes an Off state,  $S_1$ , which is the default state in the absence of osmotic shock, and three On states with different transcription rates and reaction rates between the states. Activation occurs when nuclear Hog1p represses the deactivation rate,  $k_{21}$ , subject to the interplay of gene- and mutant-specific (de)activation thresholds (fig. S10 and table S2). This interplay provides the main knob by which the duration of mRNA expression is finely tuned in response to different environmental conditions (e.g., different salt concentrations) or to different genetic mutations.

In this study, we have identified a single quantitative model to understand and predict *STL1*, *CTT1*, and *HSP12* gene expression dynamics in response to various environmental and genetic perturbations. We generated a large range of possible model structures and developed a dynamic single-cell assay with which to discriminate among these model structures. We combined this experimental assay with discrete stochastic analyses and parameter identification approaches. Our cross-validation analyses systematically eliminated oversimplified and overcomplex model structures. We eventually selected the model structure and parameters for a single best model to predict *STL1*, *CTT1*, and *HSP12* dynamics. Furthermore, the identified model provides detailed insight into the biophysical dynamics of signal-activated gene regulation. Because the presented experimental and computational tools are applicable to any gene or signaling pathway, this

integrated identification approach can lead to insights into complex cellular networks for other organisms.

### References and Notes

- H. Y. Chuang, M. Hofree, T. Ideker, *Annu. Rev. Cell Dev. Biol.* **26**, 721 (2010).
- M. A. Schwartz, H. D. Madhani, *Annu. Rev. Genet.* **38**, 725 (2004).
- V. M. Weake, J. L. Workman, *Nat. Rev. Genet.* **11**, 426 (2010).
- A. Raj, C. S. Peskin, D. Tranchina, D. Y. Vargas, S. Tyagi, *PLoS Biol.* **4**, e309 (2006).
- J. M. Raser, E. K. O'Shea, *Science* **304**, 1811 (2004).
- M. S. Ko, H. Nakauchi, N. Takahashi, *EMBO J.* **9**, 2835 (1990).
- C. Cheung, P. Cramer, *Nature* **471**, 249 (2011).
- C. Hodges, L. Bintu, L. Lubkowska, M. Kashlev, C. Bustamante, *Science* **325**, 626 (2009).
- H. Boeger, J. Griesenbeck, R. D. Kornberg, *Cell* **133**, 716 (2008).
- W. Ma, A. Trusina, H. El-Samad, W. A. Lim, C. Tang, *Cell* **138**, 760 (2009).
- C. Ferreira et al., *Mol. Biol. Cell* **16**, 2068 (2005).
- S. Hohmann, *Microbiol. Mol. Biol. Rev.* **66**, 300 (2002).
- P. Ferrigno, F. Posas, D. Koepf, H. Saito, P. A. Silver, *EMBO J.* **17**, 5606 (1998).
- P. Hersen, M. N. McClean, L. Mahadevan, S. Ramanathan, *Proc. Natl. Acad. Sci. U.S.A.* **105**, 7165 (2008).
- J. T. Mettetal, D. Muzzey, C. Gómez-Urbe, A. van Oudenaarden, *Science* **319**, 482 (2008).
- D. Muzzey, C. A. Gómez-Urbe, J. T. Mettetal, A. van Oudenaarden, *Cell* **138**, 160 (2009).
- S. Pelet et al., *Science* **332**, 732 (2011).
- A. Raj, P. van den Bogaard, S. A. Rifkin, A. van Oudenaarden, S. Tyagi, *Nat. Methods* **5**, 877 (2008).
- A. M. Femino, F. S. Fay, K. Fogarty, R. H. Singer, *Science* **280**, 585 (1998).
- S. L. Bumgarner et al., *Mol. Cell* **45**, 470 (2012).
- J. M. Pedraza, J. Paulsson, *Science* **319**, 339 (2008).

- B. Munsky, B. Trinh, M. Khammash, *Mol. Syst. Biol.* **5**, 318 (2009).
- B. Munsky, G. Neuert, A. van Oudenaarden, *Science* **336**, 183 (2012).
- P. M. Alepuz, E. de Nadal, M. Zapater, G. Ammerer, F. Posas, *EMBO J.* **22**, 2433 (2003).
- B. Munsky, M. Khammash, *J. Chem. Phys.* **124**, 044104 (2006).
- Using full mRNA distributions for fitting yields substantially improved predictions (fig. S13) compared to fitting with the procedure in (28) that uses only means and variances.
- Materials and methods are available as supplementary materials on Science Online.
- C. Zechner et al., *Proc. Natl. Acad. Sci. U.S.A.* **109**, 8340 (2012).

**Acknowledgments:** This work was funded by the NSF (ECCS-0835847) and Human Frontier Science Program (RGP0061/2011) to M.K.; the NSF (ECCS-0835623), National Institutes of Health–National Cancer Institute Physical Sciences Oncology Center at Massachusetts Institute of Technology (U54CA143874), and an NIH Pioneer award (1DP1OD003936) to A.v.O.; Los Alamos National Laboratory–Laboratory Directed Research and Development to B.M.; the Deutsche Forschungsgemeinschaft (Forschungs Stipendium) to G.N.; and the A\*STAR program, Singapore, to R.Z.T. We thank F. van Werven for the yeast crosses and N. Hengartner, B. Pando, S. Klemm, J. van Zon, and M. Wall for discussions on the model. We also thank M. Bienko, N. Crosetto, C. Engert, S. Itzkovitz, J. P. Junker, S. Klemm, S. Semrau, J. van Zon, and H. Youk for comments on the manuscript.

### Supplementary Materials

www.sciencemag.org/cgi/content/full/339/6119/584/DC1  
Materials and Methods  
Figs. S1 to S19  
Tables S1 and S2  
References (29–38)

12 October 2012; accepted 10 December 2012  
10.1126/science.1231456

# Molecular Mechanism of Action of Microtubule-Stabilizing Anticancer Agents

Andrea E. Prota,<sup>1</sup> Katja Bargsten,<sup>1</sup> Didier Zurwerra,<sup>2</sup> Jessica J. Field,<sup>3</sup> José Fernando Díaz,<sup>4</sup> Karl-Heinz Altmann,<sup>2</sup> Michel O. Steinmetz<sup>1\*</sup>

Microtubule-stabilizing agents (MSAs) are efficacious chemotherapeutic drugs widely used for the treatment of cancer. Despite the importance of MSAs for medical applications and basic research, their molecular mechanisms of action on tubulin and microtubules remain elusive. We determined high-resolution crystal structures of  $\alpha\beta$ -tubulin in complex with two unrelated MSAs, zampanolide and epothilone A. Both compounds were bound to the taxane pocket of  $\beta$ -tubulin and used their respective side chains to induce structuring of the M-loop into a short helix. Because the M-loop establishes lateral tubulin contacts in microtubules, these findings explain how taxane-site MSAs promote microtubule assembly and stability. Further, our results offer fundamental structural insights into the control mechanisms of microtubule dynamics.

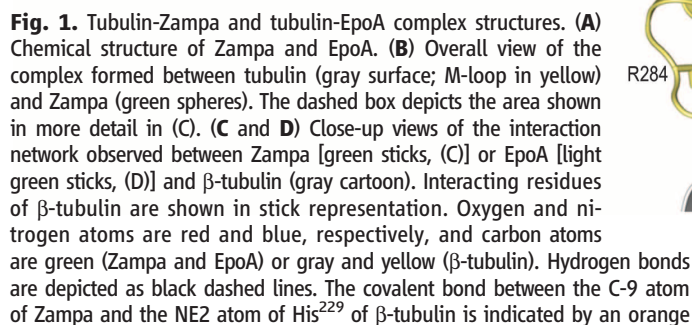
The binding of microtubule-stabilizing agents (MSAs) such as paclitaxel (Taxol, Bristol-Myers Squibb) to microtubules is generally thought to shift the assembly equilibrium of tubulin toward the polymeric state and to block cell entry into mitosis by suppressing microtubule dynamics (1, 2). However, MSAs are also known to induce microtubule polymerization under conditions in which tubulin does not assem-

ble spontaneously, suggesting a role in tubulin activation (3, 4). To provide insights into the interactions of MSAs with tubulin and microtubules at the molecular level, we crystallized the complex between  $\alpha\beta$ -tubulin (T), the stathmin-like protein RB3 (R), and tubulin tyrosine ligase (TTL) in the presence of either zampanolide (Zampa) or epothilone A (EpoA) (Fig. 1A) and determined the structures of the corresponding

protein-ligand complexes (T<sub>2</sub>R-TTL-Zampa and T<sub>2</sub>R-TTL-EpoA) at 1.8 and 2.3 Å resolution, respectively, by x-ray crystallography (fig. S1A and table S1) (5). The two tubulin heterodimers in the T<sub>2</sub>R-TTL-MSA complexes were aligned in a head-to-tail fashion and assumed a curved conformation. Their overall structures superimposed well with the ones obtained in the absence of a MSA or of tubulin in complex with RB3 alone (6) [root mean square deviation (RMSD) ranging from 0.1 to 0.6 Å over more than 650 C $\alpha$  atoms], which suggests that the binding of MSAs and TTL does not induce major structural changes in the T<sub>2</sub>R complex. Both Zampa and EpoA were deeply buried in a pocket formed by predominantly hydrophobic residues of helix H7;  $\beta$  strand S7; and the loops H6-H7, S7-H9 [designated the M-loop (7)], and S9-S10 of  $\beta$ -tubulin—this pocket is commonly known as the taxane pocket (Fig. 1, B to D) (8, 9).

<sup>1</sup>Biomolecular Research, Paul Scherrer Institut, Villigen PSI, Switzerland. <sup>2</sup>Department of Chemistry and Applied Biosciences, Institute of Pharmaceutical Sciences, Swiss Federal Institute of Technology (ETH) Zürich, Zürich, Switzerland. <sup>3</sup>Centre for Biodiscovery, Victoria University of Wellington, Wellington, New Zealand. <sup>4</sup>Chemical and Physical Biology, Centro de Investigaciones Biológicas, Consejo Superior de Investigaciones Científicas CIB-CSIC, Madrid, Spain.

\*To whom correspondence should be addressed. E-mail: michel.steinmetz@psi.ch



A comparison of the tubulin-Zampa taxane pocket with that of tubulin-EpoA showed that its conformation is very similar in both complex structures (RMSD of 0.4 Å over 55 Ca atoms) and revealed that the side chains of Zampa and EpoA superimposed well (fig. S2B). In contrast, completely different sets of interactions were established by the two MSAs to anchor their

The “curved” structure of tubulin in the tubulin-RB3 complex corresponds to the conformation of unassembled, free tubulin (*12, 13*). In contrast, a “straight” conformation of tubulin is found in microtubules (*8, 14*). To assess possible structural differences between the taxane pocket in unassembled tubulin and microtubules, we compared models of  $\beta$ -tubulin in the curved (T<sub>2</sub>R-TTL-Zampa) and straight (*14*) conformational states. Superimposition of these structures showed that the overall architecture of the taxane pocket is only slightly affected by the curved-

The M-loop of both  $\alpha$ - and  $\beta$ -tubulin is a crucial element for lateral tubulin contacts between protofilaments in microtubules in the absence of ligands (7, 16). To provide structural insights into lateral tubulin contacts, we modeled the helical conformation of the M-loop in the context of the microtubule lattice. For this purpose, we used the straight tubulin structure (14) and cryogenic electron microscopy (cryo-EM) reconstructions of microtubules at  $\sim 8$  Å resolution (7, 16). In contrast to the non-native M-loop conformation in zinc-stabilized tubulin sheets (14), the MSA-stabilized helical M-loop conformation of  $\beta$ -tubulin adequately explains the corresponding density of EM reconstructions of microtubules (Fig. 3B). In our model, Tyr<sup>283</sup> of the M-loop is inserted across protofilaments into a pocket shaped by the S2'-S2''  $\beta$  hairpin and the H2-S3 loop (residues Ala<sup>56</sup>, Thr<sup>57</sup>, Val<sup>62</sup>, Gln<sup>85</sup>, Arg<sup>88</sup>, Pro<sup>89</sup>, and Asp<sup>90</sup>) of a neighboring  $\beta$ -tubulin subunit (Fig. 3C), secondary structure elements that were not considerably affected by the curved-to-straight tubulin conformational transition (RMSD of 0.7 Å over 91 C $\alpha$  atoms) (Fig. 3A). In addition, the M-loop



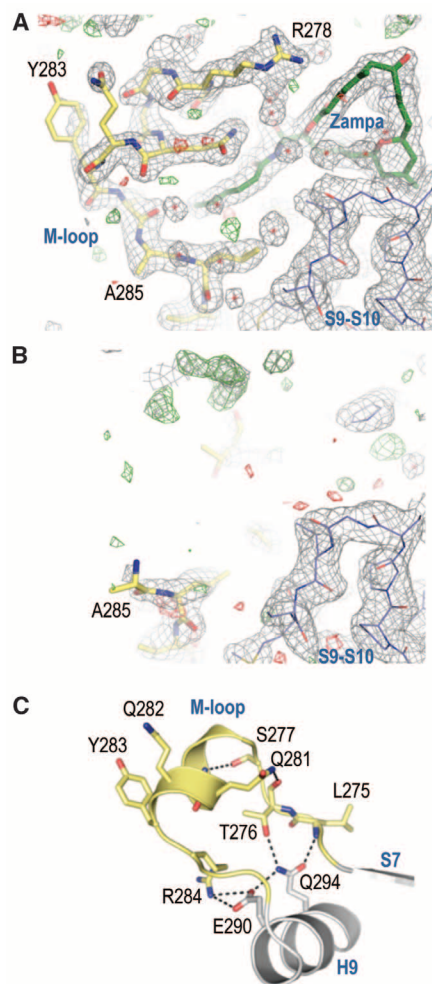


**Fig. 2.** Conformation of the M-loop of  $\beta$ -tubulin. (A and B) 2mFo-DFc (gray mesh, contoured at  $1.0\sigma$ ) and mFo-DFc (green and red mesh,  $\pm 3.0\sigma$ ) electron density maps of the region surrounding the M-loop of  $\beta$ -tubulin in the  $T_2$ R-TTL-Zampa (A) and  $T_2$ R-TTL (B) complexes. (C) Close-up view of the Zampa-induced intramolecular interaction network that contributes to the stabilization of the M-loop helix.

residues Ser<sup>280</sup>, Gln<sup>282</sup>, Arg<sup>284</sup>, and Ala<sup>285</sup> were favorably positioned to form additional contacts to the neighboring  $\beta$ -tubulin. The M-loop of  $\alpha$ -tubulin in our tubulin-MSA complexes was also stabilized in a similar helical conformation, in this case due to a crystal contact (fig. S3). In combination with molecular dynamics simulations (17), these data collectively suggest that the disordered M-loops of both  $\alpha$ - and  $\beta$ -tubulin exhibit an intrinsic propensity to form a helix that establishes lateral tubulin contacts in microtubules.

Our study provides fundamental structural information on the molecular mechanism of action of MSAs (Fig. 3D). Apart from additional global effects (17–19), a common feature of tubulin activation by MSAs is the formation of a short helix in the M-loop of  $\beta$ -tubulin upon MSA binding. As M-loop structuring is a crucial pre-

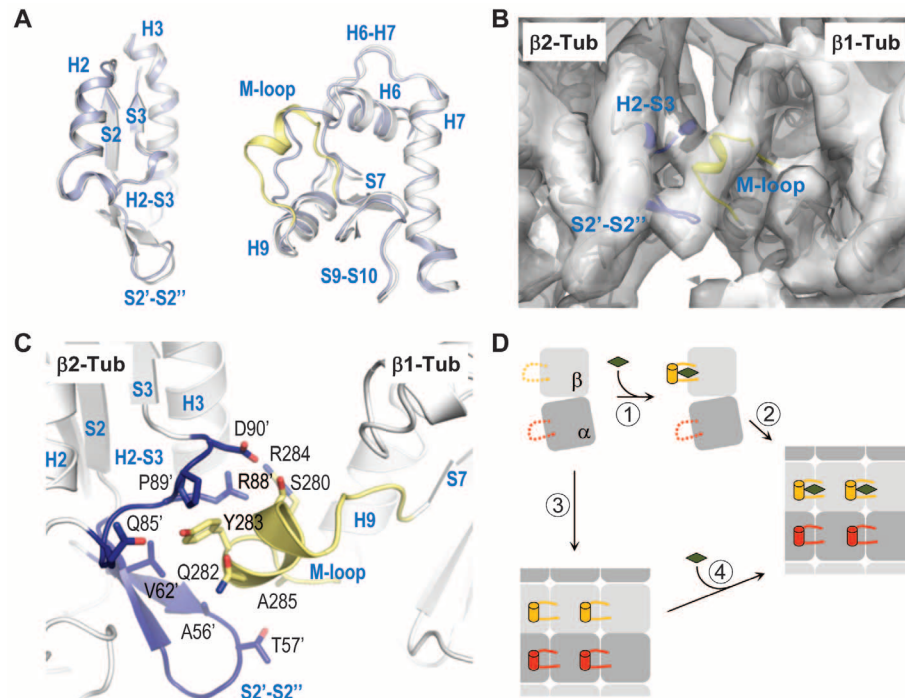


**Fig. 3.** Lateral tubulin interactions in microtubules. (A) Superimposition of the taxane pocket (right) and M-loop-contacting secondary structure elements across protofilaments (left) in curved ( $T_2$ R-TTL-Zampa; gray) and straight (PDP ID 1JFF; light blue)  $\beta$ -tubulin. (B) Cryo-EM map at 8.2 Å resolution of a microtubule viewed from its luminal side (gray surface; Electron Microscopy Data Bank map 1788). Two chimeric molecules composed of straight  $\beta$ -tubulin (cartoon representation) and elements shaping the taxane pocket in the curved tubulin-Zampa complex (A) are fitted in the map. (C) Close-up view of the lateral  $\beta$ -tubulin contact model shown in (B). (D) Proposed molecular mechanism of action of MSAs on tubulin and microtubules. (1) Binding of a MSA (rhomboid) to the taxane-site structures the disordered M-loop of  $\beta$ -tubulin (dashed line) into a helix (cylinder). (2) The MSA-stabilized M-loop promotes tubulin polymerization. (3) The M-loop helices of  $\alpha$ - and  $\beta$ -tubulin are also formed in the context of the microtubule in the absence of a ligand. (4) All taxane-site MSAs bind to tubulin in the microtubule to stabilize lateral contacts. For more details, see text.

requisite for lateral tubulin interactions, this effect explains how MSAs promote microtubule assembly and stabilization. Our data further suggest that the intramolecular interaction network that stabilizes the M-loop helix of both  $\alpha$ - and  $\beta$ -tubulin also forms in microtubules in the absence of a ligand. We propose that the helical structuring of the M-loop facilitates the curved-to-straight conformational change that occurs upon incorporation of tubulin into microtubules. In this context, the binding of a MSA leads to tubulin preorganization according to the gross structural requirements of the assembly process, thus reducing the entropy loss associated with microtubule formation. In turn, our model implies that dissolution of the helical structure of the M-loops is an early molecular event in the process of microtubule disassembly.

The high-resolution structural information obtained for the tubulin-MSA complexes reported here opens the possibility for structure-guided drug engineering. Whereas the structure-activity relationship of epothilones has been explored extensively (20) and one epothilone derivative, ixabepilone, has been approved by the U.S.

Food and Drug Administration for breast cancer treatment (21), little structure-activity work has been reported on Zampa (22). Zampa exhibits favorable properties that could make it an attractive lead compound (10). It is a very potent MSA that exerts its action through covalent binding to tubulin, which might provide superior activity in the case of P-glycoprotein-mediated multidrug resistance.

#### References and Notes

1. C. Dumontet, M. A. Jordan, *Nat. Rev. Drug Discov.* **9**, 790 (2010).
2. P. B. Schiff, J. Fant, S. B. Horwitz, *Nature* **277**, 665 (1979).
3. J. F. Díaz, J. M. Andreu, *Biochemistry* **32**, 2747 (1993).
4. J. F. Díaz, M. Menéndez, J. M. Andreu, *Biochemistry* **32**, 10067 (1993).
5. Materials and methods are available as supplementary materials on Science Online.
6. R. B. Ravelli *et al.*, *Nature* **428**, 198 (2004).
7. E. Nogales, M. Whittaker, R. A. Milligan, K. H. Downing, *Cell* **96**, 79 (1999).
8. E. Nogales, S. G. Wolf, K. H. Downing, *Nature* **391**, 199 (1998).
9. J. H. Nettles *et al.*, *Science* **305**, 866 (2004).
10. J. J. Field *et al.*, *Chem. Biol.* **19**, 686 (2012).

11. J. H. Nettles, K. H. Downing, *Top. Curr. Chem.* **286**, 209 (2009).
12. P. Ayaz, X. Ye, P. Huddleston, C. A. Brautigam, L. M. Rice, *Science* **337**, 857 (2012).
13. L. Pecqueur *et al.*, *Proc. Natl. Acad. Sci. U.S.A.* **109**, 12011 (2012).
14. J. Löwe, H. Li, K. H. Downing, E. Nogales, *J. Mol. Biol.* **313**, 1045 (2001).
15. M. Reese *et al.*, *Angew. Chem. Int. Ed.* **46**, 1864 (2007).
16. F. J.ourniol *et al.*, *J. Cell Biol.* **191**, 463 (2010).
17. A. Mitra, D. Sept, *Biophys. J.* **95**, 3252 (2008).
18. C. Elie-Caille *et al.*, *Curr. Biol.* **17**, 1765 (2007).
19. H. Xiao *et al.*, *Proc. Natl. Acad. Sci. U.S.A.* **103**, 10166 (2006).
20. K.-H. Altmann, B. Pfeiffer, S. Arseniyadis, B. A. Pratt, K. C. Nicolaou, *ChemMedChem* **2**, 396 (2007).
21. R. J. Lechleider *et al.*, *Clin. Cancer Res.* **14**, 4378 (2008).
22. D. Zurwerra *et al.*, *Chemistry* **18**, 16868 (2012).

**Acknowledgments:** We thank R. Kammerer, F. Winkler, and Y. Barral for critical reading of the manuscript; V. de Lucas de Segovia for providing calf brains for tubulin purification; and V. Olieric and M. Wang for excellent technical assistance with the collection of x-ray data at beamline X06SA and X06DA of the Swiss Light Source (Paul Scherrer Institut, Villigen, Switzerland). J.J.F. received a short-term fellowship from the European Molecular Biology Organization and a Professional Development Grant from the Genesis Oncology Trust. This work was supported by grants from the Ministerio de Economía y Competitividad (BIO2010-16351) and the Comunidad Autónoma de Madrid (S2010/BMD-2457) (to J.F.D.), a Ph.D. fellowship from the Roche Research Foundation (to D.Z.),

and grants from the Swiss National Science Foundation (310030B\_138659) and the Swiss SystemsX.ch initiative (BIP-2011/122) (to M.O.S.). Coordinates have been deposited at the Protein Data Bank (PDB) under identification (ID) nos. 4I4T (T<sub>2</sub>R-TTL-Zampa), 4I50 (T<sub>2</sub>R-TTL-EpoA), and 4I55 (T<sub>2</sub>R-TTL).

#### Supplementary Materials

www.sciencemag.org/cgi/content/full/science.1230582/DC1  
Materials and Methods

Figs. S1 to S3

Table S1

References (23–30)

21 September 2012; accepted 4 December 2012

Published online 3 January 2013;

10.1126/science.1230582

# A Strategy for Modulation of Enzymes in the Ubiquitin System

Andreas Ernst,<sup>1</sup> George Avvakumov,<sup>2</sup> Jiefei Tong,<sup>3</sup> Yihui Fan,<sup>4</sup> Yanling Zhao,<sup>4</sup> Philipp Alberts,<sup>3</sup> Avinash Persaud,<sup>3,5</sup> John R. Walker,<sup>2</sup> Ana-Mirela Neculai,<sup>1</sup> Dante Neculai,<sup>2</sup> Andrew Vorobyov,<sup>1</sup> Pankaj Garg,<sup>1</sup> Linda Beatty,<sup>1</sup> Pak-Kei Chan,<sup>6</sup> Yu-Chi Juang,<sup>7</sup> Marie-Claude Landry,<sup>7</sup> Christina Yeh,<sup>7,8</sup> Elton Zeqiraj,<sup>7</sup> Konstantina Karamboulas,<sup>1</sup> Abdellah Allali-Hassani,<sup>2</sup> Masoud Vedadi,<sup>2</sup> Mike Tyers,<sup>6,7</sup> Jason Moffat,<sup>1,8,9,10</sup> Frank Sicheri,<sup>7,8</sup> Laurence Pelletier,<sup>7,8</sup> Daniel Durocher,<sup>7,8</sup> Brian Raught,<sup>10</sup> Daniela Rotin,<sup>3,5</sup> Jianhua Yang,<sup>4</sup> Michael F. Moran,<sup>3,8,9</sup> Sirano Dhe-Paganon,<sup>2,11</sup> Sachdev S. Sidhu<sup>1,8,9,10,\*</sup>

The ubiquitin system regulates virtually all aspects of cellular function. We report a method to target the myriad enzymes that govern ubiquitination of protein substrates. We used massively diverse combinatorial libraries of ubiquitin variants to develop inhibitors of four deubiquitinases (DUBs) and analyzed the DUB-inhibitor complexes with crystallography. We extended the selection strategy to the ubiquitin conjugating (E2) and ubiquitin ligase (E3) enzymes and found that ubiquitin variants can also enhance enzyme activity. Last, we showed that ubiquitin variants can bind selectively to ubiquitin-binding domains. Ubiquitin variants exhibit selective function in cells and thus enable orthogonal modulation of specific enzymatic steps in the ubiquitin system.

**T**he biological importance of the ubiquitin system for protein posttranslational modification rivals and may exceed that of phosphorylation (1, 2). Consequently, there is great interest in deciphering the role of protein

ubiquitination and deubiquitination in both normal and disease states (1). Ubiquitin (Ub) is a small, highly conserved protein that is covalently conjugated to proteins through a cascade of enzyme activities, E1→E2→E3, which can be read by a cohort of Ub-binding domains (UBDs) and reversed by deubiquitinating enzymes (DUBs). Ub monomers and chains of different linkages can be assembled on the substrate, and this complex code can target the substrate for degradation by the 26S proteasome or alter its interactions, localization, or activity (3).

The 58 human ubiquitin-specific proteases (USPs) (4), which represent more than half of the known DUBs, have attracted attention as potential therapeutic targets (5, 6). Numerous USPs have been implicated in cancer and other pathologies, including neurodegenerative, haematological, and infectious diseases (7–13). USPs are cysteine proteases that share a structurally conserved catalytic domain with a well-defined catalytic cleft (14). Thus, it may be possible to develop a general structure-based strategy for inhibiting family members by using similar yet specific molecular entities, as has been the case for kinases that have been targeted with small

molecules built on common scaffolds (15). However, only a few weak inhibitors of USPs or other DUBs have been reported (16–18). The paucity of specific inhibitors for DUBs has hampered attempts to understand and manipulate deubiquitination pathways for therapeutic benefit.

We developed a strategy to use Ub as a scaffold to generate highly specific and potent inhibitors of USPs and then extended the approach to target other DUB families, E2 enzymes, E3 enzymes, and UBDs. USP substrates contain a proximal Ub moiety that is conjugated through its C-terminal carboxyl group to a lysine in a target Ub or protein substrate (19, 20). Despite low sequence similarity, USP catalytic domains share a common fold that includes a structurally conserved Ub-binding site for the proximal Ub.

To aid our inhibitor design strategy, we solved the structure of USP21 in complex with a suicide-substrate Ub moiety that forms a covalent bond between its C terminus and the catalytic cysteine of the enzyme (table S1) (21, 22). Superposition of the Ub:USP21 complex structure with structures of four other Ub:USP complexes shows that Ub occupies a similar site on all five enzymes (Fig. 1A). The contact surface between Ub and the USPs is large; for example, 1835 and 1645 Å<sup>2</sup> are buried on the surfaces of Ub and USP21, respectively. Approximately 75% of the Ub-binding surface on USP21 is composed of residues that are not conserved within the USP family (Fig. 1B and fig. S1).

Because Ub binds to USPs with low affinity but through a large contact area, we reasoned that we should be able to make mutations in Ub that optimize intermolecular contacts and enhance affinity for a particular USP. Because the Ub-binding sites of USPs vary in sequence, Ub variants that bind tightly to one USP should not interact with other USPs. Tight binding Ub variants should act as competitive inhibitors of catalytic activity by blocking the recognition of natural ubiquitinated substrates. To test our hypothesis, we constructed combinatorial, phage-displayed libraries of Ub variants for selection against different USPs and other Ub-associated proteins.

We defined the USP-binding site as ~30 Ub residues that make contact with USP21 in the

<sup>1</sup>Terrence Donnelly Center for Cellular and Biomolecular Research, University of Toronto, 160 College Street, Toronto, Ontario M5S 3E1, Canada. <sup>2</sup>Structural Genomics Consortium, MaRS Centre, 101 College Street, Suite 700, Toronto, Ontario M5G 1L7, Canada. <sup>3</sup>Hospital for Sick Children, 101 College Street, Toronto, Ontario M5G 1L7, Canada. <sup>4</sup>Texas Children's Cancer Center, Department of Pediatrics, Dan L. Duncan Cancer Center, Baylor College of Medicine, Houston, TX 77030, USA. <sup>5</sup>Biochemistry Department, University of Toronto, Toronto, Ontario M5S 3E1, Canada. <sup>6</sup>Institut de Recherche en Immunologie et Cancérologie, Université de Montréal, Montreal, Quebec H3C 3J7, Canada. <sup>7</sup>Samuel Lunenfeld Research Institute, Mount Sinai Hospital, 600 University Avenue, Toronto, Ontario M5G 1X5, Canada. <sup>8</sup>Department of Molecular Genetics, University of Toronto, 160 College Street, Toronto, Ontario M5S 3E1, Canada. <sup>9</sup>Banting and Best Department of Medical Research, University of Toronto, 160 College Street, Toronto, Ontario M5S 3E1, Canada. <sup>10</sup>Ontario Cancer Institute and McLaughlin Centre for Molecular Medicine, University of Toronto, 101 College Street, Toronto, Ontario M5G 1L7, Canada. <sup>11</sup>Department of Physiology, University of Toronto, 101 College Street, Toronto, Ontario M5G 1L7, Canada.

\*To whom correspondence should be addressed. E-mail: sachdev.sidhu@utoronto.ca



Ub:USP21 complex structure (Fig. 1, C and D). We constructed two phage-displayed libraries using a soft randomization strategy that favored the wild-type (wt) sequence but allowed for diversity across the entire Ub-binding site (23, 24). This approach enabled the selection of variants with mutations that improve affinity for a particular USP without drastically altering the binding interaction.

Binding selections yielded variants that bound to either USP8, USP21, or USP2a (Fig. 2A and table S2) but not to 10 other USPs (Fig. 2B). We also isolated variants that bound selectively to members of two other DUB families: the ovarian tumor protease (OTU) family member OTUB1 (25, 26) and the JAB1/MPN/MOV34 metallo-enzyme (JAMM) family member Brcc36-containing isopeptidase complex (BRISC) (27, 28). We also identified variants that bound selectively to the homologous to the E6-AP carboxyl terminus (HECT) domains of the E3 enzymes neural precursor cell expressed developmentally down-regulated protein 4 (NEDD4) or itchy homolog E3 ubiquitin protein ligase (ITCH) (29, 30), to the noncatalytic UBDs of USP37 (USP37-UBD) (31, 32), and to the E2 enzyme Cdc34 (Fig. 2, A and B, and table S2) (33).

Ub variants that bound selectively to USP8, USP21, or USP2a were purified as free proteins in a truncated form lacking the last two glycines

that are required for conjugation to substrates (19). In vitro proteolysis assays with the substrate Ub-AMC (34) showed that each Ub variant potentially inhibited its cognate USP [median inhibitory concentration ( $IC_{50}$ ) = 4.8 nM, 2.4 nM, or 25 nM for Ubv.8.2CA2, Ubv.21.4CA2, or Ubv.2.3CA2, respectively] (Fig. 2C). In contrast, neither the variants, nor Ub.wt, inhibited non-cognate USPs ( $IC_{50} \gg 1 \mu M$ ) (fig. S2). Purified Ubv.B1.1 bound to OTUB1 with a dissociation constant ( $K_d$ ) of 20 nM (fig. S3A) and efficiently inhibited the cleavage of K48-linked di-Ub (fig. S3B), which is consistent with a substrate-competitive binding mode. OTUB1 binds to the activated E2-conjugating enzyme Ub~UbcH5b, and binding is enhanced by Ub.wt (35). Although Ubv.B1.1 binds to OTUB1 much more tightly than does Ub.wt, it shows a compromised ability to promote complex formation (Fig. 2D), suggesting an alteration in binding mode to OTUB1 relative to Ub.wt.

To elucidate the molecular details of enzyme inhibition, we determined the structures of USP21, USP8, USP2a, and OTUB1 in complex with their cognate inhibitors at 2.0, 2.6, 1.85, or 2.5 Å, respectively (Fig. 3 and table S1).

The structures of USP21 in complex with Ubv.21.4 or Ub.wt were highly similar; the Cα atoms of the USP and Ub moieties superimpose with root-mean-square deviation (RMSD)

of less than 0.7 or 0.4 Å<sup>2</sup>, respectively (Fig. 3A). Ubv.21.4 was purified with a C-terminal extension, but mass spectrometry of protein sample before crystallization showed a mass consistent with cleavage of the tail after Gly<sup>76</sup>, the last residue of natural Ub (fig. S4 and table S3). These results indicate that Ubv.21.4 is a substrate for USP21 but is not released after cleavage. This result is consistent with the crystal structure, which shows excellent superposition between the tails of Ubv.21.4 and Ub.wt in the catalytic cleft of the enzyme.

The three mutated residues in Ubv.21.4 contact residues of USP21 that are not conserved in the USP family (Fig. 3B), and this provides a structural explanation for the selectivity of Ubv.21.4 for USP21 (fig. S5). Compared with Ub.wt, two of the three substitutions in Ubv.21.4 serve to remove repulsive interactions and optimize hydrophobic packing with USP21. The Glu<sup>64</sup> side chain in Ub.wt is located close to Asp<sup>438\*</sup> of USP21 (USP residues are marked with asterisks), but in Ubv.21.4, this unfavorable charge interaction is abrogated by substitution with Trp<sup>64</sup>, which makes a hydrogen bond with Asp<sup>438\*</sup> and hydrophobic contacts with the side chains of Pro<sup>435\*</sup> and Val<sup>436\*</sup>. (Fig. 3C, left). The Ub side chain at position 68 packs against three hydrophobic side chains of USP21, and consequently, the hydrophobic Phe<sup>68</sup> of Ubv.21.4 appears to make more favorable interactions than those of the polar His<sup>68</sup> side chain of Ub.wt (Fig. 3C, center).

We could not solve the structure of USP8 in complex with Ub.wt, but we compared the structure of USP8 in complex with Ubv.8.2 with a previous structure of the USP8 catalytic domain alone (apo-USP8) (36). An auto-inhibited or inactive state was ascribed to apo-USP8 because the Ub-binding site is partially occluded by a zinc finger domain, implying an induced fit mechanism for substrate binding. Overall, the structures of apo-USP8 and USP8 in complex with Ubv.8.2 are similar, and the Cα atoms superimpose with a RMSD of 1.4 Å<sup>2</sup> (Fig. 3D). However, there are substantial changes in the zinc finger region, which is opened by ~8 Å (measured by the change in position of Asn<sup>980\*</sup>) in the inhibitor-bound form. Additionally, the BL2 loop adjacent to the active site of the protein is shifted slightly outward by ~3 Å (measured by the change in position of Gly<sup>1018\*</sup>). Surprisingly, Ubv.8.2 is rotated by ~85° and shifted by ~5 Å relative to the positions of the Ub moieties in the complexes with USP21 and other USPs (Figs. 1 and 3). Consequently, the tail of Ubv.8.2 does not extend into the active site cleft, and consistently, mass spectrometry showed no cleavage of the C-terminal extension that was added downstream of Gly<sup>76</sup> (fig. S2 and table S3). Thus, Ubv.8.2 binds to a conformation of USP8 that resembles apo-USP8 but in an orientation that differs drastically from known structures of Ub.wt bound to active USPs. Despite these unusual features, Ubv.8.2 occludes the Ub-binding site and potentially inhibits USP8 activity.

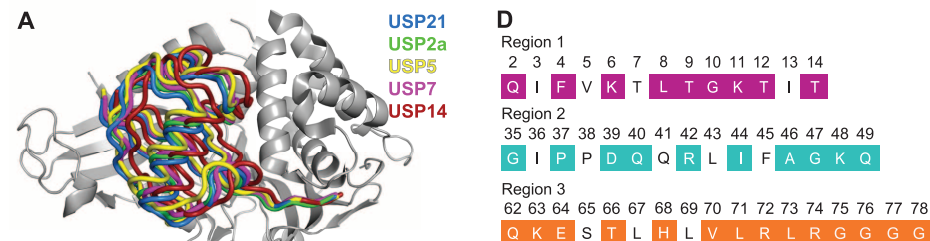


**Fig. 1.** Structural rationale and library design for Ub-based USP inhibitors. **(A)** Superposition of Ub in complex USP21 (blue; PDB entry 3I3T), USP2a (green; PDB entry 2HD5), USP5 (yellow; PDB entry 3IHP), USP7 (magenta; PDB entry 1NBF), and USP14 (red; PDB entry 2AYO) (22, 45, 46). The superposition was performed with complete coordinates for the Ub:USP complexes, but for clarity, only USP21 is shown (gray). **(B)** The Ub-binding site of USP21. USP21 is shown as a molecular surface, and residues that form the Ub-binding site are colored red or blue, indicating residues that are <50% or ≥50% conserved, respectively, in the sequences of 48 human USPs (fig. S1). **(C)** The phage-displayed Ub library design mapped onto the Ub structure (PDB entry 1UBQ). The Ub main chain is shown as a gray tube, and positions that were diversified in the libraries are shown as spheres, colored as follows: region 1, purple; region 2, blue; and region 3, orange. **(D)** The primary sequence of the regions targeted in the library design. Diversified sequences are shaded and colored as in (C). Two libraries were constructed. Amongst the shaded sequences, library 1 ( $7 \times 10^{10}$  distinct variants) did not target six of the positions in region 3 (73 to 78), and library 2 ( $9 \times 10^9$  distinct variants) did not target four of the positions in region 2 (35, 37, 39, and 40).

colored as follows: region 1, purple; region 2, blue; and region 3, orange. **(D)** The primary sequence of the regions targeted in the library design. Diversified sequences are shaded and colored as in (C). Two libraries were constructed. Amongst the shaded sequences, library 1 ( $7 \times 10^{10}$  distinct variants) did not target six of the positions in region 3 (73 to 78), and library 2 ( $9 \times 10^9$  distinct variants) did not target four of the positions in region 2 (35, 37, 39, and 40).

Nine of the 12 mutated residues in Ubv.8.2 make contacts with USP8, and 70% of these contacts involve nonconserved residues in the USP family (Fig. 3E), likely accounting for the high specificity of Ubv.8.2 for USP8 (Fig. 2B). The tail of Ubv.8.2 contains three mutated contact residues (Ala<sup>66</sup>, Tyr<sup>68</sup>, and Leu<sup>70</sup>) and interacts with an  $\alpha$ -helix formed by residues 870\* to 882\* of USP8 (Fig. 3F, left). A second cluster of contacts involving mutated residues is formed by the interactions of Arg<sup>2</sup>, Val<sup>4</sup>, Ile<sup>14</sup>, and His<sup>64</sup> with residues 891\* to 895\* (Fig. 3F, center). The remaining two mutated contact residues (Met<sup>9</sup> and Arg<sup>11</sup>) are in close proximity (Fig. 3F, right).

The structures of USP2a in complex with Ub. wt or Ubv.2.3 are highly similar (Fig. 3G) because the Ca atoms of the USP and Ub moieties superimpose with a RMSD of 1.0 or 0.3 Å, respectively. The three mutated residues in Ubv.2.3 make contacts with residues that are not conserved in the USP family (Fig. 3H), again explaining the selectivity. Relative to Ub.wt, the three substitutions alter hydrogen-bonding patterns (Fig. 3I). Whereas Lys<sup>6</sup> of Ub.wt formed a hydrogen bond with Asp<sup>466\*</sup>, Asn<sup>6</sup> of Ubv.2.3 forms a hydrogen bond with Lys<sup>503\*</sup> (Fig. 3I, left). Consequently, Asp<sup>466\*</sup> reorients and forms a hydrogen bond with His<sup>12</sup> of Ubv.2.3 (Fig. 3I, middle).

The structure of the OTUB1 OTU domain (OTUB1<sup>45-271</sup>) in complex with Ubv.B1.1 (table S1) reveals that Ubv.B1.1 binds to the distal Ub-binding site of OTUB1 (Fig. 3J) and enables a rationalization of its altered binding and allosteric properties. Compared with a previously published Ub-UbcH5b-OTUB1-Ub complex structure (35), Ubv.B1.1 is rotated by 22° relative to the distal site Ub.wt (Fig. 3J). This deviation in binding mode may account for the compromised ability to allosterically promote binding of Ub-UbcH5b to OTUB1. Four of the six mutated residues in Ubv.B1.1 are in contact with OTUB1 (Fig. 3K) and bind to a turn motif connecting  $\alpha$ 8 and  $\alpha$ 9 of OTUB1. Most prominent in this interaction are Leu<sup>44</sup>, Arg<sup>47</sup>, and Tyr<sup>68</sup>, which improve polar and hydrophobic contacts. Arg<sup>47</sup> establishes hydrogen bonds to four main chain carbonyl groups in the turn motif (Fig. 3L, left), whereas Tyr<sup>68</sup> makes favorable packing interactions with His<sup>192\*</sup> and Phe<sup>193\*</sup> (Fig. 3L, middle). Leu<sup>44</sup> establishes van der Waals contacts with the peptide bonds of the  $\alpha$ 8: $\alpha$ 9 loop (Fig. 3L, right). These results demonstrate that high-affinity Ub variants can be developed against specific UBDs.

We investigated the in vivo effects of different variants expressed as C-terminal fusions with Flag-tagged green fluorescent protein in mammalian cells. Mass spectrometric analysis of associated proteins showed that each inhibitor interacted specifically with its cognate USP (table S4).

Ubiquitinated receptor-interacting protein 1 (RIP1) is a positive regulator of nuclear factor

$\kappa$ B (NF- $\kappa$ B) activation induced by tissue necrosis factor- $\alpha$  (TNF $\alpha$ ), and in turn, USP21 has been shown to down-regulate TNF $\alpha$ -induced NF- $\kappa$ B activation by deubiquitinating RIP1 (37). Ubv.21.4C $\Delta$ 2 coimmunoprecipitated with USP21 in cotransfected human embryonic kidney (HEK) 293T cells (Fig. 4A), blocked the deubiquitination of RIP1 by USP21 (Fig. 4B), and restored NF- $\kappa$ B activation (Fig. 4C). No such effects were observed when Ub.wt was cotransfected rather

than Ubv.21.4C $\Delta$ 2. These results show that Ubv.21.4C $\Delta$ 2 binds and inhibits USP21 in cells and establish that Ub variants can act as orthogonal genetic probes of USP function.

USP8 regulates ligand-mediated endocytosis of several receptors (38–40), including the epidermal growth factor receptor (EGFR), deubiquitination of which protects it from degradation in lysosomes (38). Immunoprecipitated Ubv.8.2C $\Delta$ 2, but not Ub.wtC $\Delta$ 2, was associated

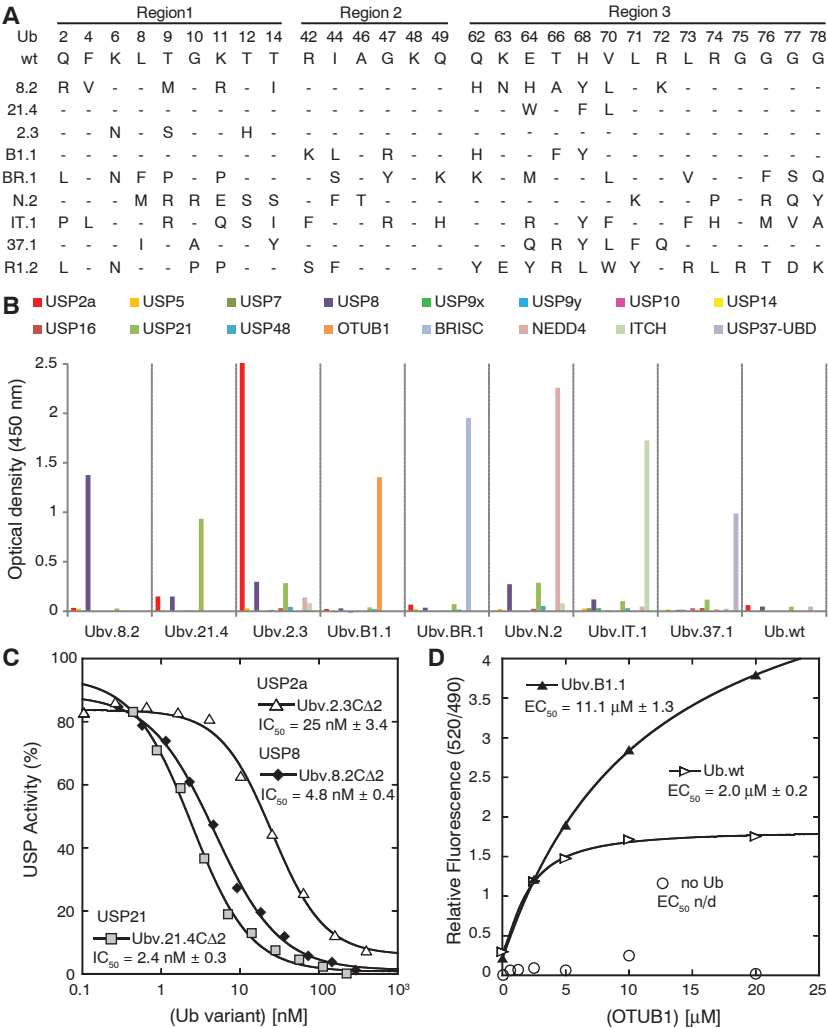


**Fig. 2.** Selective binding of Ub variants to DUBs, Ub ligases, and UBDs, and inhibition of DUB function in vitro. **(A)** Sequence alignment of Ub.wt and representative Ub variants selected for binding to USP8 (8.2), USP21 (21.4), USP2a (2.3), OTUB1 (B1.1), the BRISC protein complex (BR.1), NEDD4 (N.2), ITCH (IT.1), USP37-UBD (37.1), or Cdc34 (R1.2). The alignment shows only those positions that were diversified in the Ub library, and positions that were conserved as the wt sequence are indicated by dashes. A complete list of selected variants is provided in table S2. **(B)** Ub variants bind selectively to their cognate targets, as shown by phage enzyme-linked immunosorbent assays for binding to the following immobilized proteins (color coded as indicated in the panel): USP2a, USP5, USP7, USP8, USP9x, USP9y, USP10, USP14, USP16, USP21, USP48, OTUB1, BRISC, NEDD4, ITCH, and USP37-UBD. Bound phage were detected spectrophotometrically (optical density at 450 nm), and background binding to neutravidin was subtracted from the signal. **(C)** Inhibition of USP2a, USP8, or USP21 shown as dose-response curves for Ub variants. The IC<sub>50</sub> value was determined as the concentration of Ub variant that reduced USP activity by 50%. **(D)** The effects of Ubv.B1.1 or Ub.wt on binding of OTUB1 to Ub-UbcH5b measured as relative fluorescence by means of time-resolved Förster-energy transfer. The median effective concentration (EC<sub>50</sub>) value is defined as the half-maximal effective concentration of OTUB1.



with endogenous USP8 (Fig. 4D). EGF-stimulated ubiquitination of EGFR in transfected HEK293 cells that express large amounts of Flag-tagged EGFR ( $\sim 10^6$ /cell) (41) was greater in cells expressing Ubv.8.2 $\Delta$ 2 than in cells expressing Ub.wt $\Delta$ 2 (Fig. 4E). Expression of Ubv.8.2 $\Delta$ 2 in HEK293 cells, but not Ub.wt $\Delta$ 2, resulted in more rapid down-regulation of endogenous EGFR in response

to a low dose (5 ng/ml) of EGF (Fig. 4F), which is the expected outcome of USP8 inhibition (38, 42). These data illustrate that Ubv.8.2 $\Delta$ 2 can modulate EGFR ubiquitination over a broad range of receptor densities.

Confocal microscopy of cells expressing Ubv.8.2 $\Delta$ 2 or Ub.wt $\Delta$ 2 (fig. S6) showed no difference in the colocalization of EGFR with

the early endosomal antigen 1 (EEA1), indicating that endosomal uptake of EGFR in response to EGF stimulation was not affected by the Ub variant (Fig. 4G). However, Ubv.8.2 $\Delta$ 2, but not Ub.wt $\Delta$ 2, resulted in greater colocalization of EGFR with the lysosome-associated protein 1 (LAMP1) and correspondingly less colocalization with the endosomal recycling

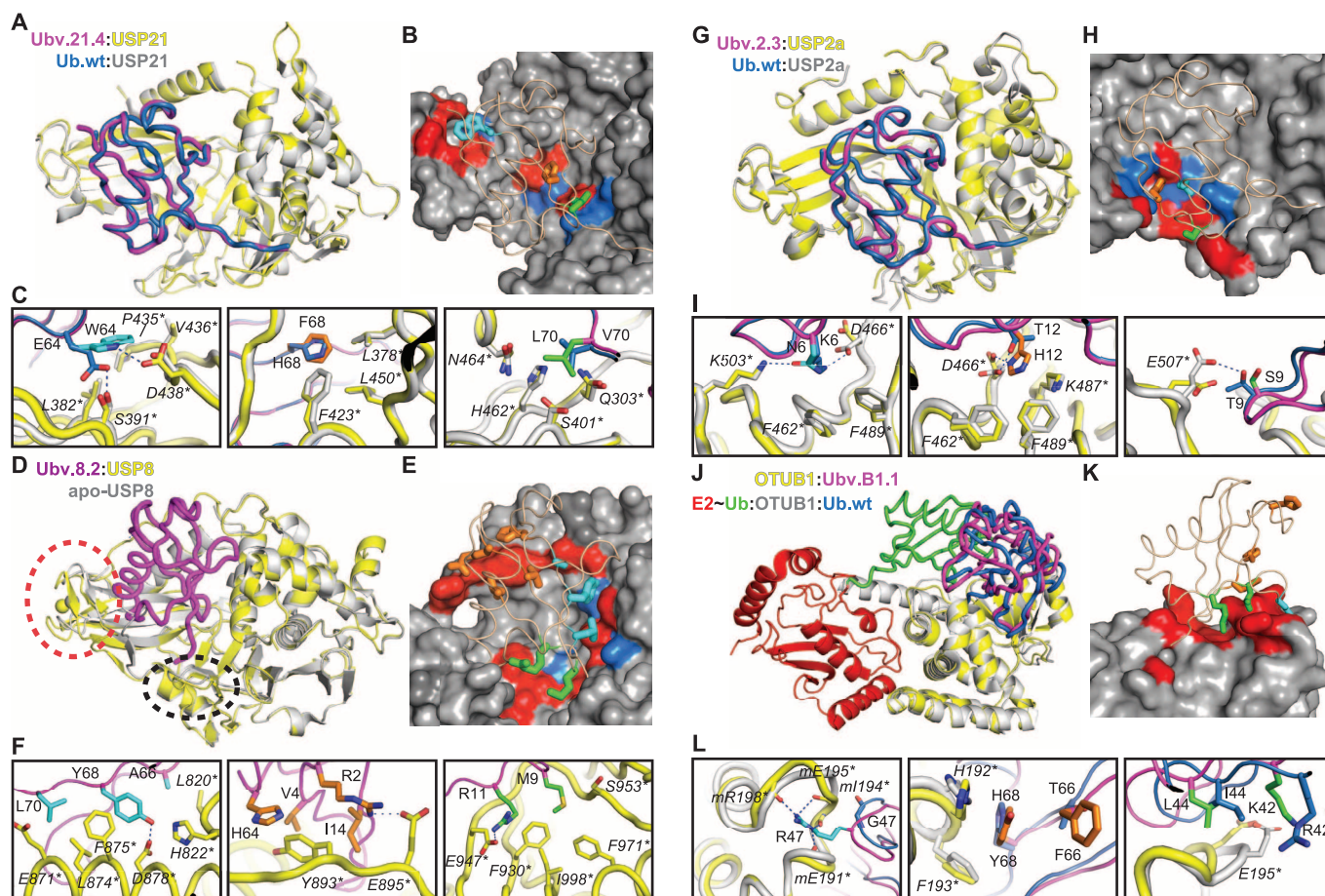
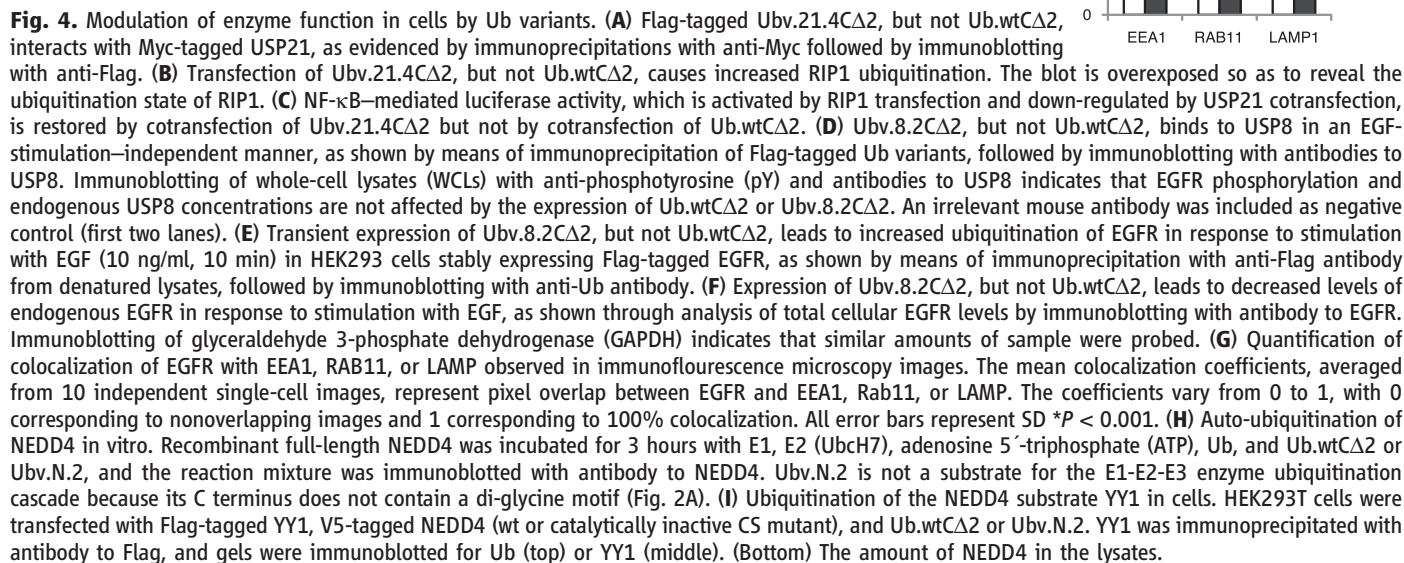


**Fig. 3.** Molecular basis for DUB inhibition by Ub variants. **(A)** Superposition of USP21 (yellow) in complex with Ubv.21.4 (purple) and USP21 (gray) in complex with Ub.wt (blue). **(B)** Surface representation of the Ub-binding site of USP21 in complex with Ubv.21.4 (wheat tube). Residues in Ubv.21.4 that are mutated relative to Ub.wt are shown as colored sticks, and residues on the USP21 surface that make contact with these residues are colored red or blue if they are <50% or  $\geq$ 50% conserved in the sequences of 48 human USPs, respectively. **(C)** Details of the superposition of USP21 in complex Ubv.21.4 or Ub.wt, showing the changes in molecular interactions caused by the mutations at positions 64 (left), 68 (center), and 70 (right). The Ubv.21.4 side chains are colored as in (B), and Ub.wt side chains are colored blue. Main chains and USP21 side chains are colored as in (A). Residues are numbered according to the PDB files, and asterisks indicate USP residues. **(D)** Superposition of USP8 (yellow) in complex with Ubv.8.2 (purple) and apo-USP8 (gray). Dashed ovals demarcate structural changes in the zinc finger region (red) or the BL2 loop (black) of USP8. **(E)** Surface representation of the Ub-binding site of USP8 in complex with Ubv.8.2 (wheat tube). Residues in Ubv.8.2 that are mutated relative to Ub.wt and make contact with USP8 are shown as colored sticks, and residues on the USP8 surface that make contact with these residues are colored red or blue, as in (B). **(F)** Details of USP8 in complex with Ubv.8.2, showing molecular interactions involving residues in Ubv.8.2 that are mutated relative to Ub.wt and are in contact with USP8. The Ubv.8.2 side chains are

colored as in (E). Main chains and USP8 side chains are colored as in (D). **(G)** Superposition of USP2a (yellow) in complex with Ubv.2.3 (purple) and USP2a (gray) in complex with Ub.wt (blue). **(H)** Surface representation of the Ub-binding site of USP2a in complex with Ubv.2.3 (wheat tube). Residues in Ubv.2.3 that are mutated relative to Ub.wt are shown as colored sticks, and residues on the USP2a surface that make contact with these residues are colored red or blue, as in (B). **(I)** Details of the superposition of USP2a in complex with Ubv.2.3 or Ub.wt, showing changes in molecular interactions caused by the mutations at positions 6 (left), 12 (center), and 9 (right). The Ubv.2.3 side chains are colored as in (H). Main chains and USP2a side chains are colored as in (G). **(J)** Superposition of OTUB1 (yellow) in complex with Ubv. B1.1 (purple) and OTUB1 (gray) in complex with distal Ub.wt (blue) and an E2-Ub covalent conjugate consisting of E2 conjugating enzyme UbcH5b (red) and Ub.wt (green). **(K)** Surface representation of the Ub-binding site of OTUB1 in complex with Ubv.B1.1 (wheat tube). Residues in Ubv.B1.1 that are mutated relative to Ub.wt are shown as colored sticks, and residues on the OTUB1 surface that are in contact with these residues are colored red. **(L)** Details of the superposition of OTUB1 in complex with Ubv.B1.1 or Ub.wt, showing changes in molecular interactions caused by the mutations at positions 47 (left), 66 and 68 (center), and 42 and 44 (right). The Ubv.B1.1 side chains are colored as in (K). Main chains and OTUB1 side chains are colored as in (J).



cells by monitoring a NEDD4 substrate, the transcription factor Ying-Yang1 (YY1) (43). No ubiquitination of YY1 was detected in cells transfected with catalytically inactive NEDD4, whereas YY1 was ubiquitinated in cells transfected with wt NEDD4, and this ubiquitination was strongly enhanced by the presence of Ubv.N.2 as compared



with Ub.wt $\Delta$ 2 (Fig. 4I). NEDD4 is auto-inhibited by intramolecular protein-protein interactions (44), and it is likely that Ubv.N.2 alleviates this inhibition.

Through engineered optimization of the low-affinity interactions between Ub and enzymes of the ubiquitin system, we were able to develop potent and selective modulators of ubiquitin system activity. Structural analyses explained the higher affinity of the Ub variants and underscored the plasticity of the Ub fold as a recognition scaffold. Ub variants cause target-specific effects on enzyme activity and can act as simple competitive inhibitors in the case of some USPs, as both a competitive inhibitor of catalytic function and an allosteric attenuator of Ub~UbCH5b docking in the case of OTUB1, or as enhancers of ubiquitin ligase activity in the case of NEDD4.

Collectively, these results show that the dynamic interactions of Ub can be harnessed to develop selective modulators of major enzyme classes in the ubiquitin system. Our findings illustrate a previously unappreciated feature of ubiquitin itself, namely that the extreme sequence conservation of ubiquitin is likely dictated by the constraints of low-affinity interactions with hundreds of partners, few if any of which can tolerate mutational drift toward higher-affinity interaction. As we illustrate here, Ub variants will serve as useful genetic probes to assess and modulate ubiquitin system function in vivo. Applications of Ub variants in drug discovery will include target validation, competition-based screening assays, and structure-guided design of small-molecule mimetics of the stabilized Ub-target interface.

## References and Notes

1. P. Cohen, M. Tcherpakov, *Cell* **143**, 686 (2010).
2. D. Komander, *Biochem. Soc. Trans.* **37**, 937 (2009).
3. D. Komander, M. Rape, *Annu. Rev. Biochem.* **81**, 203 (2012).
4. S. M. B. Nijman *et al.*, *Cell* **123**, 773 (2005).
5. Y. L. Yang, J. Kitagaki, H. Wang, D. X. Hou, A. O. Perantoni, *Cancer Sci.* **100**, 24 (2009).
6. L. Daviet, F. Colland, *Biochimie* **90**, 270 (2008).
7. M. J. Edelmann, B. M. Kessler, *Biochim. Biophys. Acta* **1782**, 809 (2008).
8. S. Hussain, Y. Zhang, P. J. Galardy, *Cell Cycle* **8**, 1688 (2009).
9. J. M. Grunda *et al.*, *J. Neurooncol.* **80**, 261 (2006).
10. X. Zhang, F. G. Berger, J. Yang, X. Lu, *EMBO J.* **30**, 2177 (2011).
11. J. M. Cummins, B. Vogelstein, *Cell Cycle* **3**, 687 (2004).
12. M. Y. Li, C. L. Brooks, N. Kon, W. Gu, *Mol. Cell* **13**, 879 (2004).
13. C. Priolo *et al.*, *Cancer Res.* **66**, 8625 (2006).
14. D. Komander, M. J. Clague, S. Urbé, *Nat. Rev. Mol. Cell Biol.* **10**, 550 (2009).
15. O. Fedorov *et al.*, *Proc. Natl. Acad. Sci. U.S.A.* **104**, 20523 (2007).
16. F. Colland, *Biochem. Soc. Trans.* **38**, 137 (2010).
17. B. H. Lee *et al.*, *Nature* **467**, 179 (2010).
18. V. Kapuria *et al.*, *Cancer Res.* **70**, 9265 (2010).
19. C. M. Pickart, M. J. Eddins, *Biochim. Biophys. Acta* **1695**, 55 (2004).
20. W. Li, Y. Ye, *Cell. Mol. Life Sci.* **65**, 2397 (2008).
21. K. D. Wilkinson, T. Gan-Erdene, N. Kolli, *Methods Enzymol.* **399**, 37 (2005).
22. M. Hu *et al.*, *Cell* **111**, 1041 (2002).
23. F. A. Fellouse, G. Pal, in *Phage Display in Biotechnology and Drug Discovery*, S. S. Sidhu, Ed. (Taylor and Francis Group, Boca Raton, FL, 2005), vol. 3, pp. 111–142.
24. S. S. Sidhu *et al.*, in *Methods in Enzymology* (Academic Press, 2000), vol. 328, pp. 333–IN5.
25. M. J. Edelmann *et al.*, *Biochem. J.* **418**, 379 (2009).
26. S. Nakada *et al.*, *Nature* **466**, 941 (2010).
27. E. M. Cooper, J. D. Boeke, R. E. Cohen, *J. Biol. Chem.* **285**, 10344 (2010).
28. E. M. Cooper *et al.*, *EMBO J.* **28**, 621 (2009).
29. W. L. Perry *et al.*, *Nat. Genet.* **18**, 143 (1998).
30. G. Melino *et al.*, *Cell Death Differ.* **15**, 1103 (2008).
31. J. H. Hurley, S. Lee, G. Prag, *Biochem. J.* **399**, 361 (2006).
32. X. Huang *et al.*, *Mol. Cell* **42**, 511 (2011).
33. D. M. Wenzel, K. E. Stoll, R. E. Klevit, *Biochem. J.* **433**, 31 (2010).
34. L. C. Dang, F. D. Melandri, R. L. Stein, *Biochemistry* **37**, 1868 (1998).
35. Y.-C. Juang *et al.*, *Mol. Cell* **45**, 384 (2012).
36. G. V. Awakumov *et al.*, *J. Biol. Chem.* **281**, 38061 (2006).
37. G. F. Xu *et al.*, *J. Biol. Chem.* **285**, 969 (2010).
38. I. Berlin, H. Schwartz, P. D. Nash, *J. Biol. Chem.* **285**, 34909 (2010).
39. C. M. Balut, C. M. Loch, D. C. Devor, *FASEB J.* **25**, 3938 (2011).
40. I. M. J. Meijer, J. E. M. van Leeuwen, *Cell. Signal.* **23**, 458 (2011).
41. J. Tong, P. Taylor, S. M. Peterman, A. Prakash, M. F. Moran, *Mol. Cell. Proteomics* **8**, 2131 (2009).
42. S. Niendorf *et al.*, *Mol. Cell. Biol.* **27**, 5029 (2007).
43. A. Persaud *et al.*, *Mol. Syst. Biol.* **5**, 333 (2009).
44. S. Wiesner *et al.*, *Cell* **130**, 651 (2007).
45. M. Renatus *et al.*, *Structure* **14**, 1293 (2006).
46. M. Hu *et al.*, *EMBO J.* **24**, 3747 (2005).

**Acknowledgments:** The authors thank I. Pot and J.J. Adams for helpful comments on the manuscript and Y. Li for cloning protease constructs. This project was supported by operating grants from the Canadian Institutes for Health Research to S.S.S. (MOP-111149), D.R. (MOP-13494), F.S., M.T. (MOP-57795), and M.F.M. (MOP-102536). J.Y. receives funding from a NIH–National Institute of Neurological Disorders and Stroke grant (1R01NS072420-01). F.S., D.R., M.T., and M.F.M. hold Canada Research Chairs (Tier 1) in Structural Principles of Signal Transduction, Canadian Foundation for Innovation, Systems and Synthetic Biology, and Molecular Signatures, respectively. The Structural Genomics Consortium is a registered charity (number 1097737) that receives funds from the Canadian Institutes for Health Research, the Canada Foundation for Innovation, Genome Canada through the Ontario Genomics Institute, GlaxoSmithKline, Karolinska Institutet, the Knut and Alice Wallenberg Foundation, the Ontario Innovation Trust, the Ontario Ministry for Research and Innovation, Merck & Co., the Novartis Research Foundation, the Swedish Agency for Innovation Systems, the Swedish Foundation for Strategic Research, and the Wellcome Trust. The funders had no role in study design, data collection and analysis, decision to publish, or preparation of the manuscript. A.E., G.A., S.D., and S.S.S. designed the study. A.E., A.V., P.G., and L.B. performed phage display selections, protein purification, and in vitro inhibition assays. G.A., A.-M.N., D.N., J.W., Y.-C.J., and S.D. purified proteins used in this study and solved all the crystal structures. J.T. and M.F.M. performed intracellular USP8 inhibition experiments. Y.F., Y.Z., and J.Y. performed intracellular USP21 inhibition experiments. Y.-C.J., M.-C.L., C.Y., E.Z., F.S., L.P., M.T., and D.D. purified proteins used as targets for phage display selections. K.K. and J.M. performed initial intracellular characterizations of Ub variants. A.A.-H. and M.V. performed in vitro enzymatic assays. P.-K.C. and B.R. provided Ub variants expressing stable cell lines and performed mass spectrometry experiments. P.A., A.P., and D.R. performed NEDD4 ubiquitination experiments; A.E. and S.S.S. analyzed data, prepared figures, and wrote the paper. S.S.S., L.B., and A.E. are inventors on a pending patent, "Specific Active Site Inhibitors of Enzymes or Substrate Binding Partners and Methods of Producing the Same" (PCT/US11/39601).

## Supplementary Materials

[www.sciencemag.org/cgi/content/full/science.1230161/DC1](http://www.sciencemag.org/cgi/content/full/science.1230161/DC1)  
Materials and Methods  
Supplementary Text  
Figs. S1 to S7  
Tables S1 to S5  
References (47–69)

13 September 2012; accepted 7 December 2012  
Published online 3 January 2013;  
10.1126/science.1230161



### WORKSTATION

The WS6 downflow workstation is designed especially for histology and pathology laboratory analysis. The compact, versatile design of the WS6 makes a variety of installation formats possible according to individual needs. By drawing contaminated air downward into the stainless steel work surface, the WS6 provides excellent containment of potentially harmful vapors present when cutting or staining samples. Contaminated air is then drawn through a two-stage filter system for maximum fume adsorption. The advanced coconut shell carbon filtration media is designed to adsorb chemical vapors as well as neutralize a wide range of chemicals commonly used in histology and pathology. The open design and downward airflow pattern of the WS6 makes the unit particularly suited for microscopy work, or where close visibility is required. The workstation is ergonomically designed with integral fluorescent lighting to evenly illuminate the entire work surface, providing glare-free viewing, and helping eliminate operator fatigue.

#### MYSTAIRE MISONIX

For info: 919-229-8511 | [www.mystaire.com](http://www.mystaire.com)

### LASER SHUTTERS

SafeClose laser shutters, based on the proven rotor drive actuation technology modified to close on power down. The proprietary Rotor Drive actuator provides a reliable, multimillion-cycle operation and ability to withstand harsh environmental conditions, including wide temperature variations (from  $-40^{\circ}\text{C}$  to  $+70^{\circ}\text{C}$ ), high shock, and vibration in a clean environment. Designed for laser safety and laser switching, the SafeClose shutter was designed to be highly reliable and to always maintain laser safe conditions by closing automatically when power is interrupted. The fail-safe magnetic return mechanism guarantees that the blade will reliably close upon signal interruption. The SafeClose shutter does not require a separate controller and a simple 9V DC signal is sufficient to actuate the shutter and hold it open. With its small diameter/aperture, SafeClose shutters work efficiently with small beam diameter lasers and provided with a standard gold-plated blade design for high laser damage thresholds.

#### CVI MELLES GRIOT

For info: 505-296-9541 | [www.cvimellesgriot.com](http://www.cvimellesgriot.com)

### DIGITAL PCR SYSTEM

The QuantStudio 3D Digital PCR System is a scalable, chip-based instrument that features a simple workflow with minimal hands-on time. Designed with a scalable architecture, the QuantStudio 3D Digital PCR System's first generation chips enable up to 20,000 data points in a single run—coverage that satisfies the needs for most digital polymerase chain reaction (PCR) applications today. The capacity of future chips will increase exponentially to meet increasing demands of the research community. Digital PCR takes researchers beyond the limits of real-time PCR for applications that require absolute quantitation of targeted DNA molecules. Additionally, Life's simple workflow and chip-based platform reduce the risk of sample contamination and loss of DNA normally associated with droplet-based systems. The technology is ideal for accurately detecting rare mutations important in cancer or infectious diseases. It is also increasingly used as a mechanism to perform quality control experiments on next generation sequencing libraries.

#### LIFETECHNOLOGIES

For info: 800-955-6288 | [www.lifetechnologies.com](http://www.lifetechnologies.com)

### CHILLER UNIT

The FlowSyn Polar Bear is a state-of-the-art chiller unit which, in combination with FlowSyn Continuous Flow Reactor, allows users to perform and control reactions down to  $-88^{\circ}\text{C}$ . The FlowSyn Polar Bear is ideal for precooling reagents and controlling temperature in highly exothermic reactions. The system is compatible with the FlowSyn range of reactor modules and is designed to prevent ice formation so that you can clearly observe reactions as they occur. With its fully integrated plug-and-play design, the Polar Bear is both easy to install and simple to operate as well as providing superb cooling performance. The Polar Bear uses advanced cooling technology without the need for solid  $\text{CO}_2$ , solvents, or heat transfer fluids to deliver rapid cooling down to  $-88^{\circ}\text{C}$  at the simple touch of a button. The Polar Bear module is compatible with all Uniqsis coil reactors and mixer blocks and works in combination with and can be controlled by any FlowSyn flow reactor system.

#### UNIQUISIS

For info: +44-(0)-8458-647747 | [www.uniqsis.com](http://www.uniqsis.com)

### COMBUSTION SYSTEM

The Model OFCU-1 from Exeter Analytical provides a safe tool for preparing samples for elemental analysis of halogens, phosphorus, and sulfur using the Oxygen Flask Combustion procedure. The oxygen flask combustion procedure is provided as the preparatory step in the determination of bromine, chlorine, fluorine, iodine, phosphorus, and sulfur in some Pharmacopeial articles. Combustion of the material under test (usually organic) yields water-soluble inorganic products, which may be analyzed for specific elements as directed in the individual Pharmacopeia monograph or general chapter. The oxygen flask combustion procedure using the OFCU-1 can be used for repeatable determination of elemental composition from percentage levels to parts per million. The durably constructed Oxygen Flask Combustion Unit (OFCU-1) copes easily with a wide range of sample types and is very simple to set up, use, and maintain. The OFCU-1 remotely ignites samples inside a safety interlocked chamber using focused infrared heat from two tungsten-halogen lamps.

#### EXETER ANALYTICAL

For info: +44-(0)-2476-323223 | [www.exeteranalytical.co.uk](http://www.exeteranalytical.co.uk)

Electronically submit your new product description or product literature information! Go to [www.sciencemag.org/products/newproducts.dtl](http://www.sciencemag.org/products/newproducts.dtl) for more information. Newly offered instrumentation, apparatus, and laboratory materials of interest to researchers in all disciplines in academic, industrial, and governmental organizations are featured in this space. Emphasis is given to purpose, chief characteristics, and availability of products and materials. Endorsement by Science or AAAS of any products or materials mentioned is not implied. Additional information may be obtained from the manufacturer or supplier.



# 2012 LILIANE BETTENCOURT PRIZE FOR LIFE SCIENCES



**2012 PRIZE WINNERS**  
**CÉDRIC BLANPAIN**

**Cédric Blanpain** is Professor of Stem Cell and Developmental Biology and WELBIO Investigator at the Université Libre de Bruxelles (ULB). He qualified as a Doctor of Medicine at the ULB in 1995 and holds a PhD in Medical Science from the same University. After postdoctoral research at the Rockefeller University in New York, he returned in 2006 to his native Belgium, where he heads his own lab at the Interdisciplinary Research Institute for Human and Molecular Biology.

Cédric Blanpain's work on skin cancer has shown that cancerous tissue may contain stem cells responsible for tumor growth and which may explain resistance to anticancer treatments. He has also demonstrated the existence of two separate populations of mammary stem cells; a paradigm shift with major implications for the understanding of the cellular origin of breast cancer and variations in prognosis. He is currently focusing on a new type of stem cell that contributes to wound healing in the skin epidermis, as well as further investigating the different types of mammary gland stem cells and whether the cancer stem cell mechanisms identified in skin tumors are also present in other cancers.

0102013 / THERA Conseil

The 16<sup>th</sup> Liliane Bettencourt Prize for Life Sciences was awarded to Cédric Blanpain, Professor of Stem Cell and Developmental Biology and WELBIO investigator, at the Interdisciplinary Research Institute of the Université Libre de Bruxelles.

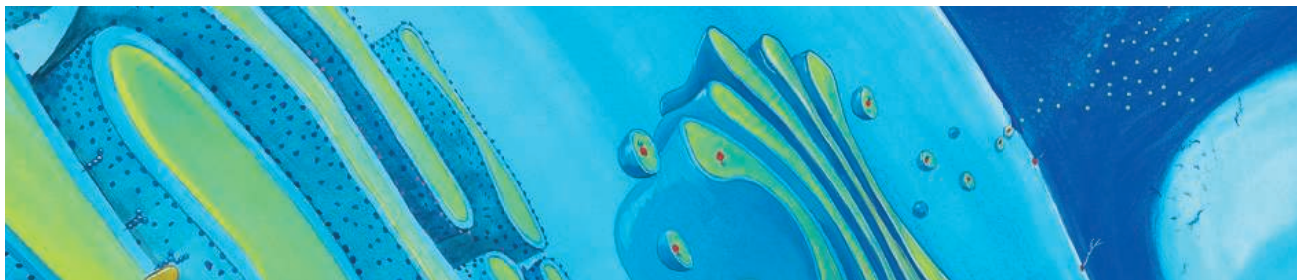
The Liliane Bettencourt Prize for Life Sciences, worth € 250,000, has been awarded every year since 1997 to a European researcher under the age of 45, who is recognised within the scientific community for the quality of his international publications. In addition to his status as an author and leader in his own scientific field, the candidate must be leading a particularly promising research project and have the personal qualities for mobilising an entire team.

Recognised in 1987 as a public interest foundation, the Bettencourt Schueller Foundation was set up by Liliane Bettencourt, in memory of her father Eugène Schueller, a renowned researcher and chemist. Its goal is to constantly expand the boundaries of knowledge in the life sciences in order to improve public health; to reveal talent and pass on expertise within the field of artistic creativity; and to relieve suffering, combat exclusion and respond to social welfare emergencies.



**FONDATION  
BETTENCOURT  
SCHUELLER**

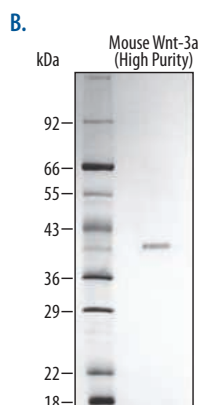
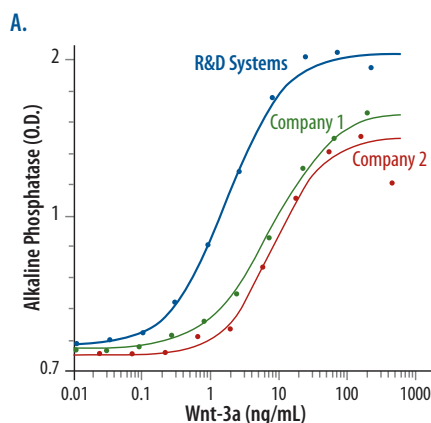
**Bettencourt Schueller Foundation**  
27-29 rue des Poissonniers  
92200 Neuilly-sur-Seine • France  
[www.fondationbs.org](http://www.fondationbs.org)  
Contact : [sciences@fondationbs.org](mailto:sciences@fondationbs.org)



# R&D Systems Cytokines & Growth Factors

## Setting the Standard for the Life Science Industry for over 25 Years

- ✓ R&D Systems currently offers more than 3,000 bioactive recombinant proteins
- ✓ We are the most referenced manufacturer of recombinant & natural proteins
- ✓ Our scientists are dedicated to developing the highest quality products & new processes that meet the needs of researchers  
High purity proteins, traditional & cell culture grade • Animal-free proteins • GMP proteins



**A. Activity Comparison Data for Recombinant Mouse Wnt-3a.** The MC3T3-E1 mouse preosteoblast cell line was treated with increasing concentrations of R&D Systems Recombinant Mouse Wnt-3a (Catalog # 1324-WN) or with mouse Wnt-3a from two other companies. The R&D Systems protein shows greater than a four-fold increase in activity compared to the other commercially available proteins.

**B. SDS-PAGE Analysis of High Purity Recombinant Mouse Wnt-3a.** High Purity Recombinant Mouse Wnt-3a (Catalog # 1324-WNP; 1 µg/lane) was loaded on a 12% SDS-PAGE gel under reducing conditions and visualized by silver staining.

[www.RnDSystems.com/CytokinesGrowthFactors](http://www.RnDSystems.com/CytokinesGrowthFactors)

R&D Systems Tools for Cell Biology Research™

For research use only. Not for use in diagnostic procedures.







## ~ 28<sup>TH</sup> ANNUAL ~ MOLECULAR BIOLOGY SUMMER WORKSHOPS

### Learn Molecular Biology in 2 Weeks!

We are pleased to announce the twenty-eighth annual Molecular Biology Summer Workshops, sponsored by New England Biolabs in conjunction with Smith College. Workshops are held at Ford Hall, Smith College, Northampton, MA, USA. Well over 3,000 people have graduated from this intensive training program in the past twenty-seven years. These intensive courses emphasize hands-on molecular biology laboratory work and cover a wide variety of topics and techniques. This course is the largest and longest running molecular biology course for professionals in the world. No prior experience in molecular biology is required.

#### when:

two-week sessions:

Session 1: June 9 - June 22, 2013

Session 2: July 7 - July 20, 2013

#### where:

Ford Hall

Smith College

Northampton, MA USA 01063

Dr. Steven A. Williams, Director

#### to apply:

website:

<http://www.science.smith.edu/neb>

email:

[biolabs@smith.edu](mailto:biolabs@smith.edu)

phone:

(413) 585-3915

### Two-week Molecular Biology Sessions Available

Both two-week long courses cover in-depth DNA cloning, PCR, DNA sequencing, genomics, next-gen sequencing and bioinformatics. Learn hands-on techniques used in gene expression analysis including microarray analysis, RNAi and quantitative RT-PCR, bioinformatics and genomics and proteomics.

**application information:** No previous experience in molecular biology is required or expected. Forty participants per session will be selected from a variety of disciplines and academic backgrounds, including principal investigators, directors of programs, medical doctors, postdoctoral fellows, graduate students, research assistants, sales associates, equipment engineers, etc.

**fee:** \$4300 per participant. This fee includes lab manual, use of all equipment and supplies, and room and board (all rooms are singles).

**application deadlines:** June 1, 2013 for session 1 and July 1, 2013 for session 2.

First come, first served (apply now!). Late applications will be accepted on a space available basis.

**payment deadline:** Three weeks following receipt of your email acceptance letter.

### topics / techniques:

- gene cloning  
(and library construction)
- gene expression analysis
- PCR and quantitative RT-PCR
- genomics and bioinformatics
- DNA sequencing  
& next-gen sequencing
- RNAi, siRNA and microarrays
- and much more — visit our  
website for a complete list!



# Our lab window.

# Your lab window.

## Space Is Closer Than You Think.

The International Space Station provides research conditions that simply can't be replicated on Earth. CASIS offers cost-effective access to the International Space Station – enabling groundbreaking discoveries and advancements that will give your research a competitive edge.

Access to microgravity, extreme temperature cycling, ultra-vacuum, and much more – in the world's most advanced lab – it's all closer than you think. Visit [iss-casis.org](http://iss-casis.org) to learn more today.





Cambridge Healthtech Institute's Twelfth Annual

# Bio-IT World

## CONFERENCE & EXPO '13

April 9 – 11, 2013 • World Trade Center • Boston, MA



## Register Early for Maximum Savings!

*Enabling Technology. Leveraging Data. Transforming Medicine.*

### CONFERENCE TRACKS:

- 1 IT Infrastructure – Hardware
- 2 Software Development
- 3 Cloud Computing
- 4 Bioinformatics
- 5 Next-Gen Sequencing Informatics
- 6 Systems Pharmacology
- 7 eClinical Trials Solutions
- 8 Data Visualization **NEW!**
- 9 Drug Discovery Informatics
- 10 Clinical Omics **NEW!**
- 11 Collaborations and Open Access Innovations
- 12 Cancer Informatics

### KEYNOTE PRESENTERS:



*Atul Butte, M.D., Ph.D., Division Chief and Associate Professor, Stanford University School of Medicine; Director, Center for Pediatric Bioinformatics, Lucile Packard Children's Hospital; Co-founder, Personalis and Numedi*



*Andrew L. Hopkins, D.Phil, FRSC, FSB, Division of Biological Chemistry and Drug Design, College of Life Sciences, University of Dundee*

### PLENARY SESSION:

#### The Life Sciences CIO Panel

From managing big data and cloud computing capabilities to building virtual communities and optimizing drug development, the life sciences CIO has to be a firefighter, evangelist, visionary. In this special plenary roundtable, Bio-IT World invites a select group of CIOs from big pharma, academia and government to discuss the major issues facing today's biosciences organization and the prospects for future growth and organizational success.

#### Special guests:

*Remy Evard – CIO, Novartis Institutes for BioMedical Research  
Martin Leach – CIO, Broad Institute  
Andrea T. Norris – Director, Center for Information Technology (CIT) and CIO, NIH  
Gunaretnam Rajagopal – CIO, Johnson & Johnson  
Cris Ross – CIO, Mayo Clinic*

Organized by:  
Cambridge Healthtech Institute

Be Sure to Mention Keycode L35  
when Registering

[Bio-ITWorldExpo.com](http://Bio-ITWorldExpo.com)

Produced by the Science/AAAS Custom Publishing Office

Focus on Careers  
Faculty Positions

## Five Steps to a Successful Sabbatical

University life can be a grind of teaching, grant writing, and department politics. But every seven years, faculty members get a magical opportunity that is coveted by nonacademics: sabbatical leave. In this period of career development, a professor might learn new techniques, expand a research program, or finish off that book or pile of languishing manuscripts. The dream starts with meticulous advanced planning, but ends best for those who are adaptable and open-minded. Here are five pointers from professors with recent sabbatical experience.

See full story on page 599.



### Upcoming Features

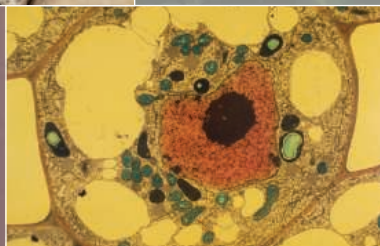
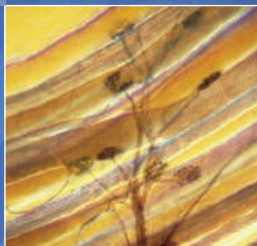
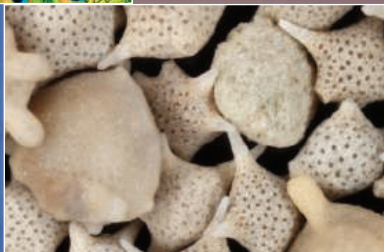
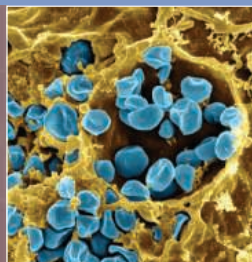
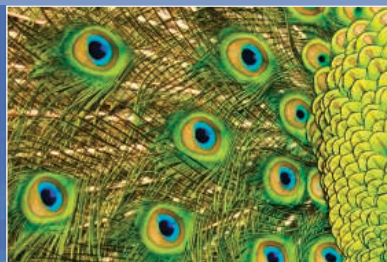
Innovations and Opportunities: India—February 22  
Postdocs: Identifying Opportunities—March 8  
Regional Focus: Germany—March 22

# AAAS|2013 ANNUAL MEETING

14-18 FEBRUARY • BOSTON

## THE BEAUTY AND BENEFITS OF SCIENCE

HYNES CONVENTION CENTER

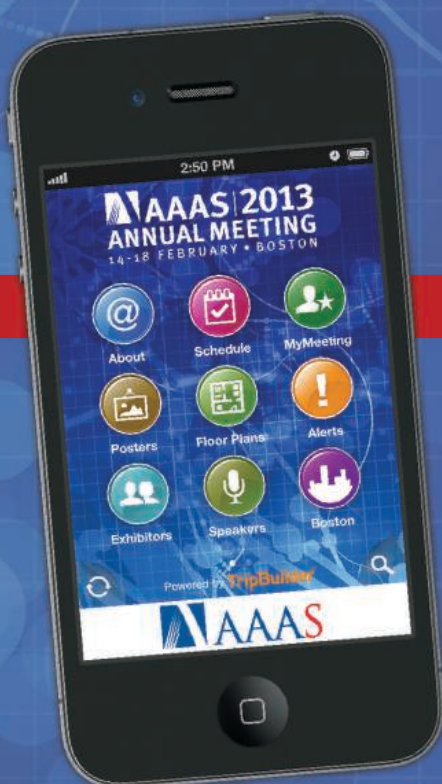


Final reminder to register online before joining us in Boston.

Visit the Annual Meeting website for registration and program information.

See you soon in Boston!

Register at  
[www.aaas.org/meetings](http://www.aaas.org/meetings)



## Connect to the meeting on your mobile device.

[www.aaas.org/go/app](http://www.aaas.org/go/app)

### The 2013 AAAS Annual Meeting app gives you complete access:

Build your itinerary and take it with you.  
Browse sessions, speakers, and maps.  
Be connected...wherever you go.



# WEBINAR

## Advancing Cancer Genomics:

### The Impact of Personalized Genome Sequencing

**MONDAY, FEBRUARY 25, 2013**

**12 noon ET, 9 a.m. PT, 5 p.m. GMT, 6 p.m. CET**

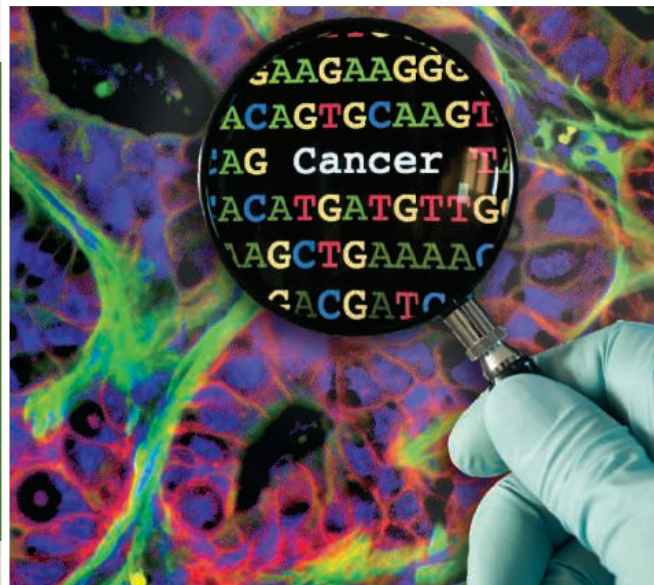
High throughput sequencing technologies have proven to be critical tools in understanding the molecular basis of disease, particularly in oncology. Recent advances have enabled characterization of the genetic mechanisms of cancer, revealing variants associated with novel pathways that determine tumor formation and response to treatment. The clinical potential of sequencing technologies in the diagnosis and treatment of diseases has now been demonstrated, but challenges remain, particularly in sample preparation and data interpretation. In this webinar our expert panel will describe recent discoveries in cancer genomics and inherited diseases, and how these advances are enabling personalized medicine and the individualization of treatment.

#### **During this webinar, viewers will:**

- Gain insight into how mining tumor genomes can lead to better understanding of cancer
- Learn how technologies are being applied to tumor genome analysis
- Improve their understanding of the pain points in genome analysis and how they can be overcome.
- Have the opportunity to ask questions of the expert panel, live!

**REGISTER NOW!**

[webinar.sciencemag.org](http://webinar.sciencemag.org)



#### **SPEAKERS**



**Elaine Mardis, Ph.D.**  
Washington University School  
of Medicine  
St. Louis, MO



**Michael Snyder, Ph.D.**  
Stanford University  
Stanford, CA



**Philip Stephens, Ph.D.**  
Foundation Medicine  
Cambridge, MA

Webinar sponsored by



Brought to you by the  
*Science/AAAS* Custom  
Publishing Office





# Illuminate Cancer Biology

The complexity of cancer systems biology requires innovative tools for interrogating the signaling pathways responsible for oncological transformation.

Promega's integrated tools for reporter gene analysis assure biologically relevant results in cancer research.

# FuGENE® HD

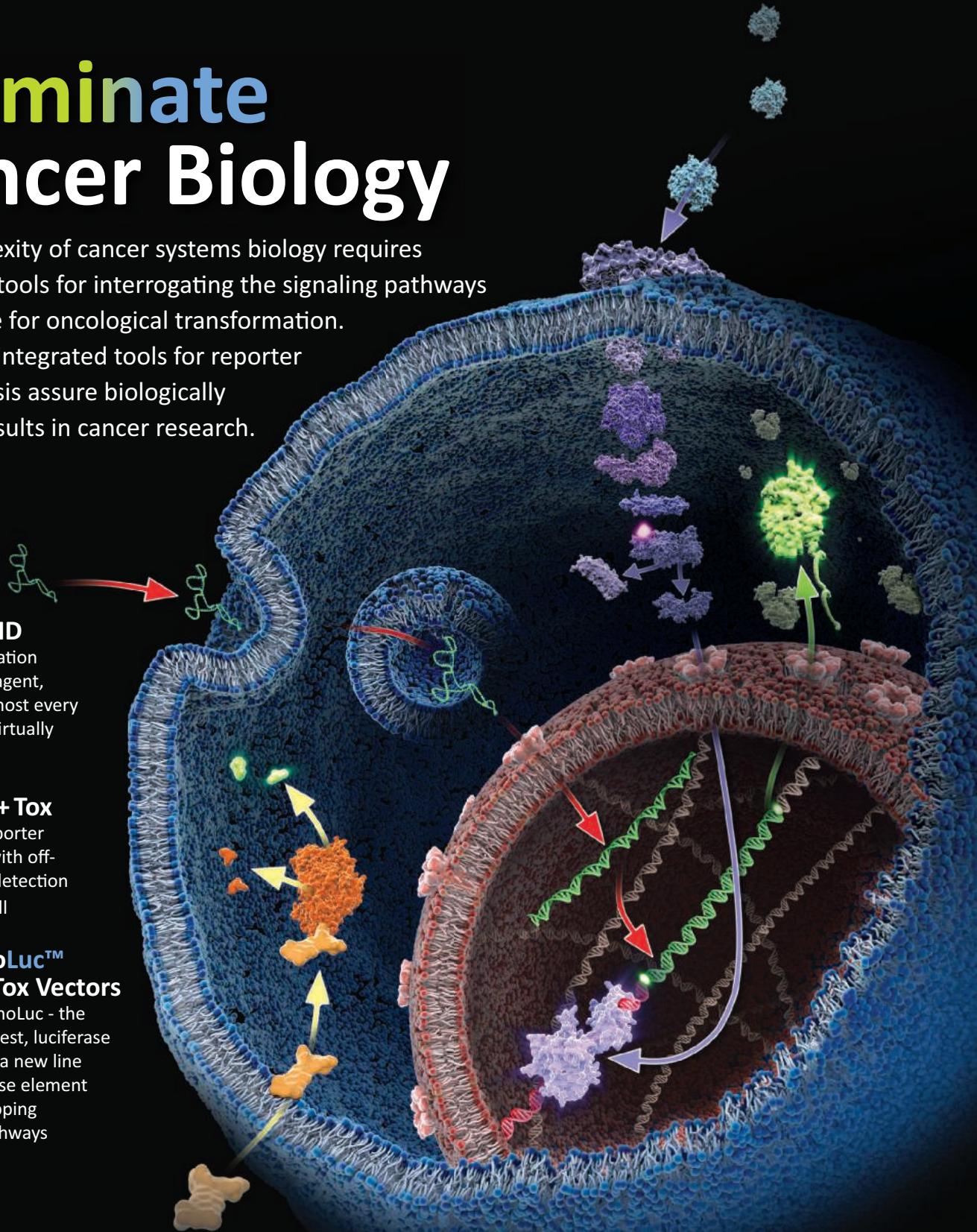
The next generation  
transfection reagent,  
effective on almost every  
cell type with virtually  
no cell toxicity

## ONE-Glo™ + Tox

Multiplexed reporter gene analysis with off-target toxicity detection in the same well

## New! NanoLuc™ and pGL4 Tox Vectors

Introducing NanoLuc - the brightest, smallest, luciferase available - plus a new line of pGL4 response element vectors for mapping oncological pathways



# Promega

**To get a FREE sample of any one of these reagents, visit:**

**[www.promega.com/pathwaybiology](http://www.promega.com/pathwaybiology)**



# *There's only one* GALILEO GALILEI

Born in 1564, Galileo Galilei once contemplated a career in the priesthood. It's perhaps fortunate for science that upon the urging of his father, he instead decided to enroll at the University of Pisa. His career in science began with medicine and from there he subsequently went on to become a philosopher, physicist, mathematician, and astronomer, for which he is perhaps best known. His astronomical observations and subsequent improvements to telescopes built his reputation as a leading scientist of his time, but also led him to probe subject matter counter to prevailing dogma. His expressed views on the Earth's movement around the sun caused him to be declared suspect of heresy, which for some time led to a ban on the reprinting of his works.

Galileo's career changed science for all of us and he was without doubt a leading light in the scientific revolution, which is perhaps why Albert Einstein called him the father of modern science.

Want to challenge the status quo and make the Earth move? At *Science* we are here to help you in your own scientific career with expert career advice, forums, job postings, and more — all for free. For your career in science, there's only one *Science*. Visit [ScienceCareers.org](http://ScienceCareers.org) today.



For your career in science, there's only one **Science**

AAAS

[ScienceCareers.org](http://ScienceCareers.org)

There's only one

**Science**

## Science Careers Advertising

For full advertising details, go to ScienceCareers.org and click For Employers, or call one of our representatives.

### Tracy Holmes

Worldwide Associate Director  
Science Careers  
Phone: +44 (0) 1223 326525

### THE AMERICAS

E-mail: [advertise@sciencecareers.org](mailto:advertise@sciencecareers.org)  
Fax: 202-289-6742

### Tina Burks

East Coast/West Coast/South America  
Phone: 202-326-6577

### Allyson Rosen

Midwest/Canada/Corporate  
Phone: 202-326-6578

### Marci Gallun

Sales Administrator  
Phone: 202-326-6582

### Online Job Posting Questions

Phone: 202-312-6375

### EUROPE/INDIA/AUSTRALIA/ NEW ZEALAND/REST OF WORLD

E-mail: [ads@science-int.co.uk](mailto:ads@science-int.co.uk)  
Fax: +44 (0) 1223 326532

### Lucy Nelson

Phone: +44 (0)1223 326527

### Kelly Grace

Phone: +44 (0) 1223 326528

### JAPAN

### Yuri Kobayashi

Phone: +81-(0)90-9110-1719  
E-mail: [ykobayas@aaas.org](mailto:ykobayas@aaas.org)

### CHINA/KOREA/SINGAPORE/ TAIWAN/THAILAND

### Ruolei Wu

Phone: +86-1367-1015-294  
E-mail: [rwu@aaas.org](mailto:rwu@aaas.org)

All ads submitted for publication must comply with applicable U.S. and non-U.S. laws. Science reserves the right to refuse any advertisement at its sole discretion for any reason, including without limitation for offensive language or inappropriate content, and all advertising is subject to publisher approval. Science encourages our readers to alert us to any ads that they feel may be discriminatory or offensive.

**Science Careers**From the journal *Science*

ScienceCareers.org

## FOOD ALLERGY RISK ASSESSMENT SPECIALIST ASSISTANT PROFESSOR

The Department of Food Science and Technology, University of Nebraska – Lincoln is seeking applicants for a 9-month, tenure-track Food Allergy Risk Assessment Specialist faculty position. The successful candidate will be one of four faculty involved in the world-renowned Food Allergy Research & Resource Program (FARRP), a food industry-funded consortium with more than 70 member companies. The candidate will be expected to develop and lead a food allergy research team on the development and application of quantitative risk assessment approaches related to food allergen residues. This will include assembling critical input information for risk assessments by conducting and coordinating research on the threshold levels for food-allergic individuals, the consumption patterns of food-allergic individuals, and the distribution of allergen residue levels in various food product categories. The candidate will also contribute to existing national and international extension efforts assisting food and related industries in the quantitative assessment of food allergen risks, implementation of allergen control programs, and application of appropriate sanitation approaches. The candidate will also provide training in the use of analytical systems for detection of allergen residues using individual consultations, seminars, workshops, webinars, and on-site and distance education approaches. The position will have a teaching component through regular and distance learning approaches. The appointment split will be 50% research, 40% Extension, and 10% teaching.

Additional opportunities are available through FARRP's existing worldwide network of clinical, biochemical, risk assessment, and applied research and outreach collaborators in the U.S., Canada, Europe, and Australia. A candidate with the ability to expand those collaborations is sought. National and international travel is integral to this position. Collaborative opportunities also exist at UNL especially with faculty in the Department of Statistics where a courtesy appointment is available to an interested and capable candidate. The Department of Food Science and Technology is housed in a modern, well-equipped facility.

Applicants must have a Ph.D. or equivalent in food science, statistics, toxicology, immunology or a related field and experience related to chemical and/or food-related risk assessment. Experience related to allergenic foods is preferred but not required. Experience interacting with food and related industries is preferred but not required. Excellent verbal and written communication skills are also required.

For further details and to apply for this position visit <http://employment.unl.edu>, REQUISITION NUMBER 130008. Complete the Faculty/Administrative form and attach a Curriculum Vitae, the names and contact information of three (3) references and a Letter of Application that includes a two page description of your proposed research program, a one page description of your vision for Extension efforts related to food allergies and risk assessment together with a brief statement of your experiences interacting with the food industry. Letters from your three references must be sent to Sara Weixelman, University of Nebraska – Lincoln, 221 Chase Hall, Lincoln, NE 68583-0726 and must be received no later than March 10, 2013. Application review will begin on March 15, 2013 and continue until the position is filled.

*The University of Nebraska has an active National Science Foundation ADVANCE gender equity program, and is committed to a pluralistic campus community through affirmative action, equal opportunity, work-life balance, and dual careers.*


**DALHOUSIE  
UNIVERSITY**
*Inspiring Minds*

## Neural Circuits Underlying Movement Assistant Professor Dalhousie University Department of Medical Neuroscience Halifax, Nova Scotia, Canada

The Department of Medical Neuroscience at Dalhousie University invites applications to fill a probationary tenure-track position at the rank of Assistant Professor. Applicants must hold a PhD or MD degree or the equivalent, with a minimum of three years postdoctoral training in biomedical sciences. The successful candidate will be expected to establish a research program in the development or function of neural circuits underlying movement. The candidate will join a dynamic group of neuroscientists in the Life Sciences Research Institute, studying the development, physiology, and pathophysiology of motor system circuitry. This group forms the core of the Atlantic Mobility Action Project ([www.amap.ca](http://www.amap.ca)), which undertakes a combination of basic and clinical neuroscience research and is part of an interdisciplinary neuroscience community at Dalhousie University. Outstanding core facilities available within the Faculty of Medicine include: Cellular and Molecular Digital Imaging, Proteomics, Maritime Brain Tissue Bank, Gene Analysis, Flow Cytometry, a new Animal Facility, and a Zebrafish Facility ([research.medicine.dal.ca/core.htm](http://research.medicine.dal.ca/core.htm)).

Salary will be commensurate with qualifications and experience. The candidate will be expected to compete for external research and salary support, supervise graduate students, and contribute to the teaching activities of the Department. We are committed to the success of our faculty members and provide modern laboratory space, startup funds, and mentorship. Further information concerning the members of the Department may be obtained by consulting our website ([www.medical-neuroscience.medicine.dal.ca](http://www.medical-neuroscience.medicine.dal.ca)). Dalhousie University is located in the historic port city of Halifax, with excellent recreational, cultural, and lifestyle opportunities ([www.halifax.ca/visitors.asp](http://www.halifax.ca/visitors.asp)).

Applicants should submit a *curriculum vitae*, a brief statement of research plans, teaching goals/interests and should arrange to have three letters of reference sent under separate cover to: **Search Committee, Department of Medical Neuroscience, Faculty of Medicine, 5850 College St., PO Box 15000, Sir Charles Tupper Medical Building, Dalhousie University, Halifax, Nova Scotia B3H 4R2 Canada.** Closing date for receipt of applications is April 1, 2013. Starting date is negotiable, however it is intended that the position will be filled by September 1, 2013.

*All qualified applicants are encouraged to apply; however, Canadians and permanent residents will be given priority. Dalhousie University is an Employment Equity/Affirmative Action Employer. The University encourages applications from qualified Aboriginal people, persons with a disability, racially visible persons, and women.*



# Five Steps to a Successful Sabbatical

University life can be a grind of teaching, grant writing, and department politics. But every seven years, faculty members get a magical opportunity that is coveted by nonacademics: sabbatical leave. In this period of career development, a professor might learn new techniques, expand a research program, or finish off that book or pile of languishing manuscripts. The dream starts with meticulous advanced planning, but ends best for those who are adaptable and open-minded. Here are five pointers from professors with recent sabbatical experience. **By Chris Tachibana**



## Go For It

A sabbatical leave can mean interrupting your research, getting paid less, and disrupting family life. But ask professors if their sabbatical was worth the effort and they answer with one voice: yes. Go all the way, they say. Take a full year and go to a new city or country, if you can.

Why? New environments, fresh perspectives, and unfamiliar routines boost your creativity. **Robert Austin** offers personal and empirical evidence. In 10 years he has held faculty positions at Harvard and Copenhagen Business Schools, and is now dean of business administration at the University of New Brunswick, Canada. He says, “Being out of your ordinary surroundings makes you establish new relationships and collaborations and lets you present your ideas in a different context.” People in other countries or even other institutes view your work from a different perspective, informed by the prevailing models and cultures of their region, he says. “They give you reactions and feedback that are different from your colleagues at home.” Austin’s research shows that groundbreaking ideas can develop when unexpected events—accidents—happen to people with the expertise to recognize potential innovations. Being in a new situation invites these serendipitous events.

## Get Away (At Least Mentally)

A sabbatical can be revitalizing. A 2010 study ([www.ncbi.nlm.nih.gov/pubmed/20718526](http://www.ncbi.nlm.nih.gov/pubmed/20718526)) compared faculty members at 10 universities in Israel, New Zealand, and the United States who did and did not take sabbatical leave. People who had a sabbatical had better self-reported scores for life satisfaction, stress, and other measures of well-being than those who did not. The secret to achieving benefits was detachment: escaping the usual routine and being left alone by the home institution.

“The trick to a sabbatical is getting away from things that you find

stressful,” says **Paul Spector**, professor of organizational psychology at the University of South Florida, and an author on the study. “Don’t just do the same work somewhere else.” At the University of New Brunswick, Austin advises his own faculty members to leave campus for their sabbaticals, “although I say this at some risk as a dean, because they might not come back.”

People with children and working spouses might find this advice impractical, but **Glenn Starkman**’s entire family came along on his sabbatical. He is a professor of physics and astronomy at Case Western Reserve University, currently working at CERN in Switzerland, site of the Large Hadron Collider. The family knew about life abroad from earlier years at Oxford and CERN, and Starkman said they thought carefully about how to get the most out of their opportunity. His wife, Debby Rosenthal, is a literature professor who planned a sabbatical at the same time. They lured their teenage children with promises of the world’s best cheese and chocolate, and the chance to experience a different culture and language but attend school in English. Fortunately, CERN contributes to tuition at an international school, which Starkman says “brings the cost [down] to merely expensive.” Planning a sabbatical abroad takes time. Especially if you are taking your family, says Starkman, expect two rather unproductive transition months. The payoff? “You’ll gain nine or 10 very productive months, and it’ll all be worth it.” **continued>**

“You’ll gain nine or 10 very productive months, and it’ll all be worth it.”

—Glenn Starkman

Paul Spector



Michal Feldman



## Upcoming Features

Innovations and Opportunities: India—February 22  
Postdocs: Identifying Opportunities—March 8  
Regional Focus: Germany—March 22

Paul Spector took his own advice about getting away when he took a sabbatical without leaving town. “I had a young kid, so I stayed home for eight months and worked. I didn’t go to the office, I told my colleagues I’d be away, and they left me alone.” Spector told his graduate students in advance to not schedule their defense during his sabbatical. He used his time for professional development that he had been putting off. “I spent a week learning about logistic regression,” he says, “because it was something I wanted to learn but never had time before. I had a great eight months and came back recharged.”

### Start Planning, Now

Reconfiguring a professional and personal life takes serious planning. Sabbaticalhomes.com can help with relocation. Meet with your university’s human resources department to find out how a leave will affect paychecks, taxes, and benefits, advises a blog at The Chronicle of Higher Education ([chronicle.com/blogs/profhacker/author/nhighberg](http://chronicle.com/blogs/profhacker/author/nhighberg)). Since many universities reduce salary during sabbaticals, look for funding opportunities, but start early. Applications for government and foundation grants such as Fulbright or Guggenheim fellowships are due more than a year before funding starts. Finally, tell your institution what other resources you need. Universities realize that sabbaticals promote recruitment and retention, so they want to help.

The University of North Carolina (UNC) Department of Medicine gave **Michael Pignone**, chief of general internal medicine, a physician’s assistant to support his six-month visit to the University of Sydney, Australia in 2010. After working alongside Pignone for several months, the assistant managed Pignone’s primary care patients while he was gone. Pignone’s sabbatical project was part of a five-year National Institutes of Health (NIH) Established Investigator grant and was also funded by an Australian-American Health Policy fellowship. Pignone says the formal applications made him start thinking about his sabbatical about three years in advance. “They forced me to plan ahead, and I’m glad I did that,” he says. He arranged his administrative and mentoring responsibilities to avoid major decisions, grants, or activities while he was away.

Pignone’s school-age children and his wife Lisa Fail, who could work remotely, went along and had a great time. He says going to an English-speaking country and returning in June, as summer vacation was starting, made the transition easier for his family. If you’re making the effort to go to another country, consider a full year, he says, because “honestly, six months went by pretty fast.”

Professors at small colleges can also get NIH support through the Academic Research Enhancement Award (AREA, or R15) program, which supports biomedical and behavioral sciences research at educational institutions that do not have large NIH grants. National Science Foundation funding is another option. **Rebecca Whelan**, a newly tenured chemistry/biochemistry associate professor at Oberlin College in Ohio, which has 3,000 undergraduates, received an R15 grant for her sabbatical. Whelan is developing new cancer tests based on synthetic



“Being out of your ordinary surroundings makes you establish new relationships and collaborations and lets you present your ideas in a different context.”

—Robert Austin

DNA molecules that bind to a specific target. To develop the assays, she needed two resources not available at Oberlin: specific ovarian cancer cell lines and a flow cytometer to test binding to the cells. “Flow cytometry is the type of technology that requires a core facility,” says Whelan. “It’s just not something we have at Oberlin.”

Detailed, advanced planning drove the success of Whelan’s sabbatical. She had to develop her idea, line up a host lab, and submit a grant proposal in time to receive funding during her planned leave. Her advice: “Begin thinking strategically two or three years ahead to get funding and establish a relationship with the lab where you’ll spend your sabbatical.”

To find a host lab, Whelan cold-called (or rather, e-mailed) a researcher she cited often in her publications but hadn’t met. Manish Patankar, associate professor of obstetrics and gynecology at University of Wisconsin-Madison said Whelan’s sabbatical proposal caught his eye because it was clear, complete, and within the scope of his main research program, but with a different angle and a new approach. It was the beginning of a fruitful collaboration. Back in her Oberlin lab, Whelan has enthusiastic undergraduates advancing the project and continues working with Patankar. “We’re writing a manuscript with one or two in the pipeline,” she says, “and we’re working on getting Oberlin students to the University of Wisconsin for a summer.” Patankar urges professors at large universities to consider sabbatical requests from motivated researchers from small colleges. He says, “A place like

Oberlin is small only in terms of student population. They have some really nice resources and research.”

Both Whelan and Pignone reiterate the importance of getting away. “Most of us are conscientious and want to participate in our department, so we’ll always be pulled back,” says Whelan. But she recommends protecting your time and setting a high threshold for participating in meetings. “I did a phone conference for a tenure case in our department, but I let all the other stuff slide by,” she says. “You don’t have to physically get away, but you must get away mentally.” If you think you could be persuaded to return to your home institution, make it hard to travel back. Pignone said being in Australia, nearly a full day’s travel from North Carolina, was an advantage. Flying back was simply impractical.

If you are in the European Union or an associated country or arranging a sabbatical there, Marie Curie Actions offer a variety of fellowship opportunities. Although known as an excellent source of postdoctoral funding, the fellowships can also support established investigators as visiting scientists. **Michal Feldman**, an associate professor at the Hebrew University of Jerusalem, is visiting the Harvard School of Engineering and Applied Sciences on a Curie grant. She offers this advice: The application for her International Outgoing Fellowship was complex, she says, so plan ahead. You’ll need details about your research plan, your collaborative arrangement, and the facilities at the institute you will be visiting. In addition, you must describe the larger goals of your fellowship and how you intend to achieve them. The application requires a complete description **continued**



Department of Health and Human Services  
National Institutes of Health  
Center for Human Immunology, Autoimmunity, and Inflammation  
Division of Intramural Research

**STAFF SCIENTIST/LAB LEADER**

The NIH Center for Human Immunology, Autoimmunity and Inflammation (CHI) is a trans-NIH initiative that studies the human immune system in health and disease using high-throughput multi-dimensional assays, and then integrating the dense data sets using advanced computational approaches. The Staff Scientist/Lab Leader position is located in CHI's Genomics Laboratory, and leads a group of 3 who perform the work of the laboratory. Responsibilities include: gene expression profiling, miR profiling, SNP scan, next generation sequencing, and biomarker validation using cutting edge technologies and instruments for clinical samples, and generating metadata spread sheets for data analysis; clinical sample processing and preservation (up to 40 samples/day for both serum and cells, hundreds of samples/ year), biorepository inventory, sample tracking, and distribution; development of SOP's and experimental QC; maintenance of lab instruments; training research fellows, lab technicians and collaborators in new technologies; working a flexible schedule as dictated by clinical protocols.

The selected individual will have the following qualifications: M.D. or Ph.D. in a life sciences-related discipline, M.D./Ph. D. or M.D./M.S. preferred; minimum of 8 years experience in life sciences research, and more than 5 years hands on experience in biomedical research utilizing multiple high throughput technologies, with multidimensional data collection and analysis; extensive experience and capability in adapting new technologies and platform validation; experience and skill in gene expression profiling, micro RNA profiling, genome wide SNP scan, and next generation sequencing (NGS); demonstrated ability to integrate processing of high volume of clinical samples while also carrying out high throughput technologies, daily lab multitasking activity, instrument monitoring, and prioritization based on scientific need; the focus and organization to consistently produce research data of the highest quality; upbeat personality and ability to be a team player; track record of training research fellows, lab technicians and collaborator in new technologies.

The position is **not** for a candidate who is seeking an independent research position.

**How to Apply:** The successful candidate will be offered salary and benefits commensurate with experience and accomplishments. The appointment would be through the Title 42 mechanism. Applicants may be U.S. Citizens, resident aliens, or non-resident aliens holding or eligible for a valid employment visa. Applications must be received within one month of the date of publication of this ad. Please submit a curriculum vitae and brief statement of how your experience relates to the needed qualifications along with 3 letters of reference to: **Neal S. Young, M.D. Director CHI c/o Christen Sandoval Building 15F2 MSC 2664 NIH Bethesda MD 20892**, or electronically to **christen.sandoval@nih.gov**

*The NIH is dedicated to building a diverse community in its training and employment programs.  
DHHS, NIH, and the NHLBI are Equal Opportunity Employers.*



**Genomic Regulatory Systems  
Biology - Faculty Position**

The California Institute of Technology invites applications for a tenure-track junior faculty position in the Division of Biology. Relevant experimental research areas include systems biology approaches to gene regulatory circuits; evolution of gene regulatory networks; design principles in gene regulatory circuits; genomics oriented, quantitative exploration of less understood aspects of gene regulatory systems such as cis-regulatory module choice, molecular biology of enhancer function, mechanisms of enhancer-promoter interaction.

Candidates with strong commitments to research and teaching excellence are encouraged to apply. Initial appointments at the assistant professor level are for four years, and are contingent upon completion of the Ph.D. degree.

Please submit on-line application at: **http://biology.caltech.edu/Positions**, and include a brief cover letter; curriculum vitae; relevant publications, a description of proposed research; and a statement of teaching interests. Applicants should arrange to have four reference letters uploaded. Application review will commence immediately and continue until **March 15, 2013**.

*The California Institute of Technology is an Equal Opportunity/Affirmative Action Employer. Women, minorities, veterans, and disabled persons are encouraged to apply.*



Eidgenössische Technische Hochschule Zürich  
Swiss Federal Institute of Technology Zurich

**Assistant Professor (Tenure Track)  
of Environmental Microbiology**

The Department of Environmental Systems Science ([www.usys.ethz.ch](http://www.usys.ethz.ch)) at ETH Zurich invites applications for an Assistant Professorship (Tenure Track) in Environmental Microbiology.

Candidates with outstanding scientific track records in any related field will be considered, but preference is given to applicants working on microbial processes in environmental systems. The new Professor should establish a world-class research group and integrate into research activities in related fields at ETH Zurich. In addition, he or she should contribute to the teaching of undergraduate level courses (German or English) and graduate level courses (English) for students of Environmental Science and Biology. The Professorship will be equipped with a generous personnel and operational budget, but it will be expected to attract further funds for research through competitive grants.

The appointment is expected to be made at the Assistant Professor level. Assistant Professorships have been established to promote the careers of younger scientists. The initial appointment is for four years with the possibility of renewal for an additional two-year period and promotion to a permanent position.

Your application should include your curriculum vitae, a list of refereed publications as well as a statement of your research and teaching interests. The letter of application should be addressed to the **President of ETH Zurich, Prof. Dr. Ralph Eichler**. **The closing date for applications is 30 April 2013**. ETH Zurich is an equal opportunity and affirmative action employer. In order to increase the number of women in leading academic positions, we specifically encourage women to apply. ETH Zurich is further responsive to the needs of dual career couples and qualifies as a family friendly employer. **Please apply online at [www.facultyaffairs.ethz.ch](http://www.facultyaffairs.ethz.ch).**

Featured Participants	Additional Resources
<b>Case Western Reserve University</b> case.edu	<b>Australian-American Health Policy Fellowship-</b> www.commonwealthfund.org/Fellowships/Australian-American-Health-Policy-Fellowships.aspx
<b>CERN</b> cern.ch	
<b>Harvard School of Engineering and Applied Science</b> seas.harvard.edu	<b>Fulbright Program</b> www.cies.org/Fulbright
<b>Hebrew University of Jerusalem</b> huji.ac.il/huji/eng	<b>Guggenheim Foundation</b> www.gf.org
<b>Oberlin College</b> oberlin.edu	<b>Marie Curie Actions</b> ec.europa.eu/research/mariecurieactions/index_en.htm
<b>University of New Brunswick</b> unb.ca	<b>National Institutes of Health</b> grants.nih.gov
<b>University of North Carolina</b> unc.edu	<b>National Science Foundation</b> www.nsf.gov
<b>University of South Florida</b> usf.edu	<b>Nels Highberg sabbatical blog</b> chronicle.com/blogs/profhacker/author/nhighberg
<b>University of Sydney</b> sydney.edu.au	<b>Sabbatical Homes</b> sabbaticalhomes.com
<b>University of Wisconsin-Madison</b> wisc.edu	

of your collaborator's research and mentoring achievements, so Feldman says, "work with someone who is well respected in the field."

## Expect the Unexpected

From the other side of their sabbatical, professors say that although some people accomplish everything they propose—developing methods, publishing manuscripts, and writing books—many find that their plan simply isn't feasible. Be flexible and be ready to change the project if necessary, or even better, if something more interesting comes along. University of New Brunswick's Robert Austin says, "It's exceeding unlikely that your sabbatical project will proceed exactly as planned, but be open-minded and you'll see opportunities for collaborations and other sources of value that you didn't see going into your sabbatical."

Even Whelan, whose project went as planned, had unexpected scientific benefits from working at a new institution. After a colleague mentioned the university's high throughput sequencing equipment, she used the facilities to enhance her research by characterizing the most successful DNA molecules from her screen. Some professors advise building flexibility into a research plan from the start. Propose a practical project that you know you can accomplish, to ensure that you get something done, but also work on something risky—that's the point of a sabbatical.

## Can't Do It? Let Them Come To You

If you simply can't get away, consider hosting a sabbatical professor. Manish Patankar, Whelan's host at the University of Wisconsin-Madison, didn't take a sabbatical when he earned tenure a few years ago, but says his research program benefited when a sabbatical came to him in the form of Whelan's visit. "She brought in skills and techniques we didn't have in the lab," he says. Whelan's analytical chemistry background unexpectedly came in handy when she performed gas chromatography analysis on anticancer compounds the Patankar lab is exploring. Says Patankar, "You never know where things will go."

The positive effects of a visiting scientist can ripple beyond your research group. **Lyndal Trevena**, an associate professor at the Sydney school of public health, University of Sydney, hosted Pignone on his sabbatical leave from UNC, and says his work had national impact. Pignone and his Sydney colleagues did a cost-effectiveness study on colorectal cancer screening in Australia. Trevena says that being on sabbatical, without teaching and administrative duties, meant Pignone could focus intensely on the project, including traveling to the capital of Canberra to talk to people in the government. Being an outside expert also gave extra weight to his perspective. All this raised the profile of their work, says Trevena. "The study has really been influential for advancing a program for colorectal cancer screening in Australia," she says.

One of the study coauthors was Professor **Kirsten Howard**. Before Pignone arrived in her department, she knew of his work, but had never met him. Howard and Pignone quickly discovered common interests in shared decision-making—studying how patients and physicians can cooperatively make informed health care decisions. They now make up a forceful collaborative team, with Pignone contributing clinical expertise and Howard developing the health economics methods for two projects funded by grants they applied for while Pignone was in Australia. Howard's department supported her own sabbatical the next year to UNC. To encourage the type of informal interactions that can develop into new scientific partnerships, Howard suggests integrating visiting scientists as much as possible into the department. She says, "Attending seminars, research presentations, and student talks creates chance encounters and conversations that can lead to spin-off collaborations and new research directions."

Trevena recommends hosting a sabbatical professor whose work fits well with your research program. Then, make the most of every minute. The visit goes by quickly, she says, so squeeze as much time as possible with your visitor into your already busy schedule. She says, "You'll see that you can really do some meaty, productive work in that time and cement a collaboration."

*Chris Tachibana is a science writer based in Seattle, USA, and Copenhagen, Denmark.*

DOI: 10.1126/science.opms.r1300127

**“Attending seminars, research presentations, and student talks creates chance encounters and conversations that can lead to spin-off collaborations and new research directions.”**

**—Kirsten Howard**





The University of Texas Health Science Center at Tyler invites applications from an extramurally funded, outstanding investigator to serve as **Chairman of Infectious Lung Diseases**. The candidate should have a track record of successful research and extramural funding, and will oversee faculty members who are working on tuberculosis and influenza. Resources to support this recruitment include ample laboratory space, all necessary equipment, an endowment and unique UT System resources.

Tyler is located midway between Dallas and Shreveport amidst the picturesque lakes and piney woods of East Texas. The Department of Infectious Lung Disease is part of the Center for Biomedical Research, which focuses on lung injury, coagulation and oncology, as well as pulmonary infectious diseases. A description of current faculty research interests can be found online at UTHSCT's website <http://www.uthct.edu/Research>.

Associate and Full Professor level candidates will be considered. Applicants should submit their *curriculum vitae*, a statement of future research plans and the names of three references to: **Dr. Anna Kurdowska, Faculty Search Committee Chair, University of Texas Health Science Center at Tyler, 11937 US Highway 271, Tyler, Texas 75708-3154**, or by email to [anna.kurdowska@uthct.edu](mailto:anna.kurdowska@uthct.edu).

**UTHSCT** is an EEO/AA Employer M/F/V/D. This position is security sensitive and subject to Texas Education Code 51.215 which authorizes the employer to obtain criminal history information.



The University of Texas Health Science Center at Tyler invites applications from outstanding scientists for state-funded faculty positions at all levels. Tyler is located midway between Dallas and Shreveport amidst the picturesque lakes, hills and forests of East Texas. The mission of the basic and clinical research at the UT Health Science Center focuses on **lung injury/repair and therapeutics, pulmonary infectious diseases, and oncology**. Applicants in these and related fields are welcome. **A strong track record of scientific accomplishment and current extramural funding are required.**

A complete listing and description of current faculty research interests can be found online via UTHSCT's website <http://www.uthct.edu/Research>. The successful candidate will bring or establish a dynamic independent research program in a discipline related to the mission of UTHSCT. Teaching in the biotechnology graduate program is encouraged but commensurate with committed research time. Our institution is growing and substantive resources are being allocated to build its translational research portfolio.

Applicants should submit their *curriculum vitae*, a statement of future research plans and the names of three references to: **Dr. Anna Kurdowska, Faculty Search Committee Chair, University of Texas Health Science Center at Tyler, 11937 US Highway 271, Tyler, Texas 75708-3154**, or by email to [anna.kurdowska@uthct.edu](mailto:anna.kurdowska@uthct.edu).

**UTHSCT** is an EEO/AA Employer M/F/V/D. This position is security sensitive and subject to Texas Education Code 51.215 which authorizes the employer to obtain criminal history information.



#### TEMASEK RESEARCH FELLOWSHIP (TRF)

A globally connected cosmopolitan city, Singapore provides a supportive environment for a vibrant research culture. Its universities Nanyang Technological University (NTU), National University of Singapore (NUS) and Singapore University of Technology and Design (SUTD) invite outstanding young researchers to apply for the prestigious TRF awards.

Under the TRF scheme, selected young researchers with a PhD degree have an opportunity to conduct and lead defence-related research. It offers:

- A 3-year research grant of up to S\$1 million commensurate with the scope of work, with an option to extend for another 3 years
- Postdoctoral or tenure-track appointment (eligibility for tenure-track will be determined by the university)
- Attractive and competitive remuneration

Fellows may lead, conduct research and publish in these areas:

- Advanced Materials for Aerospace Applications
- Bio-mimetic Aerodynamics
- Cognitive Science and Neuroengineering
- Cyber Security
- High Power Laser Diode
- High Speed High Voltage Switching Devices

For more information and application procedure, please visit:

NTU – [http://www3.ntu.edu.sg/trf/index\\_trf.html](http://www3.ntu.edu.sg/trf/index_trf.html)  
NUS – <http://www.nus.edu.sg/dpr/funding/trf.html>  
SUTD – <http://www.sutd.edu.sg/trf>

**Closing date: 15 March 2013 (Friday)**

Shortlisted candidates will be invited to Singapore to present their research plans, meet local researchers and identify potential collaborators in July 2013.



The University of Texas Health Science Center at Tyler invites applications from extramurally funded, outstanding scientist/administrators to serve as **Chair of Oncology Research**. Administrative experience required. Administrative responsibilities include overall leadership and professional mentorship of faculty within the department. Track record of successful research and current extramural funding required. Resources to support this recruitment include ample laboratory space, additional faculty positions to support growth of research programs and unique UT System resources.

Tyler is located midway between Dallas and Shreveport amidst the picturesque lakes and piney woods of East Texas. A new \$40 million academic building housing the Oncology Program opened in November 2011. A complete listing and description of current faculty research interests can be found online via UTHSCT's website <http://www.uthct.edu/Research>.

The successful candidate will bring or a dynamic independent research program in **oncology**. Essential functions include: promoting research excellence and productivity, supporting education and training, and advancing community outreach. Associate and Full Professor level candidates will be considered.

Applicants should submit their *curriculum vitae*, a statement of future administrative and research plans and the names of three references to: **Dr. Anna Kurdowska, Faculty Search Committee Chair, University of Texas Health Science Center at Tyler, 11937 US Highway 271, Tyler, Texas 75708-3154**, or by email to [anna.kurdowska@uthct.edu](mailto:anna.kurdowska@uthct.edu).

**UTHSCT** is an EEO/AA Employer M/F/V/D. This position is security sensitive and subject to Texas Education Code 51.215 which authorizes the employer to obtain criminal history information.

## THE GEORGE WASHINGTON UNIVERSITY

WASHINGTON DC

### Medical Educator Physiology/Pharmacology

The Department of Pharmacology and Physiology at The George Washington University School of Medicine and Health Sciences invites applications for a full-time non-tenured faculty teaching position at the Assistant or Associate Professor level. The successful candidate will teach Physiology/Pharmacology courses to medical and health science students. Courses are team-taught with a strong clinical emphasis; the candidate will become course director for one or more of these courses.

**Basic qualifications:** a Ph.D. in physiology, pharmacology or related discipline and/or an M.D. Strong teaching credentials as evidenced by teaching evaluations and experience in teaching physiology, pharmacology or a related discipline.

**Application process:** Please complete an online faculty application at <http://www.gwu.jobs/postings/13282> and upload curriculum vitae, a letter of introduction describing relevant teaching experience. Only completed applications will be considered. Review of applications will begin **March 1, 2013** and continue until the position is filled.

*The George Washington University is an Equal Opportunity/  
Affirmative Action Employer.*

## THE GEORGE WASHINGTON UNIVERSITY

WASHINGTON DC

### Senior Faculty Position in Molecular Cancer Biology The George Washington University School of Medicine and Health Sciences

The Department of Biochemistry and Molecular Biology at The George Washington University School of Medicine and Health Sciences invites application for a tenured Associate or Full Professorship. We seek an outstanding scientist with an innovative research program in cancer.

**Basic Qualifications:** Applicants must hold a Ph.D. and/or M.D. degree in appropriate discipline and shall have an established research program supported by extramural funding.

Current cancer strengths of the department include phenotypic signaling, epigenetic control, DNA damage, NO signaling, and cancer genomic and bioinformatics. The School of Medicine and Health Sciences is located on Foggy Bottom campus of GWU. The presence of basic and applied science departments and the proximity of the NIH, Children's National Research Institute and other medical centers in the area, offer ample opportunities for collaboration.

**Application process:** George Washington University will provide a competitive start-up package to successful candidates. Interested applicants must complete an online faculty application at <http://www.gwu.jobs/postings/13422> and upload a complete CV and a statement of current and future research interests. Review of applications will begin on **March 3, 2013** and continue until the position has been filled. Only complete applications will be considered.

*The George Washington University is an Affirmative Action/Equal  
Opportunity Employer.*

## UAB THE UNIVERSITY OF ALABAMA AT BIRMINGHAM

### Faculty Positions in Microbiology

The Department of Microbiology is expanding its research program by inviting applications for multiple **tenure track/tenured faculty positions** on any level. Successful candidates will have demonstrated records of originality and productivity in research in microbial sciences. UAB Microbiology is a national leader in NIH research funding and offers a uniquely interactive research environment.

Collaborations among basic science disciplines and between basic and clinical faculty are stimulated by multidisciplinary centers at UAB: Center for AIDS Research, Comprehensive Cancer Center, Southern Research Institute for drug development, Center for Structural Biology, Center for Clinical and Translational Sciences, Center for Emerging Infections, Cystic Fibrosis Research Center and a campus-wide Program in Immunology. A world-class BSL3/ABSL3 building is available. UAB is one of the top clinical and research institutions in the nation, located in an affordable city with many cultural and outdoor attractions.

Microbiology at UAB ([www.microbio.uab.edu/micro-genetics/](http://www.microbio.uab.edu/micro-genetics/)) is a diverse group of scientists with a focus on microbial pathogens. Investigators with expertise in microbiome research are particularly encouraged to apply. Review of applications will continue until positions are filled. Applicants should submit their CV including a research plan (1 p), the contact information of three references and their three top publications as a single pdf file to: **Michael Niederweis, Ph.D., c/o Kristina Sinclair, email: [ksinc@uab.edu](mailto:ksinc@uab.edu).**

*A pre-employment background investigation is performed on candidates for employment. UAB is an Equal Opportunity/Affirmative Action Employer committed to fostering a diverse, equitable and family-friendly environment in which all faculty and staff can excel and achieve work/life balance irrespective of ethnicity, gender, faith, gender identity and expression as well as sexual orientation. UAB also encourages applications from individuals with disabilities and veterans.*



### Tenure-Track Faculty Position Neuroscience and Experimental Therapeutics

The Department of Neuroscience and Experimental Therapeutics invites applications for a tenure-track faculty position at the level of **ASSISTANT/ASSOCIATE PROFESSOR**. We are interested in outstanding scientists in the neurosciences, neuropharmacological or translational sciences with a strong record of extramural funding, research achievement and a commitment to graduate and medical education. Candidates should have a high level of competence and research productivity by way of scholarly publications, and a strong track record of external research grant support. The ideal candidate's research program should also complement existing research strengths in the department. Current research programs focus on molecular, cellular and behavioral approaches to study brain development, aging, circadian biology, epilepsy, neurodegenerative diseases and stroke (for more details see <http://medicine.tamhsc.edu/basic-sciences/index>).

In addition to the departmental faculty, the neuroscience community at the Texas A&M consists of 70+ faculty located in the departments of Biology/Psychology/Veterinary Medicine with an active graduate program through the Texas A&M Institute for Neuroscience (<http://tamin.tamu.edu>). Clinical collaborations are possible through the Texas Brain and Spine Institute (<http://www.txbsi.com/>) as well as the Department of Psychiatry and Behavioral Science.

This position offers an outstanding research environment in a newly built research facility with a modern vivarium, and highly competitive start up packages, compensation and benefits. Successful candidates are expected to develop independent research programs that are well funded, and that take advantage of the diverse collaborative opportunities available. Candidates will also participate in teaching programs and service assignments within the Department. Review of applications will begin as they are received and continue until the positions are filled. Applicants should submit a current curriculum vitae, a statement of research goals and names/addresses of three references to: **Dr. Farida Sohrabji, Chair of Search Committee, Department of Neuroscience and Experimental Therapeutics, Texas A&M Health Science Center, College of Medicine, Medical Research and Education Building, 8447 State Highway 47, Bryan, TX 77807 (Sohrabji@medicine.tamhsc.edu).**

*The TAMHSC is an Affirmative Action/Equal Opportunity Employer.*





Faculty of Arts & Science  
**University of Lethbridge**



# RESEARCH CHAIR SEARCH

## DEPARTMENT OF CHEMISTRY & BIOCHEMISTRY

The **University of Lethbridge** is seeking **two** exceptional scholars to fill the positions of (i) **Alberta Innovates Health Solutions (AIHS) Translational Health Chair: RNA in Health & Disease**, and (ii) **Campus Alberta Innovates Program (CAIP) Chair: Synthetic Biology & RNA Based Systems**.

(i) The **AIHS Translational Health Chair** will address the priority area of Chronic Disease and will contribute to enhancing the province's capacity to provide evidence-informed decisions regarding health promotion and disease prevention, and to translate research outcomes into effective treatment and prevention strategies and health care solutions.

The goal of this Chair position will be: (1) to develop internationally-recognized, long-term research that will build upon our understanding of factors that contribute to chronic diseases, and (2) to develop and implement effective and integrated knowledge mobilization strategies to ensure that new knowledge is transferred to end users to support disease prevention and to promote health equity in the province.

The candidate should have demonstrated expertise in the study of **structure and function of RNA-based systems** in vivo and/or in vitro using rational-design

approaches to the biological systems under study (**synthetic biology**), **biochemical, biophysical or molecular biology approaches**, and bring a special focus on applications in chronic health conditions such as cancer, inherited diseases or acquired chronic conditions, including but not limited to viral infections like HIV and hepatitis.

(ii) The **CAIP Chair**, along with a special focus on the energy sector, must bring demonstrated expertise in the engineering of biological systems (**synthetic biology**) and the study of **structure and/or function of RNA-based systems**, using in vivo and/or in vitro approaches, having made major impacts in his or her fields of research. Candidates will be expected to play a lead role in contributing to the University's capacity in synthetic biology and RNA Research.

The AIHS Translational Health Chair as well as the CAIP Chair will be appointed to the **Department of Chemistry & Biochemistry** at the University of Lethbridge.

The University of Lethbridge is home to the **Alberta RNA Research and Training Institute (ARRTI)**, the first of its kind in Western Canada. Through first-class RNA research and training excellence, ARRTI

contributes to the multidisciplinary research and teaching community at the University of Lethbridge and facilitates the transfer of leading-edge knowledge into the private and public sectors, as well as academia. Members of the Institute operate several focused laboratories including: a laboratory for **structure and function of small noncoding RNAs**, a laboratory for **biomolecular design and engineering**, a laboratory for **systems biology and mathematical modeling**, and a laboratory for **synthetic biology**.

For more information about **Canada's Research Infosource 2012 Undergraduate Research University of the Year**, please visit our website at [www.uleth.ca](http://www.uleth.ca).

For a detailed job descriptions, including submission requirements, please visit: [uleth.ca/artsci/ResearchChairSearch](http://uleth.ca/artsci/ResearchChairSearch)

For more information please contact Dr. René Boéré at [boere@uleth.ca](mailto:boere@uleth.ca).



Faculty of Arts & Science



## RISE TO THE OPPORTUNITY

with the fastest-rising universities in the world's Top 50. **NTU.**



### Faculty Positions at School of Chemical and Biomedical Engineering (SCBE)

Nanyang Technological University (NTU) in Singapore is ranked 47<sup>th</sup> in the QS World University Rankings 2012. SCBE at NTU invites applications for Assistant, Associate or Full Professors. For more information, visit [www.scbe.ntu.edu.sg/About\\_Us/Pages/Open\\_Positions.aspx](http://www.scbe.ntu.edu.sg/About_Us/Pages/Open_Positions.aspx)

#### Research Areas

##### Chemical and Biomolecular Engineering Division

- Process systems engineering
- Product and process design
- Pharmaceutical engineering
- Food engineering
- Separation technology
- Colloid and interface science

##### Bioengineering Division

- Cardiovascular biomechanics
- Bioinstrumentation
- Biosignal processing and imaging
- Biofluid
- Neuro bioengineering
- Nature inspired bioengineering
- Mechanobiology of cell-cell and cell-matrix interactions

#### Application Details

Guidelines: [www.ntu.edu.sg/ohr/Career/SubmitApplications/Pages/Faculty.aspx](http://www.ntu.edu.sg/ohr/Career/SubmitApplications/Pages/Faculty.aspx)

Email: [scbe\\_recruit@ntu.edu.sg](mailto:scbe_recruit@ntu.edu.sg)

[www.ntu.edu.sg](http://www.ntu.edu.sg)

**PURDUE**  
UNIVERSITY

### Purdue University Center for Animal Welfare Science Cluster Hire

Purdue University has a well-established record of excellence in research and teaching programs in Human Animal Bond and Farm Animal Welfare. The newly created Purdue Center for Animal Welfare Science hosts the largest collaborative group of scientists in the United States working in these fields; utilizing diverse, cross-disciplinary approaches in the areas of animal and poultry science, veterinary medicine, psychology, philosophy, genetics, public health, and zoology. The mission of the Center is to promote the welfare of animals through innovation in research, education and outreach. To further enhance our capacity, we are currently looking to fill three new tenure track positions: a Center Director and two Assistant Professors.

**Director position:** A tenure-track senior faculty position in domestic animal welfare is available to head the Center for Animal Welfare Science. This individual will lead a team of scientists and educators in the Department of Animal Sciences (College of Agriculture) and Comparative Pathobiology and Veterinary Clinical Sciences (College of Veterinary Medicine) by facilitating research, teaching, and extension efforts. For details regarding the position, please go to: <http://www.vet.purdue.edu/cpb/employment.php>

**Assistant Professor, Human-Animal Interactions position:** A tenure-track faculty position is available in Human-Animal Interactions based in the Department of Comparative Pathobiology at Purdue University College of Veterinary Medicine. For details regarding the position, please go to: <http://www.vet.purdue.edu/cpb/employment.php>

**Assistant Professor, Animal Welfare position:** A tenure-track faculty position in Animal Welfare is available at Purdue University. The home department will be determined based on the area of expertise of the successful applicant. For details regarding the position, please go to: <http://www.vet.purdue.edu/cpb/employment.php>

*A background check is required for employment in these three positions. Purdue University is an Equal Opportunity/Equal Access/Affirmative Action Employer fully committed to achieving a diverse workforce.*

### FACULTY POSITION IN STRUCTURAL BIOLOGY and/or IMAGING Department of Biochemistry and Molecular Biology Thomas Jefferson University

The Department of Biochemistry and Molecular Biology at Thomas Jefferson University in Philadelphia invites applications for faculty positions in structural biology and/or molecular/cellular imaging, with the possibility of leading development of a new research center in the field of interest. We seek outstanding investigators to complement our existing strengths in structural biology, receptor signaling and protein trafficking, DNA repair, and transcriptional-translational regulation. The Department offers a highly collaborative culture and in conjunction with the Kimmel Cancer Center provides state-of-the-art core resources for structural biology, imaging and cancer biology research (<http://www.kimmelcancercenter.org/research/>). All faculty ranks will be considered, and the successful candidate will have a demonstrated track record of research excellence and extramural funding, and will participate in graduate training.

Thomas Jefferson University is located in the vibrant Center City area of Philadelphia surrounded by a wide variety of cultural, historical, and recreational attractions. There is convenient housing for both faculty and trainees nearby, while the Philadelphia suburbs are readily accessible to Jefferson by mass transit or car. Thomas Jefferson University is an Affirmative Action/Equal Opportunity Employer.

Candidates should submit curriculum vitae, a brief statement of research interests and future plans, and contact information for three references to:

**Dr. James Keen, Chair  
Faculty Search Committee  
c/o Ms. Lisa Waites  
Department of Biochemistry & Molecular Biology  
Thomas Jefferson University  
233 South 10th Street, BLSB 350  
Philadelphia, PA 19107-5541  
[James.Keen@jefferson.edu](mailto:James.Keen@jefferson.edu)  
Or apply online at: [www.jeffersonhr.org](http://www.jeffersonhr.org)**



**Jefferson™**  
University



### McLaughlin Research Institute for Biomedical Sciences

#### Professor in Neurodegenerative Disease Research

McLaughlin Research Institute (MRI) seeks an innovative scientist at the Professor level with an established program in neurodegenerative disease research who can take advantage of the Institute's strengths in mouse genetics and animal models. Low animal care costs and transgenic services at MRI facilitate mouse-intensive projects that would be cost-prohibitive at many other centers. Applicants with interests in human stem cell models for Alzheimer's and related diseases are particularly encouraged to apply. Faculty have opportunities for collaborations with physicians at Benefis Health System which serves a patient population of 250,000. Candidates should have a record of research excellence and a demonstrated ability to compete successfully for funding. The ability to establish intramural and extramural collaborations is essential. An endowed chair is a possibility for the successful candidate.

The Institute is a small non-profit organization located near Montana's Rocky Mountain Front and offers a non-bureaucratic, interactive research environment in a spacious, modern research facility. Faculty members also benefit from the active involvement of MRI's Scientific Advisory Committee (**Irv Weissman, David Baltimore, David Cameron, Neal Copeland, Jeff Frelinger, Leroy Hood, and Nancy Jenkins**). Contact George Carlson, MRI's Director, for more information. Applications, including names and contact information for three to five individuals who may serve as references, should be sent to: **Search Committee, 1520 23<sup>rd</sup> Street South, Great Falls, MT 59405** or [admin@mri.montana.edu](mailto:admin@mri.montana.edu)



## Director of Research – Van Andel Research Institute

Van Andel Research Institute currently seeks an accomplished, energetic, and visionary Director of Research to lead the strategic development of its basic oncology science, neurodegenerative science, and translational programs. The Director will have a unique opportunity to shape and influence the focus of these research initiatives, guiding the private, independent biomedical institute to achieve its full potential.

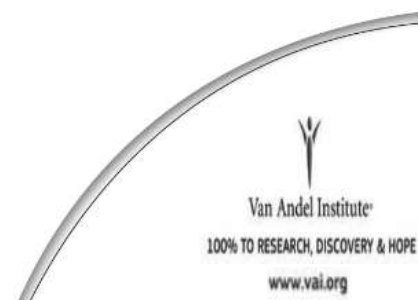
VARI is located in a rapidly growing life sciences community in Grand Rapids, Michigan; it currently houses 23 laboratories devoted to basic science/translational research and dedicated to exploring the genetic and molecular mechanisms underlying disease.

Applications are invited from candidates who have a Ph.D. in biological sciences, an M.D., or both. Candidates will be expected to have a reputation for outstanding scholarship and a track record of significant research contributions, preferably in cancer, in order to build upon our established foundation and legacy. Experience in basic science and background in translational research are requirements. Experience in clinical research is desirable, as are connections to the scientific, biotechnology, and pharmaceutical communities.

Learn more about this exceptional opportunity by visiting

<http://www.vai.org/en/about-vai/careers.aspx>

Van Andel Research Institute is an Equal Opportunity Employer.



### Established Cardiovascular Investigator

The new Department of Integrative Biology and Physiology at the University of Minnesota Medical School seeks outstanding faculty candidates in integrative systems biology of the cardiovascular system and related fields at the Associate or Full Professor levels. Substantial resources including leading focused junior faculty cluster hires for program development and new state-of-the-art research buildings are committed to this effort: <http://www.ahc.umn.edu/research/bdd/>. Successful candidates will have an established and innovative research program that embraces biological complexity from molecular building blocks to the living organism. Applicants must have a strong record of research accomplishments, as documented by publications in leading peer-reviewed journals. A commitment to excellence in teaching is essential. An outstanding record of extramural funding with a multiple grant portfolio is required. Minimum requirements are a PhD, MD or MD/PhD with tenure at an academic research institution. Additional information about the department: <http://physiology.med.umn.edu/>. Information on the vibrant Twin Cities community and Minnesota's acclaimed high quality of life: <http://www1.umn.edu/wishyouwerehere/>. **Nominations are appreciated: Dr. Randi Lundell [rmlunde@umn.edu](mailto:rmlunde@umn.edu).** Applicants please apply on-line (<http://www1.umn.edu/ohr/employment/> – requisition number #179062; submit cover letter, curriculum vitae, statement of programmatic and research goals, and reference letters to this web address).

*The University of Minnesota is an Equal Opportunity Educator and Employer.*

### ASU<sup>®</sup> SCHOOL OF Life Sciences

ARIZONA STATE UNIVERSITY

### New Faculty Position in Biology and Education

The School of Life Sciences at Arizona State University is making a commitment to enhancing life science education at the undergraduate level. ASU is a dynamic, progressive university dedicated to interdisciplinary collaborations, to rethinking university education, and to integrating excellence in research and teaching. The School of Life Sciences at Arizona State University's Tempe campus is committed to reflective curricular development and innovation, with a focus on learner-centered education and teaching excellence. We are revising introductory courses, promoting active learning, and introducing a diversity of innovative approaches to instruction. ASU offers opportunities for collaboration with diverse science education initiatives across the university. To support this effort, the School invites applications for a tenure-track position at any level. The successful applicant will have a strong disciplinary content knowledge in biological sciences, established expertise in and commitment to biology education including scholarship related to teaching and learning and evidence of the capacity for leadership. Candidates must have a primary research focused on teaching and learning in biology at the undergraduate level, which will promote quality undergraduate instruction through independent and collaborative efforts and will promote the SoLS teaching mission. The successful candidate will demonstrate scholarly excellence with the capacity to develop and sustain a creative, extramurally-funded research program in education-related work in the biological sciences, with evidence of interdisciplinary collaboration. In addition, candidates with demonstrated records of mentoring at the undergraduate, graduate, and/or postdoctoral levels, strong records of outreach and service, and experience working in a highly-interdisciplinary environment like the ASU School of Life Sciences are preferred. The start-up package, teaching, and service loads will support the expected high research productivity. Candidates must have a Ph.D. in biological sciences or education, with experience or training equivalent to a Master's degree in the other area. All qualifications will be evaluated as appropriate to the level of appointment.

To apply, send a cover letter, curriculum vitae, three representative publications, separate statements of research focus/plans, teaching philosophy/experience, and three reference letters of support to **Anna Fields, attn. Biology Education Faculty Search Committee, School of Life Sciences, PO Box 874501, Tempe, AZ 85287-4501**, with electronic applications sent as PDF files to [solsfacultysearch@asu.edu](mailto:solsfacultysearch@asu.edu) preferred. The initial closing date for receipt of complete applications is **February 22, 2013**; the committee will review applications weekly thereafter until the search is closed. For additional information, please feel free to contact **James Collins** ([jcollins@asu.edu](mailto:jcollins@asu.edu)) or **Jane Maienschein** ([Maienschein@asu.edu](mailto:Maienschein@asu.edu)).

*A background check is required for employment at Arizona State University, which is an Equal Opportunity/Affirmative Action Employer committed to excellence through diversity. We especially encourage women and minorities to apply. For additional information on this position and the School of Life Sciences, please visit <http://sols.asu.edu/jobs>.*

## The best ideas in medicine start with the best people.

At Stony Brook Medicine, our highest calling is to put the power of ideas to work in our patients' lives. Stony Brook Medicine integrates and elevates all of Stony Brook University's health-related initiatives: education, research and patient care. It includes Stony Brook University Hospital, Long Island's premier academic medical center. With 597 beds, SBUH is the region's only tertiary care center and Regional Trauma Center. We are home to the Stony Brook Heart Institute, Stony Brook Cancer Center, Stony Brook Long Island Children's Hospital, Stony Brook Neurosciences Institute and Stony Brook Digestive Disorders Institute. At Stony Brook Medicine, we put the power of ideas to work. Join our team at Stony Brook Medicine — the best ideas in medicine.

### Assistant/Associate Professor

Stony Brook University's Department of Physiology and Biophysics and the Stony Brook Cancer Center invite applications for a tenure-track Assistant Professor Position. Exceptional candidates at the Associate Professor level will also be taken into consideration. The successful candidate is expected to have an externally funded program in cancer-related research. The position includes a generous start-up package and laboratory space in the Department of Physiology and Biophysics. Departmental and Institutional support facilities include cores for advanced microscopy and imaging, proteomics, microarray, metabolomics/lipidomics and bioinformatics. The Department also has access to the facilities at Brookhaven National Laboratory. For a description of departmental research activities, please visit <http://www.pnb.sunysb.edu/>. For additional information about the Cancer Center, visit <http://cancer.stonybrookmedicine.edu>. To qualify for an appointment as an Associate Professor, the candidate must meet the criteria established by the School of Medicine (School of Medicine's Criteria for Appointment, Promotion and Tenure). A PhD, MD or MD/PhD; postdoctoral research experience; and a record of peer-reviewed publications are required. The priority deadline is May 1, 2013.

For a full position description, application procedures or to apply online, visit [www.stonybrook.edu/jobs](http://www.stonybrook.edu/jobs) (Job Reference #: F-7698-13-01) or submit a State employment application, curriculum vitae, list of publications, description of research interests and three letters of reference to:

Search Committee Chair  
Department of Physiology and Biophysics  
Stony Brook University  
Stony Brook, NY 11794-8661



**Stony Brook  
Medicine**

Stony Brook University/SUNY is an affirmative action, equal opportunity educator and employer.



UNIVERSITY OF MINNESOTA  
Driven to Discover™

### TWIN CITIES CAMPUS FACULTY POSITIONS SUSTAINABLE HORTICULTURE TENURE-TRACK ASSISTANT PROFESSOR POSITIONS (2) IN SUSTAINABLE & ORGANIC FOOD SYSTEMS

The University of Minnesota has openings for two nine-month, tenure-track Assistant Professor positions in Sustainable & Organic Horticultural Food Systems. The tenure home for these positions will be in the Dept. of Horticultural Science. The successful candidates will each develop and teach one foundational course in the Sustainable and Organic Food Systems initiative and another upper-level course for undergraduates in his/her area of specialization. The individuals will also be expected to lead and participate in graduate-level seminar courses, advise undergraduates and graduate students.

**Assistant Professor – Sustainable & Organic Horticultural Food Production Systems**, 60% teaching, 40% research. Requisition #182205.

**Assistant Professor – Biological Principles of Sustainable & Organic Food Systems**, 60% teaching, 40% research. Requisition #182695.

For complete job descriptions, go to: <https://employment.umn.edu> and search postings. Review of applications will begin **March 15, 2013**.

*The University of Minnesota is an Equal Opportunity Educator and Employer.*



### Faculty Positions in Human Immunology at the Vaccine & Gene Therapy Institute of Florida

At the Vaccine & Gene Therapy Institute of Florida (VGTI Florida), we are committed to discovering innovative therapies and vaccines to improve human health. It is ultimately the researchers we recruit that determines our success and our state-of-the-art technologies and resources that enables our institute to realize these successes. Our scientists are the most important asset in our pursuit of achieving excellence in research. Our staff not only enjoys outstanding benefits but also work in an environment noted for community involvement, intellectual excitement, and natural beauty.

We are seeking to recruit outstanding Immunologists in the areas of Infectious Disease and Cancer Immunobiology to direct programs in basic and translational human immunology. Candidates are expected to assist in establishing clinical research immunology programs and recruit additional Principal Investigators. VGTI Florida is one of the internationally acclaimed research institutes invited to locate to Florida as part of a State-sponsored initiative to enhance biomedical research in Florida. Research at VGTI Florida focuses on Global Health initiatives utilizing systems biology approaches to study the human innate and adaptive immune response to infectious diseases and cancer.

Research themes of VGTI-FL include:

- HIV-1 and emerging infectious pathogens
- Influenza
- Vaccine development and adjuvants
- Cancer Immunology
- Ageing and the immune response

VGTI Florida has ongoing basic and clinical research collaborations with the University of Miami, Moffitt Cancer Center and Martin Health Systems. The institute occupies a new 100,000 sq. ft. state of the art and LEED Gold Certified facility in Port St. Lucie, FL. The institute is located on the sunny Atlantic coast in a Biotech cluster that includes Torrey Pines Institute for Molecular Studies, the Mann Research Center, and the new Tradition Medical Center. Florida Atlantic University, the Scripps Research Institute of Florida and the Max Planck Florida Institute for Neuroscience are within 30 minutes' drive.

Successful candidates (M.D. and/or Ph.D.) will have an established extramurally funded research program and a strong publication record in one of the priority areas described above. The positions have highly competitive salary and startup packages, with access to state-of-the-art Genomics, Bioinformatics and Flow Cytometry core facilities as well as BSL3/ ABSL3 containment facilities within the institute. For more information, including a description of the Faculty and their research interests, please visit: [www.vgtifl.org](http://www.vgtifl.org). Qualified candidates should apply by submitting their curriculum vitae and a description of their proposed research program: <https://home.eease.adp.com/recruit/?id=3795661>

*VGTI Florida is an Equal Opportunity Institution, committed to recruiting, hiring, and promoting qualified minorities, women, individuals with disabilities, and veterans.*

## CAREER TRENDS

Running  
Your Lab



Download your free copy today at  
[ScienceCareers.org/booklets](http://ScienceCareers.org/booklets)

**Science Careers**

From the journal *Science*



Brought to you by the  
AAAS/Science Business Office



Joint Conference of HGM 2013 and 21<sup>st</sup> International Congress of Genetics

# Genetics & Genomics OF GLOBAL HEALTH AND SUSTAINABILITY

13-18 April 2013 | The Sands Expo and Convention Center, Marina Bay Sands

Join over 100 speakers worldwide and explore two of the most important issues in the 21<sup>st</sup> century: **Human Health and Global Sustainability.**

Among the prominent speakers are:

• **Peer Bork**, European Molecular Biology Laboratory • **Allan Bradley**, Wellcome Trust Sanger Institute • **Caroline Dean**, John Innes Centre, Norwich Research Park Colney • **Wang Jun**, BGI • **Jay D Keasling**, Joint BioEnergy Institute • **Narry Kim**, Seoul National University • **Barbara Meyer**, University of California Berkeley • **Linda Partridge**, University College London • **Luis Serrano**, Centre for Genomic Regulation • **Mike Stratton**, Wellcome Trust Sanger Institute • **Mike Snyder**, Stanford Center for Genomics and Personalised Medicine • **Joseph Takahashi**, South Western Medical Center • **Krishnaswamy Vijayraghavan**, National Centre for Biological Sciences • **Qifa Zhang**, Huazhong Agricultural University

Attractive rates available for HUGO members and graduate students! Visit [www.hgm2013-icg.org](http://www.hgm2013-icg.org) to find out more.

For enquiries, email [info@hgm2013-icg.org](mailto:info@hgm2013-icg.org) or call +65 6411 6695.

**hgm  
icg 2013**  
SINGAPORE

[www.hgm2013-icg.org/a](http://www.hgm2013-icg.org/a)



## POSITIONS OPEN

### UW Medicine SCHOOL OF MEDICINE

The Seattle Children's Research Institute and the Department of Pediatrics at the University of Washington School of Medicine are recruiting a qualified individual to serve as the **Director for the Center for Childhood Infections and Prematurity Research** at Seattle Children's Research Institute. The Center's research vision is to translate basic biology to strategies for the diagnosis, treatment and prevention of infectious diseases and conditions that impact children locally, nationally, and globally. The Center for Childhood Infections and Prematurity Research is located on one floor of the modern 225,000sq ft. Seattle Children's Research Institute and has mature programs in host-pathogen interactions, global and emerging infectious diseases, vaccine discovery and evaluation, mechanisms of microbial drug resistance.

The Center Director will be responsible for the allocation of research space and available resources within the policies of the SCRI and will develop a vision for the Center, recruit outstanding scientists, support and collaborate with current scientists within the Center, mentor current and future faculty, and actively participate in philanthropic efforts on behalf of the Center and Seattle Children's Research Institute. This is a full-time academic appointment at the rank of Professor, without tenure (MD and/or PhD required). The successful candidate must have an established record of academic achievement and leadership experience and active NIH-funded research grants. For more information see: [www.seattlechildrens.org/research](http://www.seattlechildrens.org/research). Please send CV and a statement of current and future research interests to: **Danielle Zerr, MD, MPH, Chair, Search Committee, Professor, Department of Pediatrics, Division of Infectious Disease, Danielle.Zerr@seattlechildrens.org**

*University of Washington faculty engage in teaching, research, and service. In order to be eligible for University sponsorship for an H1-B visa, graduates of foreign (non-U.S.) medical schools must show successful completion of all three steps of the U.S. Medical Licensing Exam (USMLE), or equivalent as determined by the Secretary of Health and Human Services. The University of Washington is building a culturally diverse faculty and strongly encourages applications from female and minority candidates. The University is an Equal Opportunity Affirmative Action Employer.*

**If you have a question about the details of this search/position please contact the hiring unit directly. Thank you for your interest in this position at the University of Washington.**

## FACULTY POSITIONS

### UT SOUTHWESTERN MEDICAL CENTER

#### CHAIR Department of Bioinformatics

The University of Texas Southwestern Medical Center is searching for a Chairperson to establish a new Department of Bioinformatics. We are seeking an individual to form a world-class department within an exceptionally strong biomedical research environment. The successful candidate will have a robust and internationally recognized research program in bioinformatics, a record of superb scientific achievement, outstanding leadership skills, and a strong vision for establishing and leading the department. The Chair will be expected to recruit six new faculty members who are leaders in bioinformatics and informatics-driven biomedical discovery. The Chair will also foster and grow a research environment that integrates with existing departments, programs, and infrastructure and will establish a graduate program in bioinformatics and genomics. Significant resources will be provided to accomplish these endeavors.

Interested individuals should send a curriculum vitae and a cover letter to the **Chair of the Search Committee, W. Lee Kraus, Ph.D. ([lee.kraus@utsouthwestern.edu](mailto:lee.kraus@utsouthwestern.edu))**.

*The University of Texas Southwestern Medical Center is an Equal Opportunity Institution.*

## Postdoc Careers

Special Career Feature: March 8, 2013

Reserve your ad by February 19 to guarantee space.\*

\*Ads accepted until March 4 if space is still available.

ScienceCareers.org

**Special  
Distribution:**  
Additional mailing  
to 100,000 scientists  
beyond our regular  
circulation

### Here's why you should advertise in this issue:

Scientific collaborations are a key element of success in the current economic climate. Postdocs, more than ever, must be effective at identifying and forging relationships with fellow scientists and organizations. This special feature examines how to best develop these types of partnerships, and Ph.D.s from around the globe will be reading this important content. Tell these scientists what exciting postdoc experiences await them at your university or organization.

Your job ad is seen by 700,000 readers around the globe from varied backgrounds and it sits on special bannered pages promoting postdoctoral opportunities. Over 57% of our weekly readers work in academia and 67% are Ph.D.s. *Science* connects you with more scientists in academia than any other publication.

- Bonus distribution to National Postdoctoral Association, 15–17 March, Charleston, SC
- Bonus distribution to PittCon, 17–21 March, Philadelphia, PA
- Special distribution to 100,000 additional scientists beyond our regular circulation

### To Book Your Ad:

E-mail:  
[advertise@sciencecareers.org](mailto:advertise@sciencecareers.org)

Or telephone us:  
**US:** 202-326-6582  
**Europe/RoW:** +44 (0) 1223 326500  
**Japan:** +81-(0) 90-9110-1719  
**China/Korea/Singapore/Taiwan/  
Thailand:** +86-1367-1015-294

For recruitment in science,  
there's only one **Science**





## Postdoctoral Fellowships in Genomic Biology at the University of Illinois at Urbana-Champaign

The Institute for Genomic Biology at the University of Illinois at Urbana-Champaign offers a number of fellowships for truly exceptional young scholars who have completed their Ph.D. within the last several years, and are looking for a stimulating and supportive interdisciplinary environment to carry out independent and collaborative research in the field of genomic biology. IGB Fellows will spend up to three years conducting research in one of several research themes in the Institute, and ideally this research will also overlap with two or more of these thematic areas. Visit [www.igb.illinois.edu/content/fellows-application](http://www.igb.illinois.edu/content/fellows-application) for more information about the Institute, the research themes and the application procedures. The closing date for all positions is April 1, 2013. Fellows will be announced on or about May 15, 2013.

### Biocomplexity

We seek a postdoc with a strong quantitative background to join a multidisciplinary group exploring collective effects in biology from the genome to the ecosystem scale. Ongoing research addresses the emergence of life and the nature of evolution prior to the Last Universal Common Ancestor, the evolution of core cellular machinery in Archaea and other domains of life, the role of horizontal gene transfer in shaping communities of microbes and phages, geomicrobiology, and the systems biology of microbes, biofilms and ecosystems. We are also developing an interest in evolutionary medicine, with special interest in combating the emergence of antibiotic resistance. (Nigel Goldenfeld, Theme Leader)

### Genomic Ecology of Global Change

The Fellow will be involved in a cross-disciplinary project investigating how changes in networks of genes affect plant and ecosystem function when challenged by elements of global change, including greater carbon dioxide, ozone, drought, temperature, disease and herbivory. The ideal candidate will have a strong background in plant biology and a record of expertise in molecular biology, genomic ecology, physiology or modeling of gene networks or ecosystem function. The ability to work creatively and productively in a highly interdisciplinary and collaborative environment is essential. (Don Ort, Theme Leader)

### Energy Biosciences Institute

The Energy Biosciences Institute (EBI) is an externally funded theme within the IGB. It is the largest academia collaboration to date, currently receiving \$500 million over ten years and focusing on the development of second-generation biofuels intended to significantly slow the rate of global climate change. Its research ranges from systems biology of fermentative organisms to quantification of ecosystem services provided by new sustainable biofuel crops. The EBI also has an interest in geomicrobial approaches to increasing the efficiency of oil extraction. The full range of research can be seen at [www.energybiosciencesinstitute.org](http://www.energybiosciencesinstitute.org). We seek an outstanding candidate across these areas interested in applying genomic biology to understanding and developing opportunities for improving sustainable biofuel production. Research can be at any point in the supply chain from improving feedstocks and their environmental sustainability to producing fuel. The appointee will work in an interdisciplinary laboratory of over 100 exceptional colleagues focused on this challenge. The appointment would also involve collaboration with our partners: UC Berkeley and BP. (Isaac Cann, Theme Leader)

### Cellular Decision Making in Cancer

We seek an individual with interest in quantitative biology. Our theme faculty members have expertise in single molecule biophysics, genomics and chemical biology. Building on the current strengths on cell death, antiviral signaling, stem cell differentiation, live cell probing of decision making and genome instability modeling, we aim to develop a multiple-scale narrative on how single molecule events in the cell are integrated into the protein networks to determine the cell fate. Cancer is a major focus area of research. (Taekjip Ha, Theme Leader)

### Business, Economics, and Law of Genomic Biology

We seek an individual with training in economics, business, law, or strategy and with an interest in technology entrepreneurship, technology industries, and biotechnology. The Fellow will join a multidisciplinary group that includes business, law, and technology experts; agricultural economics faculty; and personnel from the campus Office of Technology Management. Our theme is exploring issues in university-industry technology transfer, industry evolution,

intellectual property protection, the competitive and cooperative dynamics for both entrepreneurial start-ups and existing corporations, the impact that globalization of biotechnology has on the evolution of industry, and the position of U.S. firms in the global marketplace. (Jay Kesan, Theme Leader)

### Regenerative Biology & Tissue Engineering

The Fellow will be involved in one or more of our multidisciplinary projects related to regenerative biology and harnessing the potential of adult/embryonic stem cells for tissue engineering applications. Of particular interest is leveraging theme expertise in biomaterials fabrication, drug delivery systems, microfluidics-based *in vitro* experimental platforms, and *in vivo* evolutionary biology and regeneration medicine studies. The ideal candidate will have experience in one or more areas of (stem) cell biology, induced pluripotent cell technology, biomaterials, microfluidics, and/or tissue engineering. (Paul Kenis, Theme Leader)

### Mining Microbial Genomes

The Fellow will be involved in one of several multidisciplinary projects focused on (1) the discovery, design, and development of novel antibiotics, or (2) the assignment of function to novel enzymes discovered in genome projects. The ideal candidate will have a proven record of expertise in microbially produced natural products and/or enzyme evolution. We are interested in candidates with previous experience in bacterial metabolism, bacterial genetics, molecular biology, biochemistry, enzyme evolution, metabolic engineering, organic synthesis, mass spectroscopy, bioinformatics and/or metagenomics. (Bill Metcalf, Theme Leader)

### Gene Networks and Diversity

We seek a biologist with strong bioinformatics skills and training in one or more of the following areas: gene regulation (especially relating to transcription factor dynamics or epigenomics), evolutionary biology, neuroscience, or systems biology. Applicants with expertise in both experimental biology and bioinformatics will be strongly preferred. The successful candidate will join a multidisciplinary team using systems biology approaches to analyze regulatory mechanisms underlying complex developmental and behavioral phenotypes, and components that may define determinants of inter- and intraspecies diversity. Fellows are expected to conduct research that contributes to the development of theme goals by integrating components from multiple theme members' areas of expertise. (Lisa Stubbs, Theme Leader)

### Host-Microbe Systems

The Fellow will be responsible for developing DNA isolation, microbial isolation, 16S rRNA gene sequencing and other metagenomic analysis techniques for surveying microbial content of the human and nonhuman primate vaginal and intestinal microbiomes. Additional responsibilities will include the culture isolation and genome sequencing and other molecular biology techniques to examine microbial, metabolic, and immunologic contents, phylogenetic comparisons, and performing analyses using bioinformatics and other computational and analytical methods. The ideal candidate will have a strong background in microbiology, biochemistry, or a related field with experience and expertise in molecular microbial ecology and bioinformatics and/or biostatistics. (Brenda Wilson, Theme Leader)

### The University of Illinois is an Affirmative Action/ Equal Opportunity Employer

[www.igb.illinois.edu](http://www.igb.illinois.edu)



## Postdoctoral Position Announcement at the University of Illinois at Urbana-Champaign, Institute for Genomic Biology

We are seeking postdoctoral research associates to conduct research on a five-year research award from the Bill & Melinda Gates Foundation (BMGF). The project, titled "RIPE – Realizing Increased Photosynthetic Efficiency," has the potential to benefit farmers around the world by increasing productivity of staple food crops. The goal of the research is to improve the photosynthetic properties of key food crops, particularly rice and cassava. Increasing photosynthetic efficiency has not yet been addressed by conventional breeding methods, though it has the potential to increase yields and increase efficiency of water and nitrogen use. Project team members will apply recent advances in photosynthesis research and crop bioengineering in RIPE. In addition, computer simulation models of the highly complex photosynthetic system, from metabolic networks to field crop biophysics, combined with practical engineering, will identify the best targets for improving photosynthesis efficiency.

**DUTIES & RESPONSIBILITIES:** The postdoctoral positions will conduct research to improve photosynthesis and yield in C3 crop plants. Responsibilities of the team of appointees will be to develop a computational engineering framework for selecting systems and synthetic approaches to increasing crop photosynthesis, practical engineering of the selected changes, and molecular, biochemical and whole crop physiological phenotyping in the laboratory and field.

**EDUCATION & EXPERIENCE:** Prospective candidates need a PhD in plant biology, plant genetics, plant biotechnology or a closely related discipline. Demonstrated skills in one or more of the following areas of photosynthesis research is required: molecular biology and genetics, plant transformation, use of available bioinformatics resources, gas exchange and/or mechanistic modeling which could be at the level of metabolic pathways or field crop biophysics/micrometeorology. The duties of this position require that the incumbent have a strong background in plant molecular biology, plant biochemistry/physiology, or computational biology and be broadly knowledgeable of photosynthesis. Good oral and written communication skills coupled with the ability to work independently and cooperatively are required.

**PROPOSED START DATE:** As soon as possible.

**SALARY:** Commensurate with qualifications and experience.

**APPOINTMENT STATUS:** Up to five years, contingent on changes in project scope and performance.

**APPLICATION PROCESS:** Please send a letter of application, resume/CV, and three professional references including phone number and email address to the RIPE Program Manager, Lisa Emerson <lemerson@illinois.edu>.

Universität  
Konstanz



The University of Konstanz, with its Institutional Strategy to promote Top-Level Research, has been receiving continuous funding since 2007 within the framework of the Excellence Initiative by the German Federal and State Governments.

The *Zukunftskolleg* of the University of Konstanz is offering:

**A. up to fifteen ZIF Marie Curie 2-year Postdoctoral Fellowships in any discipline represented at the University of Konstanz (Salary Scale 13 TV-L)**

for researchers in the early stage of their career, so as to enable them to develop and implement individual and independent research projects.

Fellowships will begin on September 1, 2013, and end on August 31, 2015. **Reference number 2013/015**

**B. up to seven ZIF Marie Curie 5-year Research Fellowships in any discipline represented at the University of Konstanz (Salary Scale 14 TV-L)**

for the development and implementation of individual research projects.

Fellowships will begin on November 1, 2013, and end on October 31, 2018. **Reference number 2013/014**

Applications, supporting materials, and two letters of reference should be submitted in English **by March 15, 2013 (17:00:00 GMT + 1:00) using the Online Application Platform:**

**[www.zukunftskolleg.uni-konstanz.de/online-application](http://www.zukunftskolleg.uni-konstanz.de/online-application)**

Details concerning application requirements and information about the *Zukunftskolleg* are available on our website: <http://www.zukunftskolleg.uni-konstanz.de>

**Contact:** Dr. Nani Clow  
e-mail: [n.clow@uni.kn](mailto:n.clow@uni.kn)  
phone: +49 (0) 75 31/88-5678



**Research Position at  
ICYS, NIMS, Japan**



The International Center for Young Scientists (ICYS) of the National Institute for Materials Science (NIMS) is now seeking a few researchers. Successful applicants are expected to pursue innovative research on broad aspects of materials science using most advanced facilities in NIMS (<http://www.nims.go.jp/eng/index.html>).

In the ICYS, we offer a special environment that enables young scientists to work independently based on their own idea and initiatives. All management and scientific discussions will be conducted in English. An annual salary between 5.03 and 5.35 million yen (level of 2012) will be offered depending on qualification and experience. The basic contract term is two years and may be renewed to one additional year depending on the person's performance. A research grant of 2 million yen per year will be supplied to the ICYS researcher.

All applicants must have obtained a PhD degree within the last ten years. Applicants should submit an application form, which can be downloaded from our web site, together with a resume (CV) and a list of publications. A research proposal on an interdisciplinary or integrated area related to the materials science should also be submitted. The application letter should reach the following address via e-mail or air mail **by March 29, 2013**. Visit our website for more details (<http://www.nims.go.jp/icys/>).

ICYS Administrative Office,  
National Institute for Materials Science  
Sengen 1-2-1, Tsukuba, Ibaraki 305-0047, Japan  
e-mail: [icys-recruit@nims.go.jp](mailto:icys-recruit@nims.go.jp)



## FACULTY POSITIONS

### FACULTY POSITION

University Of Florida

Department of Geography and the  
Emerging Pathogens Institute (EPI)

Department of Geography and the Emerging Pathogens Institute (EPI) invite applications for a full-time position at the level of **ASSISTANT** or **ASSOCIATE PROFESSOR**, starting August 16, 2013. This is a nine-month, tenure accruing, research-oriented position, with a specialization in quantitative spatial and spatio-temporal models to address questions in infectious diseases or public health. Specialties can include (but are not limited to) geospatial or mathematical modeling for transmission of human and animal diseases, interactions between climate and disease ecology, relationships between socio-economics and disease risk, and health intervention strategies. We seek individuals with demonstrated success in grant activity and publications in top journals. The successful candidate should possess a doctoral degree in Geography or other relevant disciplines and will be expected to engage deeply in the EPI research program while maintaining good standing in teaching and service to the Geography Department and its mission. Submit a curriculum vitae and letter of application describing research program and its future to **Dr. Peter Waylen, Search Committee Chair, Department of Geography, University of Florida, Box 117315, Gainesville, FL, 32611**. We prefer that application materials be sent electronically to **e-mail: prwaylen@ufl.edu** and the application be completed online at **website: <http://jobs.ufl.edu/postings/31925>**. All application materials must be received by March 15, 2013. Short-listed candidates will be contacted to provide three letters of reference. *Minorities, women, and those from underserved groups are encouraged to apply. The University of Florida is an Equal Opportunity Institution.*

### ASSISTANT/ASSOCIATE PROFESSOR of Biology

Morris College, a private four year Liberal Arts College in Sumter, South Carolina, is seeking to fill the following position(s): Assistant/Associate Professor of Biology. Will teach three sections of a laboratory-based, general education (for non-majors), introductory biological sciences course. Duties also include student advising, committee assignments, participation in registration, and other duties as needed. Must have a Ph.D. or M.S. degree in biology. Must be available for employment in August 2013.

Submit a letter of application, personal resume, three letters of recommendation, and official academic transcripts to: **Director of Personnel, Morris College, 100 W. College, Sumter, SC 29150-3599**. *Morris College is an Equal Opportunity/Affirmative Action Employer.*

The Department of Biological Sciences at Chicago State University (CSU) seeks applications for three tenure-track **ASSISTANT PROFESSOR** positions. Appointments begin in August 2013. All areas of biology will be considered; however, preference will be given to candidates in microbiology, cell biology, zoology, urban agriculture/aquaponics, and secondary education. Selected individuals are expected to establish a research program involving undergraduate and graduate students, supported by extramural funding. Ph.D. in Biology or related fields required; postdoctoral and/or teaching experience preferred. Only electronic applications are accepted. Instructions are available at **website: <https://chicagostate.peopleadmin.com/postings>**. Review will start immediately and will continue until February 28, 2013. Reference letters (3) will be accepted electronically at **e-mail: [bhome@csu.edu](mailto:bhome@csu.edu)**. *CSU is an Equal Opportunity/Affirmative Action Employer.*

### UNIVERSITY OF HAWAII at Manoa Cancer Center

**ASSISTANT RESEARCHER** (Cancer Biology Program), **Position #70209**, Tenure-track, Continuous—application review begins February 5, 2013. Refer to **website: <http://www.pers.hawaii.edu/wuh/>** for complete information. *The University of Hawaii is an Equal Opportunity/Affirmative Action Institution. Women and minorities are encouraged to apply.*



*EMBL offers a highly collaborative, uniquely international culture. It fosters top quality, interdisciplinary research by promoting a vibrant environment consisting of young, independent researchers with access to outstanding graduate students and postdoctoral fellows. EMBL is an inclusive, equal opportunity employer offering attractive conditions and benefits appropriate to an international research organisation.*

## Group Leader Membrane Protein Structural Biology at EMBL/CSSB Hamburg, Germany

This Group Leader position will be associated with EMBL as a partner of the future Center for Structural Systems Biology (CSSB) on DESY Campus, which will allow highly interdisciplinary research across its members.

State-of-the-art infrastructures for applications in Life Sciences on DESY Campus, Hamburg, Germany, provide a world-class environment for most challenging experiments in Structural Biology with high scientific significance. The Hamburg Unit of EMBL has built an integrated facility in Structural Biology with three synchrotron radiation beamlines for applications in macromolecular X-ray crystallography and small angle X-ray scattering of biological samples at the new PETRA III ring.

The successful candidate is expected to have his/her research focus matching experience and research projects in membrane protein crystallography with medically relevant research interests, preferably in infection biology. It should include:

- Innovative use of synchrotron radiation in structural biology
- Complementary “hybrid” structural biology approaches
- Interest into Free Electron Laser applications (optionally)
- Plans for complementary functional experiments

The candidate will take a leading role both at CSSB and the EMBL Hamburg Unit. She/he should have a PhD or similar degree in a relevant research area, at least three years of postdoctoral experience and an excellent research record.

Please apply online through **[www.embl.org/jobs](http://www.embl.org/jobs)** and include a cover letter, CV and a concise description of research interests and future research plans. Please also arrange for 3 letters of recommendation to be emailed to **[references@embl.de](mailto:references@embl.de)** at the latest by 17 March 2013.

**Interviews** are planned for 22 and 23 April 2013.

Further details on Group Leader appointments can be found under **[www.embl.org/gl\\_faq](http://www.embl.org/gl_faq)**.

For further information about the position and about research at EMBL please visit ...

**[www.embl.org](http://www.embl.org)**



## AAAS is here – helping scientists achieve career success.

Every month, over 400,000 students and scientists visit ScienceCareers.org in search of the information, advice, and opportunities they need to take the next step in their careers.

A complete career resource, free to the public, *Science* Careers offers a suite of tools and services developed specifically for scientists. With hundreds of career development articles, webinars and downloadable booklets filled with practical advice, a community forum providing answers to career questions, and thousands of job listings in academia, government, and industry, *Science* Careers has helped countless individuals prepare themselves for successful careers.

As a AAAS member, your dues help AAAS make this service freely available to the scientific community. If you're not a member, join us. Together we can make a difference.

To learn more, visit [aaas.org/plusyou/sciencecareers](https://aaas.org/plusyou/sciencecareers)

